

Influence of Water on the Mechanical Properties of Wood Investigated Using X-Ray and Neutron Scattering

Dissertation

zur Erlangung des Doktorgrades

der Mathematisch-Naturwissenschaftlichen Fakultät

der Christian-Albrechts-Universität

zu Kiel

vorgelegt von

Ingo Grotkopp

Kiel

2006

Referent: Professor Dr. M. Müller

Korreferent: Professor Dr. W. Press

Tag der mündlichen Prüfung: 10. Juli 2006

Zum Druck genehmigt: Kiel, den 31. Juli 2006

gez. Professor Dr. J. Grotemeyer, Dekan

Kurzfassung

Einfluss von Wasser auf die mechanischen Eigenschaften von Holz, untersucht mittels Röntgen- und Neutronen-Streuung

Beträchtliches Wissen über Holzbearbeitung wurde in tausenden von Jahren angesammelt. So sind die Veränderungen in den mechanischen Eigenschaften von Holz durch Wasseraufnahme, wie Schwellen und Erweichen, allgemein bekannt. Jedoch auf molekularer Ebene sind die zugrunde liegenden Mechanismen nicht immer vollständig verstanden und daher Gegenstand dieser Arbeit.

Holz ist ein Verbundwerkstoff der hauptsächlich aus steifen Zellulosekristallen besteht, die von einer weicheren wasseraufnehmenden Matrix umgeben sind. Die mechanischen Eigenschaften bei unterschiedlichen Wassergehalten wurden am Beispiel von Kiefer-Frühholz in kombinierten Röntgen-Diffraktions- und Streck-Experimenten untersucht. Die Streckkurve kann in vier Bereiche unterteilt werden. Diese Bereiche sind begleitet von zugehörigen Veränderungen in der Orientierung und Dehnung der Zellulosekristalle. Dabei ist das Erweichen auf den Anfang der Streckkurve beschränkt. Hingegen ist das für alle Proben gefundene Kaltverfestigen unabhängig vom Wassergehalt. Zusätzlich an Flachsfasern mit hochorientierten Zellulosekristallen durchgeführte inelastische Neutronen-Streuexperimente zeigten, dass das Wasser die starken Bindungen entlang der Zelluloseketten nicht beeinflusst. Vermutlich bilden die Wassermoleküle ein anisotropes Netzwerk aus einigen Wassermolekülen zwischen den Hydroxylgruppen der Polymerketten.

All diese Experimente waren nur möglich durch diverse technische Verbesserungen die im Rahmen dieser Arbeit entstanden, wie z.B. die Apparatur HUSTEN oder die Detektor-entzerrung mittels „Thin-Plate-Splines“.

Abstract

Influence of Water on the Mechanical Properties of Wood Investigated Using X-Ray and Neutron Scattering

An enormous amount of empirical knowledge about woodworking has been collected during thousands of years. Changes in the mechanical properties of wood due to water uptake, such as swelling and softening, are common knowledge. However, on the molecular level the mechanisms behind these effects are not always fully understood and are the focus of the present thesis.

Wood is a composite material that mainly consists of stiff cellulose crystals surrounded by a softer, water adsorbing matrix. The mechanical properties of pine earlywood have been studied in combined X-ray diffraction and stretching experiments at different water content. The stress-strain curve can be divided into four regions. These regions are accompanied by corresponding changes in the orientation and elongation of the cellulose crystals. The material softening is localised in the beginning of the stress-strain curve, additionally, the strain-hardening found in all samples is independent of moisture content. Additionally, inelastic neutron scattering experiments have been performed on flax fibres with highly oriented microfibrils leading to different spectroscopic data for the directions along and perpendicular to the cellulose crystals. Water does not affect the strong bonds along the cellulose chains. Possibly, the water molecules are situated in an anisotropic network, consisting of a few water molecules between the hydroxyl groups of the polymer chains.

All these experiments have been possible only due to the technical improvements developed in the context of this thesis, for example, the apparatus HUSTEN or the detector distortion compensation based on ‘thin-plate-splines’.

To my wife, Janina!

© This work is subject to copyright. All rights reserved, whether the whole or part of the material is concerned, specifically the rights of translation, reprinting, reuse of illustrations, recitation, broadcasting, reproduction on microfilms or in other ways, and storage in data banks. Duplication of this publication or parts thereof is only permitted under the provisions of the German Copyright Law.

® The use of registered names, trademarks, etc. in this thesis does not imply, even in the absence of a specific statement, that such names are exempt from the relevant protective laws and regulations and therefore free for general use.

Contents

1	Introduction	1
2	Structure of Wood	5
2.1	Polymerization of Native Cellulose During Cell Growth	7
2.2	Composite Structure of Wood.....	10
3	Mechanical Properties of Wood	13
3.1	Stress-Strain-Relations.....	13
3.1.1	Stress-Strain Curves in General	15
3.1.2	Stress-Strain Curves of Wood	19
3.1.3	Stress Distribution in Building Materials.....	22
3.1.4	Stress Distribution in the Living Tree	23
3.2	Influence of Wood on Adsorbed Water and Vice Versa.....	24
4	Scattering Theory	27
4.1	Scattering Events	27
4.2	Spectroscopy.....	31
4.3	Scattering by Crystals	34
4.4	Debye-Waller-Factor	36
4.5	Phonon Expansion	37
4.6	Bragg Scattering.....	38
4.7	Fibre Diffraction	40
4.8	Hermans' Orientation Function.....	43
4.9	Powder Diffraction.....	44
5	Experimental Techniques	45
5.1	X-ray Diffraction Studies.....	45
5.1.1	Experimental Station A2 at HASYLAB.....	46
5.1.2	Experimental Station ID13 at ESRF	47
5.1.3	The Big Kiel Stretching Device	47
5.1.4	Humid Stretching Environment (HUSTEN)	49
5.1.5	X-ray CCD Imaging System	59
5.1.6	Data Reduction.....	60
5.2	Inelastic Neutron Scattering.....	74
5.2.1	Time-of-Flight Instrument.....	74
5.2.2	Data Reduction.....	77
5.2.3	Neutron Spectroscopy of Anisotropic Dynamics	103
5.3	Water Content.....	107

6	Results and Discussion	109
6.1	Synchrotron X-ray Experiments	109
6.1.1	Experiments on Earlywood	110
6.1.2	Single Fibre Experiments	136
6.2	Inelastic Neutron Scattering Experiments	143
6.2.1	Measurement Schedule	143
6.2.2	Neutron Diffraction Patterns	145
6.2.3	Neutron Spectroscopy on Wet and Dry Flax.....	153
6.2.4	Discussion	160
7	Conclusions and Outlook.....	161
8	Appendix	165
8.1	Broadening of Time-of-Flight Spectra due to Slab-Angle	165
8.2	Technical Details	168
8.3	Jacobian Determinants of the Transformations.....	170
8.3.1	The Time-of-Flight to Energy Gain Transformation.....	170
8.3.2	Wave Vector Transfer Calculation.....	171
9	References and Notes	177

1 Introduction

'For all our familiarity with trees, we are hardly aware of the awesome complexity of their internal structure. Understanding this structure is basic to successful woodworking.'

As stated above (Hoadley 2000)^{p. 7} there is still a lot left to learn about wood. An enormous amount of empirical knowledge about woodworking has been collected during thousands of years. The properties of wood are highly influenced by its water content. Beams are used in dry conditions, e.g. in constructions, such as a house roof, and their mechanical properties are well-known, in particular, their load carrying capabilities. Changes in the mechanical properties of wood due to water uptake, such as swelling and softening, are common knowledge. These changes have been used since ancient times, for example to crack rocks. However, on the molecular level the mechanisms behind these effects are not always fully understood, and still further research is needed in this field.

The interaction of wood and water is of vital importance for the living tree, where wood has to fulfil several demands. One of the major tasks of a tree is to stand upright, against gravitational forces and wind loads. Additionally, the trunk of a living tree is wet, and the water flow is needed for several essential biochemical tasks. Understanding the mechanical challenges a tree faces, therefore, involves a detailed understanding of the influence of water on the mechanical properties of wood. This theme is the focus of the present thesis.

Wood is a composite material that mainly consists of stiff cellulose crystals surrounded by a softer, water adsorbing matrix. Hence, the molecular interaction between water and cellulose has to be taken into account in future models for the composite structure of wood. At present, such models mainly concentrate on the empirical macroscopic properties, e.g. (Navi 1997), and the important interaction with water is not included properly. The struc-

tural changes present in wood under mechanical load can be monitored, in particular, it is possible to study the orientation and lattice spacing of the cellulose crystals by means of X-ray micro-diffraction with high spatial resolution (Keckes et al. 2003; Kölln et al. 2005; Peura et al. 2006b). However, it is necessary to investigate the structural changes as a function of the water content to clarify its influence. Therefore, a special instrument ‘HUSTEN’ has been designed, built and used in the context of this thesis, allowing for *in situ* stretching experiments combined with X-ray diffraction studies in a controlled climate. The instrument enables experiments with high spatial resolution on wood pieces (up to $1 \times 1 \text{ mm}^2$ cross section) as well as on single fibres (about $\text{\O} 40 \text{ }\mu\text{m}$), in order to identify the interaction mechanisms on different structural levels.

As mentioned above, water influences the mechanics of the wood, but the reverse is also true, in the sense of a host-guest interaction. The influence of wood on water is evident from trees surviving cold temperatures far below the freezing point of water. In winter trees reduce the water content of their outermost layers (Zweifel 1999), but the trunk remains wet. Nevertheless, the trunk does not split due to the formation of crystalline ice, as would be expected from a bottle of water exposed to the same climatic conditions. In addition to its importance for the living tree, this effect is of major interest for basic physical research and has been the subject of several recent studies about water in confinement.

Clearly, the mechanisms shown above are not limited to wood, but are rather of general importance for all plants. All plants build cell walls, mainly consisting of cellulose, as does wood. Many features of water in the plant cell walls have been reported over the last decades. Water adsorbed in the disordered regions of cellulose exhibits liquid dynamics below $0 \text{ }^\circ\text{C}$ and is therefore termed ‘non-freezing’ (Czihak 2000). However, neither the structural properties of water in cellulose nor the nature of the freezing transition are fully understood. Inelastic neutron scattering experiments can monitor such local dynamics of disordered mate-

rial (Müller et al. 2000b). A refinement of this technique has been developed, in order to enable such an investigation – despite the expected small signals – as a function of water content and of the orientation of the cellulose crystals.

The present thesis is divided into 9 chapters. In chapter 2 the complex structure of wood is briefly explained. This structure is of basic importance in any experiment carried out on a composite material like native wood. This thesis concentrates on the mechanical properties of wood, introduced in chapter 3. The X-ray and neutron scattering experiments are based on well-known scattering theory briefly mentioned in chapter 4. The experiments motivated above required many technical improvements, which have been developed in the context of this thesis. The instruments and data analysis tools are discussed in full detail in chapter 5. The results of the X-ray diffraction experiments and the inelastic neutron scattering experiments are given in chapter 6. Finally, in the concluding chapter 7 the impact of this study is considered and future prospects are put forward. Additional information is contained in the appendix in chapter 8 and cited references are given in chapter 9.

(This page is intentionally left blank.)

2 Structure of Wood

Wood is a highly hierarchically structured material. From a macroscopic point of view, there is first of all the tree itself. In spite of the fact that it is a living being, most of its inside is dead material. If we look for example at the trunk of a felled tree, it has grown over several years which lead to the well-known *annual rings* in its

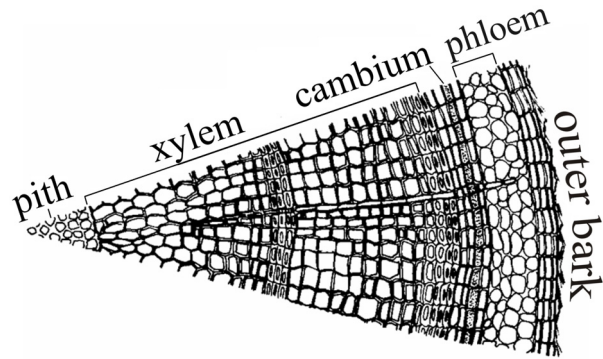


Figure 2-1: Illustration of a transverse section of a young dormant pine stem showing the arrangement of the tissues, taken from (Zimmermann et al. 1971)^{Fig. II-8(a)}.

cross section. These rings consist of the cell walls from dead cells that had once been generated in the *cambium* of the tree. The cambium is the source of both, *phloem* and *xylem*, as illustrated in Figure 2-1. The detailed arrangement of the cells as well as their shape depend on the species of the tree investigated. In the case of *softwood*, as for example pine, the structure is quite simple. It consist of about 90 to 95 % of tracheids. These *tracheids* are long and slender cells and their longitudinal extension is aligned along the axes of the stem (Fengel and Wegener 1984)^{p. 6}. The length of the tracheids for example in *Pinus sylvestris* is found in the range from 1.4 to 4.4 mm and their cross section measures 10 to 50 μm in diameter (Fengel and Wegener 1984)^{Table 2-2}.

The phloem cells build the bark, whereas the xylem-related cells let the stem grow from inside to outside. A more detailed discussion concerning this growth process can be found, for example, in (Zimmermann et al. 1971)^{chap. II}. The resulting wood density varies along the radius of the stem, depending on the growth rate of these cells. This rate depends on several parameters, like the CO_2 concentration of the surrounding atmosphere (Ceulemans et

al. 2002), the light, water and nitrogen level, phosphorus (Arnold and Mauseth 1999) or the tree size (Enquist et al. 1999). These density fluctuations lead to the familiar ring-like pattern in the cross section, where darker regions correspond to higher density and slower growth rate of the cells. The high contrast at the ring boundary matches the beginning of a new year. The brighter band of the annual ring, which has been produced in spring, is called *earlywood*. It consists out of thinner walls and larger cavities. The part grown in autumn is called *latewood*. It consists of smaller cells with thicker walls. The differences in the shape of the cell cross sections are evident from Figure 2-2.

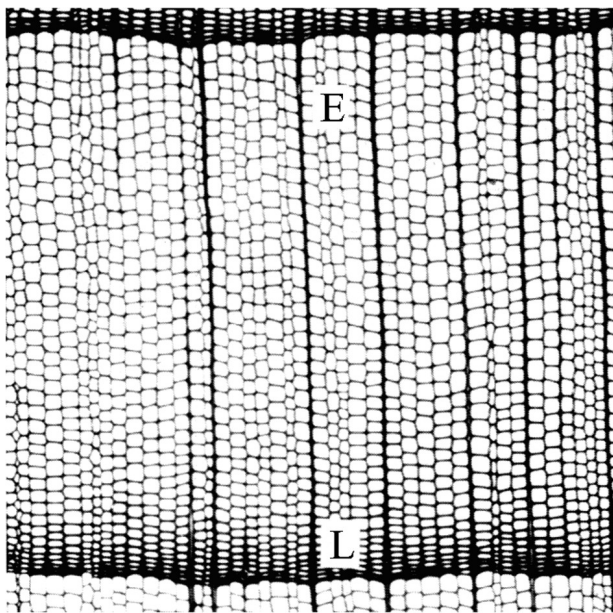


Figure 2-2: Transverse section of wood from *Pinus ponderosa* taken from (Zimmermann et al. 1971)^{Fig. II-11}. The earlywood (E) region shows greater tracheids with thinner walls than the latewood (L) region.

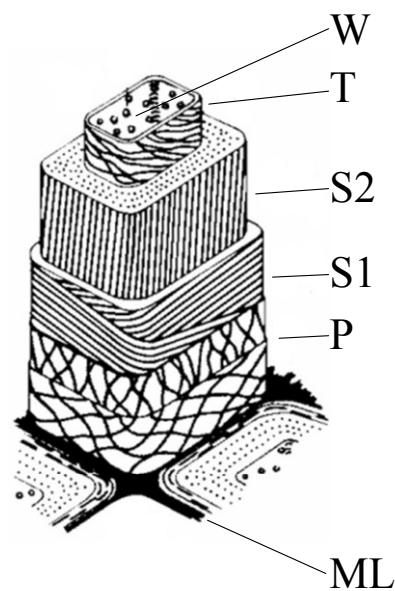


Figure 2-3: Illustration of a model for the cell wall structure of softwood tracheids consisting of several layers, namely the middle lamella (ML), primary wall (P), secondary wall (S1, S2), tertiary wall (T) and the wart layer (W), as found in (Fengel and Wegener 1984)

It is possible to actually determine the date at which a given tree has been growing, using this pattern of the annual rings, due to the strong correlation of the growth conditions to the ring pattern, as done in *dendrochronology*, as explained for example in (Schweingruber 1993).

2.1 Polymerization of Native Cellulose During Cell Growth

The growth process mentioned above leads to a layered structure of the cell walls, as illustrated in Figure 2-3. Cellulose is the main compound of the walls. This cellulose is polymerized by so-called *terminal complexes* during the life cycle of the cell, as recently reviewed in (Saxena and Brown 2005). The cellulose chains are more or less well-ordered and aligned with respect to the main cell axis, as illustrated in Figure 2-3. The degree of polymerization of cellulose in wood reaches up to a molecular weight of 10,000 (Preston 1974)^{tab. 3.3}.

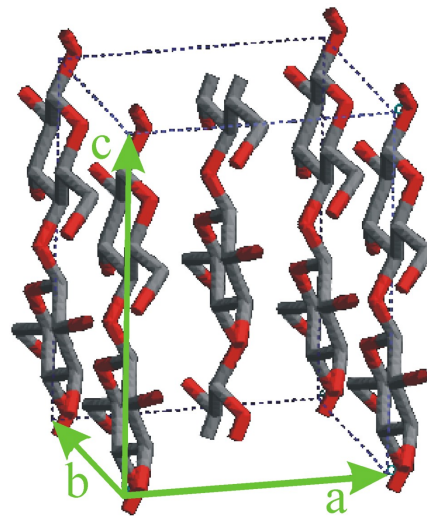


Figure 2-4: Unit cell of cellulose crystal type I_{β} . The carbon are given in grey and the oxygen in red. The fundamental vectors of the unit cell a , b and c are shown in green. As found in (Kölln 2004)^{Fig. 1.4}.

The cellulose chains form small cellulose crystals surrounded with some less ordered material, as shown in the right of Figure 2-5. The resulting degree of crystallinity varies from 60 to 70 %, as found in wood pulp (Fengel and Wegener 1984)^{p. 90}. Some authors propose a composed structure of *elementary fibrils* and *microfibrils* (Fengel 1971; Frey-Wysseling 1954; Krässig 1993). This concept can be traced back to (Frey-Wysseling 1937). It is illustrated in the left of Figure 2-5. Contrarily, others did not find such structures, e.g. (Sugiyama et al. 1985). A discerning discussion can be found in (Preston 1974)^{chap. 7.3}. Several similar models for the structure are compared in (Fengel and Wegener 1984)^{chap. 8.4}. However, in this thesis, the term microfibril is used to refer to the cellulose crystals.

There are several crystal structures known for cellulose, as reviewed in (O'Sullivan 1997) and analysed by means of molecular dynamics simulations in (Kroon-Batenburg et al. 1996). Type I_{β} is the most abundant occurrence in plant cell walls and its unit cell is given in

Figure 2-4. The type I_β is sometimes accompanied with type I_α (Imai and Sugiyama 1998). The best structure determination using X-ray and neutron diffraction can be found in (Nishiyama et al. 2003b; Nishiyama et al. 2002). The resulting parameters of the unit cell are given in Table 2-1. The structure of type I_β is compared to that of I_α in Figure 2-6, where two different projections are shown. The main difference between the two structures is the displacement of the sheets in the chain direction. With reference to Figure 2-6, in both structures the second sheet, designated B, is shifted ‘upwards’ by about $c/4$ with respect to the first sheet, designated A. The third sheet, designated C, is shifted relative to sheet B by about $c/4$ in the case of I_α in the same direction, but in the case of I_β ‘downwards’. Therefore, the positions of sheet C with respect to sheet B differs by about $c/2$ between I_α and I_β .

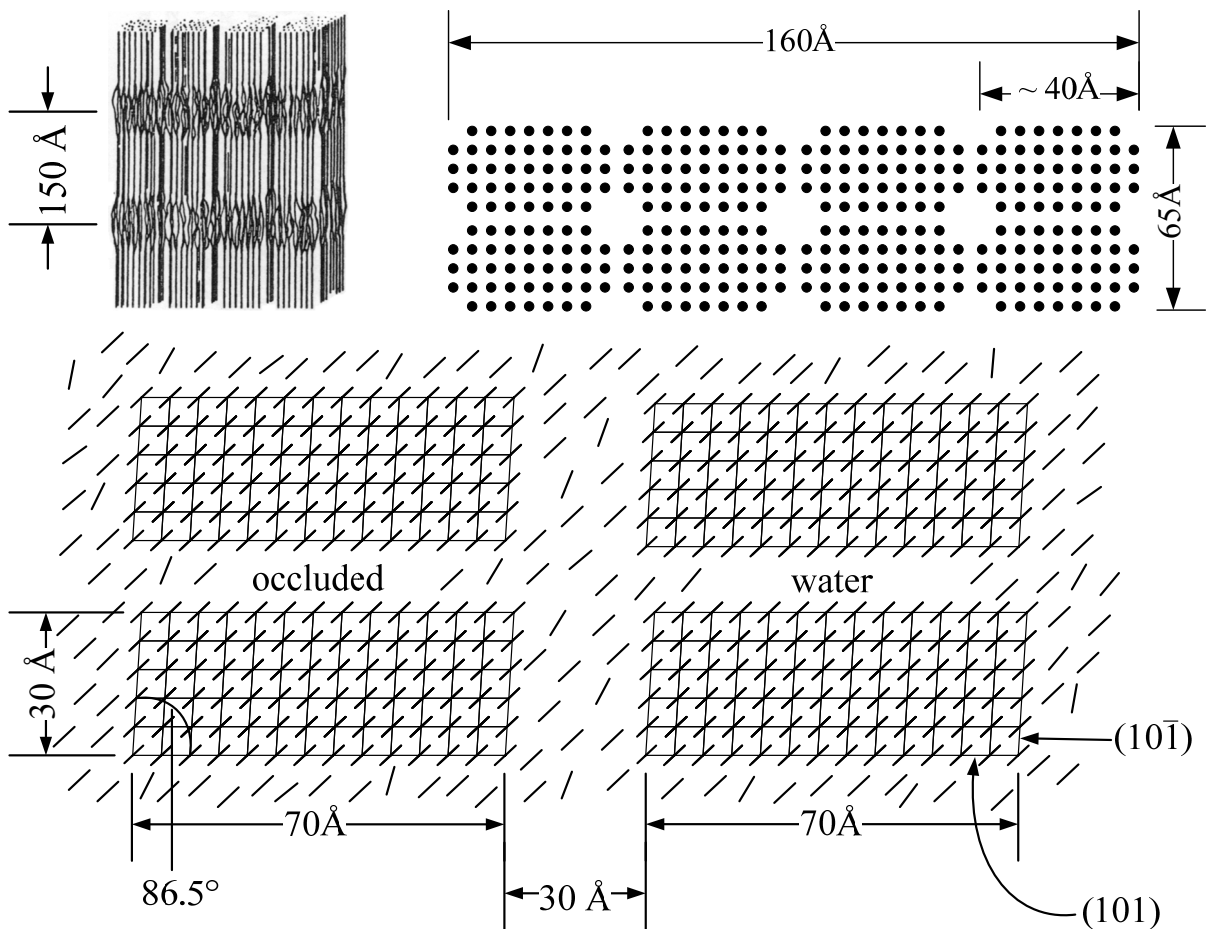


Figure 2-5: The architecture of elementary fibrils and microfibrils of native cellulose fibres in plant cell walls, after (Krässig 1993)^{Fig. 9}.

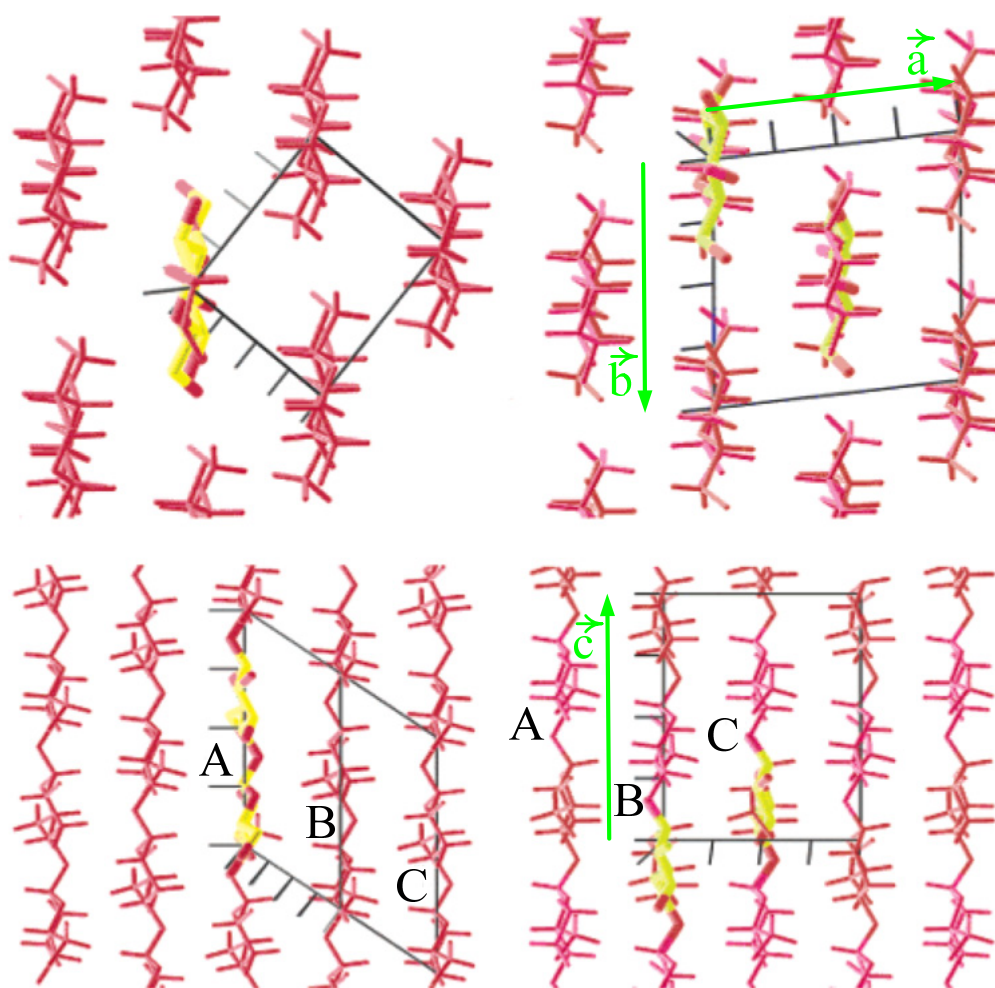


Figure 2-6: Projection of the crystal structures of cellulose I_α (left) and I_β (right). The projection along the cellulose chains is given at the top. The projection perpendicular to the chains and in the plane of the hydrogen bonded sheets is shown at the bottom. The cellulose chains are illustrated with red skeletal models. The asymmetric unit of each structure is marked with carbons in yellow. The unit cell is given in black and the orientation of their axis a , b and c are shown in green. Taken from (Nishiyama et al. 2003b)^{Fig. 5}.

The cellulose crystals are held together with strong O–H \cdots O hydrogen bonds in the planes of the cellulose sheets, i.e. in the b - c -plane of the unit cell. Additionally, there are only van der Waals bonds and weak C–H \cdots O hydrogen bonds between the sheets, i.e. in the a -direction of the unit cell (Nishiyama et al. 2003b; Nishiyama et al. 2002). Form and size of native cellulose crystals varies, as visible from Table 2-2, where the dimensions of the crystal cross section found in experiments is given. The length of the crystals along the c -axis can be estimated to be of the order of μm (Favier et al. 1995; Wardrop 1953). There are hints on periodic disorder along the chains of ramie fibres every 150 nm (Nishiyama et al. 2003a). Sev-

eral studies revealed that the crystal surfaces are given by the (110) and $(1\bar{1}0)$ layers, e.g. (Hofstetter et al. 2006; O'Sullivan 1997; Sugiyama et al. 1985), as shown in Figure 2-5, but there are exceptions (Helbert et al. 1998).

Type	I_α	I_β
Space group	triclinic P1	monoclinic P2 ₁
a / Å	6.717(7)	7.784(8)
b / Å	5.962(6)	8.201(8)
c / Å	10.400(6)	10.38(1)
α / 1°	118.08(5)	90.0
β / 1°	114.80(5)	90.0
γ / 1°	80.37(5)	96.5
Reference	(Nishiyama et al. 2003b) ^{Tab. 1}	(Nishiyama et al. 2002) ^{Tab. 1}

Table 2-1: Parameters of the unit cell of cellulose I_α and I_β . The values in the parantheses show the uncertainties of the last digit.

Source	Size	Reference
cotton	49 Å × 66 Å	(Müller et al. 2000b)
flax	41 Å × 44 Å	(Müller et al. 2000b)
tunicate	100...200 Å × 100...200 Å	(Favier et al. 1995)
wood	25 Å × 25 Å	(Jakob et al. 1994)

Table 2-2: Size of cellulose crystal cross section in a-b-plane.

2.2 Composite Structure of Wood

It is possible to distinguish several layers in the cell wall that have common orientations of the cellulose crystals and common chemical composition. The layers are labelled, as shown in Figure 2-3 and Figure 2-8. The chemical composition of these layers is given in Table 2-3. The actual thickness of the layers varies among species and growth conditions, an average found for spruce tracheids is shown in Table 2-4.

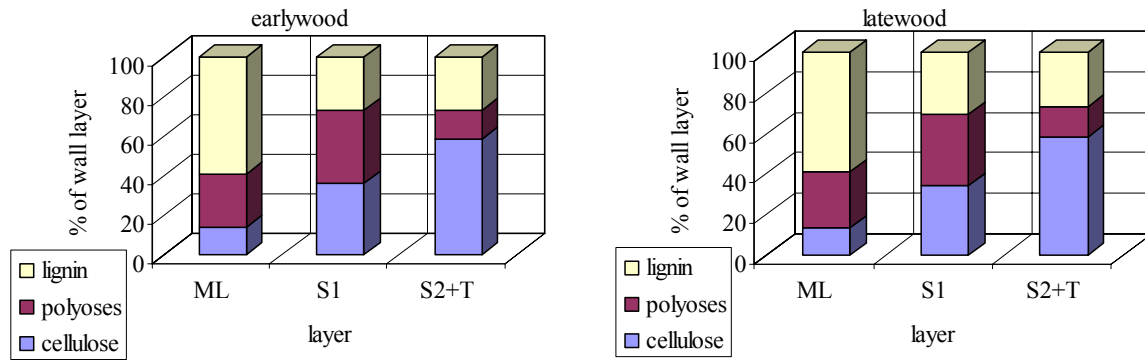


Figure 2-7: Relative composition of the cell wall layers found in earlywood (left) and latewood (right) according to Table 2-3.

Region	Cell wall layer	Cellulose		Polyoses		Lignin	
		% of the wall layer	% of total Cellulose	% of the wall layer	% of total Polyoses	% of the wall layer	% of total Lignin
early-wood	ML	13.9	4.1	27.1	20.6	59.0	26.8
	S1	36.4	8.9	36.4	23.2	27.2	10.4
	S2 + T	58.5	87.0	14.4	56.1	27.1	62.8
late-wood	ML	13.7	2.5	27.4	15.0	58.9	18.4
	S1	34.6	5.2	34.6	15.6	30.8	7.9
	S2 + T	58.4	92.3	14.5	69.4	27.1	73.7

Table 2-3: Calculated distribution of the components in the cell wall layers of spruce tracheids (Fengel and Wegener 1984)^{tab. 8-1}.

Layer of cell wall	Earlywood		Latewood	
	μm	%	μm	%
P + ML/2	0.09	4.3	0.09	2.1
S1	0.26	12.4	0.38	8.8
S2	1.66	79.0	3.69	85.8
T	0.09	4.3	0.14	3.3
Total wall	2.10	100	4.30	100

Table 2-4: Average thickness and percentage of the cell wall layers in spruce tracheids (*Picea abies*), according to (Fengel and Wegener 1984)^{tab. 2-3}.

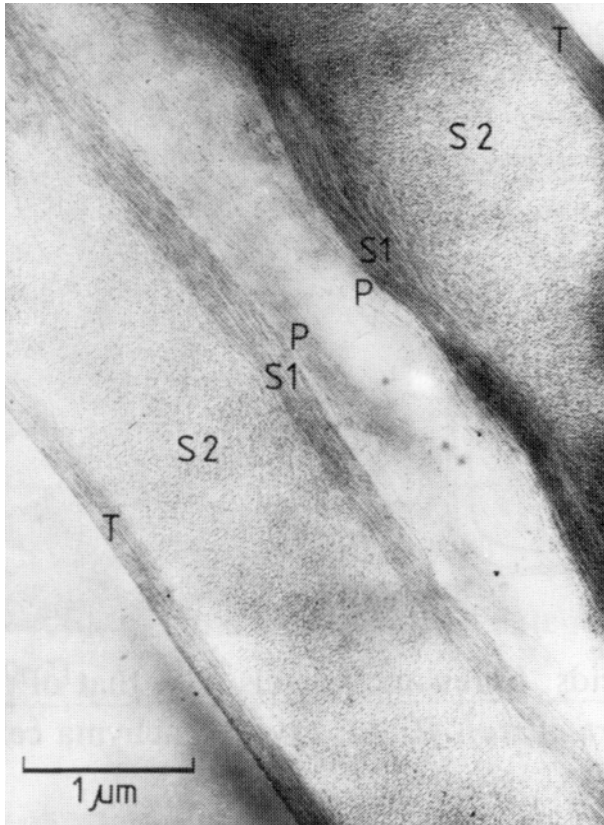


Figure 2-8: Ultrathin section of the cellulose skeleton of tracheid walls in softwood (*Picea abies*). The different orientations of the various wall layers are visible. This TEM micrograph is taken from (Fengel and Wegener 1984)^{Fig. 2-13}. The layers from left to right are the tertiary wall (T), secondary wall two (S2), secondary wall one (S1) and primary wall (P) of the left cell, and the same layers in opposite order from the right cell. The middle lamella (ML) lies between the two primary walls.

The small *middle lamella* consists mainly of lignin, as illustrated in Figure 2-7. The middle lamella holds together adjacent cells, with lignin acting as a kind of glue. The thickest layer of the wall, S2, mainly consists of cellulose. As mentioned above, the cellulose forms small fibrillar crystals up to a considerable degree. These crystals are oriented along the polymer chains of the cellulose. The angle between the *c*-axis of these crystals and the axis of the cell is called the *microfibril angle* (MFA). The crystals of one cell wall layer show common MFA, resulting in a helical arrangement of the cellulose in that cell wall layer, as illustrated in Figure 2-3 and visualised by means of X-ray microdiffraction (Lichtenegger et al. 1999).

3 Mechanical Properties of Wood

The mechanical properties of wood are of major interest if it is used as building material. This is true in the case of the felled wood, when it is used for example to build structures as houses, as well as in the case of the living tree. Nevertheless, these two cases are different with respect to the water content of the wood. In the case of the living tree it is found to be between 30 and 220 wt% (Dietenberger et al. 1999)^{Tab. 3-3}. In the case of wood as an engineering material it is mostly used in a region below 15 wt% of water (Dietenberger et al. 1999)^{Fig. 9-4}. This difference in moisture content has a huge influence on the mechanical properties of wood, as will be shown in this chapter. In any case the strength of wood is unmatched by artificial materials, if compared to its weight, even for the case of modern high performance fibres, as will be discussed in the following.

3.1 Stress-Strain-Relations

The behaviour of condensed matter under mechanical load can be investigated on a macroscopic scale with simple experiments, where force and deformation are monitored over time. It is possible to distinguish between several modes of mechanical testing according to the direction of the force, i.e. compression or tension, and with respect to the time axis of the ex-

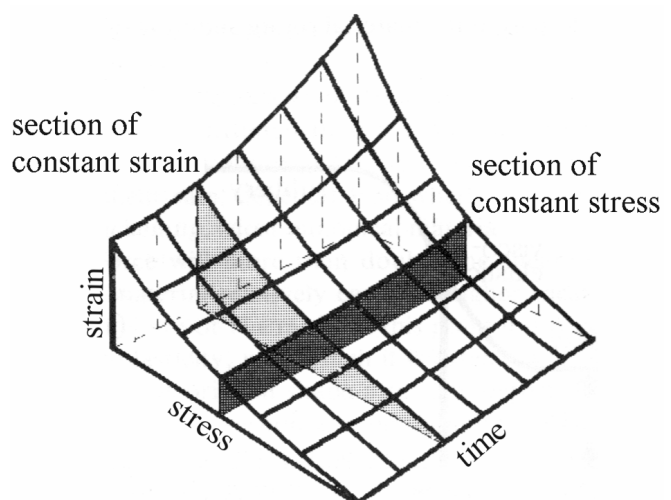


Figure 3-1: Three-dimensional representation of the relationship between stress, strain and time. Derived from isochronal stress-strain curves along the stress axis and creep curves along the time axis, according to (Vincent 1990)^{Fig. 1.13} and references therein.

periment, as illustrated in Figure 3-1. Especially, the cases of static constant load or elongation, periodically recurring deformation and continuously increasing deformation can be distinguished. The first case leads to so-called *creep experiments*, where a constant mechanical load is applied and the reaction of the material over time is investigated. Similarly, a constant elongation leads to *relaxation experiments*. The case of periodically deformation reveals the *fatigue resistance* of the material and is of great importance for any design that has to take alternating loads, such as bridges or trees in the wind. The last case finally reveals the maximum load a material can sustain if applied once. It is possible with such an experiment to give a quick overview of the mechanical characteristics of a material and to separate several regions of different mechanical behaviour, as illustrated in Figure 3-2. All mechanical tests presented in this thesis are of the last type and limited to the tension case, called *stretching experiment*. The tension case is of major interest for the living tree, as will be shown in the subsection 3.1.4. The forces F measured in such an experiment has to be divided by the cross section A of the sample and the elongations by its length to gain comparable quantities for the stress σ and strain ε that are independent of the sample dimensions. The values used for this scaling are typically the cross section and length¹ of the sample at the beginning of the measurement. Additionally, the density ρ of the material can be used for scaling, as it is useful in the case of a native porous material like wood, leading to the *normalized stress* $\sigma_{normalised}$:

$$\sigma_{normalised} := \frac{F}{A\rho} \quad (3.1)$$

¹ This leads to the conventional, nominal, engineering or *Cauchy strain*.

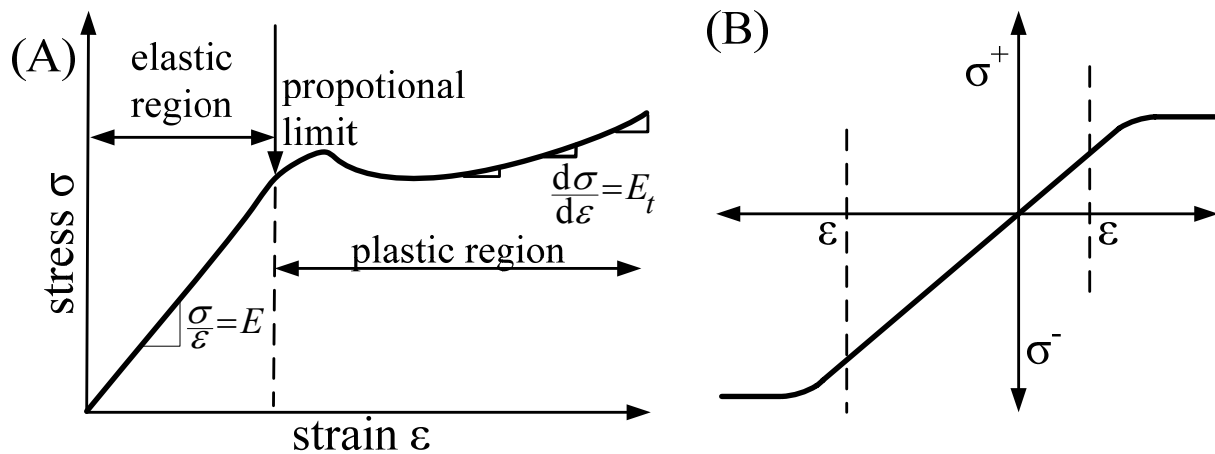


Figure 3-2: Schematic stress-strain curves illustrating linear elastic and plastic behaviour; redrawn from (Niklas 1992)^{Fig. 2.8}. (A) Linear elastic behaviour is evident by an initial linear region of the stress-strain curve. The slope of this elastic region is the elastic or Young's modulus E . The plastic region is nonlinear. The slope measured anywhere on the stress-strain curve gives the tangent modulus E_t . (B) The proportional limits of the same material measured under tensile and compressive stress σ^+ and σ^- , respectively, may not be equivalent even if the elastic moduli measured in tension and compression are equivalent.

3.1.1 Stress-Strain Curves in General

There are many numerical values that can be derived from the experiments described above in order to characterise the material under investigation, as shown in Figure 3-3. However, the actual figures obtained in such an experiment are influenced by many parameters, for example the dimensions² of the sample or its temperature. Therefore, the experimental determination is standardised to enable comparison. This is done for example in the technical standard DIN 52 188 for the case of stretching experiments with wood samples parallel to the fibre direction. The sample geometry defined in that standard is given in Figure 3-4.

Experiments carried out in compliance with this norm produce values that are averaged over several annual rings, due to the sample dimensions, as visible in Figure 3-5. Beside their good suitability for the needs of the building industry, such experiments are of little use in order to understand the detailed nature of the composite material wood. Therefore, all ex-

² The dimensions of the sample influence the experimental results even though the forces and elongations are scaled to the actual measures of the sample.

periments presented later have been performed with samples of much smaller dimensions. Mostly, they have been restricted to material from one growth period, for example earlywood, as described in chapter 2, or even to single cells. Nevertheless, the results obtained in these experiments can be analysed in the same way, as done normally for larger samples.

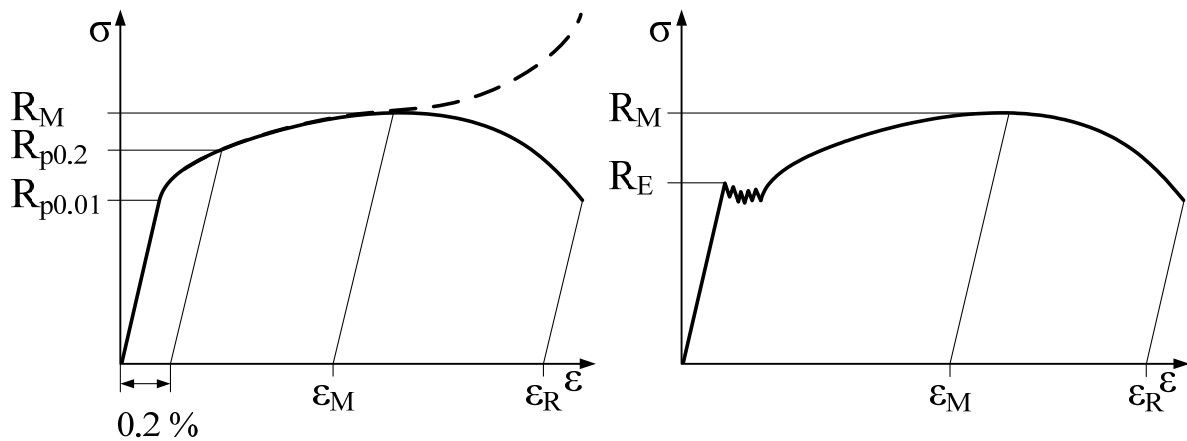


Figure 3-3: Schematic stress-strain curve of a stretching experiment with a ductile (left) material and a typical building steel (right). The nominal stress σ is shown versus strain ϵ as thick black curve. The dashed line shows the true stress inside the material. The proportional limits $R_{p0.01}$ and $R_{p0.2}$ are marked. The maximum nominal stress gives the tensile strength R_M at strain ϵ_M . The permanent strain after rupture ϵ_R remains after fracture of the sample and after recovery of all elastic deformations. The pronounced yield point is marked with R_E .

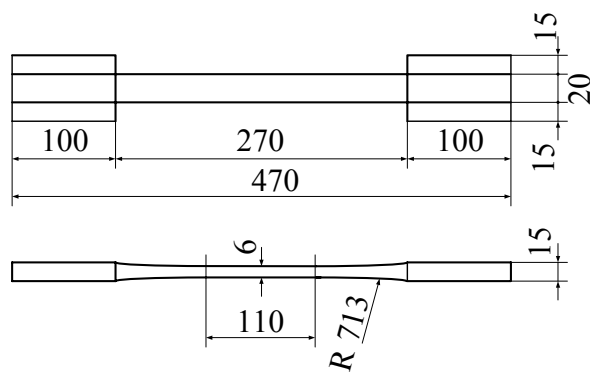


Figure 3-4: Sample dimensions given in mm for a stretching experiment according to DIN 52 188. The length of 110 mm in the centre of the sample is taken as starting length of the sample to calculate the Cauchy strain during the stretching experiment.

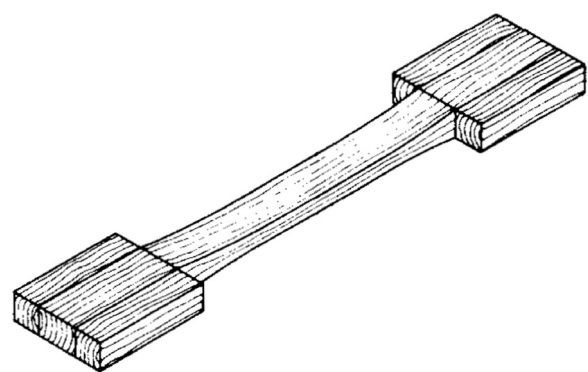


Figure 3-5: Orientation of the annual rings in the sample for a stretching experiment according to DIN 52 188.

The different regions of the *stress-strain curve* shown in Figure 3-2. Especially, the *elastic region* of the stress-strain curve shown in Figure 3-2 is of great technical importance, because any deformation limited to this region causes no permanent change. In this region the force, which is necessary to produce the deformation of the sample, vanishes if the deformation does. This region is identical to the region of proportionality for many materials. In that region the material obeys Hooke's law, where the stress is proportional to the elongation. The quotient of stress σ over strain ε is known as *Young's modulus* or *modulus of elasticity* E . It can easily be derived from the slope at the beginning of the stress-strain curve, as illustrated in Figure 3-2. In this region the material acts as a simple linear spring, as illustrated in Figure 3-6. The Young's modulus is a measure of the stiffness of the material.

With greater strain, the proportionality vanishes and plastic deformation can occur, depending on the class of the material, as classified in Figure 3-7. The transition between the elastic and *plastic region* is smooth for most of the materials. For some steels this transition is very pronounced and the corresponding point is called *yield point*, as illustrated in Figure 3-3. For all other materials an arbitrary fraction of plastic deformation is tolerated, typically 0.2 %, to define the elastic or *proportional limit*, as given in Figure 3-3. This fraction has to be given together with the numbers derived from the stress-strain curve, if presented for example in tables or used for comparison. A special case is given for so called *visco-elastic* materials. Their principal stress-strain curve is shown in Figure 3-6, showing no plastic deformation at all in the case of *linear visco-elasticity*.

At greater elongations the stress-strain curve reaches its maximum indicating the *ultimate strength* of the material, its *tensile strength* R_M . This value gives the maximum stress σ_M that can be taken by a construction material. This stress is calculated by dividing the forces measured during the experiment by the cross section of the sample at the beginning of the experiment, as mentioned above. The variation of the cross section during the experiment is known as *Poisson effect*. Normally, it leads to a smaller cross section at higher elongations. Hence, the stress typically shown in the stress-strain curves is a nominal one. It is well suited

for calculating the necessary dimension of a part in a given construction scenario, because these dimensions must be given for the unstressed part, in order to enable its production.

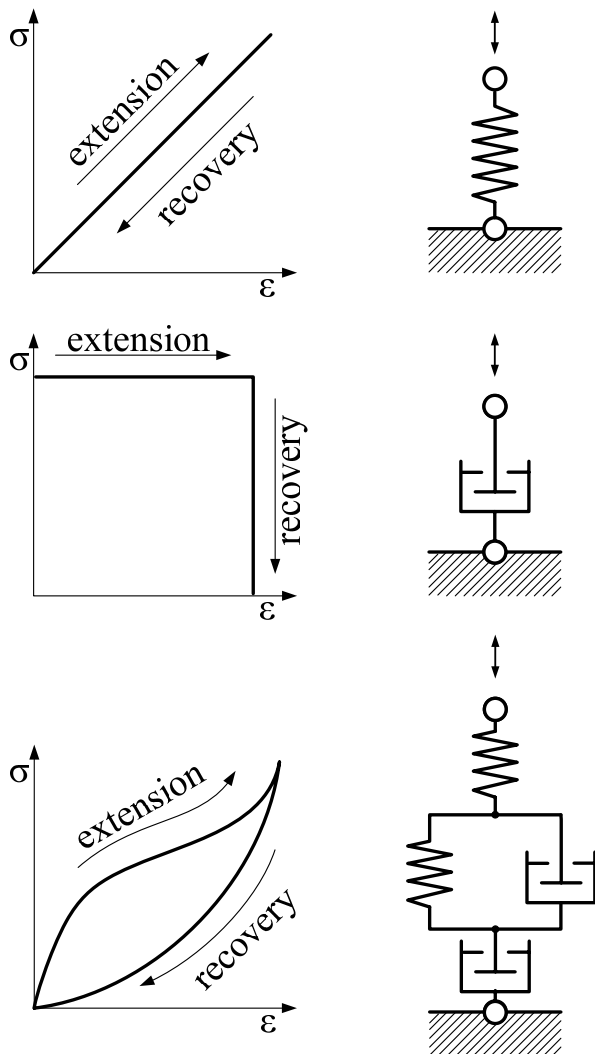


Figure 3-6: Schematic stress-strain curve and mechanical model system of ideal linear viscoelastic material (bottom), and ideal elastic material (top) and ideal Newtonian liquid (middle).

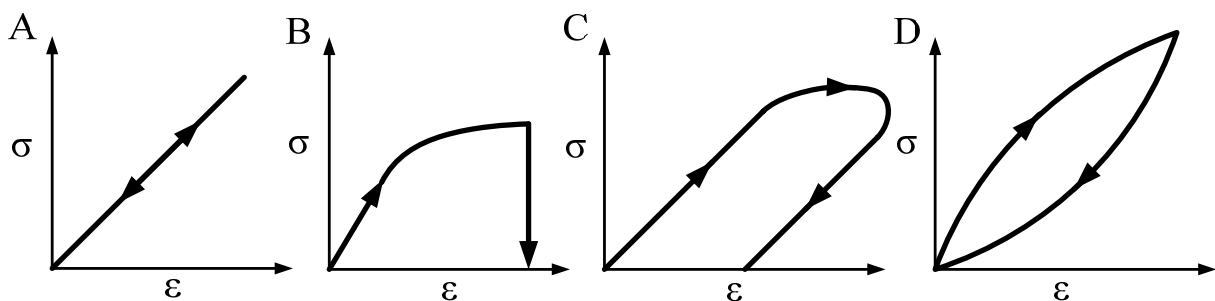


Figure 3-7: Schematic comparisons between the stress-strain curves of an ideal elastic material (A), a hypothetical material showing no elastic recovery (B), an elastic-plastic material (C), and a linear visco-elastic material (D). Redrawn from (Niklas 1992)^{Fig. 2.9}. Stress σ is shown versus strain ϵ .

The real or true stress existing inside the sample can be determined if the measured force is divided by the actual cross section, and it would lead to a curve, as shown in Figure 3-3. The true stress can be of interest, for example, if numbers for the internal mechanisms of the material should be found. Nevertheless, the determination of the cross section during a stretching experiment is not straightforward if the behaviour of the sample should not be interfered. Hence, all experimental stress-strain curves presented later are nominal ones with respect to the discussion given above.

3.1.2 Stress-Strain Curves of Wood

Tensile tests on wood specimen have to be performed with respect to the fibre axis and the location of the annual rings. Therefore, the orientation of the specimen with respect to the former tree has to be mentioned. The coordinate system used for this purpose is shown in Figure 3-8.

An example for a force-displacement curve obtained with a wood sample is shown in Figure 3-9. The length of the sample has measured 30 mm and its cross section has held 3 mm tangential and 0.14 mm radial. The underlying experiment is explained and reported in more detail in (Navi et al. 1995). Some points along the curve are labelled to ease the explanation. The points have been reached during the experiment in the given order. The sample has been elongated by displacing its end until rupture at point 19. The force that has been recorded in the experiment increases first approximately proportionally up to the yield point at point 3. Beyond this point the material becomes less stiff. It undergoes a large mainly irreversible deformation. With further increasing load the curve shows a third region indicating a *strain-hardening* of the sample. Further investigations with holographic interferometry, reported in (Navi 1997), have revealed that non-local deformations occur in the second region of the stress-strain curve between yield point and stiffening, i.e. point 3 and 14.

The dependency of the stress-strain curves of single wood fibres on the microfibril angle is shown in (Page and El-Hosseiny 1983) and illustrated in Figure 3-10. The importance of the MFA for the mechanical strength is evident. The curves obtained from samples with low mean MFA show a non-linear single segment. The curves from samples with higher MFA show three regions comparable to the three regions found for small wood pieces described above.

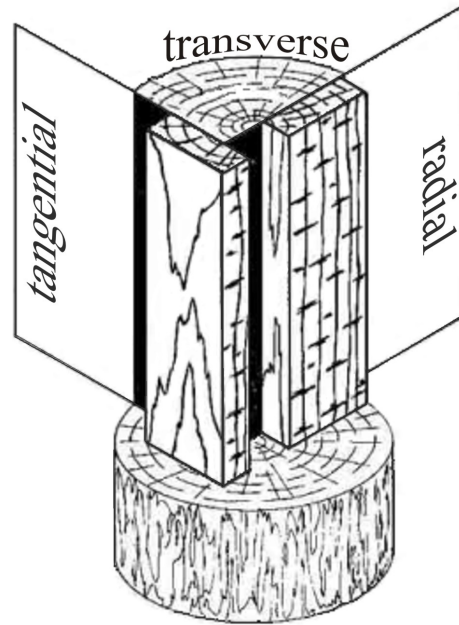


Figure 3-8 Diagrammatic log section that illustrates the relationship of tangential, radial, and transverse or cross surfaces, according to (Beals and Davis 1977)^{Fig. 2}.

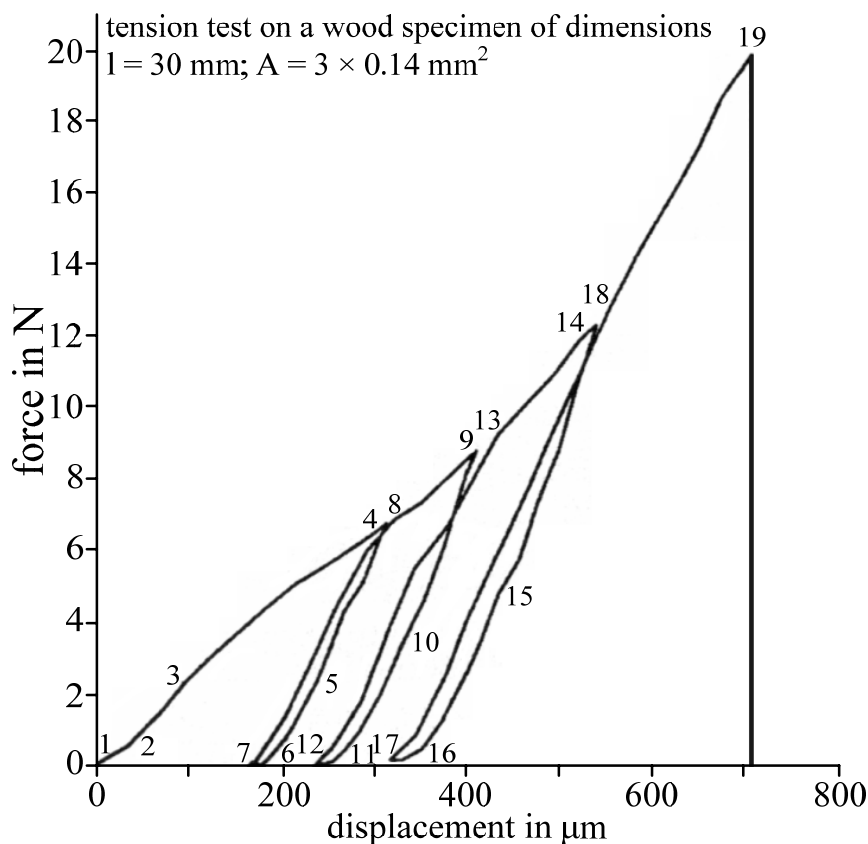


Figure 3-9: Force-displacement curve of a controlled cyclic tensile test on thin, non-homogeneous wood specimen, taken from (Navi 1997)^{Fig. 4}. The sample of 30 mm length and $3 \times 0.14 \text{ mm}^2$ cross section has been elongated in grain direction.

The shape of the stress-strain curves shown in Figure 3-9 and Figure 3-10 can be explained with a simple model introducing the concept of an effective modulus for the whole sample, proposed in (Navi 1997). The necessary assumptions are the following:

- The material consists of microfibrils embedded in a matrix.
- The stiffness E varies along the sample, as does the MFA.
- The stiffness E is a decreasing function of the MFA.
- The local ultimate strength is a decreasing function of the MFA.
- Every local damage in the sample leads to irreversible local decrease in the stiffness, depending on the MFA.
- Apart from the damages the material acts linearly elastic.

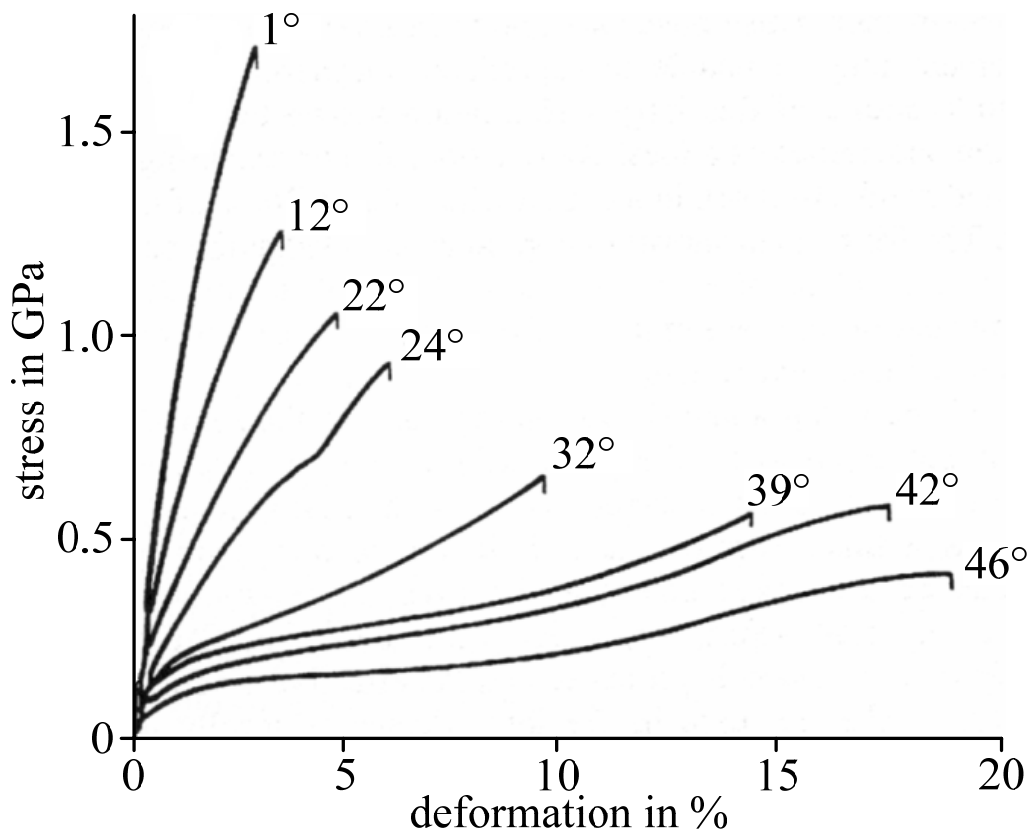


Figure 3-10: Stress-strain curves of single wood fibres with different mean microfibril angles, according to (Page and El-Hosseiny 1983), taken from (Navi 1997)^{Fig. 7}.

The *effective modulus* E_{eff} of a sample of length l can be computed with the local Young's modulus $E(z)$ at position z along the direction of elongation according to this serial model as follows from (Navi 1997)^{eq. (4)}:

$$\frac{1}{E_{eff}} = \frac{1}{l} \int_0^l \frac{dz}{E(z)} \quad (3.2)$$

This effective modulus has to be recomputed after any damage occurring somewhere in the sample. The region of the sample with the lowest MFA is liable for such a damage. As a result of this model, the degradation of the matrix under tensile load is accompanied by a tendency of the microfibrils to line up along the direction of the external force. Hence, after each local deformation the remaining sample has a higher effective modulus, visible in the strain-hardening. This model can be applied to both cases, that of single fibres and that of small wood pieces. In the latter case the local MFA is given by the mean MFA of the single fibres contained in the sample. The model explains qualitatively all three regions found in experimental stress-strain curves mentioned above, without any detailed description of the dependency of the local Young's modulus on the MFA.

Additionally, a helical spring model for the first and second region of the stress-strain curves has been proposed in (Keckes et al. 2003), capable of describing the main features in terms of two moduli before and after the yield point. These two moduli can be computed from the MFA of the unstressed state and the elastic and shear moduli of the matrix. However, this model fails to describe the strain-hardening in the third region of the curves (Keckes et al. 2003)^{p. 813tr} and the quantities obtained for a MFA smaller than 20° are false (Kölln 2004)^{p. 125}.

3.1.3 Stress Distribution in Building Materials

The stress in parts of engineering constructions is typically kept in the elastic region of the building material. In this region the design can be performed to exact and simple calculations and safety, if a concern, can be guaranteed. In this case, the stress distribution inside the material can be assumed to follow Hooke's law and the deformation is proportional to the applied force. Hence, most of the industrial research on material properties is concentrated on

this region. Nevertheless, the plastic deformation is of importance during the production processes, for example to achieve a permanent bending of a sheet. In the case of wood, such a bending can be supported with a steam of hot water, as known for long time, indicating the importance of water in this context.

3.1.4 Stress Distribution in the Living Tree

The stress distribution in a living tree is well known, e.g. (Mattheck 1991; Mattheck and Kubler 1995) and determined on a macroscopic scale to follow the shape shown in Figure 3-11. It is evident from Figure 3-11 that most of the material in the stem bears tensile stresses. Therefore, all mechanical experiments presented later are performed in stretching mode to closely resemble the situation in the living tree.

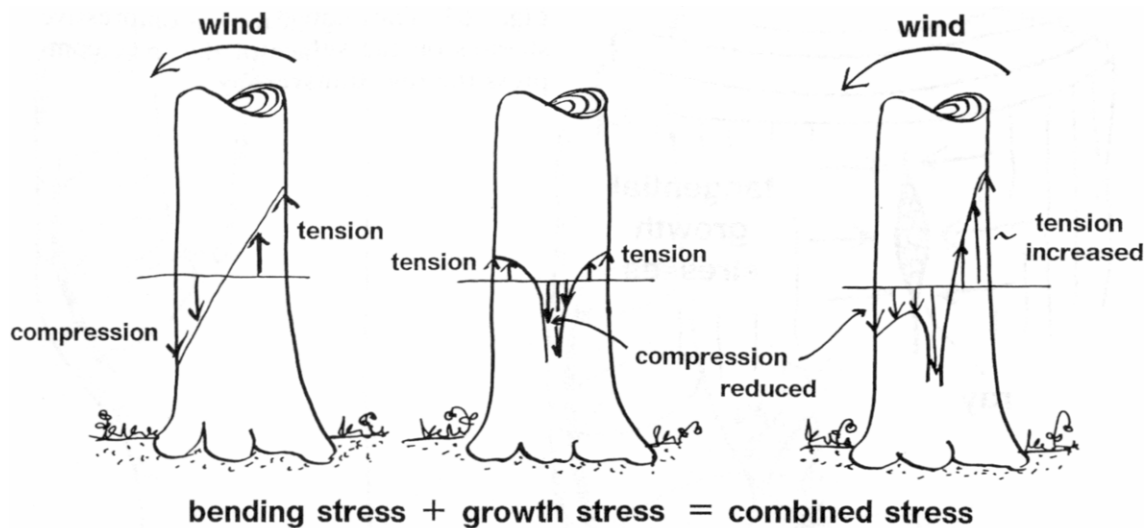


Figure 3-11: The axial tensile stresses on the surface of the tree minimise the critical compressive stresses induced by bending due to wind loads. Taken from (Mattheck and Kubler 1995)^{Fig. 63}.

The stress distribution found in living trees results in a sort of preloading due to *growth stresses*. In this way, the material in the stem is as much as possible operated in its tension range when external loads are applied, for example by wind blowing, as illustrated in Figure 3-11. The tensile strength of the cellulose fibres is much higher than their compression strength. Hence, this design leads to an optimal usage of the mechanical capability of the wood, avoiding the high risk of fibre buckling.

3.2 Influence of Wood on Adsorbed Water and Vice Versa

The living tree needs water for example to support the assimilation reactions. The water transport and its rhythm are described for example in (Skaar 1988; Tyree and Zimmermann 2002; Zweifel 1999). Hence, the wood found in a living tree is always wet, but also the building material wood has a relevant content of moisture. If wood is situated in an atmosphere of constant relative humidity, the water content established after some time is well known, and reported for example in (Dietenberger et al. 1999)^{chap. 3}. Examples for the corresponding isotherms are shown in Figure 3-12. The value found in equilibrium is called the *equilibrium moisture content*. It reaches a value of about 30 wt% at 100% relative humidity (RH) of the surrounding atmosphere at the so-called *fibre saturation point* (FSP). Up to this limit, any water intake leads to diffusion of water molecules into the cell walls, resulting in adsorbed water. If more water is present, capillary condensation takes place and so-called ‘free’ water is found.

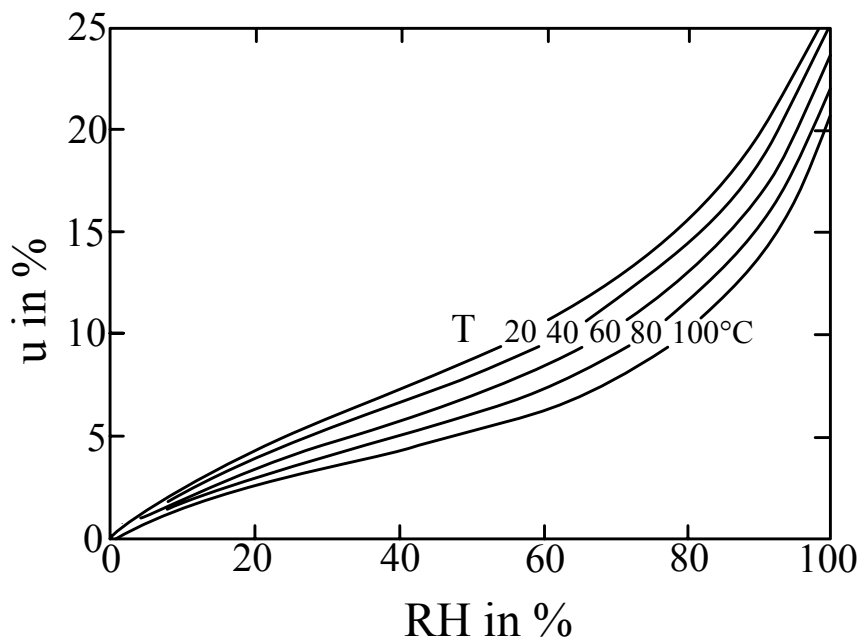


Figure 3-12: Desorption isotherms for Sitka spruce at several temperatures T , redrawn from (Skaar 1988)^{Fig. 1.22}. The moisture content u is plotted versus relative humidity RH of the surrounding air.

The amount of water present in wood has a huge influence on its properties, for example its electrical attributes (Skaar 1988)^{sec. 1.6.}. In particular, the mechanical properties vary up to the fibre saturation point, as shown in Figure 3-13 for the Young's modulus, as does the whole stress-strain curve, as will be presented later in section 6.1.1.

One of the more commonly known water-related features of wood is that of swelling or shrinking, as illustrated in Figure 3-14. This effect can be quantified following DIN 52 184, leading to linear swelling or shrinking factors, respectively. The technological importance of the effect is obvious from Figure 3-14 . It is also used since ancient times, for example as tool to crack rocks. The mechanical stresses that can emerge from hindered expansion under swelling conditions are immense.

In the same way that water influences the properties of wood, wood has an influence on the behaviour of the adsorbed water. It is common knowledge that trees do not suffer any damage due to the growth of ice crystals in the winter period, even if the ambient temperature drops far below 0 °C. For some trees it is known that they reduce the water content of their outer layers during cold times, as shown in a study on a macroscopic scale presented in (Zweifel 1999). In an investigation with inelastic neutron scattering it has been found that water adsorbed to amorphous cellulose undergoes a continuous freezing procedure leading to molecular dynamics comparable to those known for amorphous ice (Czihak 2000). However, the detailed nature of the underlying interaction still needs further investigations.

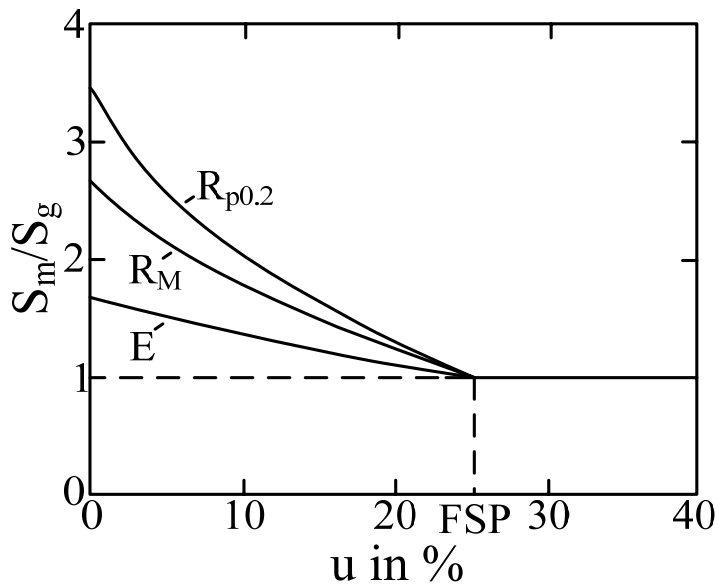


Figure 3-13: Idealised curves showing the ratio of strength S_m at moisture content u to the strength of green wood S_g for defect-free wood. The properties shown are modulus of elasticity (E), modulus of rupture (R_M), and fibre stress at proportional limit ($R_{p0.2}$), all found in flexural tests, redrawn from (Skaar 1988)^{Fig. 1.28}. The properties show no significant variations for moisture contents above the fibre saturation point (FSP).

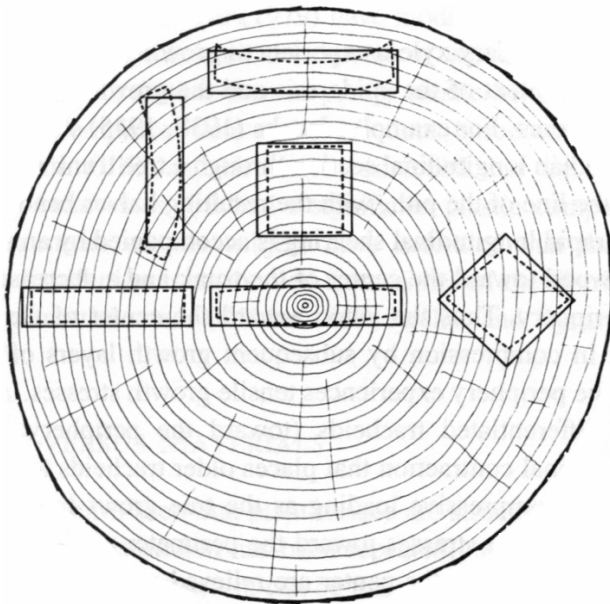


Figure 3-14: Diagram of a transverse section through a tree trunk illustrating the deformations that result when blocks of secondary xylem (wood) are taken out and allowed to dry. The in situ geometry of each block of wood is shown by solid lines; the bent outline of each block, once it is removed from its original location, is shown by dotted lines. Taken from (Niklas 1992)^{Fig. 6.11}.

4 Scattering Theory

The internal structure and the dynamics of matter can be investigated with scattering methods. There are mainly two different experimental techniques used in the context of this thesis:

- *X-ray diffraction* and
- *inelastic neutron scattering*.

The basic theories of these two techniques are mentioned in the following sections, as far as they are linked to the experiments shown in the later chapters. A comprehensive introduction can be found in textbooks like (Byrne 1994), (Bée 1988), (Lovesey 1984), (Squires 1978) or (Bacon 1975) concerning neutrons and (James 1982), (Alexander 1979) or (Warren 1990) in the case of X-rays. General introductions into scattering or diffraction theory of both, particles and waves, are given in (Cowley 1995), (Newton 2002) or (Authier and Malgrange 1998).

4.1 Scattering Events

The scattering methods mentioned above have some principals in common that are illustrated in Figure 4-1. The methods differ in the physical realisation of the incident beam used as a probe. In one case it consists of photons, in the other case of particles, namely neutrons. In both cases a wavelength λ_0 can be associated. It is coupled to the modulus of the wave vector \vec{k}_i :

$$|\vec{k}_i| = \frac{2\pi}{\lambda_0}. \quad (4.1)$$

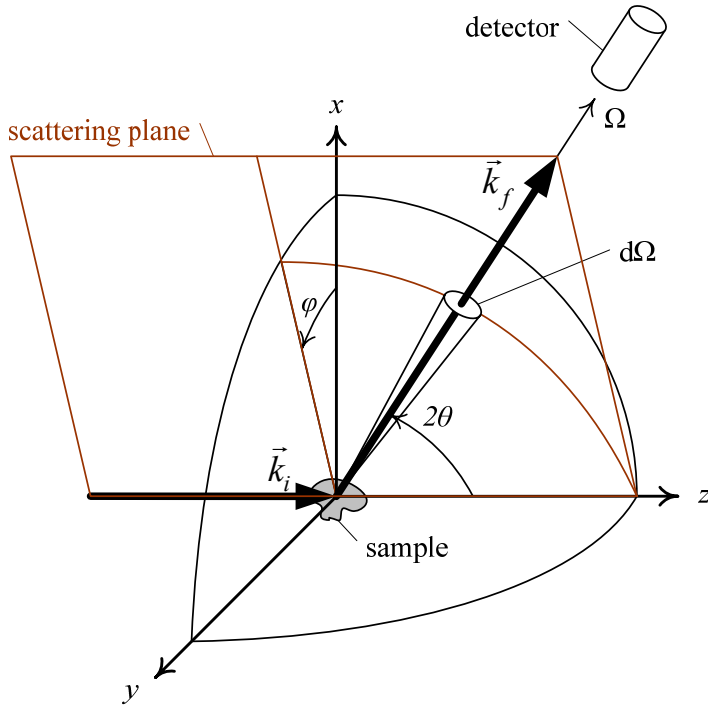


Figure 4-1: Schematic drawing of the geometry of a scattering experiment with incident wave of wave vector \vec{k}_i and scattered wave with wave vector \vec{k}_f . The resulting scattering plane is shown in brown. The sample is located in the origin of the coordinate system. The scattering shown here leads to a change of the propagation direction of the probe. This change is measured by the scattering angle 2θ in the scattering plane. It points into the direction of the outgoing wave given by Ω . The scattering is detected through a solid angle element $d\Omega$ with the symbolised detector. The projection of the outgoing wave vector \vec{k}_f onto the x - y -plane yields the azimuth angle φ .

This wave vector points into the direction of propagation of the probing beam and hence into the direction of the sample as shown in Figure 4-1. The scattering event inside the sample leads to a change of the momentum of the probe from wave vector \vec{k}_i to \vec{k}_f . These two vectors define the so-called *scattering plane* shown in brown in Figure 4-1. The difference of this two wave vectors is the *wave vector transfer* \vec{q} given by eq. (4.2), hence it also lies in the scattering plane.

$$\vec{q} = \vec{k}_f - \vec{k}_i \quad (4.2)$$

The modulus of this wave vector transfer can be calculated as is evident from Figure 4-2 in terms of the *scattering angle* 2θ :

$$|\vec{q}| = \sqrt{|\vec{k}_i|^2 + |\vec{k}_f|^2 - 2|\vec{k}_i||\vec{k}_f|\cos(2\theta)}. \quad (4.3)$$

The interaction between sample and probe can be inelastic as illustrated in Figure 4-2. Hence, the energy of the probe can differ before E_0 and after E_f the scattering. This leads to a change in the modulus of the wave vector according to the energy change E of the probe given by eq. (4.4), (Myers 1997)^{p. 127}.

$$E = E_f - E_0 \tag{4.4}$$

This change in energy is denoted positive, if the probe gains energy from the sample and negative if the probe loses energy to the sample. This energy transfer is sometimes given in terms of an angular frequency ω using the normalised Planck constant \hbar .

$$E = \hbar\omega \tag{4.5}$$

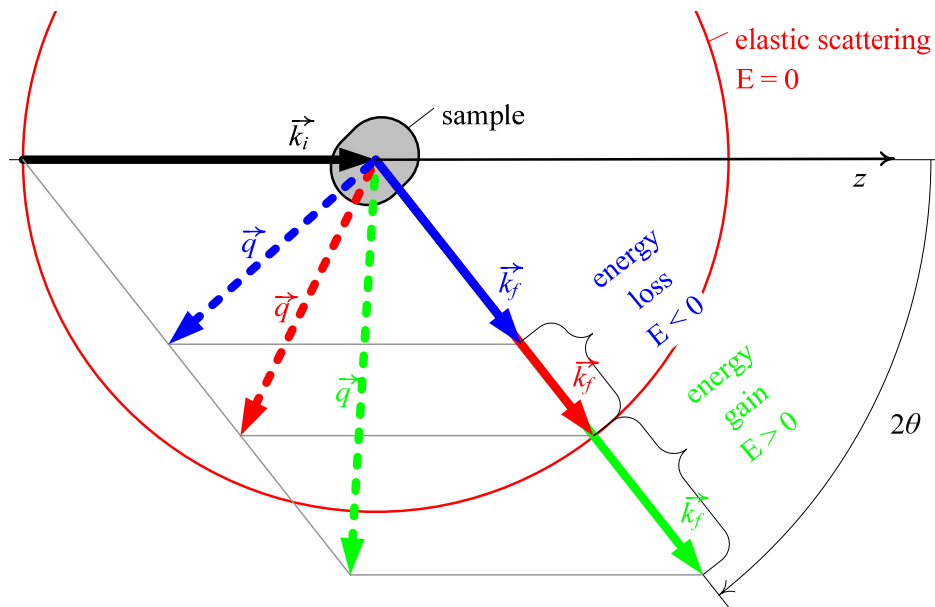


Figure 4-2: Diagram of the wave vectors and the wave vector transfers seen in the scattering plane for an exemplary scattering angle 2θ . The incident wave is presented in black with its wave vector \vec{k}_i . The outgoing waves after interaction with the sample (grey) are presented with their wave vectors \vec{k}_f . The case of elastic scattering is depicted in red, the case of energy loss in blue and that of energy gain in green. The resulting wave vector transfers \vec{q} are shown with dashed lines. The red circle gives the intersection line from the scattering plane with the sphere of elastic scattering. The endpoints of outgoing wave vectors of elastic scattering events lie on the surface of that sphere.

Only a fraction I_s of the incoming beam intensity I_i is scattered given by the total scattering cross section σ_{total} of the sample that consists of N scattering centres.

$$I_s = \sigma_{total} N I_i \tag{4.6}$$

There is no uniform treatment of the scattering cross section in the literature. The way it is used in eq. (4.6) implies a quantity that is meant per scattering centre as it is done for example in (Bée 1988)^{eq. (2.41)}, (Springer 1972)^{eq. (8)}, (Bacon 1975)^{eq. (2.5)} or (Price et al. 1986)^{eq. (1.2)}. On the contrary, it is possible to define the total scattering cross section as it is done for example in (Squires 1978)^{eq. (1.13)}, (Lovesey 1984)^{chap. 1.2}, (Brückel 2002)^{eq. (4), (40)} or (Volino 1978)^{eq. (34)–(37)}, where the factor N in eq. (4.6) is left out, leading to a cross section that depends on the number of scattering centres in the sample³. The latter definition of the cross section is more closely related to the raw data obtained in a scattering experiment than the version used in this thesis. Especially, if the scattering centres in the sample are distinguishable with respect to their contribution to the overall scattering signal, the definition from eq. (4.6) requires a quantity used for the cross section that is averaged over all scattering centres in the sample. Still, the definition is very useful in the case of monatomic samples or if the scattering is dominated by one species. At least one of these conditions is fulfilled in all experiments presented later. Furthermore, the expressions for the scattering cross section given in the following can be directly compared to tabulated values that are always given per scattering centre.

The scattered probe is detected with respect to its direction of propagation Ω and its energy after the interaction with the sample as shown in Figure 4-1. This finally gives a scattering density distribution commonly represented as *double differential cross section* depending on the solid angle Ω and the energy gain E of the probe:

$$\frac{\partial^2 \sigma(\Omega, E)}{\partial \Omega \partial E}. \quad (4.7)$$

³ Due to this different definition of the scattering cross section all expressions taken from such references will be modified by the relevant factor $\frac{1}{N}$ if presented in this thesis without any further explanatory notes.

It is linked to the total scattering cross section through a double integration over the full regions of solid angles and energy transfers (Squires 1978)^{eq. (1.14), (1.15)}.

$$\sigma_{total} = \int_{\Omega=0}^{4\pi} \int_{E=-E_0}^{E=\infty} \frac{\partial^2 \sigma}{\partial \Omega \partial E} dE d\Omega \quad (4.8)$$

The physical details of the possible scattering events determine the dependency of the double differential cross section on the solid angle and energy transfer. These details are discussed in the following sections. In the scattering experiments presented later the double differential cross section is measured and the results are compared with the calculations given in this chapter in order to gain information about the samples investigated.

4.2 Spectroscopy

The possibility of an energy transfer between sample and probe permits the use of scattering methods for spectroscopy. The spectroscopic measurements presented in section 6.2 have been performed with neutrons. Therefore, the case of inelastic interaction between sample and X-rays is left out in this section, (see e.g. (Caliebe 1997)^{chap. 2}), and the expressions developed in the following are only given for the case of neutron scattering. Nevertheless, the necessary theory for X-ray diffraction will be given in comparison to that developed for neutron diffraction at the appropriate positions below.

It is possible to describe the detailed nature of the interaction with a single number b_j called *scattering length*. It is sufficient in the case of a slow incident neutron of mass m_n scattered at \vec{R}_j to write the underlying interaction potential $V_j(\vec{r})$ as a *Fermi pseudo potential* using the three-dimensional Dirac delta functional $\delta(\vec{x})$ (Lovesey 1984)^{eq. (1.30)} where the scattering length depend only on the energy of the neutron.

$$V_j(\vec{r}) = \frac{2\pi\hbar^2}{m_n} b_j \delta(\vec{r} - \vec{R}_j) \quad (4.9)$$

The interaction between sample and neutron can be described with the following Hamiltonian H_c superimposing the potentials of all N scattering centres in the sample (Bée 1988)^{eq. (2.37)}:

$$H_c = \frac{2\pi\hbar^2}{m_n} \sum_{j=1}^N b_j \delta(\vec{r} - \vec{R}_j). \quad (4.10)$$

The measured quantity in a given scattering experiment is proportional to the transition probability of the probe from its initial state $|\vec{k}_i\rangle$ to its final state $|\vec{k}_f\rangle$. It is the thermally averaged response of the sample to the perturbation of the probe which is coupled via H_c . The sample changes its state from the initial $|n_i\rangle$ to the final $|n_f\rangle$ during the interaction. This induces a summation over all possible combinations of sample states that can lead to the measured change in states of the probe. The sample is assumed to be in thermal equilibrium at temperature T . It can be in any initial state with the probability p_i given by the Boltzmann distribution. The probability p_i can be written with the Boltzmann constant k_B for each initial sample state with energy E_i as follows (Lovesey et al. 1977)^{eq. (1.21a)}:

$$p_i = \frac{e^{-\frac{E_i}{k_B T}}}{\sum_j e^{-\frac{E_j}{k_B T}}}. \quad (4.11)$$

The thermal average of any operator A at temperature T is denoted as $\langle A \rangle_T$ and given, e.g. according to (Squires 1978)^{eq. (2.58)}

$$\langle A \rangle_T := \sum_i p_i \langle n_i | A | n_i \rangle. \quad (4.12)$$

The time-dependent Heisenberg operator of the scattering system described with the Hamiltonian H_s is defined as in (Squires 1978)^{eq. (2.55)} and (Newton 2002)^{eq. (6.69)}:

$$\vec{R}_j(t) := e^{\frac{iH_s t}{\hbar}} \vec{R}_j e^{-\frac{iH_s t}{\hbar}}. \quad (4.13)$$

Following the arguments given in (Squires 1978)^{Chap. 2} the double differential cross section can then be written^{4,5} as (Squires 1978)^{eq. (2.59)} or (Price et al. 1986)^{eq. (1.31)}:

$$\frac{\partial^2 \sigma}{\partial \Omega \partial E} = \frac{|\vec{k}_f|}{|\vec{k}_i|} \frac{1}{2\pi \hbar N} \sum_{m=1}^N \sum_{n=1}^N b_m b_n \int_{-\infty}^{\infty} \left\langle e^{-i\vec{q}\vec{R}_n(0)} e^{i\vec{q}\vec{R}_m(t)} \right\rangle_T e^{-i\omega t} dt. \quad (4.14)$$

Two abbreviations are used if the values b_i for the scattering lengths can be averaged independent from the position of the scattering centres, as in the case of monatomic samples, e.g. pure vanadium. They are called *coherent* and *incoherent scattering cross sections*, as defined in (Squires 1978)^{eq. (2.70)} or (Springer 1972)^{eq. (13b), (14)}:

$$\begin{aligned} \sigma_{coherent} &:= \frac{4\pi}{N^2} \left(\sum_{i=1}^N b_i \right)^2, \\ \sigma_{incoherent} &:= \frac{4\pi}{N} \sum_{i=1}^N b_i^2 - \sigma_{coherent}. \end{aligned} \quad (4.15)$$

The double differential cross section can be split into two summands that represent the coherent and incoherent parts of the scattering. The coherent part is defined according to (Squires 1978)^{eq. 2.68}:

$$\left(\frac{\partial^2 \sigma}{\partial \Omega \partial E} \right)_{coherent} := \frac{\sigma_{coherent}}{4\pi} \frac{|\vec{k}_f|}{|\vec{k}_i|} \frac{1}{2\pi \hbar} \sum_{m=1}^N \sum_{n=1}^N \int_{-\infty}^{\infty} \left\langle e^{-i\vec{q}\vec{R}_n(0)} e^{i\vec{q}\vec{R}_m(t)} \right\rangle_T e^{-i\omega t} dt. \quad (4.16)$$

This part depends on correlations between the positions of different scattering centres at different times and of the positions of the same centre at different times. It shows interference effects. The other part is defined as in (Squires 1978)^{eq. (2.69)}:

$$\left(\frac{\partial^2 \sigma}{\partial \Omega \partial E} \right)_{incoherent} := \frac{\sigma_{incoherent}}{4\pi} \frac{|\vec{k}_f|}{|\vec{k}_i|} \frac{1}{2\pi \hbar} \sum_{m=1}^N \int_{-\infty}^{\infty} \left\langle e^{-i\vec{q}\vec{R}_m(0)} e^{i\vec{q}\vec{R}_m(t)} \right\rangle_T e^{-i\omega t} dt. \quad (4.17)$$

⁴ The corresponding equation in (Bée 1988) is eq. (2.41), but there $\frac{\partial^2 \sigma}{\partial \Omega \partial \omega} = \hbar \frac{\partial^2 \sigma}{\partial \Omega \partial E}$ is given.

⁵ The cross section given in eq. (4.14) holds the dependency on Ω and E implicitly in the wave vectors, as it is usual in the literature. Nevertheless, the necessary Jacobian determinant has been used to derive the expressions shown in this chapter, as is shown explicitly in (Turchin 1965)^{eq. (2.123)}.

It depends only on the correlation between the positions of the same scattering centre at different times. Hence it does not show interference effects. The sum of equations (4.17) and (4.16) finally gives the double differential cross section of the total scattering:

$$\frac{\partial^2 \sigma}{\partial \Omega \partial E} = \left(\frac{\partial^2 \sigma}{\partial \Omega \partial E} \right)_{\text{coherent}} + \left(\frac{\partial^2 \sigma}{\partial \Omega \partial E} \right)_{\text{incoherent}}. \quad (4.18)$$

These two components of the double differential cross section can be calculated for a given scattering system if a model is available, leading to a deeper understanding of the scattering signal observed in an experiment. The corresponding expressions are shown in the following sections.

4.3 Scattering by Crystals

The signal obtained in a scattering experiment involving crystals can be described mathematically if the underlying lattice structure is split into two parts. The first part is the *Bravais lattice* of the average positions of the scattering centres. The second part consists of the actual displacements from that average positions.

The Bravais lattice, as defined for example in (Ashcroft and Mermin 1976)^{p. 64}, of a single crystal can be represented in terms of three linearly independent *primitive lattice vectors* $\vec{a}, \vec{b}, \vec{c}$ that point to the sides of the *primitive unit cell* as illustrated in Figure 4-3. Then any point \vec{l} of the lattice can be addressed with a set of integer numbers l_a, l_b, l_c (Ashcroft and Mermin 1976)^{eq. (4.1)}:

$$\vec{l} = l_a \vec{a} + l_b \vec{b} + l_c \vec{c}. \quad (4.19)$$

The instantaneous position \vec{R}_γ of any scattering centre in the crystal can be written with its displacement \vec{u}_γ from the average position according to (Squires 1978)^{eq. (3.9)}:

$$\vec{R}_\gamma(t) = \vec{l} + \vec{u}_\gamma(t). \quad (4.20)$$

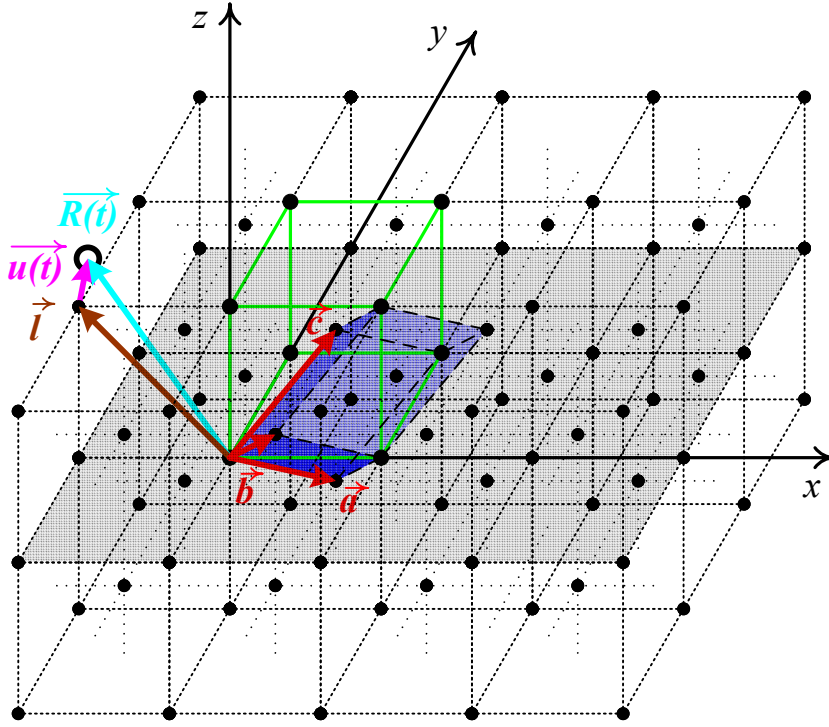


Figure 4-3: The structure shown here is formed in nature by several metals, e.g. vanadium. The conventional unit cell of the body centred cubic Bravais lattice is plotted in green. Three basis vectors are shown in red $\vec{a}, \vec{b}, \vec{c}$ for a monatomic primitive cell shaded in blue. An example lattice vector \vec{l} printed in brown points to an ideal lattice site. Any lattice point (black dot) of such an ideal crystal can be addressed with an integer linear combination of the red basis vectors. The actual position $\vec{R}(t)$ (cyan vector) of a real scattering centre (circle) is a function of time and differs from its ideal position \vec{l} by a displacement $\vec{u}(t)$ shown in pink. The x - y -plane of the coordinate system is filled in grey.

It turns out to be convenient to define the reciprocal lattice of the direct lattice described above with unit cell vectors defined as in (Ashcroft and Mermin 1976)^{eq. (5.3)}:

$$\begin{aligned}\vec{a}^* &:= 2\pi \frac{\vec{b} \times \vec{c}}{\vec{a} \cdot (\vec{b} \times \vec{c})}, \\ \vec{b}^* &:= 2\pi \frac{\vec{c} \times \vec{a}}{\vec{a} \cdot (\vec{b} \times \vec{c})}, \\ \vec{c}^* &:= 2\pi \frac{\vec{a} \times \vec{b}}{\vec{a} \cdot (\vec{b} \times \vec{c})}.\end{aligned}\tag{4.21}$$

Any point of the reciprocal lattice can be accessed via a reciprocal lattice vector \vec{G} with a set of three numbers h, k, l as a linear combination of the form (Ashcroft and Mermin 1976)^{eq. (5.6)}:

$$\vec{G} := h\vec{a}^* + k\vec{b}^* + l\vec{c}^*.\tag{4.22}$$

In particular, the wave vector transfer can be written in terms of its components q_a , q_b , q_c , projected onto the unit vectors of the basis cell:

$$\vec{q} = q_a \vec{a}^* + q_b \vec{b}^* + q_c \vec{c}^* \quad (4.23)$$

4.4 Debye-Waller-Factor

The terms on the right hand side of eq. (4.16) and (4.17) can be transformed with the definitions given in (4.20) above leading to the following expressions (Squires 1978)^{eq. (3.36), (3.127)} where the summation has to be performed over all lattice points of the crystal.

$$\left(\frac{\partial^2 \sigma}{\partial \Omega \partial E} \right)_{coherent} = \frac{\sigma_{coherent}}{4\pi} \frac{|\vec{k}_f|}{|\vec{k}_i|} \frac{N}{2\pi\hbar} e^{-\langle (\vec{q}\vec{u}_0(0))^2 \rangle_T} \sum_T e^{i\vec{q}\vec{l}} \int_{-\infty}^{\infty} e^{\langle \vec{q}\vec{u}_0(0)\vec{q}\vec{u}_i(t) \rangle_T} e^{-i\omega t} dt \quad (4.24)$$

$$\left(\frac{\partial^2 \sigma}{\partial \Omega \partial E} \right)_{incoherent} = \frac{\sigma_{incoherent}}{4\pi} \frac{|\vec{k}_f|}{|\vec{k}_i|} \frac{N}{2\pi\hbar} e^{-\langle (\vec{q}\vec{u}_0(0))^2 \rangle_T} \int_{-\infty}^{\infty} e^{\langle \vec{q}\vec{u}_0(0)\vec{q}\vec{u}_0(t) \rangle_T} e^{-i\omega t} dt \quad (4.25)$$

The exponential term present in both equations is known as the *Debye-Waller-Factor* or the *atomic temperature factor* (Squires 1978)^{eq. (3.49)}.

$$T(\vec{q}) := e^{-\langle (\vec{q}\vec{u}_0(0))^2 \rangle_T} = e^{-\langle u^2 \rangle_T \vec{q}^2} = e^{-2W} \quad (4.26)$$

This term can be simplified in the case of harmonic crystals with mean squared displacement $\langle u^2 \rangle_T$ where

$$T(\vec{q}) = e^{-\frac{1}{3}\langle u^2 \rangle_T \vec{q}^2} \quad (4.27)$$

holds according to (Squires 1978)^{eq. (3.63)}. A comprehensive discussion of the atomic temperature factor can be found in (Willis and Pryor 1975)^{chap. 4}.

4.5 Phonon Expansion

The exponential terms in the integrands of eq. (4.24) and (4.25) can be expanded as follows (Squires 1978)^{eq. (3.40)}:

$$e^{\langle \vec{q}\vec{u}_0(0)\vec{q}\vec{u}_i(t) \rangle_T} = \sum_{n=0}^{\infty} \frac{1}{n!} \left(\langle \vec{q}\vec{u}_0(0)\vec{q}\vec{u}_i(t) \rangle_T \right)^n. \quad (4.28)$$

The n^{th} summand in eq. (4.28) can be identified as a contribution to the cross section due to n -phonon processes (Squires 1978)^{p. 31} written as the n -phonon scattering cross sections, defined as follows:

$$\left(\frac{\partial^2 \sigma}{\partial \Omega \partial E} \right)_{\substack{\text{coherent,} \\ n \text{ phonons}}} := \frac{1}{n!} \frac{\sigma_{\text{coherent}}}{4\pi} \frac{|\vec{k}_f|}{|\vec{k}_i|} \frac{N}{2\pi\hbar} T(\vec{q}) \sum_{\vec{l}} e^{i\vec{q}\vec{l}} \int_{-\infty}^{\infty} \left(\langle \vec{q}\vec{u}_0(0)\vec{q}\vec{u}_i(t) \rangle_T \right)^n e^{-i\omega t} dt, \quad (4.29)$$

$$\left(\frac{\partial^2 \sigma}{\partial \Omega \partial E} \right)_{\substack{\text{incoherent,} \\ n \text{ phonons}}} := \frac{1}{n!} \frac{\sigma_{\text{incoherent}}}{4\pi} \frac{|\vec{k}_f|}{|\vec{k}_i|} \frac{N}{2\pi\hbar} T(\vec{q}) \int_{-\infty}^{\infty} \left(\langle \vec{q}\vec{u}_0(0)\vec{q}\vec{u}_0(t) \rangle_T \right)^n e^{-i\omega t} dt. \quad (4.30)$$

These definitions together with eq. (4.26) and (4.28) lead to the following forms of eq. (4.24) and (4.25):

$$\left(\frac{\partial^2 \sigma}{\partial \Omega \partial E} \right)_{\text{coherent}} = \sum_{n=0}^{\infty} \left(\frac{\partial^2 \sigma}{\partial \Omega \partial E} \right)_{\substack{\text{coherent,} \\ n \text{ phonons}}}, \quad (4.31)$$

$$\left(\frac{\partial^2 \sigma}{\partial \Omega \partial E} \right)_{\text{incoherent}} = \sum_{n=0}^{\infty} \left(\frac{\partial^2 \sigma}{\partial \Omega \partial E} \right)_{\substack{\text{incoherent,} \\ n \text{ phonons}}}. \quad (4.32)$$

A particular case is given for the first summand at $n = 0$, where no energy transfer happens between neutron and scattering centre, indicating elastic scattering events. The case of coherent elastic scattering is called *Bragg scattering* and will be discussed in section 4.6. The incoherent case of elastic scattering leads to (Squires 1978)^{eq. (3.128)}:

$$\left(\frac{\partial^2 \sigma}{\partial \Omega \partial E} \right)_{\substack{\text{incoherent,} \\ \text{elastic}}} = N \frac{\sigma_{\text{incoherent}}}{4\pi} T(\vec{q}). \quad (4.33)$$

The only dependence of the incoherent elastic scattering cross section on the direction of the scattering is in the temperature factor. The temperature factor is close to unity at low

temperatures. Therefore, a sample with dominating incoherent scattering cross section, as for example vanadium or hydrogen, is expected to give almost isotropic scattering signal at low temperatures. Therefore, vanadium is used as a calibration standard in neutron scattering experiments, in order to calibrate the efficiency of different detectors, as explained in section 5.2.2.7.1.

The creation (+1) or annihilation (-1) of a single phonon is of major interest because the incoherent scattering cross section of one phonon processes is directly related to the *density of states* $Z(\omega)$ of the N scattering centres of mass M in a cubic crystal (Squires 1978)^{eq. (3.136)} or (Price et al. 1986)^{eq. (1.70)}:

$$\left(\frac{\partial^2 \sigma}{\partial \Omega \partial E} \right)_{\substack{\text{incoherent,} \\ \pm 1 \text{ phonon}}} = \frac{\sigma_{\text{incoherent}}}{4\pi} \frac{|\vec{k}_f|}{|\vec{k}_i|} \frac{N}{4M} \bar{q}^2 T(\bar{q}) \frac{Z(E/\hbar)}{E/\hbar} \left(\coth \left(\frac{E}{2k_B T} \right) \pm 1 \right). \quad (4.34)$$

4.6 Bragg Scattering

The case of coherent elastic scattering is called Bragg scattering, as mentioned above. The corresponding double differential scattering cross section follows from eq. (4.29) for $n = 0$ with the Dirac delta functional $\delta(E)$, (Squires 1978)^{eq. (3.44)}:

$$\left(\frac{\partial^2 \sigma}{\partial \Omega \partial E} \right)_{\substack{\text{coherent,} \\ \text{elastic}}} = \frac{\sigma_{\text{coherent}}}{4\pi} N T(\bar{q}) \sum_{\vec{l}} e^{i\vec{q}\vec{l}} \delta(E). \quad (4.35)$$

The underlying scattering events are purely elastic, hence, they are localised at $E = 0$ and the integration over E can be performed directly (Squires 1978)^{eq. (3.46)}:

$$\left(\frac{d\sigma}{d\Omega} \right)_{\substack{\text{coherent,} \\ \text{elastic}}} = \frac{\sigma_{\text{coherent}}}{4\pi} N T(\bar{q}) \sum_{\vec{l}} e^{i\vec{q}\vec{l}}. \quad (4.36)$$

The sum over all lattice sites in eq. (4.36) can be calculated, for a crystal with dimensions $N_a \vec{a}$, $N_b \vec{b}$, $N_c \vec{c}$ along the directions of the unit cell, as follows from eq. (4.19), (4.23) and the orthogonality of (4.21) according to (Squires 1978)^{eq. (A.28)}:

$$\begin{aligned} \sum_{\vec{l}} e^{i\vec{q}\vec{l}} &= \sum_{\vec{l}} e^{i(q_a \vec{a}^* + q_b \vec{b}^* + q_c \vec{c}^*) \cdot (l_a \vec{a} + l_b \vec{b} + l_c \vec{c})} \\ &= \sum_{l_a = -\frac{N_a-1}{2}}^{\frac{N_a-1}{2}} e^{2\pi i q_a l_a} \sum_{l_b = -\frac{N_b-1}{2}}^{\frac{N_b-1}{2}} e^{2\pi i q_b l_b} \sum_{l_c = -\frac{N_c-1}{2}}^{\frac{N_c-1}{2}} e^{2\pi i q_c l_c} \\ &= \frac{\sin(N_a \pi q_a)}{\sin(\pi q_a)} \frac{\sin(N_b \pi q_b)}{\sin(\pi q_b)} \frac{\sin(N_c \pi q_c)}{\sin(\pi q_c)}. \end{aligned} \quad (4.37)$$

For a large crystal, i.e. $N_a \rightarrow \infty$, $N_b \rightarrow \infty$, $N_c \rightarrow \infty$, the quotients are highly peaked, and eq. (4.36) can be transformed to (Squires 1978)^{eq. (3.48)}:

$$\left(\frac{d\sigma}{d\Omega} \right)_{\substack{\text{coherent,} \\ \text{elastic}}} = \frac{\sigma_{\text{coherent}}}{4\pi} N T(\vec{q}) \frac{(2\pi)^3}{\vec{a} \cdot (\vec{b} \times \vec{c})} \sum_{\vec{G}} \delta(\vec{q} - \vec{G}). \quad (4.38)$$

From eq. (4.38) it is evident, that elastic coherent scattering occurs when

$$\vec{q} = \vec{G}. \quad (4.39)$$

Eq. (4.39) is a convenient representation of Bragg's law. All arguments given above hold also for the case of X-ray diffraction, with the classical radius of the electron r_0 , the polarisation ε_i and ε_f of the incident and scattered photons, respectively, and the *atomic scattering factor* $f(\vec{q})$, if one substitutes $\frac{\sigma_{\text{coherent}}}{4\pi}$ with $r_0^2 (\varepsilon_i \cdot \varepsilon_f)^2 |f(\vec{q})|^2$ in eq. (4.29) (Simmons 2003)^{eq. (11), (13)}, (Caliebe 1997)^{eq. (2.9)}. Finally, one obtains for unpolarised incident beams (Warren 1990)^{eq. (1.2)}:

$$\left(\frac{d\sigma}{d\Omega} \right)_{\substack{\text{coherent,} \\ \text{elastic}}} = r_0^2 (1 + \cos^2(2\theta)) |f(\vec{q})|^2 N T(\vec{q}) \frac{(2\pi)^3}{\vec{a} \cdot (\vec{b} \times \vec{c})} \sum_{\vec{G}} \delta(\vec{q} - \vec{G}). \quad (4.40)$$

Therefore, in X-ray and neutron diffraction experiments the intense scattering signals, i.e. peaks, due to eq. (4.39) are found at reciprocal lattice points \vec{G}_{hkl} , which are normal vectors to planes with *Miller indices* (h, k, l) of scattering centres that hold a distance d_{hkl} fulfilling (Warren 1990)^{p. 18}:

$$|\vec{G}_{hkl}| = \frac{2\pi}{d_{hkl}} = \frac{4\pi}{\lambda_0} \sin \theta. \quad (4.41)$$

4.7 Fibre Diffraction

The Bragg diffraction theory does not only allow to calculate diffraction patterns of single crystals. The diffraction patterns of samples consisting of many, possibly differently oriented crystals are more complex, however. The natural samples investigated mainly consist of fibrous material containing oriented cellulose crystals. Such samples can be described in terms of a fibre texture. An ideal fibre consists of a large number of small crystals, with each of the crystals aligned with a given crystallographic axis, e.g. the *c*-axis, along the fibre axis. The other axes of the crystals have a random rotation angle around the fibre axis. A comprehensive discussion of the theories involved in fibre diffraction can be found in (James 1982)^{sec. X4}.

The diffractogram obtained with a planar detector behind a sample with fibre texture is the superposition of the Bragg reflections obtained from many individual single crystal patterns. The random orientation of the crystals around the fibre axis ensures that always some of the crystals fulfil the Bragg condition. Reflections of type *hk0* or *00l* are called equatorial or meridional, respectively. Reflections of type *hkl* with constant *l* can be found on so-called *layer lines* of hyperbolic shape.

The quantities that can be derived from the diffraction pattern of a real fibre are given schematically in Figure 4-4. In a real fibre the orientation of the crystals scatters around the perfect alignment along the fibre axis. Therefore, the reflections obtained from such a real

fibre are broadened with respect to those obtained from a perfectly textured fibre. The azimuthal broadening is a measure for the scatter of the orientation of the crystals with respect to their mean orientation. The finite size of the crystals results in a radial broadening.

An example of a cellulose fibre diffractogram is shown in Figure 4-5, obtained from a single flax fibre. The designation of the reflections follows (Woodcock and Sarko 1980). The strong 200 and sharp 004 reflections are marked in red. The 200 reflections originate from planes of cellulose molecules parallel to the b - c -plane with spacing of $\frac{1}{2}|\vec{a}|$. The 004 reflections originate from planes of cellulose molecules parallel to the a - b -plane with spacing of $\frac{1}{4}|\vec{c}|$ (compare Figure 2-4). The high degree of orientation of the cellulose crystals in flax along the fibre axis leads to a diffraction pattern Figure 4-5 comparable to that in Figure 4-4. In both figures the layer lines are indicated with dashed lines.

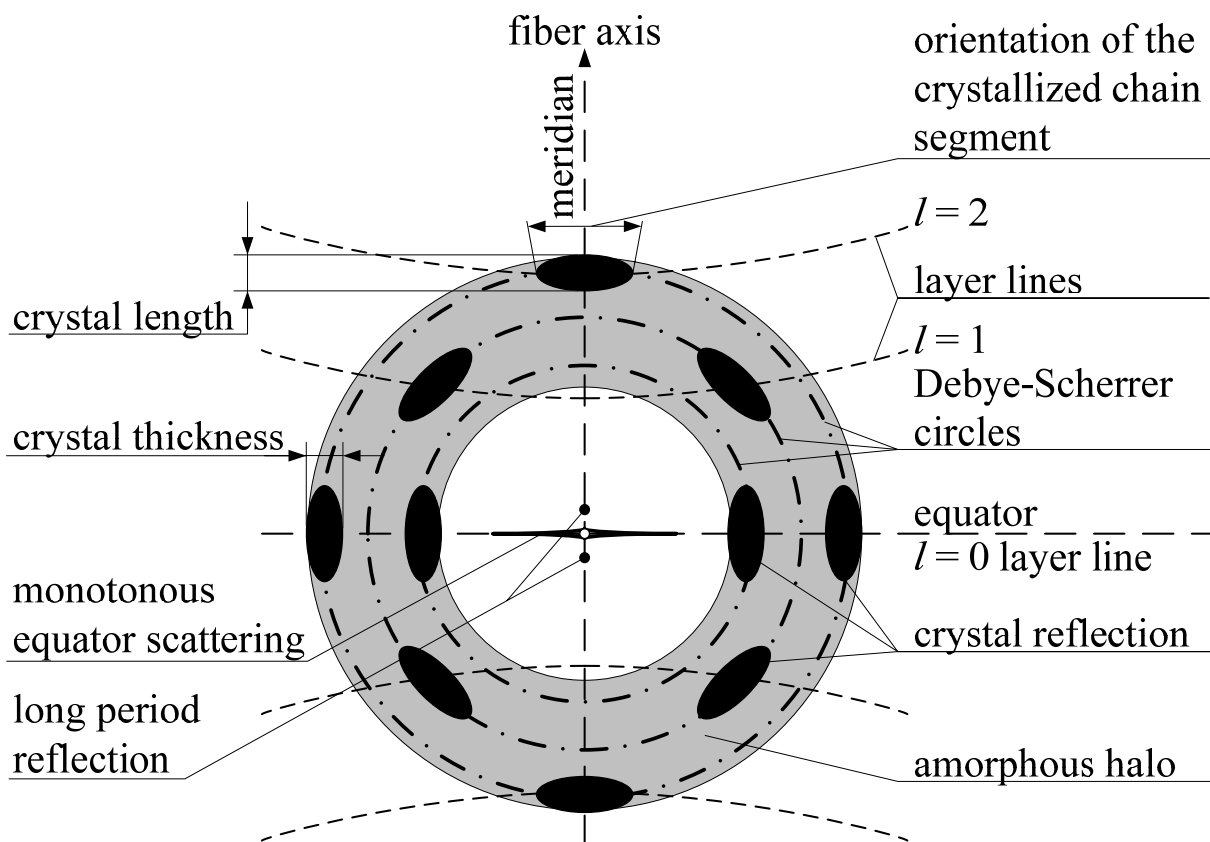


Figure 4-4: Description of the X-ray fibre diffractogram and the designation of the diffraction bands. After (Krässig 1993)^{Fig. 37}.

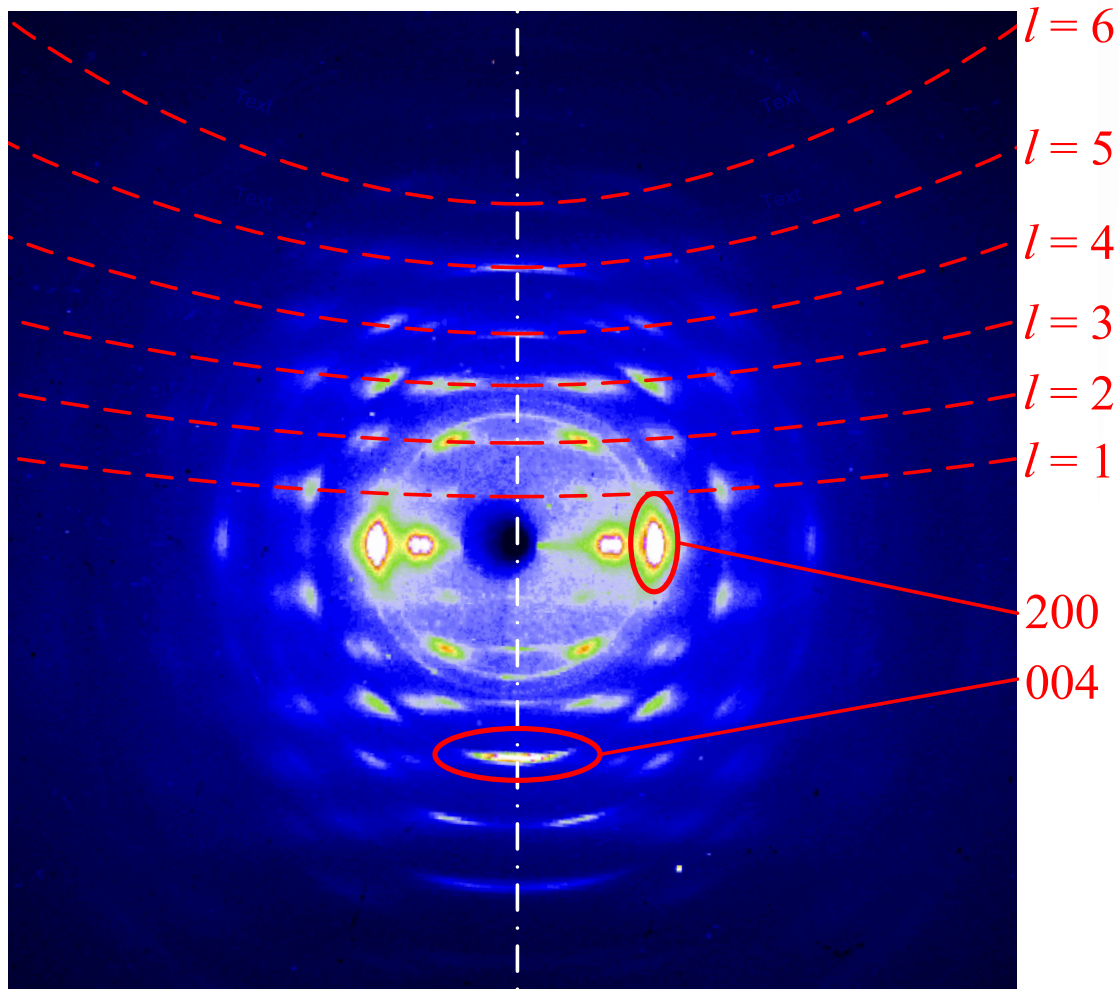


Figure 4-5: Fibre diffraction pattern of a single flax fibre, taken from (Müller et al. 2000a)^{Fig. 4}. The fibre axis is vertical (dashed white line). The layer lines are marked with red dashed lines. The hyperbolic distortion of the layer lines due to the planar detector used is evident. The strong equatorial 200 and the sharp 004 reflections are shown in red. The image has been accumulated during 120 second.

A particular case is given for tissue from plant cell walls with unique MFA. The diffraction pattern obtained from a tracheid sample with rectangular cross section is the sum of the patterns obtained from all four parts of the cell wall, if the X-ray beam passes perpendicular to the fibre axis and the beam size is greater than the lateral dimension of the cell. For high MFA and cell walls oriented perpendicularly to the beam, the MFA can be determined directly from the azimuthal symmetry angle found in the small angle diffraction patterns (Lichtenegger et al. 1997)^{(i)(a)}. The determination of a small MFA is not straightforward, due to the strong overlap of the involved reflections, but it is possible to estimate an upper limit for the MFA from the azimuthal width of the reflections.

4.8 Hermans' Orientation Function

A model-free measure for the orientation of a unit cell axis, e.g. \vec{a} , of the crystals in a textured sample with respect to a given sample axis, e.g. x , can be calculated with *Hermans' orientation function* $f_{\vec{a},x}$. A brief introduction to this measure can be found in (Kölln 2004)^{chap. 3.1.3.} and a comprehensive discussion is given in (Alexander 1979)^{chap. 4-4.} The orientation function is defined as follows in terms of the average $\langle \cdot \rangle_K$ over all crystals K with angle ψ between crystal axis and sample axis (Alexander 1979)^{eq. (4-21).}

$$f_{\vec{a},x} = \frac{1}{2} \left(3 \langle \cos^2 \psi \rangle_K - 1 \right) = 1 - \frac{3}{2} \langle \sin^2 \psi \rangle_K. \quad (4.42)$$

The orientation function yields a value of one for perfect alignment, zero for random orientation and $-1/2$ for precise perpendicularity of the crystal axis with respect to the given sample axis. The numerical value can be derived directly from the intensities $I(\varphi)$ found in the diffraction pattern of a planar detector depending on the azimuthal angle φ according to (Hermans 1946)^{p. 164, eq. (1).}

$$f_{\vec{a},x} = 1 - \frac{3 \int_0^{\frac{\pi}{2}} I(\varphi) \sin^3(\varphi) d\varphi}{2 \int_0^{\frac{\pi}{2}} I(\varphi) \sin(\varphi) d\varphi} \quad (4.43)$$

The particular case of random orientation with respect to all axes is fulfilled in a powder sample, consisting of a large number of small crystallites. This powder diffraction will be discussed in the next subsection.

4.9 Powder Diffraction

An ideal powder sample consists of a large number of small crystallites with random orientation, i.e. no preferred orientation is established in contrast to a fibre texture, discussed in section 4.7. The pattern found with a planar detector behind the sample consists of rings. Each ring of the pattern, called *Debye-Scherrer circle*, corresponds to certain lattice spacing present in the crystals. The ring-like pattern originates from scattering events with common scattering angle 2θ . The outgoing wave vectors of such scattering events lie on the surface of the so-called *Debye-Scherrer cone* with its symmetry axis along the incident beam and semi-angle 2θ . Besides its suitability for structure determination, the collection of powder diffraction patterns can be used to calibrate the position and alignment of a planar detector with respect to the sample and the incident beam, as will be shown in section 5.1.6.3. An example of a pattern is shown in Figure 5-22.

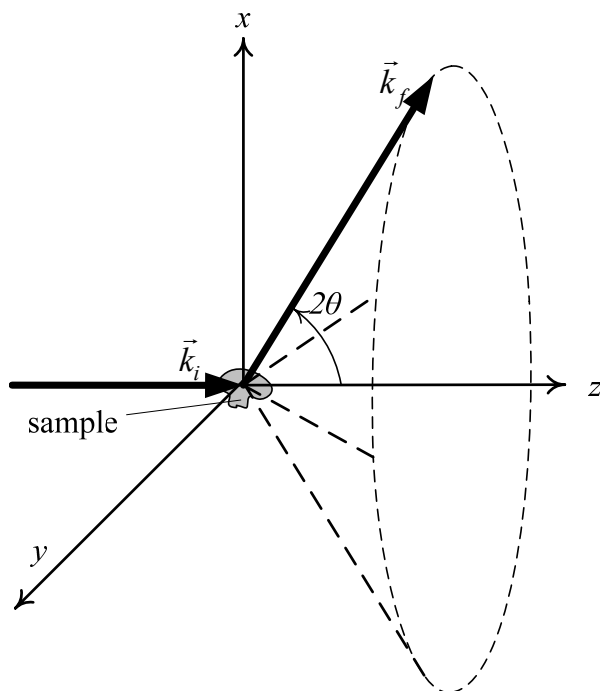


Figure 4-6: Schematic drawing of the geometry of a scattering experiment with a powder sample (grey). The wave vector \vec{k}_i of the incident wave is aligned along the z-axis. An example wave vector \vec{k}_f of the scattered wave is shown for a scattering angle 2θ . The wave vectors of all scattered waves of elastic scattering events with the same scattering angle 2θ point onto the same Debye-Scherrer circle and lie on the surface of the same Debye-Scherrer cone marked with the dashed lines.

5 Experimental Techniques

The questions posed in the introduction have been addressed with a set of experiments. The technical details of these experiments will be given in this chapter. Most of them are directly related to the results of the X-ray diffraction and inelastic neutron scattering experiments presented in chapter 6. All investigations addressed the influence of the water adsorbed to the wood, leading to specially designed apparatuses, which will be described in the following.

5.1 X-ray Diffraction Studies

Two different devices have been used for the stretching experiments to monitor the relationship between the mechanical properties of wood as described in chapter 3 and its internal structure as described in chapter 2. Both have been used at synchrotron X-ray sources to collect diffraction patterns during tensile stretching experiments. The first one has been constructed originally in the context of (Kölln 2004). It is especially suited for the needs of neutron scattering experiments and has been modified only slightly to allow the usage at a synchrotron radiation source. It is called in this thesis the ‘big Kiel stretching device’, due to its dimensions and capabilities. The other one has been designed especially for the needs at synchrotron radiation sources. It permits, besides some other benefits, a controlled humid stretching environment (HUSTEN). Both devices are described in the following in combination with the detector and the experimental stations, A2 and ID13, they have been used with. Finally, the data reduction process is explained in detail at the end of this section.

5.1.1 Experimental Station A2 at HASYLAB

Most of the experiments have been performed at the experimental station A2 at the Hamburg Synchrotron Laboratory (HASYLAB). The layout of the instrument is shown in Figure 5-1. It is a doubly focusing diffractometer that operates at a fixed wavelength of 1.5 \AA . The synchrotron radiation is monochromatized and horizontally focused by a germanium crystal. The vertical focussing is done with a bent nickel mirror. The spatial resolution of the instrument can be adjusted with a slit systems. For the experiments presented in section 6.1 the optional micro slit system has been used to produce a beam spot of about $250 \mu\text{m} \times 250 \mu\text{m}$. The actual stretching device that has been used has been placed on top of the optical bench and connected to the instrument via several translational stages.

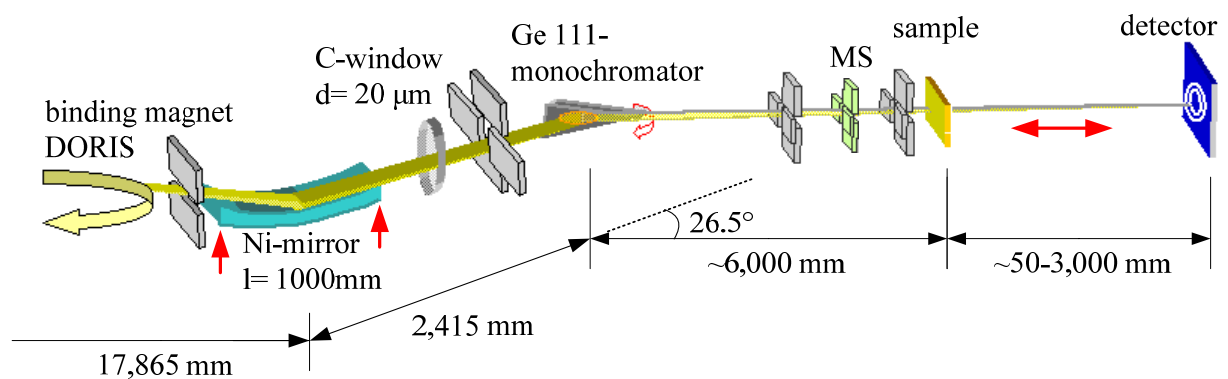


Figure 5-1: Layout of the optical system used at the beam line A2 at the HASYLAB taken from (Roth 2005). The arrows indicate possible movements of the components necessary during alignment of the instrument. The slit systems are shown in grey. The synchrotron radiation is monochromatized and horizontally focussed with the germanium monochromator. The nickel mirror permits vertical focussing. The detector is placed on the optical bench. An optional micro slit system (MS) can be installed between the last two shown slit systems.

5.1.2 Experimental Station ID13 at ESRF

The radiation used at the microfocus beamline ID13 at the ESRF is provided by two undulators optimized for 13 keV radiation. The radiation is monochromatized by a silicon (111) double monochromator and further tuned by a Kirkpatrick-Baez-mirror (KB-mirror) and collimator to about 5 μm beam size. HUSTEN has been used as stretching device, described in section 5.1.4. It has been connected through a translational stage to the instrument.

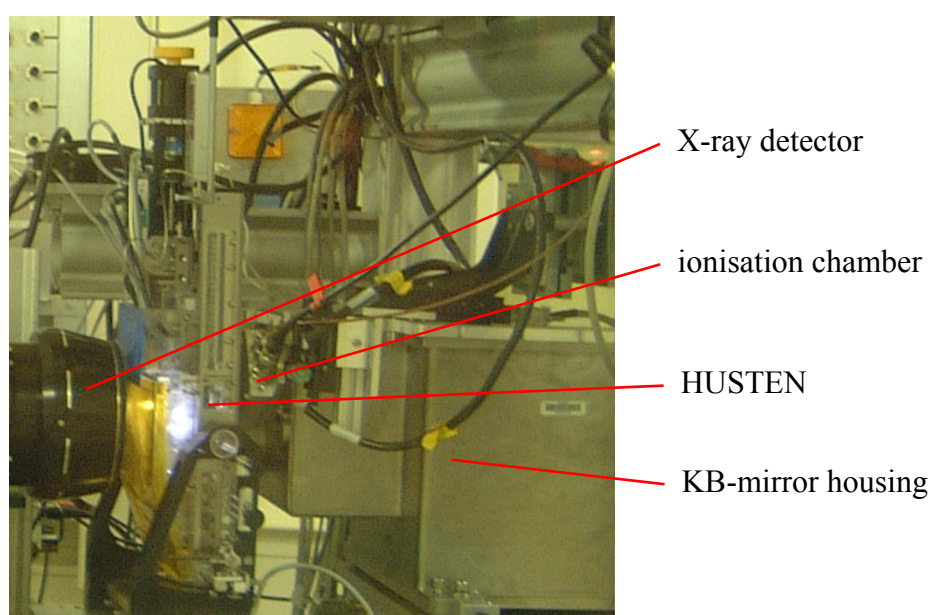


Figure 5-2: HUSTEN installed at the microfocus beamline ID13 at the third generation synchrotron radiation source ESRF.

5.1.3 The Big Kiel Stretching Device

The mechanical properties of wood described in chapter 3 can be probed with tensile tests. A simple stretching device has been developed for this purpose in the context of (Kölln 2004). It is equipped with a force sensor and driven with a servo motor. This machine can be used to measure forces up to 2.5 kN and can provide sample elongations up to 45 mm. It is mainly designed for the requirements of neutron scattering experiments. Hence, it is only partially suited for experiments at synchrotron radiation sources. The complete setup installed at the HASYLAB beam line A2 is shown in Figure 5-3. This stretching machine has been modi-

fied slightly for the experiments presented later, to enable some control of the atmosphere surrounding the sample and its moisture content.

The sample is held by two clamps. The lower clamp is fixed and the upper one is connected to the force sensor. This design requires a shift of the X-ray detector between the measurements and the mounting process of the sample. Additionally, the sample position in the stretching device can vary between the mounting position and the position during the stretching experiment, due to the flexible connection between force sensor and unguided upper clamp. This leads to a ‘starting region’ of the measurements, where the obtained diffraction patterns are strongly influenced by the change of the sample position. Nevertheless, the varying sample-to-detector distance can be monitored during the experiment with a calibration powder additionally applied to the surface of the sample, as shown in Figure 5-4.

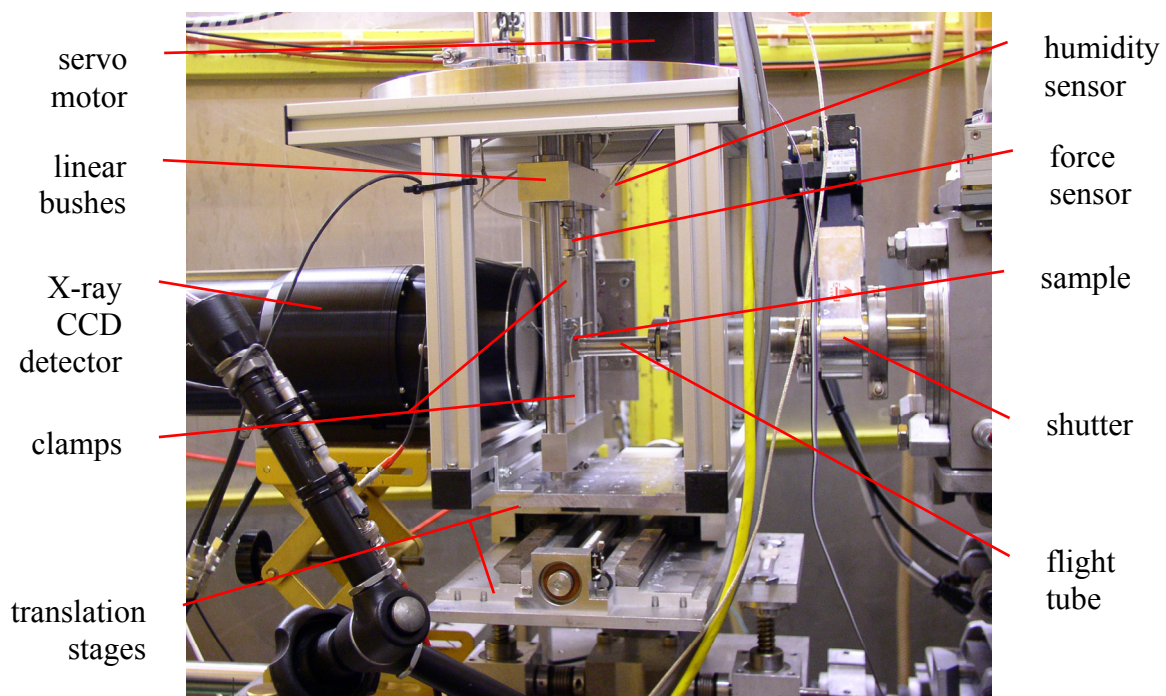


Figure 5-3: Big Kiel stretching device installed at HASYLAB beam line A2.

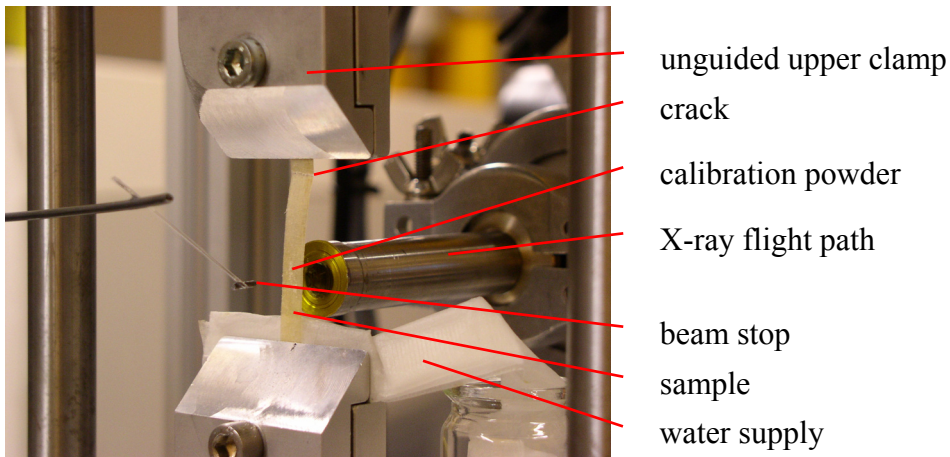


Figure 5-4: Wood sample investigated with X-ray diffraction in the big Kiel stretching device at HASYLAB beamline A2. The photo has been taken after fracture at the end of the experiment. The white powder permits online calibration of sample-to-detector distance. The X-ray flight path is kept in vacuum as close as possible to the sample. The small lead beam stop is glued to a glass capillary and positioned close behind the sample to minimize the background signal originating from air scattering. The water supply visible at the bottom keeps the moisture content in the sample at a high level during short experiments.

The force sensor of this stretching device is mounted on an aluminium beam, running on two linear bushes, as shown in Figure 5-3. This beam is driven via a ballscrew by a servo motor under control of a stand-alone motion controller. This controller is steered via a serial interface from a personal computer running a LabView[®] code. The personal computer collects all relevant data from the stretching device and synchronises the X-ray CCD camera, operated via a separate personal computer, collecting the diffraction images.

5.1.4 Humid Stretching Environment (HUSTEN)

Wood is a hierarchically structured material as explained in chapter 2. It is necessary to investigate its mechanical properties on all its hierarchical levels to understand their interactions and influence on the macroscopic properties. Therefore, tensile tests have been performed on small pieces of wood and even on single fibres. A special humid stretching environment (HUSTEN) has been designed, as shown in Figure 5-5, and built. It allows for combined X-ray and stretching experiments on small samples and single fibres in a humidity controlled atmosphere. This instrument will be explained in more detail in the following.

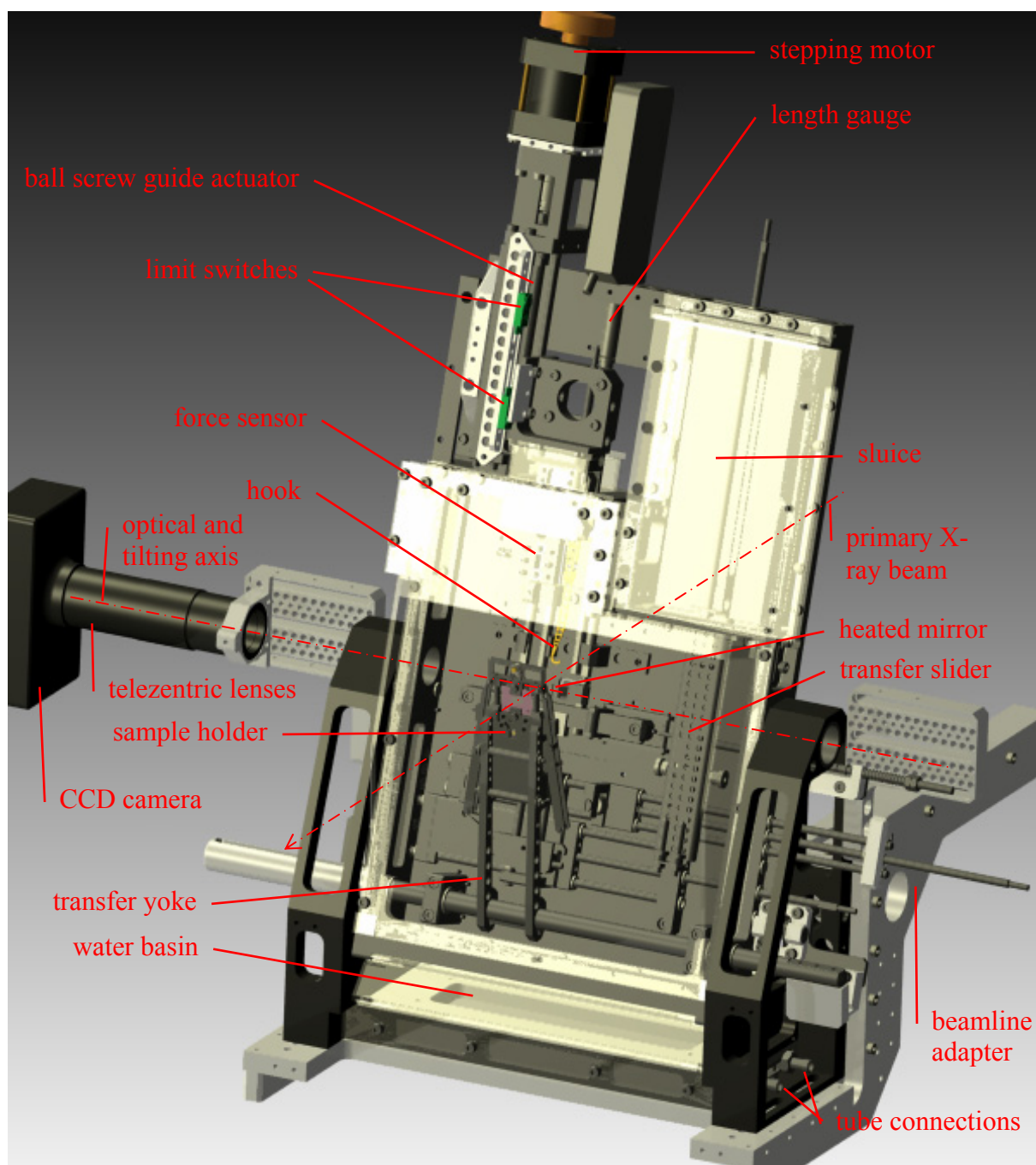


Figure 5-5: Design of the humid stretching environment HUSTEN. The translation stage is shown tilted by 20°. The sample holder is held by the transfer yoke given in a position reached during the sample exchange procedure. The exit window is not shown. The gold plated hook is displayed in its tilted position. The linear actuator has reached its lowest position. Wires and tubes for external connections are not shown.

The challenges mentioned above concerning the sample-to-detector distance due to the design of the big Kiel stretching device and the limited time available at synchrotron sources have been the motivation for the construction of HUSTEN. Additionally, the need of mechanically unstressed samples and the necessity of a controlled atmosphere in the chamber

surrounding the sample have been addressed with this design. The atmosphere is not disturbed during sample exchange, due to the sluice and transfer system shown in Figure 5-6. The time necessary between changes of samples to stabilize the climatic conditions is therefore kept small.

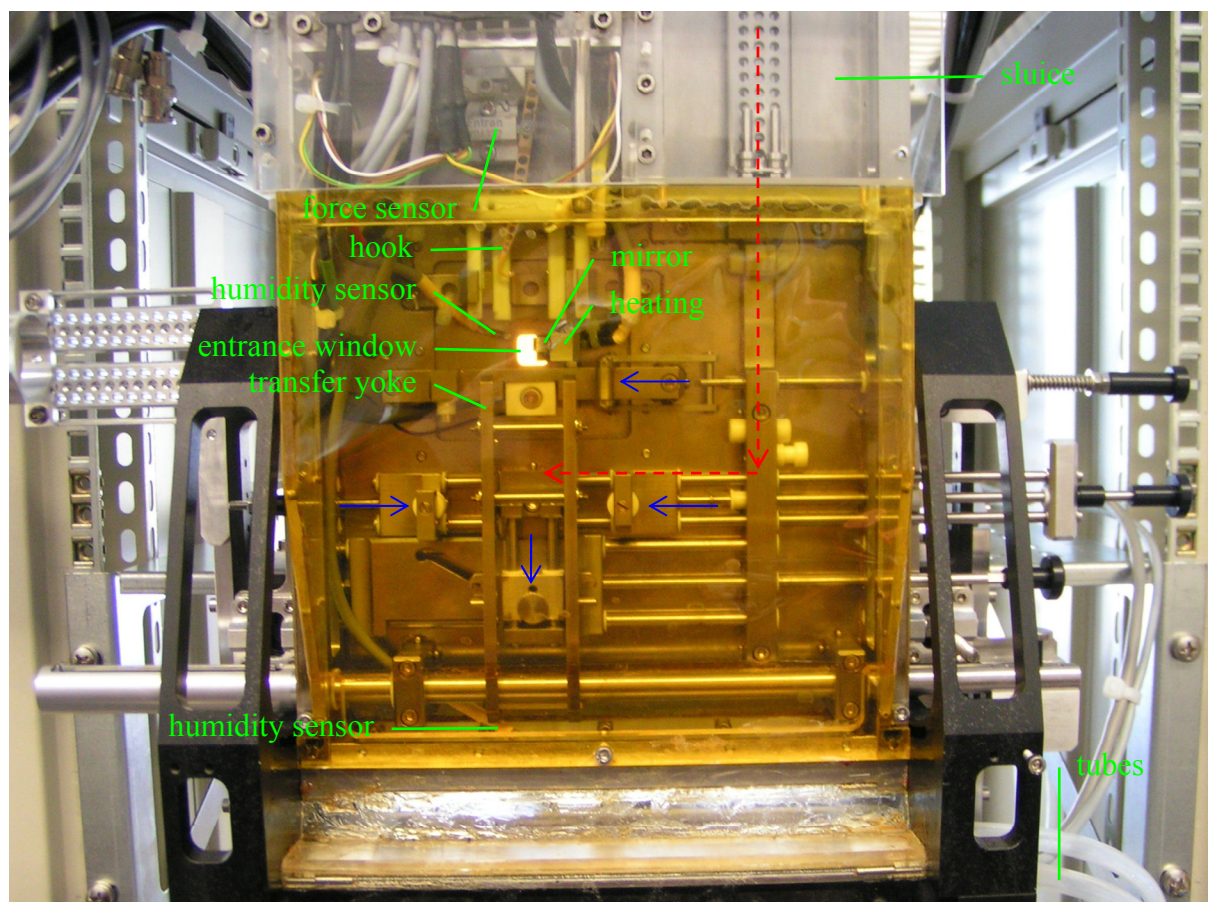


Figure 5-6: The transfer and sluice system of HUSTEN as seen from the X-ray detector position without sample holder. The red arrows show the transfer path of the sample holder. The blue arrows illustrate movements that are used to fix the sample holder and to free its upper clamp. The transfer yoke is shown in the final position.

The relative humidity of the air in the chamber is set with a water basin at the bottom of the chamber and measured with two sensors. One of the sensors is placed close to the sample. The other sensor monitors the humid air directly above the water basin. These two sensors signal stable conditions during the experiments. The temperature of the water basin is controlled with a closed loop temperature controller that drives a flat resistive heating panel beneath the water basin. A resistive temperature sensor measures the temperature of the water basin. By adding salts to the water and tuning the temperature of the water basin, the resulting

relative humidity of the atmosphere can be varied through a broad range between 10 and 100 %. The water basin has been designed as a drawer, hence, it can be exchanged or cleaned during the experiments. The level of the fluid surface in the water basin can be manipulated through two external tube connections, also allowing – if required – a constant water flow due to an optional external pump.

The X-ray detector is placed close behind the chamber during a combined experiment. It is not necessary to move it during the sample exchange. This permits an easy calibration of the sample-to-detector distance. The big exit window enables the collection of wide-angle scattering data. It consists of a thin Kapton[®] film⁶ ensuring low attenuation of the X-rays. The central mechanical part of HUSTEN used for the tensile tests and the sample exchange can be rotated from the upright position to a tilt of maximal 20°. This enables the direct measurement of the meridional reflections under exact Bragg condition. A small lead beam stop is placed between sample and detector to protect the detector against the high flux of the primary beam. It is positioned close to the sample to reduce the background signal originating from air scattering.

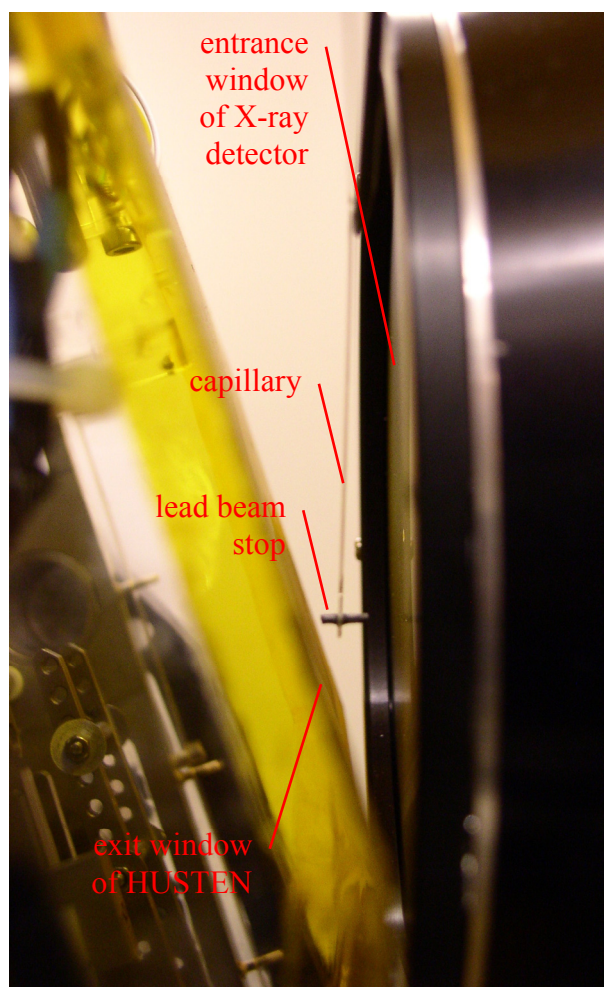


Figure 5-7: Lead beam stop and X-ray detector placed close behind the sample. The beam stop is glued to a motor driven glass capillary. The sample environment HUSTEN is shown in its tilted position, as used at the HASYLAB beamline A2.

⁶ Polyimide (PI), CAS No. 25038-81-7

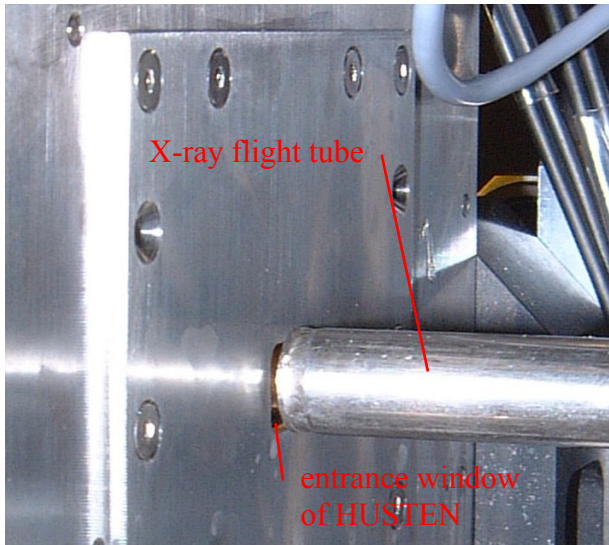


Figure 5-8: Entrance window of HUSTEN

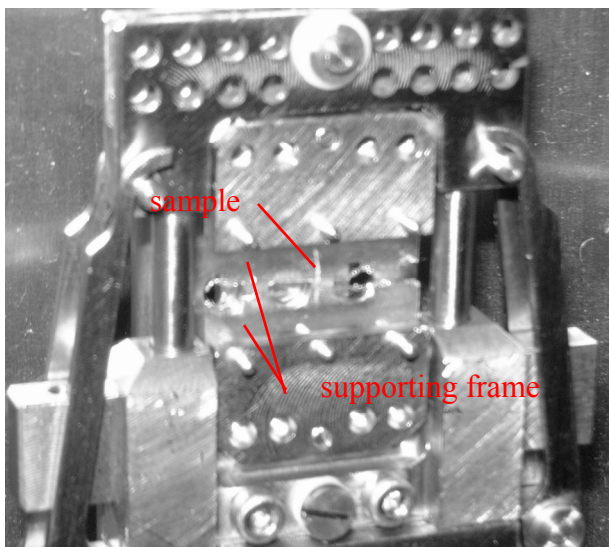


Figure 5-9: Single fibre mounted in the sample holder outside of HUSTEN. The supporting frame is divided into upper and lower part with a soldering gun.

The entrance window for the primary X-ray beam is small to reduce the background signal, but it can be dismantled via a few screws and easily exchanged to a broader one, as visible in Figure 5-8. This offers free access to the chamber and permits backward usage of HUSTEN with interchanged positions of X-ray source and detector in case of very restricted space.

The sample preparation typically needs a lot of time. The species have to be aligned carefully and any mechanical treatment has to be kept small. Otherwise, a small deformation of the sample can induce an early fracture influencing the outcome of the mechanical test. The mounting of the sample is critical in the case of single fibres.

The *sample holder* integrated in HUSTEN ensures a minimal deformation of the samples. It permits mounting the fibre outside the chamber, even outside the experimental

hutch. The sample can be held with small clamps or be glued onto a supporting frame made of paper or thin polymer foil. In the case of single fibres the later version permits convenient handling and monitoring of the samples under a light microscope during preparation. The glued sample is mounted already fixed to its supporting frame into the sample holder. After mechanical fixing with the clamps the frame is cut, for example using a soldering gun, as shown in Figure 5-9.

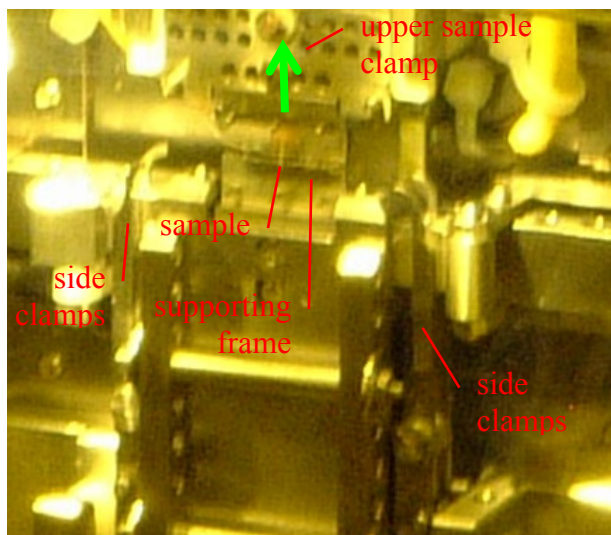


Figure 5-10: Sample holder inside of HUSTEN with released upper sample clamp. A single fibre is glued to the supporting and divided frame leading to an effective gap of less than 1 mm. The green arrow shows the direction of elongation during the stretching experiment.

The whole sample holder is then transferred into the chamber of HUSTEN. The side clamps of the sample holder fix the upper clamp on the shafts during this transfer. This side clamps are released inside HUSTEN, freeing the upper sample clamp for translation movements, as visible in Figure 5-10. This procedure ensures, that there is no mechanical deformation of the sample between bonding of the sample outside and the beginning of the stretching experiment inside HUSTEN.

The force necessary to elongate the sample is measured with a strain-gauge beam arrangement during the stretching experiment. At present HUSTEN can be equipped with several different force sensors limiting the range of the maximal measurable force between 0.5 and 5 Newton. These sensors are compensated for temperature effects but, additionally, their actual temperature is monitored during the experiment with a platinum resistance thermometer. The force sensor is mounted on a support driven with a stepping motor in high resolution micro stepping mode via a compact high precision ball screw guide actuator unit. The movement of this unit is monitored with a length gauge of accuracy better than $\pm 0.2 \mu\text{m}$. The connection of the force sensor to the upper jaw of the sample holder is established with a gold plated hook. This hook is connected with a small axis to the beam in bending of the sensor, but electrically isolated with two Teflon^{®7} bushes. The hook is rotated around this axis from outside the chamber to hook into the upper jaw at the lower position of the actuator. The actuator is then driven upwards until the weight of the upper jaw is found in the sensor signal.

⁷ PTFE, polytetrafluoroethylene, CAS No. 9002-84-0

At this point the shafts of the sample holder are taken away downwards together with the opened side clamps, allowing for free optical monitoring through the side windows of HUSTEN. During the stretching experiment the upper sample clamp is guided in a Teflon[®] track minimizing any unintended movements of the sample. Unfortunately, this design induces a small contamination of the force signal, due to friction between the upper sample clamp and its track and the weight of the clamp. These effects can be partially compensated with the signal obtained from an empty chamber measurement. Furthermore, the amount of friction can be minimized with some mechanical improvements, as already shown during experiments on silk fibres that have been performed with different types A and B of the sample holder shown in Figure 5-11 and Figure 5-12. The weight of the jaw of type B is only half of that of type A and type B permit the use of foils and fasteners together, in contrast to type A.

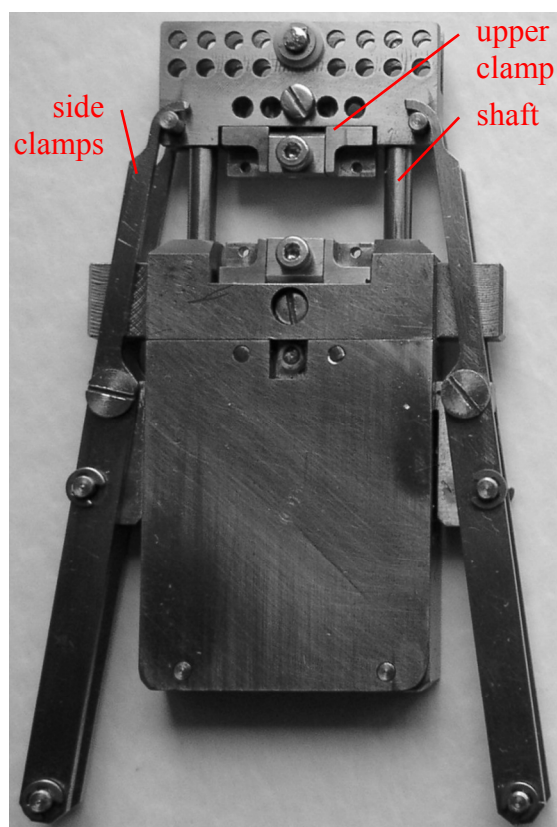


Figure 5-11: First sample holder type A used with HUSTEN.

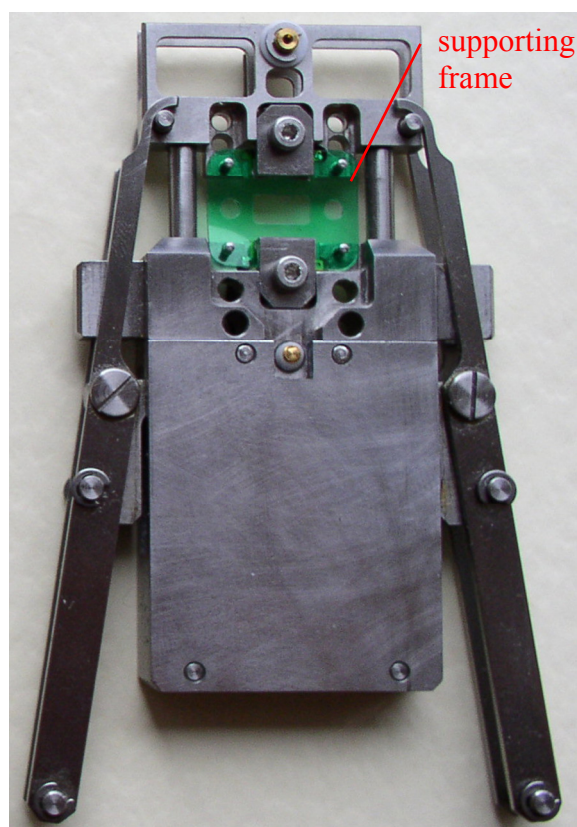


Figure 5-12: Improved sample holder type B used with HUSTEN.

The optical monitoring of the sample during the experiments has been done with a telecentric lens and a standard CCD camera. The field of view of the optical system is chosen to contain the sample position and its image from a mirror placed under about 45° close to the sample. In this way, the sample can be seen from two perpendicular directions, revealing any twisting or shifting during the experiment. In order to ensure a proper illumination several light emitting diodes (LED) are installed in the sample chamber. The temperature of the mounting point of the mirror is also controlled keeping its temperature above the condensation point. The quality of the optical images obtained this way can be improved even more with a high precision measurement lens and a cooled low noise high resolution CCD camera as preliminarily tested. With such an optical system the mechanical strain distribution along the sample should be measurable during the experiments.

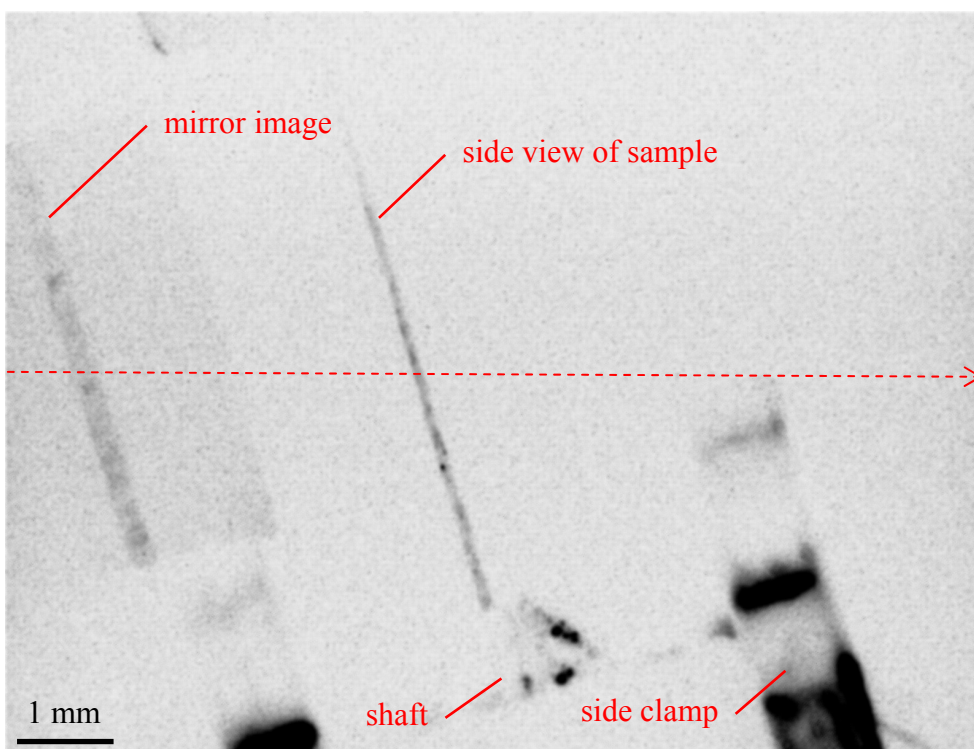


Figure 5-13: Inverted optical image of pine wood sample mounted in HUSTEN tilted to the Bragg-angle of the cellulose crystals. The path of the primary X-ray beam is given in red. The mirror image seen from the direction of the primary beam is visible at the left side. The straightened sample in the middle is seen from the side. The lowered side clamps and shafts of the sample holder are partially visible in the bottom region of the image. The black bar measures 1 mm.

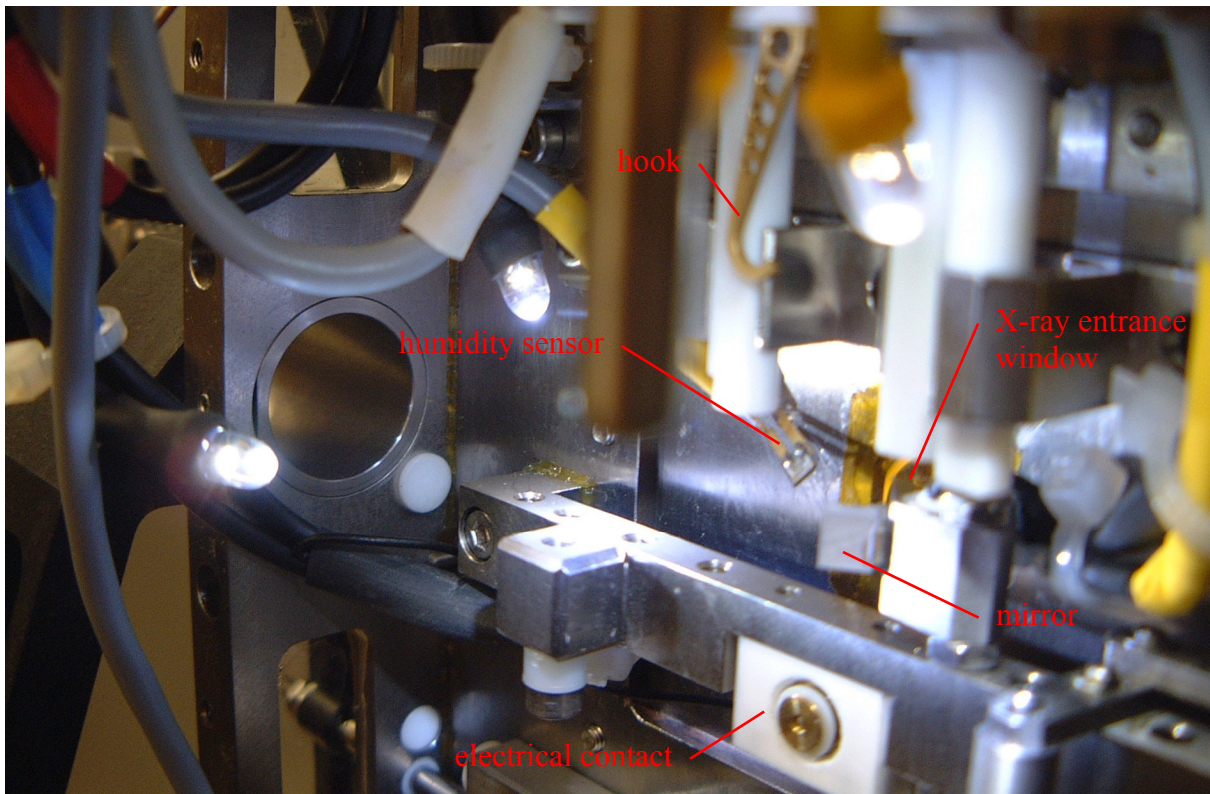


Figure 5-14: Close-up on the electrical installation close to the sample position inside HUSTEN. The bright LEDs offer enough light for the optical monitoring performed via the heated mirror. The humidity sensor gives the relative humidity of the air close to the sample. The electrical circuit for the determination of the sample impedance is closed through the contact at the bottom and the hook at the top, both gold plated to prevent corrosion.

The design of the sample holder and its connections to HUSTEN enable the measurement of the electrical properties of the sample during the experiment. For example, the electrical resistance of wood shows a strong dependency on the water content, allowing a direct monitoring of the moisture content of the sample (Dietenberger et al. 1999)^{p. 3-21}. These measurements have been performed so far with an industrial standard high speed LCR meter, not able to fully compensate the huge influence of the chamber especially in the case of dry single fibres with high resistance. However, in the case of small wet pieces of pine wood the impedance has been monitored. In Figure 5-15 an example of the raw data collected during a full stretching experiment is given. Under otherwise identical conditions the dry samples could not have been measured with this setup, always leading to an overflow of the LCR meter. At least, the wetting of the sample can be monitored this way.

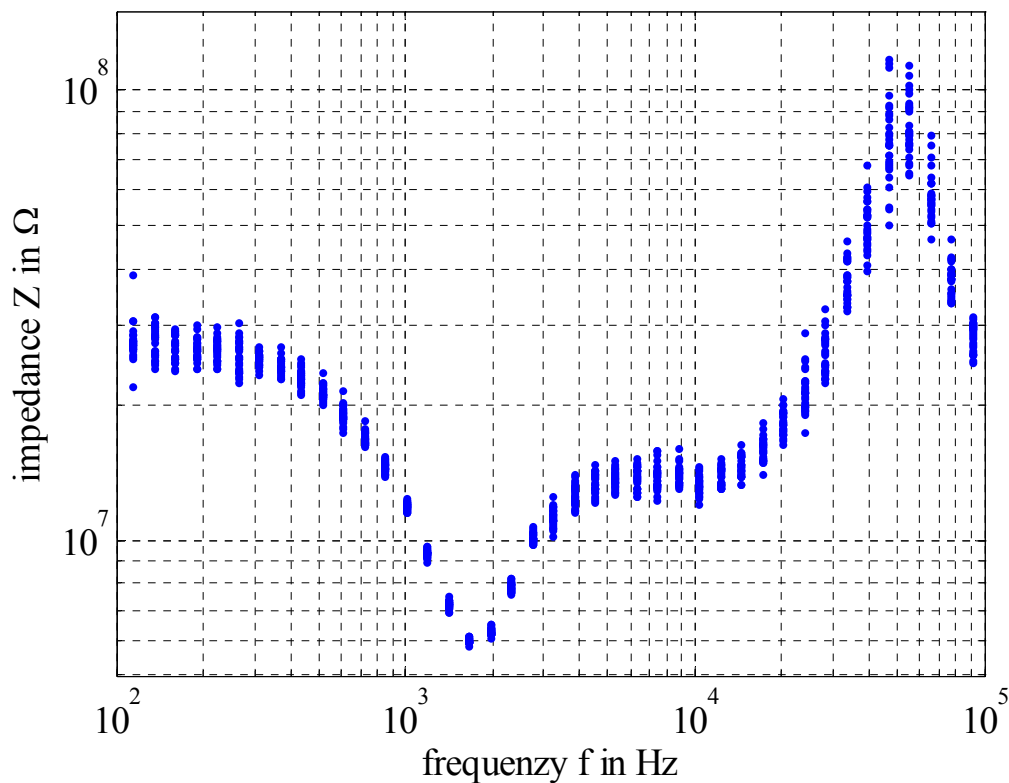


Figure 5-15: Raw electrical impedance signal collected during a combined X-ray diffraction and stretching experiment with a piece of wet pine wood mounted in HUSTEN.

All sensor signals from HUSTEN are collected with a personal computer controlling, in addition, the actuator and heaters. The signals from the humidity and force sensors of HUSTEN and from the various ionisation chambers of the synchrotron beamlines are converted with an multifunction data acquisition card inside the computer. Similarly, the signal from the length gauge is analysed with a special counter device also inside the computer. The software performing all the necessary tasks has been written in G, leading to a LabView[®] code, especially suited for the needs of experiments at synchrotron radiation sources. It is only a basic acquisition console (BACON), but it offers online data display and batch processing. The software logs all the sensor data into ASCII files. It controls the actuator of HUSTEN via a serial interface and the temperature controllers via an industrial standard GPIB-interface. Furthermore, BACON can communicate with beamline control computers running for example SPEC as done at ID13 via TCP/IP over an optional network connection (intranet). This feature has been used at ID13 in order to remote control the beamline translation stages. In

this way, it has been possible to move the sample during the stretching experiment perpendicular to the stretching direction through the X-ray beam, leading to a map of diffraction patterns over the whole width of the sample, as shown in Figure 6-21. The synchronisation of the stretching experiment with the X-ray detector and fast shutter of the beamlines is established via transistor-transistor-logic (TTL) trigger lines, also controlled from HUSTEN.

5.1.5 X-ray CCD Imaging System

There are several ways to collect X-ray diffraction patterns. A very convenient one is the use of a two-dimensional charge-coupled device (CCD). Such detectors are used for this purpose for some time, e.g. (Eikenberry et al. 1991; Gao et al. 1993; Koch 1994; Ottonello et al. 1994; Zanevsky et al. 1995). The device used for the experiments presented later is based on a design, illustrated in Figure 5-16, where an image intensifier is placed between the scintillator and the CCD. The Gadolinium oxysulphide scintillator of this device is optimised for resolution at X-ray energies of 5 to 25 keV.

In the present study the changes inside the sample have had to be investigated during the stretching experiments *in situ*. Therefore, the diffraction pattern have had to be collected with a sufficient time resolution. The standard devices offered at A2 and ID13 are well suited for the need of diffraction experiments but the minimum time between two images for these systems is 4 seconds, ac-

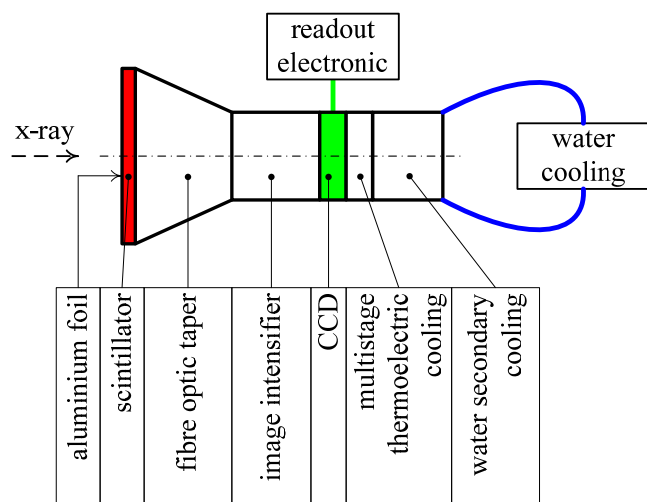


Figure 5-16: Design of the X-ray detector used to collect the diffraction patterns.

cumulation time of the images not taken into account. Such a time resolution is clearly not sufficient for the experiments presented in chapter 6, as is obvious for example from Figure 6-9. The device used in this study offers a very short readout time of less than 300 ms,

leading to a high time resolution during the stretching experiments. Unfortunately, the detector exhibits a problematic spatial distortion, as illustrated in Figure 5-18. This distortion is not compensated by the detector readout electronic nor by its software. Also, standard software freely available failed to correct for this distortion. Therefore, a MATLAB[®] code has been developed, described in the following, in order to compensate the distortion of the system.

5.1.6 Data Reduction

There are several ways to detect X-ray diffraction patterns. One convenient way is to use a two-dimensional detector that delivers the desired pattern as a numerical array that represents the intensity distribution detected. A detector placed behind the sample under investigation and aligned perpendicularly to the incident beam of the X-ray source shows the well-known diffraction pattern. Even when care is taken during the collection of these raw data, there are still a few parameters left that have to be taken into account, before the data can be compared to the theories shown in chapter 4. The steps that should be performed during the process of data analysis can be divided as follows:

- detector spatial distortion correction,
- detector intensity response correction (so-called *flat-field correction*),
- detector misalignment compensation.

Each of these steps will be discussed in detail within the following sections. It will be assumed that there is a *template image* collected with the detector under calibration conditions. This template image is given as an array of numbers I_{raw} , one for each pixel of the detector. These numbers are a measure for the intensity sensed by the detector at some a priori unknown positions. The goal of the calibration process is to determine these positions and to rescale the given intensities if necessary. The overall transformation finally leads to a representation of the data that is independent of the technical circumstances that have been present during the collection of the data.

5.1.6.1 Spatial Distortion Correction

As with any optical device the imaging process can lead to some spatial distortions that should be corrected. This can be done by a simple transformation⁸ that maps the original raw positions of the detector data $\vec{r}_{raw} := (x_{raw}, y_{raw})^T$ to the ideal positions of a theoretically undisturbed detector $\vec{r}_d := (x_d, y_d, 0, 1)^T$. That means one has to find a suitable transformation that fulfils some boundary conditions due to the given experimental situation. The problem is well-known and is called *image registration*. An overview can be found for example in (Brown 1992) or (Maintz and Viergever 1998).

Image registration can be explained in terms of a *reference image* and a *template image*. The reference image represents the ideal undisturbed case. The template image is the pattern as acquired by the real system before correction. It may be possible to identify some points in both images that can be linked together by some extra information. These corresponding points are called *landmarks*. They can be used in a so-called landmark-based approach to construct the transformation. There are several ways to produce such pairs of images. One way is to place a grid pattern of holes as a mask with known dimensions in front of the entrance window of the detector and illuminate the mask with a fixed source. This method has been used in the measurements presented later, where a ^{109}Cd source has been placed in about one decimetre distance to the grid of 0.5 mm holes spaced equally every (1.00 ± 0.01) mm.

⁸ The overall transformation developed later will be very simple if it is defined on \mathbb{R}^4 as will be clear later on. Therefore, here the output of this transformation is mapped into that space.

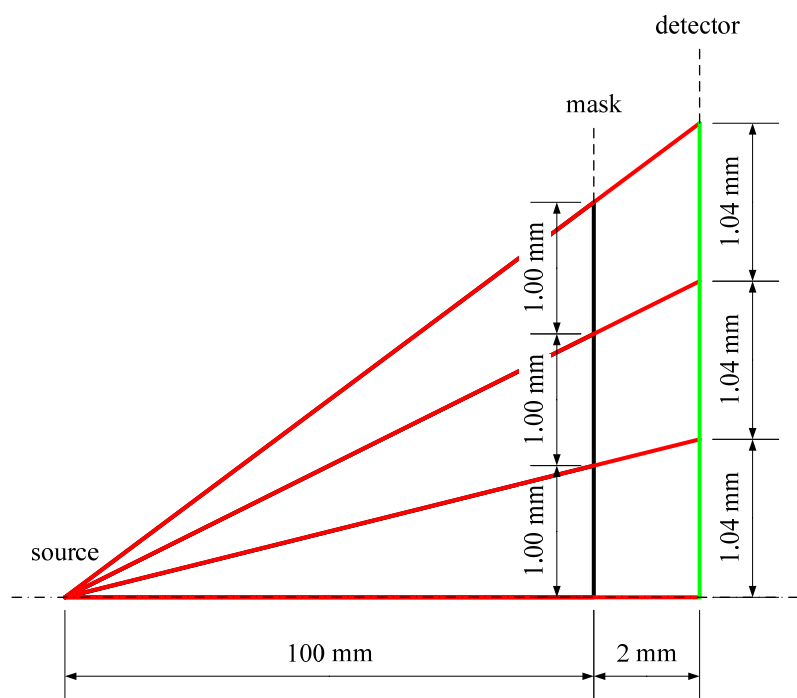


Figure 5-17: Sketch of the geometry of the resulting parallax effect if a calibration mask (black) is placed in a distance of 2 mm in front of the sensitive area of a detector (green). Here the radiation source is placed in a distance of 100 mm in front of the mask and the spacing of the grid is 1 mm, resulting in an enlarged but constant spacing of the pattern of 1.04 mm at the detector position.

The grid has been placed directly in front of the detector. In this setting the remaining distance between the grid and the fluorescence screen inside the detector housing leads to a widening of the pattern collected due to the parallax effect. It can be neglected for the further analysis, because all spatially corrected diffraction patterns are transformed into reciprocal space or lattice spacing afterwards based on a calibration procedure with a known scattering source. Therefore, this parallax effect only influences the values for the absolute positions given during the calibration run, for example the sample-to-detector distance, but it does not influence the resulting diffraction patterns in reciprocal space. Nevertheless, the widening for the experiments presented in this section has been estimated according to the geometric conditions illustrated in Figure 5-17. Consequently, the resulting effective spacing of the grid of 1.04 mm has been taken for the calibration calculus carried out, as illustrated in Figure 5-18.

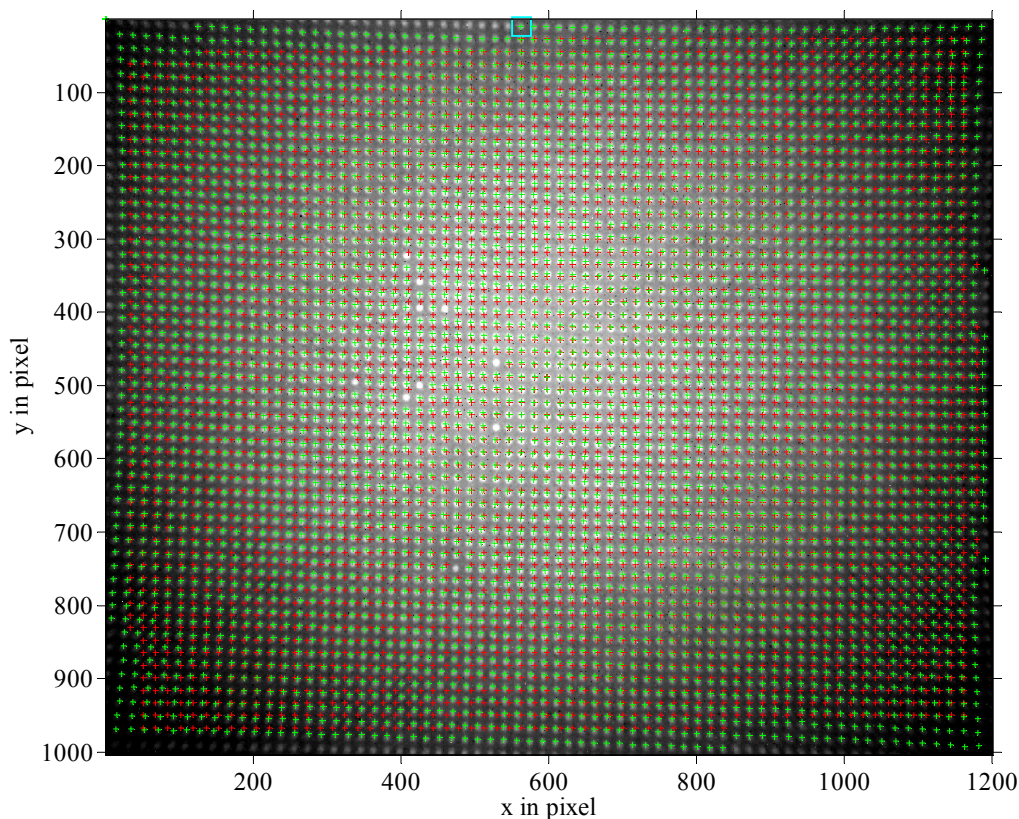


Figure 5-18: Background subtracted grey scale image of the raw intensities delivered from the detector after illuminating with a fixed point source in some distance in front of the detector masked with a grid of holes in between. The green marks correspond to positions of holes found by the developed software and the red marks are the corresponding idealized positions expected from an undistorted image.

One way of handling image registration is integrated in FIT2D, a standard software widely used for the analysis of diffraction diagrams. FIT2D uses a polynomial approach where it is assumed that the distortion of the system in one direction is independent of the other direction (Hammersley et al. 1994). Therefore, the established software is well suited for detector systems that fulfil the mentioned presumptions and can be used to produce correct results. In the case that this assumption is not fulfilled, a more complicated method is required. Such a situation has been given due to the detector used for the X-ray experiments, as illustrated in Figure 5-18. The distortion in direction of the y -axis found at different positions on the x -axis is shown in Figure 5-19. The dependency of the distortion on both axes is clearly visible.

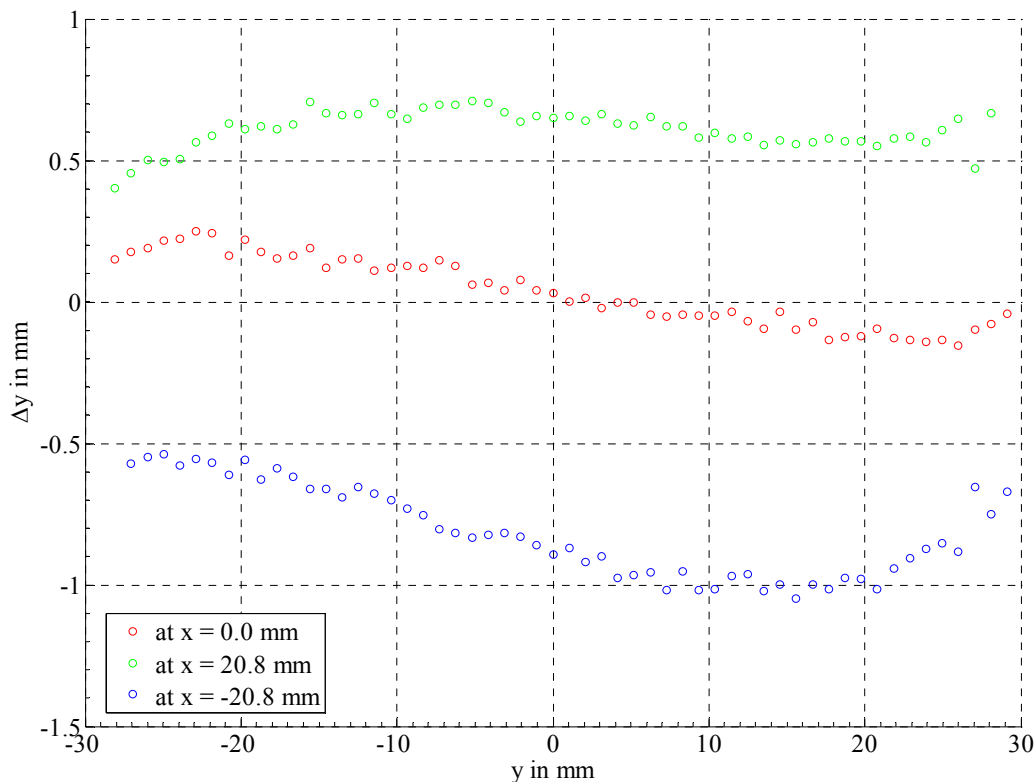


Figure 5-19: Spatial distortion along the y -axis of the detector plotted versus the y -coordinate given for three different x -coordinates showing the cross correlation of the distortions.

Therefore, in the analysis of the experiments presented in section 6.1 a different method has been used that is based on so-called *thin-plate splines*, as introduced by (Meinguet 1979). In contrast to other spline interpolation variants this version allows for the use of arbitrarily sorted landmarks that do not necessarily have to be placed on a rectangular mesh. Another advantage of this type is the opportunity to tune the output between a smooth approximation and an interpolation by one so-called *smoothing parameter*. The resulting thin-plate spline is physically comparable to an originally flat thin plate that is deformed at all the positions of the landmarks perpendicular to its infinite starting surface in a way that the bending energy⁹ is kept at a minimum (Engeln-Müllges et al. 2005)^{p. 514}.

⁹ The bending energy in this context is the energy that is required to bend the thin plate assuming only linear elastic deformation behaviour of the material.

For a mathematical treatment of the registration problem the n positions of the landmarks in the acquired template image are named $\vec{r}_{temp,i} := (x_{temp,i}, y_{temp,i})^T$ and the corresponding positions of the ideal reference image are $\vec{r}_{ref,i} := (x_{ref,i}, y_{ref,i})^T$ respectively. The transformation to be found is called $\vec{T}_s(\vec{r}_{raw}) = (T_{s,1}(\vec{r}_{raw}), T_{s,2}(\vec{r}_{raw}))^T$ and should solve the following minimization problem (5.3) for a given smoothing parameter $p \in [0,1]$ under the *error measure* $E(\vec{T}_s)$ as defined by eq. (5.1) and the *roughness measure* $R(\vec{T}_s)$ according to eq. (5.2).

$$E(\vec{T}) := \sum_{i=1}^n \left| \vec{r}_{ref,i} - \vec{T}(\vec{r}_{temp,i}) \right|^2 \quad (5.1)$$

$$R(\vec{T}) := \iint_{\mathbb{R}^2} \left(\sum_{i=1}^2 \left(\left| \frac{\partial^2 T_i}{\partial x^2} \right|^2 + 2 \left| \frac{\partial^2 T_i}{\partial x \partial y} \right|^2 + \left| \frac{\partial^2 T_i}{\partial y^2} \right|^2 \right) \right) dx dy \quad (5.2)$$

$$\vec{T}_s := \min_{\vec{T}} \left\{ p E(\vec{T}(\vec{r})) + (1-p) R(\vec{T}(\vec{r})) \right\} \quad (5.3)$$

A detailed analysis of this situation is given in (Modersitzki 2004)^{chap. 4.3}. It leads to a solution that can be written in the form of eq. (5.5) with certain m coefficients a_i and $m-2$ so-called *centres* c_i that are used in combination with the *radial basis function* $B(\vec{r})$ as defined in eq. (5.4).

$$B(\vec{r}) := |\vec{r}| \log(|\vec{r}|) \quad (5.4)$$

$$\vec{T}_s(\vec{r}_{raw}) = \sum_{i=1}^{m-2} \vec{a}_i B(\vec{r}_{raw} - \vec{c}_i) + x_{raw} \vec{a}_{m-2} + y_{raw} \vec{a}_{m-1} + \vec{a}_m \quad (5.5)$$

In this way the problem of finding the proper transformation between the raw coordinates of the detector and the positions of an idealised undisturbed detector can be solved by determining this coefficients a_i and c_i for any given smoothing parameter p and any set of linked landmarks $L := \left\{ (\vec{r}_{temp,i}, \vec{r}_{ref,i}) \right\}$.

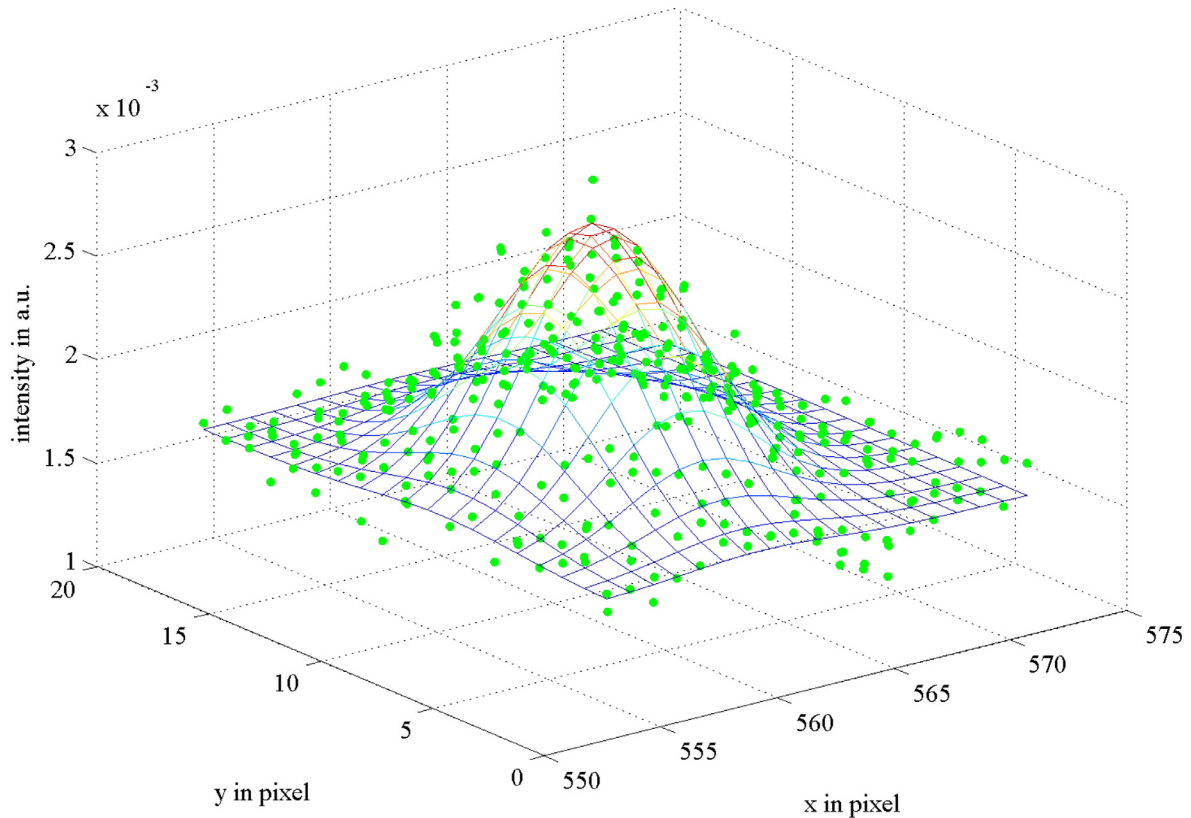


Figure 5-20: Example of the result of a two dimensional fit of a Gaussian distribution within the small rectangular area centred on the estimated position of a hole in the template image. The coloured mesh shows the fitted Gaussian surface and the blue circles are the marks of the intensities found in the template image.

To produce the set of landmarks a MATLAB[®] code has been developed. It starts after a first user interaction to find as many landmarks as possible and links them to their expected theoretical positions. Every landmark within this algorithm is the result of a two-dimensional least square fit of a Gaussian distribution with linear background, as shown in Figure 5-20. This fit is performed on a small rectangular part of the template image whose centre position is estimated from the last found landmark nearby. The procedure is illustrated in Figure 5-18 where one of these small rectangles is plotted in the top of the picture as an example. The full set of landmarks is finally used to generate the desired transformation. All further analyses has been carried out with respect to these corrected spatial coordinates:

$$\vec{r}_d = \begin{pmatrix} T_{s,1}(\vec{r}_{raw}) \\ T_{s,2}(\vec{r}_{raw}) \\ 0 \\ 1 \end{pmatrix}. \quad (5.6)$$

The performance of the transformation is evident from Figure 5-21, where the result is shown for the template image. Some lines at constant values for x and y are given in Figure 5-21 as guide for the eye. The lines for constant x values correspond to the distortion data shown in Figure 5-19.

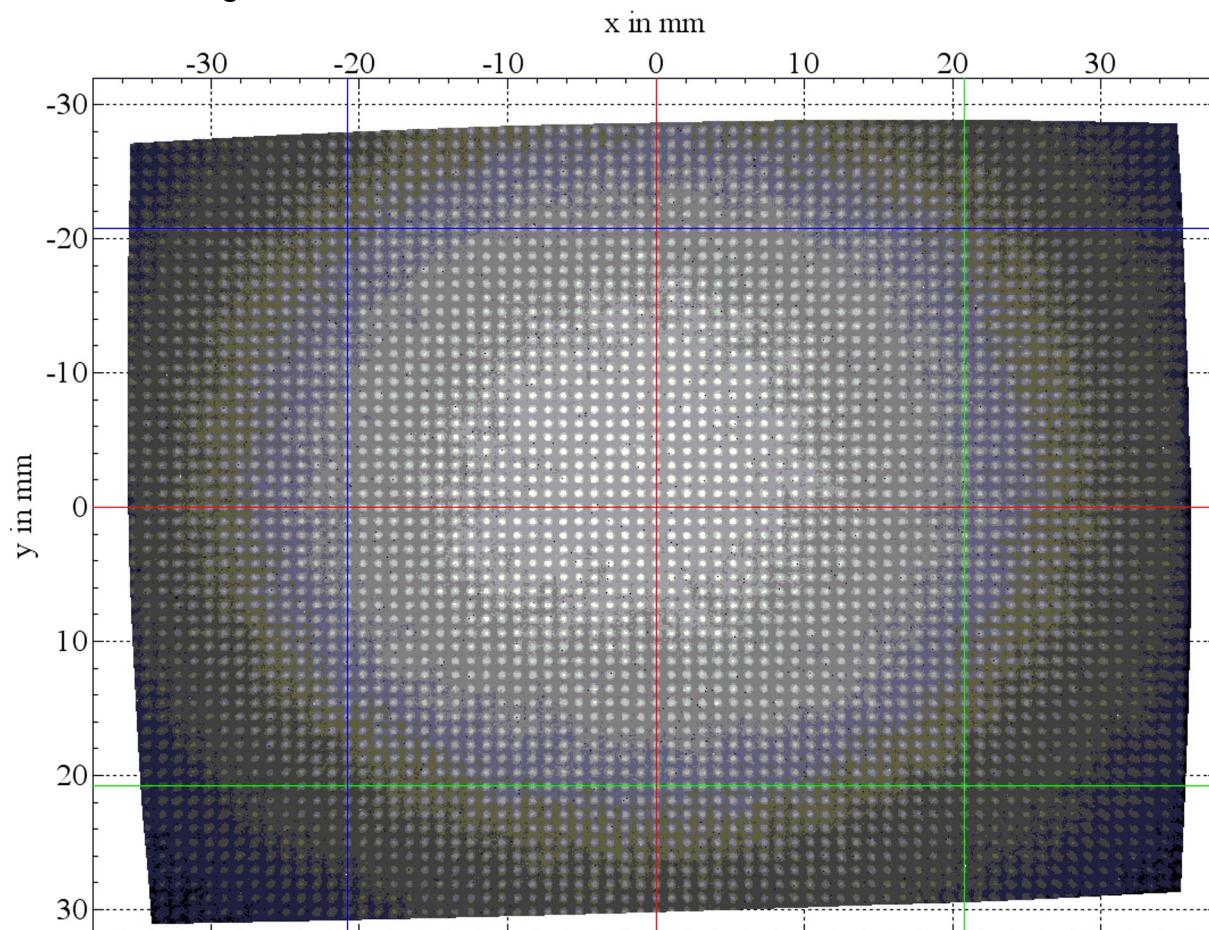


Figure 5-21: Spatially corrected template image of the holes used to find the necessary transformation between the raw detector coordinates and the theoretical positions of an undisturbed idealized detector. The coloured lines are guides to the eye drawn at constant values of -20.8 mm, 0 and 20.8 mm for x or y , respectively. The lines at constant x correspond to the data shown in Figure 5-19.

5.1.6.2 Flat Field Correction

The signals obtained from the detector give a measure for the intensities found in a certain pixel. The sensitivity of the pixel may vary, with respect to time and temperature or between different pixels. To allow for absolute intensity measurements, as required for X-ray structure determination, these different pixel responses have to be compensated for. Therefore,

a calibration measurement with a radiation source of known characteristic has to be used. This can be done, for example, with a flat field source illuminating the sensitive area of the detector homogeneously. The recorded image can then be used to calculate scaling factors for each pixel of the detector individually. However, the experiments presented in this study have not been concerned about absolute intensities of the diffraction patterns. Only the positions of the peaks found in the diffraction patterns and their relative width have been needed. The fluctuations of the sensitivities of adjacent pixels can be estimated from the collected images to be small. Hence, no flat field correction has been performed.

5.1.6.3 Detector Misalignment Compensation

To ensure a correct evaluation of acquired diffraction data a possible misalignment of the planar detector should be considered. In general, it is assumed during the further analysis that the data is collected in a plane $P_c := \{(x_c, y_c, 0, 1)^T \in \mathbb{R}^4\}$ that is oriented perpendicularly to the direction of the incoming X-ray beam at a given distance d_c behind the sample. Within such a plane, any powder sample that leads to scattering as shown in Figure 5-23 would produce a circular diffraction pattern as explained in section 4.9 and illustrated in Figure 5-24. The analysis of any other diffraction pattern in that plane is straightforward. Contrary to this idealized situation, any real measurement is affected by the orientation of the detector with respect to the incident beam. Hence, within the process of data analysis a transformation should be used between the positions $\vec{r}_u := (x_u, y_u, 0, 1)^T$ from the theoretically spatial undisturbed planar detector according to chapter 5.1.6.1 and 5.1.6.2 and the ideal plane P_c . This plane should be part of a system $S_c := \{(x_c, y_c, z_c, 1)^T \in \mathbb{R}^4\}$ that has its origin placed on the primary X-ray beam and its z -axis aligned along the beam direction, as illustrated in Figure 5-24.

To determine this transformation, a template image has been recorded with a standard powder placed at the position of the sample. The observed elliptic pattern has been used to find suitable parameters in a least square sense that represent the actual alignment of the detector in terms of tilting angles.

The cone produced by the sample in a distance d_c from the plane P_c described by eq. (5.7) in the system S_c of the scattering cone with opening angle 2θ holds (Hammersley et al. 1996)^{eq. (1)}:

$$x_c^2 + y_c^2 = ((d_c - z_c) \tan(2\theta))^2. \quad (5.7)$$

This can be written in the form of eq. (5.8):

$$(x_c, y_c, z_c, 1) \cdot \underbrace{\begin{pmatrix} 1 & 0 & 0 & 0 \\ 0 & 1 & 0 & 0 \\ 0 & 0 & -\tan^2(2\theta) & 2d_c \tan^2(2\theta) \\ 0 & 0 & 0 & -d_c^2 \tan^2(2\theta) \end{pmatrix}}_{=: M} \cdot \begin{pmatrix} x_c \\ y_c \\ z_c \\ 1 \end{pmatrix} = 0. \quad (5.8)$$

For any $\vec{r}_c \in S_c$ that fulfils eq. (5.8) and M defined as shown above the cone can be written as:

$$0 = \vec{r}_c^T \cdot M \cdot \vec{r}_c. \quad (5.9)$$

The origin of the detector coordinate system can be translated by $(x_t, y_t)^T$ onto the primary X-ray beam in a way that it has its origin in common with all the other systems used later on. Therefore, a translation according to eq. (5.11) and (5.12) is used with the definition given in eq. (5.10).

$$T_d := \begin{pmatrix} 1 & 0 & 0 & -x_t \\ 0 & 1 & 0 & -y_t \\ 0 & 0 & 1 & 0 \\ 0 & 0 & 0 & 1 \end{pmatrix} \quad (5.10)$$

$$\vec{r}_d = T_d \cdot \vec{r}_u \quad (5.11)$$

$$\vec{r}_u = T_d^T \cdot \vec{r}_d \quad (5.12)$$

The cone is tilted with respect to the (green) system of the translated detector coordinates $S_d := \{(x_d, y_d, z_d, 1)^T \in \mathbb{R}^4\}$ by an angle χ_t , as illustrated in Figure 5-25. The tilt takes place in a ‘tilt’ plane $P_t := \{(x_t, 0, z_t, 1)^T \in \mathbb{R}^4\}$ that has the same origin as the two others and is tilted around the y-axis of the system of the cone by a tilt angle $-\chi_t$. The ‘tilt’ plane is shown in blue in Figure 5-26 and is used to define an intermediate tilted coordinate system $S_t := \{(x_t, y_t, z_t, 1)^T \in \mathbb{R}^4\}$. This enables the use of $\vec{r}_t \in S_t$ instead of the former $\vec{r}_c \in S_c$ to describe the same point in laboratory space. The two systems are linked together by the following transformation:

$$\begin{aligned} \vec{r}_c &= \begin{pmatrix} \cos(-\chi_t) & 0 & \sin(-\chi_t) & 0 \\ 0 & 1 & 0 & 0 \\ -\sin(-\chi_t) & 0 & \cos(-\chi_t) & 0 \\ 0 & 0 & 0 & 1 \end{pmatrix} \cdot \vec{r}_t \\ &= \begin{pmatrix} \cos(\chi_t) & 0 & -\sin(\chi_t) & 0 \\ 0 & 1 & 0 & 0 \\ \sin(\chi_t) & 0 & \cos(\chi_t) & 0 \\ 0 & 0 & 0 & 1 \end{pmatrix} \cdot \vec{r}_t. \end{aligned} \quad (5.13)$$

With the definition of R_y as given in eq. (5.14) this leads to eq. (5.15) and (5.16), respectively.

$$R_y := \begin{pmatrix} \cos(\chi_t) & 0 & -\sin(\chi_t) & 0 \\ 0 & 1 & 0 & 0 \\ \sin(\chi_t) & 0 & \cos(\chi_t) & 0 \\ 0 & 0 & 0 & 1 \end{pmatrix} \quad (5.14)$$

$$\vec{r}_c = R_y \cdot \vec{r}_t \quad (5.15)$$

$$\vec{r}_t = R_y^T \cdot \vec{r}_c \quad (5.16)$$

The intermediate tilted (blue) system has its z-axis in common with the translated (green) system of the detector. But the intermediate system still might be rotated within the x-y-plane of the detector system by an angle χ_d , as shown in Figure 5-27. This defines a last rotational transformation as carried out in eq. (5.17). It links the coordinates $\vec{r}_t \in S_t$ of the in-

termediate (blue) system to the coordinates $\vec{r}_d \in S_d$ of the (green) system of the translated detector by eq. (5.18) or (5.19) respectively.

$$R_z := \begin{pmatrix} \cos(\chi_d) & \sin(\chi_d) & 0 & 0 \\ -\sin(\chi_d) & \cos(\chi_d) & 0 & 0 \\ 0 & 0 & 1 & 0 \\ 0 & 0 & 0 & 1 \end{pmatrix} = \begin{pmatrix} \cos(-\chi_d) & -\sin(-\chi_d) & 0 & 0 \\ \sin(-\chi_d) & \cos(-\chi_d) & 0 & 0 \\ 0 & 0 & 1 & 0 \\ 0 & 0 & 0 & 1 \end{pmatrix} \quad (5.17)$$

$$\vec{r}_t = R_z \cdot \vec{r}_d \quad (5.18)$$

$$\vec{r}_d = R_z^T \cdot \vec{r}_t \quad (5.19)$$

This situation is illustrated in Figure 5-27 with the system of the detector shown in green. It permits the following description by combining eq. (5.9), (5.11), (5.15) and (5.18) as shown below:

$$\begin{aligned} 0 &= \vec{r}_c^T \cdot M \cdot \vec{r}_c \\ &= (R_y \cdot \vec{r}_t)^T \cdot M \cdot R_y \cdot \vec{r}_t \\ &= \vec{r}_t^T \cdot R_y^T \cdot M \cdot R_y \cdot \vec{r}_t \\ &= (R_z \cdot \vec{r}_d)^T \cdot R_y^T \cdot M \cdot R_y \cdot R_z \cdot \vec{r}_d \\ &= \vec{r}_d^T \cdot R_z^T \cdot R_y^T \cdot M \cdot R_y \cdot R_z \cdot \vec{r}_d \\ &= (T_d \cdot \vec{r}_u)^T \cdot R_z^T \cdot R_y^T \cdot M \cdot R_y \cdot R_z \cdot T_d \cdot \vec{r}_u \end{aligned} \quad (5.20)$$

So finally the cut through the cone made by the detector could be written as:

$$0 = \vec{r}_u^T \cdot T_d^T \cdot R_z^T \cdot R_y^T \cdot M \cdot R_y \cdot R_z \cdot T_d \cdot \vec{r}_u \quad (5.21)$$

This is an ellipse in the plane $P_u := \{(x_u, y_u, 0, 1)^T \in \mathbb{R}^4\}$, as visualized in Figure 5-28. It is used to determine the necessary parameters $(x_t, y_t, d_c, \chi_t, \chi_d)$ for the involved transformations. A MATLAB[®] code has been developed to solve the resulting minimization problem:

$$\min_{(x_t, y_t, d_c, \chi_t, \chi_d)} \left\{ \sum_{i=1}^k \left| \vec{p}_i^T \cdot T_d^T \cdot R_z^T \cdot R_y^T \cdot M \cdot R_y \cdot R_z \cdot T_d \cdot \vec{p}_i \right| \right\}. \quad (5.22)$$

Within that procedure the value for θ has been defined by the prior knowledge about the particular powder ring used. Additionally some k points $\vec{p}_i \in P_u$ on the ellipse in the template image selected by user interaction has been used as supporting points.

For further analysis of the diffraction patterns, every point from the detector plane has to be transformed into the (red) system of the theoretical perfectly aligned plane using the transformation shown in eq. (5.23). In this way, any point from the undisturbed detector is translated into the (green) translated detector system and driven further through the intermediate (blue) system finally into the required (red) system (see Figure 5-27):

$$\vec{r}_c = R_y \cdot R_z \cdot T_d \cdot \vec{r}_u. \quad (5.23)$$

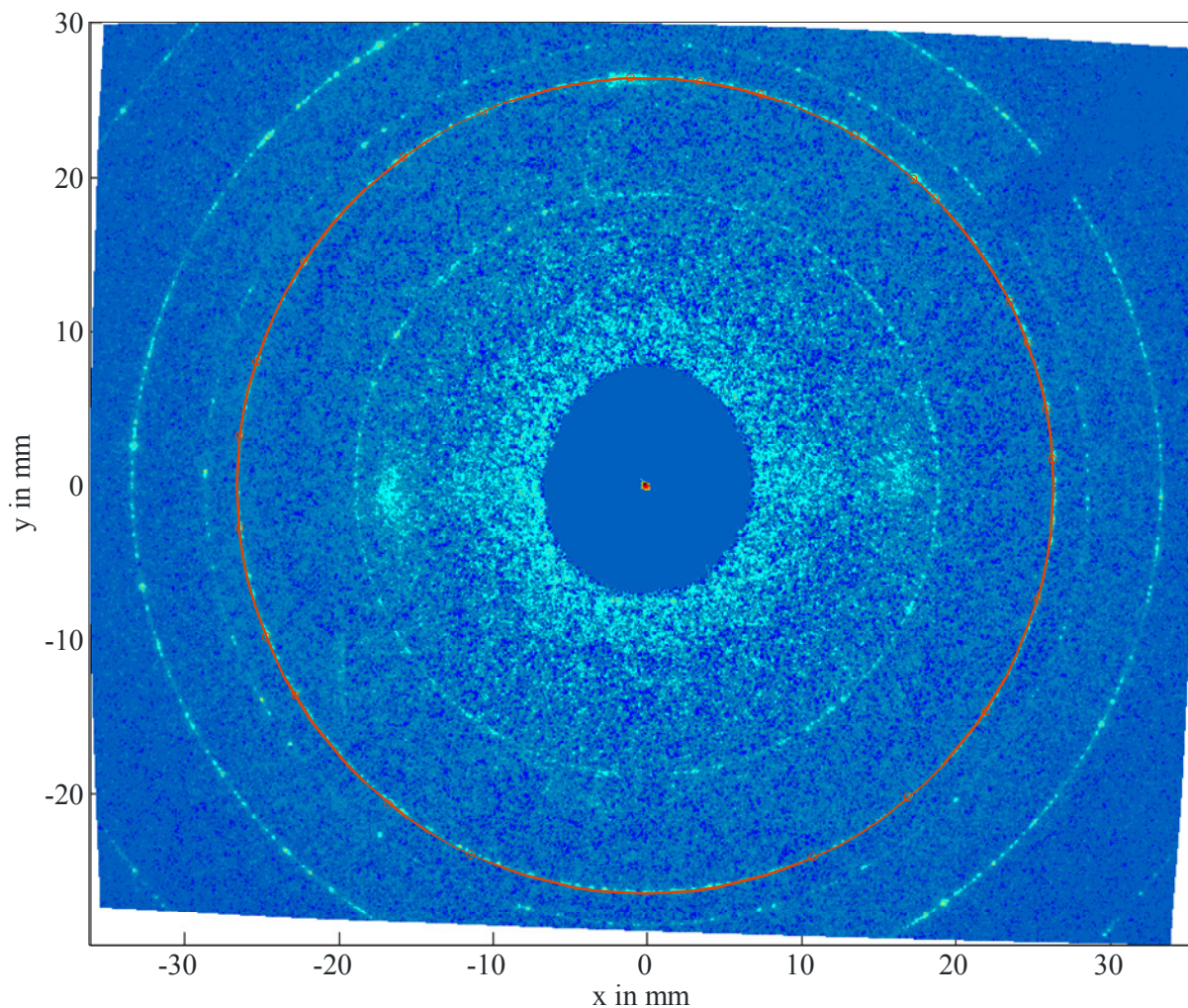


Figure 5-22: Diffraction pattern after full transformation collected at ID13 at the ESRF with Al_2O_3 powder applied on a wood sample in HUSTEN. The big red circle emphasises the powder ring used for the calibration of the detector alignment and distance between detector and sample. The small red circles give the positions of the supporting points used for the determination of the detector tilt angle.

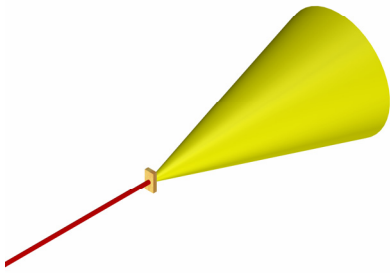


Figure 5-23: The scattering of X-rays (red) caused by a powder sample.

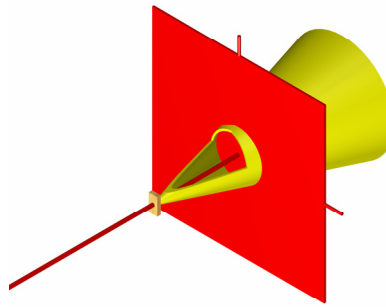


Figure 5-24: An ideal detector plane (red) placed perpendicular to the X-ray beam.

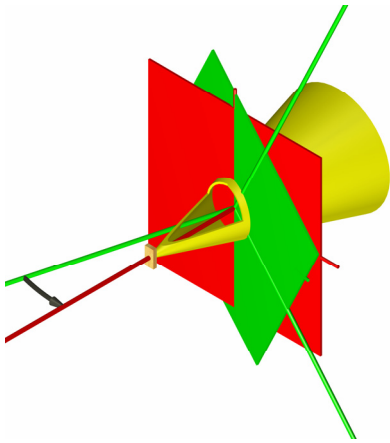


Figure 5-25: The tilt angle (black) between ideal (red) and shifted 'real' (green) detector system.

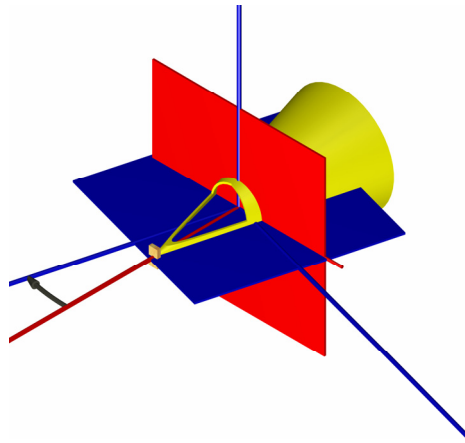


Figure 5-26: An intermediate system (blue) only tilted to the ideal detector (red) around their common y-axis.

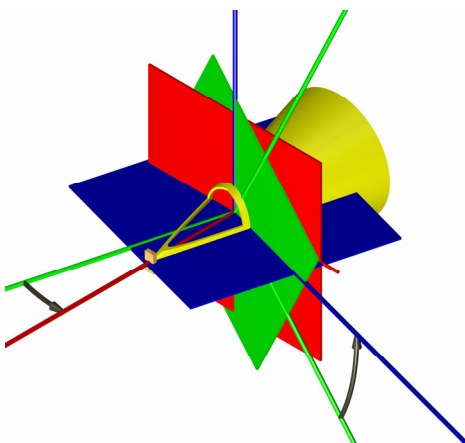


Figure 5-27: From the shifted 'real' detector system (green) through two rotations into the ideal system (red).

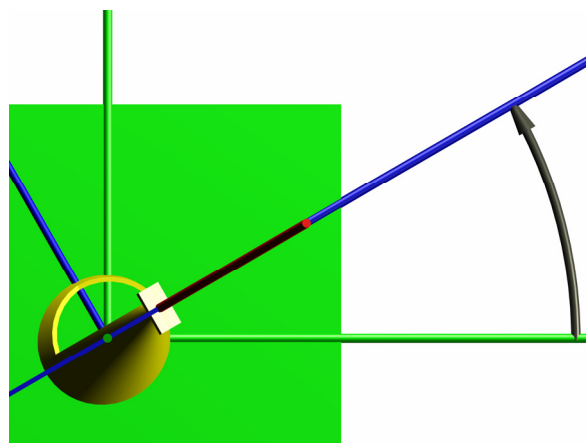


Figure 5-28: The resulting elliptic diffraction pattern seen by the 'real' detector due to the tilt against the primary X-ray beam.

5.2 Inelastic Neutron Scattering

Inelastic neutron scattering is a powerful tool in order to obtain information on both the internal structure and the dynamics of the sample under investigation. As used in the context of this study, it leads to spectroscopic data for different scattering angles. The scattering function $S(\vec{q}, E)$ is the quantity of central interest regarding this type of analysis, as shown in chapter 4. It can be measured indirectly via the double differential cross section $\frac{\partial^2 \sigma}{\partial \Omega \partial E}$. Especially, if the case of elastic scattering ($E = 0$) is included, the data also contain the diffraction pattern of the sample.

In this study, a time-of-flight spectrometer has been used. The sample in its container has been placed into a neutron beam of energy E_0 . This primary beam has been pulsed by a chopper system. The resulting sharp pulse shape measured with the primary beam monitor is illustrated in Figure 5-29. When such a neutron pulse left the Fermi-chopper close to the sample, an electronic timer has been started. Most of the neutrons that have been scattered by the sample have had changed course or energy. These neutrons have been detected with respect to their direction of propagation in a known distance s_d around the sample at some time later. The neutron time-of-flight is a measure for the velocity of the neutrons and, hence, a measure for their kinetic energy.

5.2.1 Time-of-Flight Instrument

The neutron scattering measurements have been carried out using the direct geometry time-of-flight instrument ‘FOCUS’ (Focussing Crystal University Spectrometer) at the Swiss Spallation Neutron Source ‘SINQ’ of the Paul-Scherrer-Institute (PSI). The concept of this instrument is based on a doubly focusing crystal monochromator in combination with a *Fermi-chopper*, as proposed in (Mesot et al. 1996) and (Janssen et al. 1997). First results of this instrument are shown in (Janssen et al. 2000). The instrument can be equipped either with a pyrolytic graphite or a mica monochromator (Juranyi et al. 2003) covering the wavelength

region between 2 and 15 Å. The pyrolytic graphite monochromator has been used for the experiments shown below. The instrument has been adjusted to an incident neutron wavelength of 4 Å.

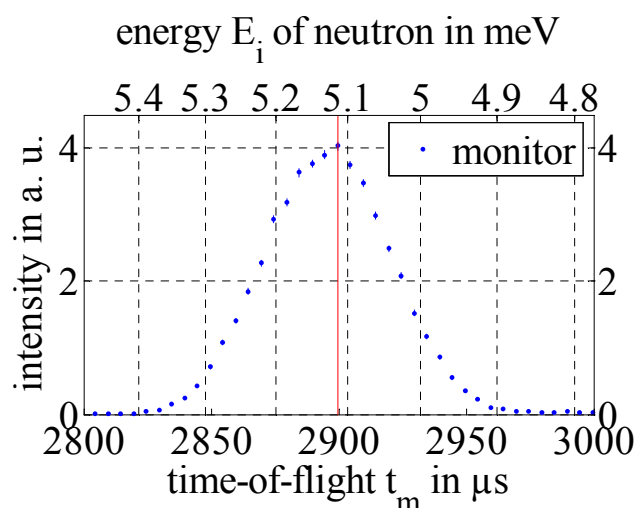


Figure 5-29: Pulse shape of the primary neutron beam obtained from the monitor signal at the Fermi-chopper of 'FOCUS'. The raw counter readings are shown versus the time-of-flight of the neutrons between disc chopper and Fermi-chopper. The case of neutrons with a wavelength of 4 Å is marked with the red line at 5.11 meV.

The spectrometer can be operated in two modes. First, it can be tuned to operate in the monochromatic focusing mode especially suited for inelastic scattering studies. Secondary, it can be used in time focusing mode preferred for quasielastic scattering experiments. The latter mode has been used for all measurements shown in the following. The optional beryllium filter has not been placed in the beam. With these parameters the instrument has been operated at the maximum possible neutron flux at the sample position of about $2 \cdot 10^4 \frac{\text{neutrons}}{\text{cm}^2 \cdot \text{s}}$.

After interaction with the sample, the scattered neutrons travel about 2.5 meters mostly through the detector chamber filled with Argon until they are detected by one of the ^3He filled detectors. These detectors lead to the desired quantity, the time-of-flight. They are arranged in three different banks. The biggest detector bank consists of 150 detectors, which are located in the horizontal plane and which correspond to scattering angles from about 10° up to 130° . The other banks are placed on two other levels below and above. The detectors from these banks are tilted azimuthally by 13° and approximate a circular arrangement running through the

corresponding detectors of the horizontal bank. This situation is illustrated in Figure 5-31. The upper bank consists of 110 detectors. It covers the region of scattering angles between 18° and 128° . In the same way the lower bank covers the same angles but consists of 115 detectors. Each detector has an entrance window of 3 cm in width and 40 cm in height.

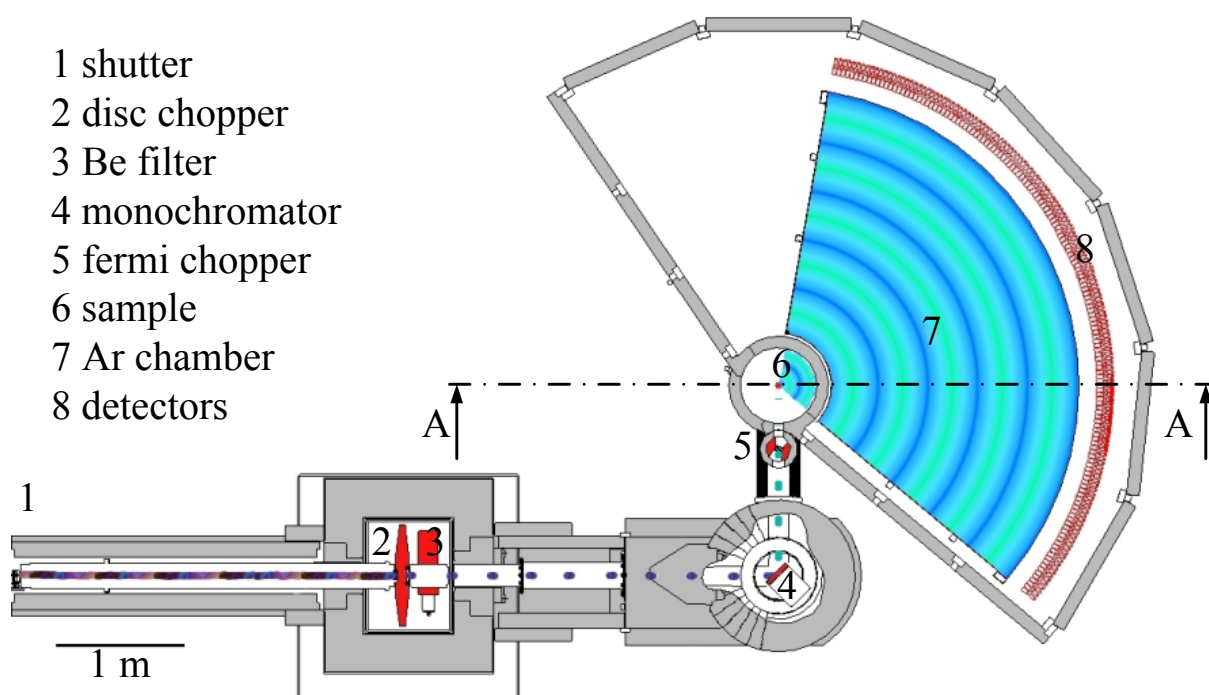


Figure 5-30: Schematic drawing of a horizontal cross section through the time-of-flight instrument FOCUS seen from top (Juranyi 2004). The dashed dotted line shows the position of the vertical cross section presented in Figure 5-31 and the arrows A point perpendicular onto the plane shown there.

The raw data offered by the instrument control software contain the counter read out of the detectors in four different tables combined with the respective time-of-flight. Three of these tables belong to the mentioned detector banks and will be referred to by their corresponding names ‘lower’, ‘middle’ and ‘upper’, respectively. The fourth table is a combination of all three groups and is therefore labelled ‘all detectors’ made up of 375 virtual detectors. This last version provides better counting statistics if the tilts of the banks are assumed to have no significant influence on the results. It offers also a compact representation of the data collected in a single run of the experiment.

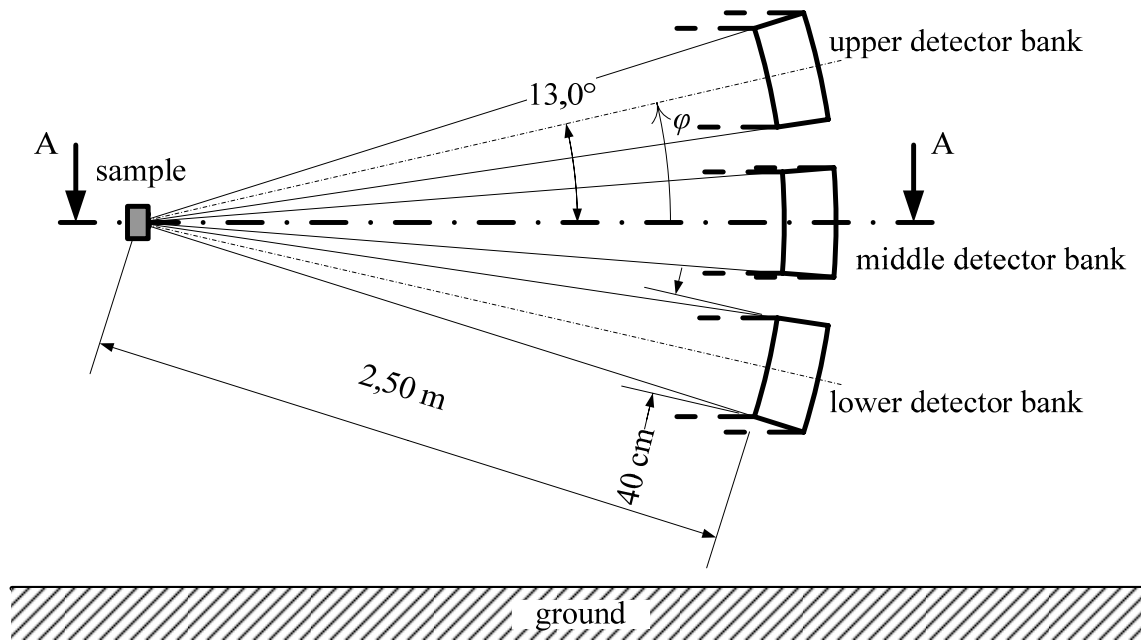


Figure 5-31: Schematic drawing of a vertical cross section through the time-of-flight instrument 'FOCUS' oriented as shown in Figure 5-30. The bold dash dotted line gives the position of the horizontal cross section shown in Figure 5-30 and the arrows A point perpendicular onto the plane shown there. The three detector banks of the instrument are represented with the bold lines. The sample (grey) is placed in the origin.

5.2.2 Data Reduction

The output of the time-of-flight instrument described above is the raw counting rate of the detectors as a function of the detector number j and the measured time-of-flight of the neutrons $I_{raw}(j, t_n)$. These raw data have to be transformed and corrected to the required quantities along the following steps to obtain the desired double differential cross section in terms of wave vector transfer $|\vec{q}|$ and energy transfer E :

- time-of-flight determination,
- primary beam normalisation,
- attenuation correction,
- multiple scattering compensation,
- background subtraction,
- time-of-flight to energy transformation,
- detector efficiency correction,
- wave vector transfer calculation.

Each of these steps will be discussed in detail in the next sections. They are a direct consequence of the technical realisation of the experiment, where the raw counter readings $I_{raw}(j, t_n)$ from the instrument are a measure for the number of neutrons that have been detected in the detector number j at scattering angle $2\theta(j)$ and after a mean time-of-flight t_n . Each detector picks up neutrons from a certain solid angle interval $\Delta\Omega(j) = \Delta 2\theta(j)\Delta\varphi$, defined by its entrance window centred around $2\theta(j)$. The time-of-flight is divided into intervals of length Δt_n due to the signal processing downstream. The detection of the neutrons of energy E_n in detector j happens with an energy dependent efficiency $p_{eff}(j, E_n)$. The absolute efficiency can differ for different detectors, even if they show the same energy dependency.

Finally, the fraction of the incoming neutrons that are scattered into direction $\Omega = (2\theta, \varphi)$ into the detector and the mentioned time interval is given by the double differential cross section $\frac{\partial^2 \sigma}{\partial \Omega \partial t_n}$ resulting from the interaction of the N scattering centres of the sample with the primary beam with an energy dependent intensity distribution $I_i(E_i)$ as follows:

$$\begin{aligned}
 I_{raw}(j, t_n) &= \int_{E_i=0}^{\infty} \int_{\Delta\Omega(j)} \int_{t=t_n-\frac{\Delta t_n}{2}}^{t_n+\frac{\Delta t_n}{2}} N \frac{\partial^2 \sigma(\Omega, t, E_i)}{\partial \Omega \partial t} I_i(E_i) p_{eff}(j, E_n(t)) dt d\Omega dE_i \\
 &= \int_{E_i=0}^{\infty} \int_{\Delta 2\theta(j) \Delta \varphi} \int_{t=t_n-\frac{\Delta t_n}{2}}^{t_n+\frac{\Delta t_n}{2}} N \frac{\partial^3 \sigma(2\theta, \varphi, t, E_i)}{\partial 2\theta \partial \varphi \partial t} I_i(E_i) p_{eff}(j, E_n(t)) dt d\varphi d2\theta dE_i.
 \end{aligned} \tag{5.24}$$

This can be expressed in terms of the desired double differential cross section $\partial^2 \sigma / (\partial |\vec{q}| \partial E)$, if the corresponding transformation $T_{q,E} : (2\theta, t_n) \rightarrow (|\vec{q}|, E)$ is used and the *Jacobian determinant* $J_{2\theta, t_n}$ of its inverse is taken into account, see for example (Krantz 2004)^{def. 13.10}, where:

$$J_{2\theta, t_n} := \begin{vmatrix} \frac{\partial 2\theta}{\partial |\vec{q}|} & \frac{\partial 2\theta}{\partial E} \\ \frac{\partial t_n}{\partial |\vec{q}|} & \frac{\partial t_n}{\partial E} \end{vmatrix}. \tag{5.25}$$

The detectors are aligned along Debye-Scherrer-circles, as mentioned above, hence, for each detector the wave vector transfer is independent from the azimuth, leading to:

$$I_{raw}(j, t_n) = \int_{E_i=0}^{\infty} \int_{\Delta 2\theta(j) \Delta \varphi} \int_{t=t_n - \frac{\Delta t_n}{2}}^{t_n + \frac{\Delta t_n}{2}} N \frac{\partial^2 \sigma(|\vec{q}|, E, E_i)}{\partial |\vec{q}| \partial E} I_i(E_i) p_{eff}(j, E_n(t)) |J_{2\theta,t}|^{-1} dt d\varphi d2\theta dE_i. \quad (5.26)$$

The incoming beam is nearly monochromatic (compare Figure 5-29) in a direct geometry scenario, as described above in section 5.2.1. This gives a significant intensity only on a small interval $\Delta E_0 = 0.2$ meV centred at $E_0 = 5.1$ meV. Therefore, it can be assumed that the double differential cross section and the detector efficiency do not vary with respect to the energy of the incoming slow neutrons. Furthermore, the intervals given by $\Delta\Omega$ and Δt_n are finite and the terms in the integrals can be represented with their averaged value on this intervals leading to¹⁰:

$$I_{raw}(j, t_n) \approx N \frac{\partial^2 \sigma(|\vec{q}|, E, E_0)}{\partial |\vec{q}| \partial E} p_{eff}(j, E_n(t_n)) |J_{2\theta,t}|^{-1} \Delta t_n \Delta 2\theta(j) \Delta \varphi \int_{E_i=E_0 - \frac{\Delta E_0}{2}}^{E_0 + \frac{\Delta E_0}{2}} I_i(E_i) dE_i. \quad (5.27)$$

Hence, the full process of data reduction can be seen as a solution of the following problem:

$$N \frac{\partial^2 \sigma(|\vec{q}|, E)}{\partial |\vec{q}| \partial E} \approx \frac{I_{raw}(j, t_n)}{E_0 + \frac{\Delta E_0}{2}} \frac{\Delta t_n \Delta 2\theta(j) \Delta \varphi}{p_{eff}(j, E_n(t_n)) |J_{2\theta,t}|} \int_{E_i=E_0 - \frac{\Delta E_0}{2}} I_i(E_i) dE_i. \quad (5.28)$$

The inverse transformation and scaling according to eq. (5.28) has to be performed if model functions from any theory are fitted to the measured data. A detailed analysis of the terms in eq. (5.28) will be given in the following sections.

The design of the instrument ensures that each detector is placed at a unique scattering angle. Hence, in the following the number j of the detector and its corresponding scattering angle 2θ are used synonymously without further notice for indexing purposes.

¹⁰ To avoid confusion, this averaging is not noted explicit at the symbols, but it is expressed with the roughly sign.

5.2.2.1 Time-of-Flight

The time-of-flight of the neutrons with velocity v_n is a measure for the kinetic energy E_n of the detected neutrons of mass m_n :

$$E_n = \frac{1}{2} m_n v_n^2 \quad (5.29)$$

The values in the tables produced by the instrument software are the *raw flight time* t_{raw} determined with a clock synchronised to the Fermi-chopper of the experiment (compare section 5.2.1). Hence, it contains the time it took the detected neutron to pass from that chopper via the sample to the detector, a total distance of about 3 meters. In the further analysis the time-of-flight t_n is defined as the time after interaction with the sample. Therefore, the initial value has to be reduced by the time the neutron of energy E_0 needs to travel the distance s_{sample} between chopper and sample (Figure 5-32):

$$t_n = t_{raw} - \frac{s_{sample}}{v_n} = t_{raw} - \frac{s_{sample}}{\sqrt{\frac{2E_0}{m_n}}} = t_{raw} - 505 \mu\text{s}. \quad (5.30)$$

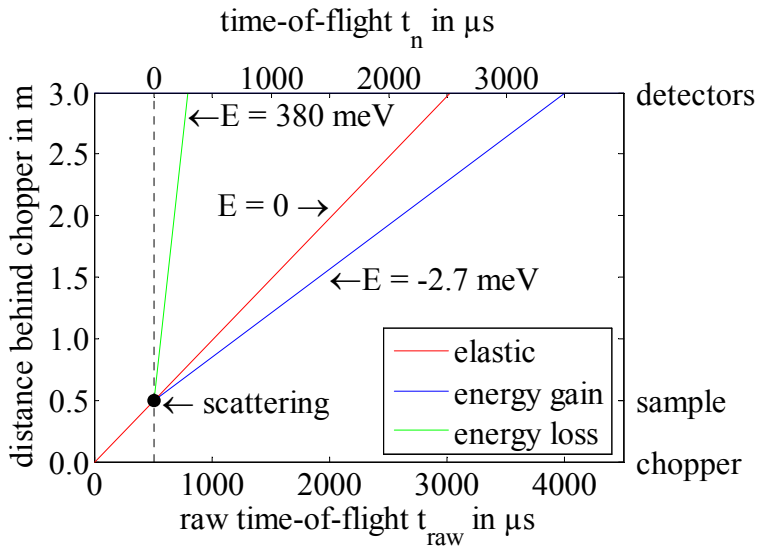


Figure 5-32: Neutron propagation versus time-of-flight at the instrument ‘FOCUS’ operating at 4 Å. The red line shows the propagation of elastically scattered neutrons. The green (blue) line gives the fastest (slowest) neutrons resolved with this instrument. The energy values given are the corresponding gains during the scattering. The scale at the top shows the time elapsed after the scattering. The scale at the bottom gives the raw time-of-flight synchronised to the chopper. They are shifted with respect to each other by 505 μs , corresponding to the time that the neutrons need to pass from the chopper to the sample.

5.2.2.2 Primary Beam Normalisation

In general, all counters of the instrument are gated synchronously during an experiment for a given period of time or until a predefined number of counting events occur, for example measured with the primary beam monitor. The latter has been done in the experiments presented in this study. The instrument offers a measure I_0 corresponding to the counter reading of the primary beam monitor, which detects neutrons with an efficiency $p_{monitor}(E_i)$. This figure I_0 is generated as a function of the energy dependent intensity distribution $I_i(E_i)$ of the incoming neutron beam, as follows:

$$I_0 = \int_{E_i=0}^{\infty} p_{monitor}(E_i) I_i(E_i) dE_i \quad (5.31)$$

This integral can be limited to the region ΔE_0 around E_0 as explained above during the development of eq. (5.27), due to the pulse shape of the primary beam. In the same way the efficiency can be estimated with its value at E_0 :

$$\begin{aligned} I_0 &\approx \int_{E_i=E_0-\frac{\Delta E_0}{2}}^{E_0+\frac{\Delta E_0}{2}} p_{monitor}(E_i) I_i(E_i) dE_i \\ &\approx p_{monitor}(E_0) \int_{E_i=E_0-\frac{\Delta E_0}{2}}^{E_0+\frac{\Delta E_0}{2}} I_i(E_i) dE_i \end{aligned} \quad (5.32)$$

Hence, to obtain a comparable quantity, referred to as ‘normalised counts’ I_{norm} , the raw readings can be normalised to the Figure derived from the monitor I_0 . It is not necessary to know the absolute value of the efficiency of the monitor for the further analysis, because its influence will be compensated within the context of the detector efficiency correction, as will be shown in chapter 0. An example for the normalised counts is given in Figure 5-33.

$$I_{norm}(2\theta, t_n) := \frac{I_{raw}(2\theta, t_n)}{I_0} \quad (5.33)$$

With this definition and eq. (5.32), eq. (5.28) is changed to:

$$N \frac{\partial^2 \sigma(|\vec{q}|, E)}{\partial |\vec{q}| \partial E} \approx I_{norm}(2\theta(j), t_n) \frac{p_{monitor}(E_0)}{p_{eff}(j, E_n(t_n))} \Delta t_n \Delta 2\theta(j) \Delta \varphi |J_{2\theta, t}|. \quad (5.34)$$

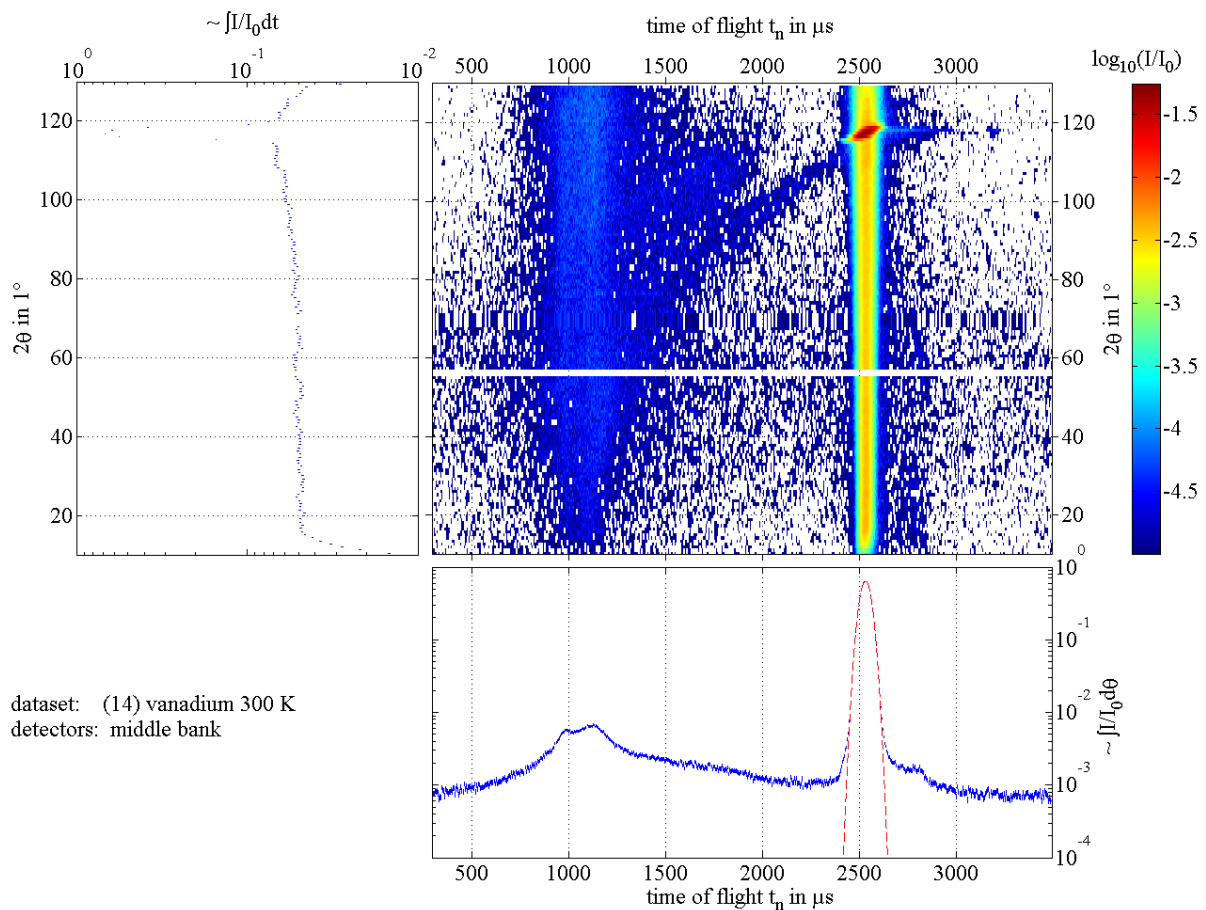


Figure 5-33: Example of normalised raw intensities obtained in a time-of-flight inelastic neutron scattering experiment with a vanadium slab calibration sample placed in an aluminium container. The intensity distribution is shown colour-coded on a logarithmic scale in the upper right graph versus scattering angle and time-of-flight. The same distribution is shown after integration over the full range of time-of-flight in the upper left graph. The graph in the bottom shows the result after integration over all scattering angles. The dashed red line shows the result of a least square fit of a Gaussian distribution to find the time-of-flight of $(2522.8 \pm 0.5) \mu\text{s}$ for elastically scattered neutrons with a wavelength of 4 \AA . It also represents the resolution function on the time axis of the instrument 'FOCUS' that has been used for this experiment.

5.2.2.3 Attenuation Correction

The neutrons travel some distance in the sample and its container before and after a scattering event until they can be detected. Therefore, in principle, the recorded intensities have to be corrected for the attenuation that takes place along their ways. However, the experiments presented in section 6.2 have been performed with a very thin cellulose sample of about 0.2 mm thickness and a sample container made out of aluminium that has had a wall

thickness of about 0.5 mm on both sides. The penetration depth¹¹ of thermal neutrons in aluminium, for example, holds 9.48 cm (Wilson 1992)^{Tab. 4.4.6.1}. Hence, the absorption effects are neglected during the further data analysis.

5.2.2.4 Multiple Scattering Compensation

The readouts of the detectors are a proper measure of the number of neutrons finally scattered into the directions of the detector signalling them. The change in the direction of propagation of the neutrons is a consequence of at least one scattering process. Unfortunately, the actual path of the detected neutrons is unknown. Hence, the output of the experiment also contains contributions from neutrons that have been scattered more than once. There are several ways to compensate for this multiple scattering effect. All of them need at least some knowledge of the scattering function $S(\vec{q}, E)$ that has to be determined with the experiment.

The influence of multiple scattering effects on the collected spectra can be kept small as long as the transmittance of the sample is high, i.e. the sample has to be thin compared to the mean free path length of the neutron in the material under investigation. For instance, the mean free path length of neutrons in liquid water has been computed to about 2 mm (Bée 1988)^{p. 108}. Nevertheless, multiple scattering can still have serious influence within the region of great and small scattering angles where the neutrons have to travel long ways inside the sample. Still, first estimates have to be done without any correction of the multiple scattering effects to obtain a suitable model function of the scattering function. Later, the actual result can be refined, for example during a Monte Carlo simulation.

According to (Bée 1988)^{p. 109} the critical limit for multiple scattering effects is 60° . In the experiments, the detectors are placed within a region of -35° to $+40^\circ$ around the surface

¹¹ The penetration depth is the length that a neutron beam has to pass through the material, here aluminium, to sustain an attenuation of its intensity to $\frac{1}{e}$ of its initial intensity.

normal of the sample. Therefore, the influence of multiple scattering should be rather small. Especially, because of the small fraction of neutrons that are scattered inelastically, the influence on the inelastic scattered signal should be not noticeable within the statistical uncertainties estimated in chapter 5.2.2.9. Consequently, no correction for multiple scattering has been calculated.

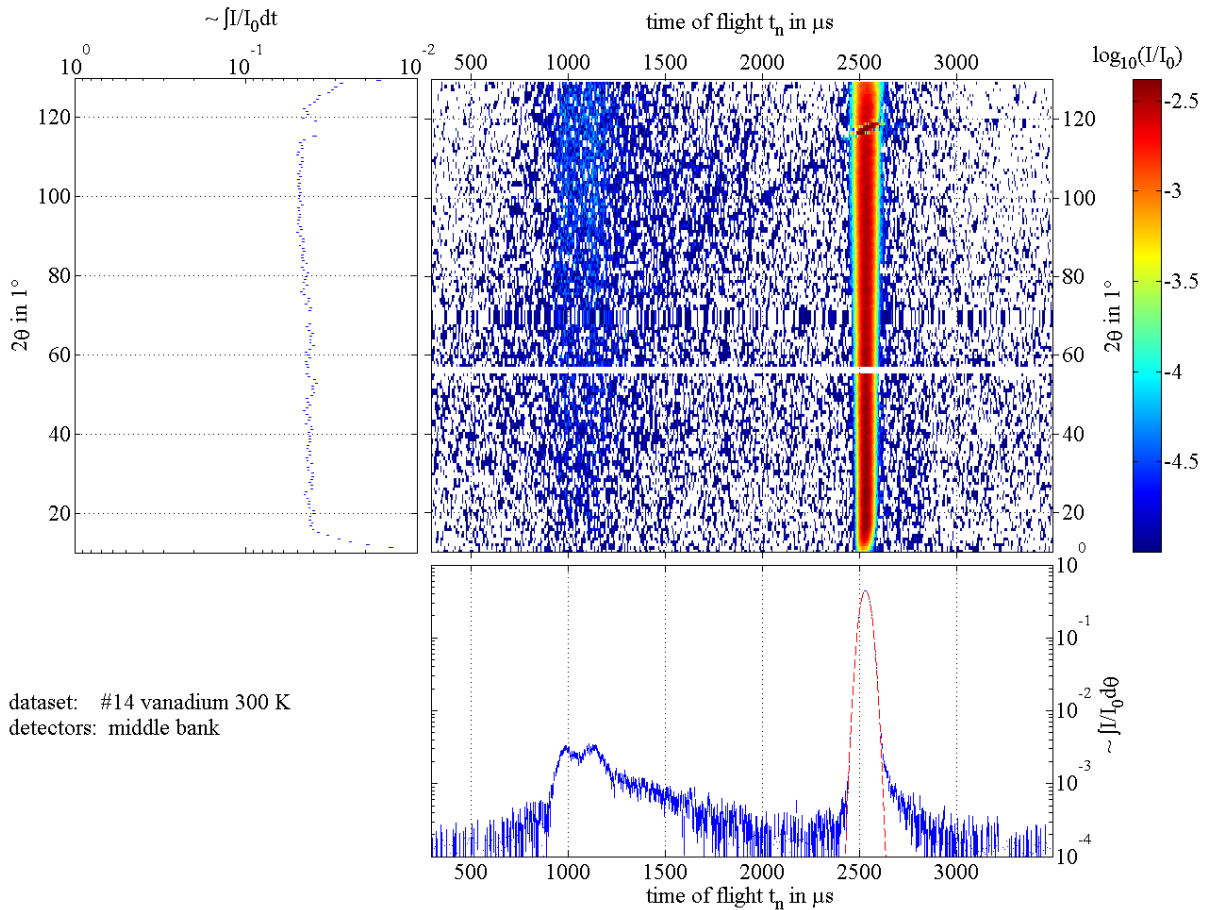


Figure 5-34: Background-subtracted normalised intensity distribution obtained from a time-of-flight inelastic neutron scattering experiment with a vanadium slab sample placed in an aluminium container. The intensity distribution is shown colour-coded on a logarithmic scale in the upper right graph versus scattering angle and time-of-flight. The same distribution is shown after integration over the full range of time-of-flight in the upper left graph. The graph in the bottom shows the result after integration over all scattering angles. The dashed red line shows the result of a least square fit of a Gaussian distribution to find the time-of-flight of $(2522.8 \pm 0.5) \mu\text{s}$ for elastic scattered neutrons with a wavelength of 4 \AA . This corresponds to about 2.5 meters of flight path between sample and detector. To allow comparison the scales used are identical to those from the plot of the raw data shown in Figure 5-33. There is still some contamination from the container visible at the position of the Bragg peak of the aluminium between 115° and 120° around $2530 \mu\text{s}$.

5.2.2.5 Background Subtraction

Since multiple scattering and attenuation effects are not taken into account in the analysis, the correction of the background is straightforward. It is assumed that the scattering signals from the sample and its chamber are purely additive. With this assumption, the part of the signal to be analysed is simply the difference of the normalised data from the two parts combined $I_{norm,1}$ and $I_{norm,2}$, for example the vanadium in the container and the empty container, obtained in different experimental runs:

$$I_{norm,difference} := I_{norm,1} - I_{norm,2} \quad (5.35)$$

$$I_{V,diff} := I_{norm,V} - I_{norm,empty} \quad (5.36)$$

5.2.2.6 Transformation from Time-of-Flight to Energy

Every detected neutron has travelled the distance between sample and detector s_d . This distance is predetermined by the layout of the time-of-flight instrument used. For travelling this path, the neutron needs the time t_n depending on its kinetic energy:

$$s_d = t_n v_n = t_n \sqrt{\frac{2E_n}{m_n}}. \quad (5.37)$$

This leads directly to the sought-after energy of the scattered neutron according to eq. (5.29):

$$E_n = \frac{m_n}{2} \left(\frac{s_d}{t_n} \right)^2. \quad (5.38)$$

With this result, the energy gain¹² E of the scattered neutrons can be written as follows:

$$E = E_n - E_0 = \frac{m_n}{2} \left(\frac{s_d}{t_n} \right)^2 - E_0. \quad (5.39)$$

¹² With the definition from eq. (4.4) or eq. (5.39) energy gain of the neutron corresponds to a positive value of E and a negative value represents energy loss of the neutron. (Compare chapter 4.)

Most of the scattered neutrons still have their initial energy E_0 . They lead to a high maximum in the detected intensity at $E = 0$. It is called the *elastic line* or the *elastic peak*. The time $t_{elastic}$ linked to this maximum can be obtained via a simple fit on the time scale with a Gaussian distribution. The angle integrated time-of-flight spectra can be used for this step, but $t_{elastic}$ may vary for different detectors. Therefore the results are based on individual values of $t_{elastic}$ for each detector. Nevertheless, this dependency will not be written explicitly in the following expressions for the sake of clarity. It leads to the following formula for the neutron energy gain in terms of the flight times:

$$E = \frac{m_n}{2} \left(\frac{t_{elastic} \sqrt{\frac{2E_0}{m_n}}}{t_n} \right)^2 - E_0 = E_0 \left(\left(\frac{t_{elastic}}{t_n} \right)^2 - 1 \right). \quad (5.40)$$

Using this transformation according to (Howie 2001)^{theo. 5.25} and following appendix 8.3.1 the intensity can be written with eq. (8.16) as follows¹³:

$$I_{energy}(2\theta, E) = I_{norm}(2\theta, t_n) \left| \frac{\partial t_n}{\partial E} \right| = \frac{t_{elastic}}{2E_0} \left(1 + \frac{E}{E_0} \right)^{-\frac{3}{2}} I_{norm}(2\theta, t_n) \quad (5.41)$$

This can be transformed into a term that is more convenient for the further analysis, if eq. (5.40) is used, as shown in detail in appendix 8.3.1 between eq. (8.17) and (8.18), and as illustrated in Figure 5-35:

$$I_{energy}(2\theta, E) := I_{norm}(2\theta, t_n) \left| \frac{\partial t_n}{\partial E} \right| = \frac{t_n^3}{2E_0 t_{elastic}^2} I_{norm}(2\theta, t_n) \quad (5.42)$$

¹³ To avoid confusion, it should be noticed that the number one within the parentheses of eq. (5.41) must not be neglected. This is especially true for so-called quasielastically scattered neutrons. These neutrons have a small energy gain E_{QNS} up to their initial energy $E_{QNS} \leq E_0$. In some literature, it is stated that the measured intensities should be multiplied with a factor proportional to $E_n^{-\frac{3}{2}}$, for example in (Müller 1996)^{p. 97}. In that case, the total kinetic energy E_n of the scattered neutron has to be taken, not only the energy transfer, as done in eq. (5.41). (Compare to eq. (5.39).)

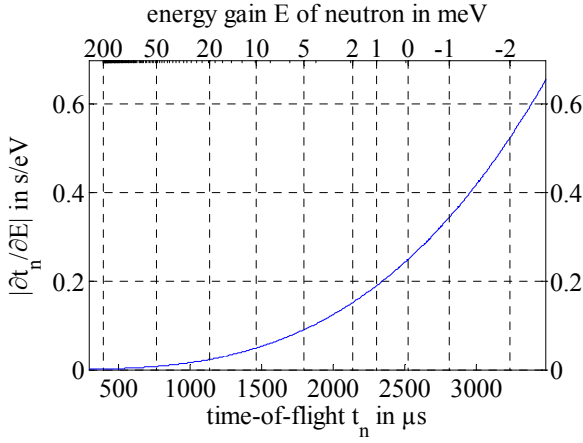


Figure 5-35: Necessary scaling factor for the normalised measured intensities if transformed from the measured time-of-flight to the scale of the energy gain of the scattered neutron. As shown in the text, the factor is the derivative of the backward transformation with respect to the energy gain.

5.2.2.7 Detector Efficiency Correction

The raw counter readings of the detectors can vary among different detectors and with respect to the energy of the detected neutrons. Hence, the recorded counting rates have to be corrected with respect to these parameters. Contrarily, no correction for detector *dead time* has to be taken into account because of the low counting rates that has occurred in the neutron scattering experiments shown later.

The dependency of the detector efficiency on the energy of the detected neutrons can be compensated by a scaling function p_{energy} , depending on the design of the detectors. The variation of the efficiency among different detectors can be compensated with a separate scaling factor $p_{detector}$. The intensities corrected for the detector efficiency effects can then be written as follows:

$$I_{eff,e}(2\theta, E) = p_{energy}(E_n) p_{detector}(2\theta) I_{energy}(2\theta, E). \quad (5.43)$$

Equally, this relation can be expressed in terms of time-of-flight instead of energy:

$$\begin{aligned} I_{eff}(2\theta, t_n) &= p_{energy}(E_n(t_n)) p_{detector}(2\theta) I_{norm}(2\theta, t_n) \\ &= p_{energy}\left(E_0 \left(\frac{t_{elastic}}{t_n}\right)^2\right) p_{detector}(2\theta) I_{norm}(2\theta, t_n). \end{aligned} \quad (5.44)$$

5.2.2.7.1 Variation Between Different Detectors

The variation between different detectors can be compensated with a simple calibration procedure (Day et al. 1969). For this purpose, a sample is used that is assumed to produce ideal isotropic incoherent scattering signals. This is fulfilled by vanadium up to a very high degree, as shown for example in (Ivanov and Rumiantsev 2000). The recorded intensities $I_{V,diff}$ that are found in the elastic line at different scattering angles after background subtraction can be used to scale all later measurements with the same detectors by the ideal values $I_{theory,V}$ expected from a perfect detector. This scaling can be written in terms of the scaling factor $p_{detector}$ that depends on the scattering angle. This factor is set to unity during the analysis of the vanadium measurement, disabling its influence. Then the full data reduction algorithm explained in this section 5.2.2 is applied. The results from the calibration run is then used to determine the correct value of the scaling factor that is used afterwards for the evaluation of all other measurements. This procedure also compensates for the efficiency of the primary beam monitor that of course only detects a small part of the incoming neutrons. At the same time the influence of the actual solid angle interval covered by the particular detectors is compensated.

$$p_{detector}(2\theta) := \frac{I_{theory,V}(2\theta)}{I_{V,diff}(2\theta)} = \frac{I_{theory,V}(|\vec{q}(2\theta)|)}{I_{V,diff}(|\vec{q}(2\theta)|)_{p_{detector}=1}} \quad (5.45)$$

According to chapter 4 the distribution of the ideal signal is dominated by the Debye-Waller-Factor that represents the influence of the thermal motion of the vanadium atoms. The expected signal can be written in terms of sample mass m_V , atomic weight M_V , the *thermally averaged mean square displacements* $\langle u^2 \rangle_T$ and the bound incoherent scattering cross section $\sigma_{incoherent,V}$ as follows, according to eq. (4.33) and (4.26):

$$I_{theory,V} = \frac{m_V}{M_V} N_A \frac{\sigma_{incoherent,V}}{4\pi} e^{-\langle u^2 \rangle_T \vec{q}^2}. \quad (5.46)$$

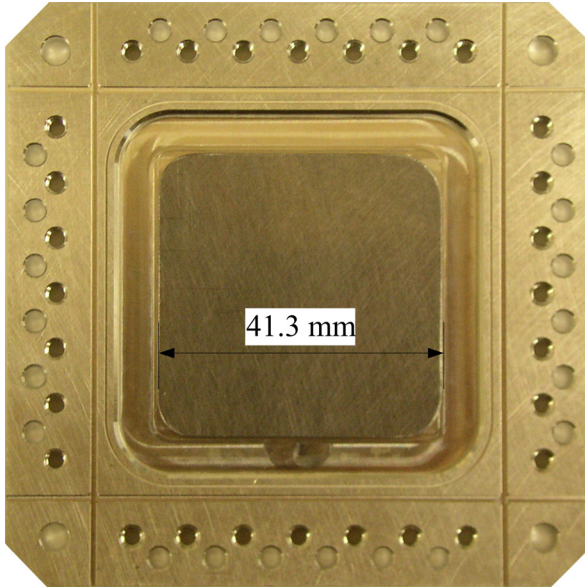


Figure 5-36: Vanadium slab used for the calibration of the detector efficiency during the inelastic neutron scattering experiments lying in the open aluminium sample container.

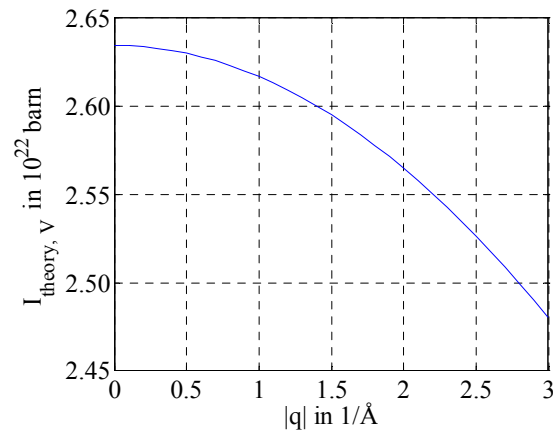


Figure 5-37: Idealised theoretical diffraction signal used for the detector calibration predicted for a measurement with a 5.3806 g vanadium standard.

In this work, the results from the vanadium measurement at 300 K presented in Figure 5-34 have been used for the evaluation of eq. (5.45) and eq. (5.46). The vanadium slab of mass $m_v = (5.3806 \pm 0.0001) \text{ g}$ has been placed in an aluminium container geometrically identical to that used in all other measurements presented later. The dimensions of the sample $((41.3 \pm 0.1) \times (41.3 \pm 0.1) \times (0.5 \pm 0.05) \text{ mm}^3)$ have been comparable to those of the flax sample shown in section 6.1, ensuring the same geometric conditions, as shown in Figure 5-36. The value of 0.0067 \AA^2 has been taken for the thermally averaged mean square displacements $\langle u^2 \rangle_T$ from an accurately performed measurement presented in (Kamal et al. 1978)^{Tab. II}. The ideal value of 5.205 barn^{14} has been taken for the bound incoherent scattering cross section $\sigma_{incoherent, V}$ from (Wilson 1992)^{tab. 4.4.4.1}. Apparently, there is no measurement of the incoherent elastic scattering cross section published for the case of slow neutrons scattered by vanadium. The number taken above is the one for the total bound scattering cross section of thermal neutrons. It is an appropriate estimate, as will be shown in the following.

¹⁴ 1 barn = $10^2 \text{ fm}^2 = 10^{-24} \text{ cm}^2 = 10^{-28} \text{ m}^2$

A number of measurements have been done that have led to results concerning the total scattering cross section of vanadium for slow neutrons, reviewed in (Dilg 1974). The dependency of the total cross section on the incident neutron energy and the influence of inelastic effects have been calculated in (Mayers 1984). Mayers¹⁵ has showed that there is a great deviation of the total scattering cross section from the elastic one in the case of slow neutrons combined with a massive anisotropy. From the calculations of Mayers, it can also be estimated that the **elastic** contribution to the **total** scattering cross section for **slow** neutrons is expected to be as high as the **total** scattering cross section for **thermal** or fast neutrons, as illustrated in Figure 5-38. This justifies the value of 5.205 barn. Similar arguments can also be found in (Lovesey 1984)^{p. 167}.

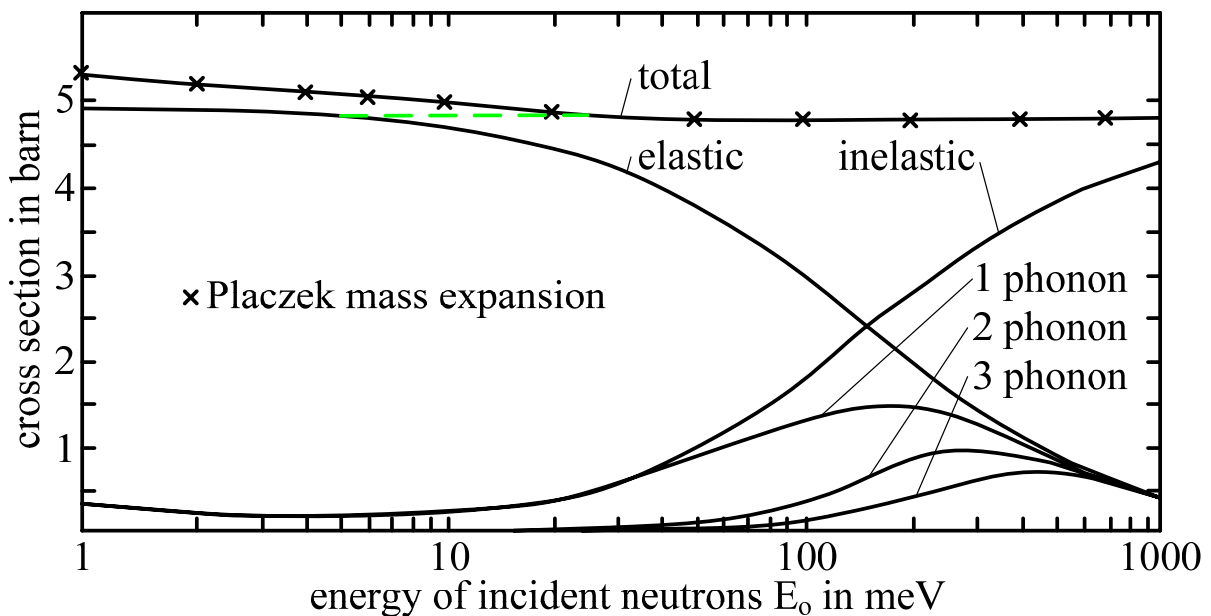


Figure 5-38: Calculated scattering cross section of vanadium at 293 K redrawn from (Mayers 1984)^{Fig. 1}. The elastic and inelastic contributions to the total scattering cross section are shown resulting from a calculation parameterised with a value of 4.98 barn. The green dashed line marks the similarity between the total scattering cross section at about 25 meV and the elastic cross section at about 5 meV.

¹⁵ In the given reference Mayers asserted that the incoherent scattering cross section of vanadium is well known referring to (Dilg 1974), but by Dilg only the total scattering cross sections have been reviewed.

Nevertheless, the absolute values presented in this thesis are all related linearly to this choice and have to be taken with caution in consideration of the discussion given above. Finally, the numbers given above, in combination with the Avogadro constant and the molecular weight of vanadium, lead to the following expression for the expected intensity distribution of the vanadium standard according to eq. (5.46), as illustrated in Figure 5-37:

$$I_{theory,V} = \frac{5.3806 \text{ g}}{50.9415 \text{ g/mol}} \frac{6.022 \cdot 10^{23}}{\text{mol}} \frac{5.205 \text{ barn}}{4\pi} e^{-0.0067 \text{ \AA}^2 \bar{q}^2}. \quad (5.47)$$

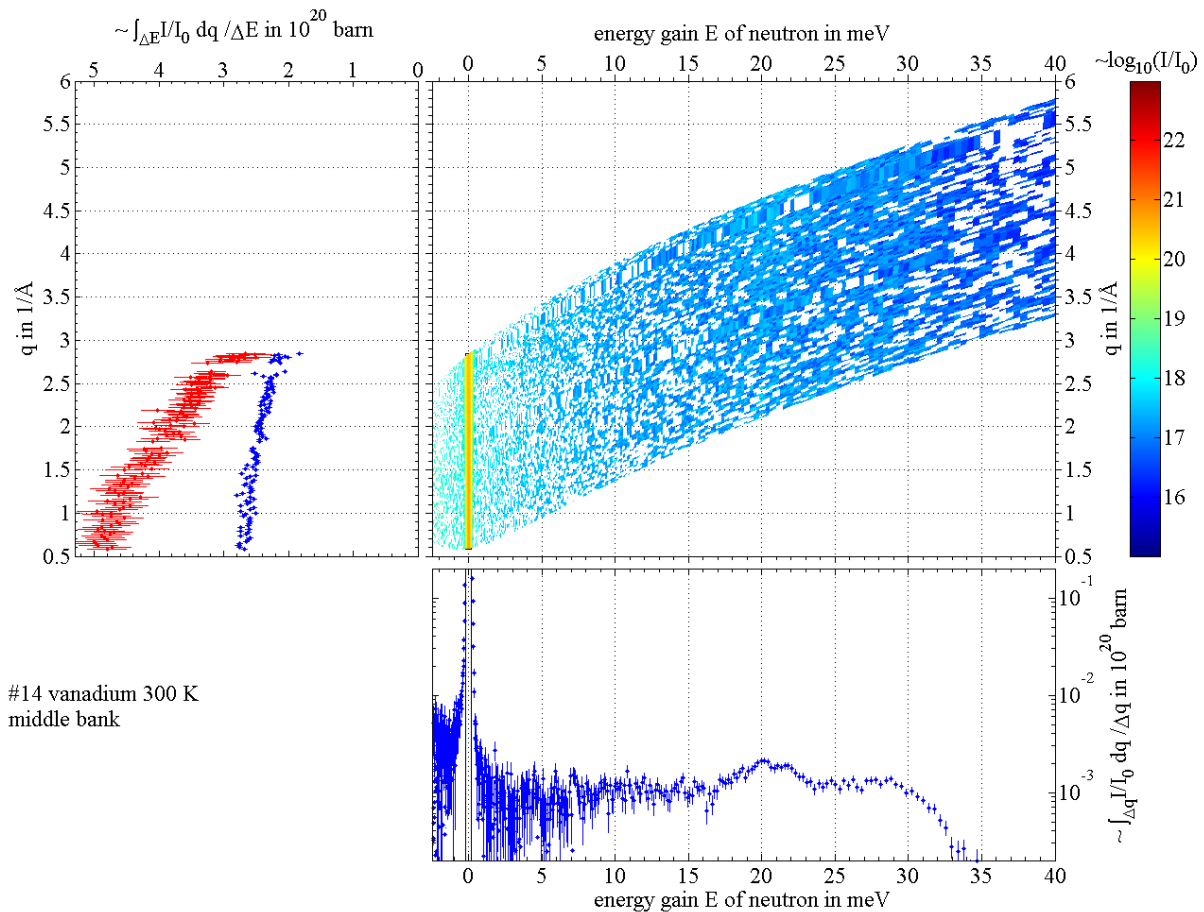


Figure 5-39: Calibration measurement with a vanadium standard after computation of the complete transformation, masking and background subtraction procedures described in the text. The intensity distribution is shown colour-coded on a logarithmic scale in the upper right graph versus energy gain of the neutron and wave vector transfer. In the upper left graph the same data are shown after integration on the black marked interval of ± 0.2 meV around the elastic line over the energy axis. The red data points belong to the intensities found at the elastic line position. The graph in the bottom shows the result after integration over all wave vector transfers.

The result of the calibration procedure is shown in Figure 5-39. The damping of the signal at the position of the elastic line due to the Debye-Waller-Factor is clear (red points). In contrast, the influence of inelastic effects increases with increasing wave vector transfer. This is visible in phonons coming up between 20 and 30 meV, as expected¹⁶ (Brockhouse 1955)^{Fig. 2a}, (Stewart and Brockhouse 1958)^{Fig. 6}, (Eisenhauer et al. 1958)^{Fig. 5}, (Haas et al. 1963)^{Fig. 7}, (Page 1967)^{Fig. 2a}, (Bacon 1975)^{Fig. 189}, (Kamal et al. 1978)^{Fig. 4}, (Squires 1978)^{Fig. 3.15}, (Ivanov and Rumiantsev 2000)^{Fig. 2}. The energy integrated intensity shows some broadening (blue points compared to red points) originating from the geometry of the experiment, as explained in appendix 8.1.

5.2.2.7.2 Energy Dependency of the Detector Efficiency

In principle the scaling function p_{energy} can be derived from some theoretical assumptions about the ^3He detectors used in combination with tabulated numbers, as shown for example in (Bertagnolli et al. 1976)^{eq. (20)} or (Yarnell et al. 1973)^{eq. (A13)}. A different commonly used approach has been chosen. The detector efficiency has been determined in a separate calibration study (Juranyi 2006). The results from that experiment has been approximated afterwards with an empirical scaling function:

$$p_{energy}(E_n) = \frac{e^{\left(5.835\sqrt{\frac{\text{meV}}{E_n}}\right)}}{0.985 \cdot e^{\left(5.818\sqrt{\frac{\text{meV}}{E_n}}\right)} - 0.015}. \quad (5.48)$$

This can be written in terms of time-of-flight:

$$p_{energy}(t_n) = \frac{e^{\left(5.835\frac{t_n}{t_{elastic}}\sqrt{\frac{\text{meV}}{E_0}}\right)}}{0.985 \cdot e^{\left(5.818\frac{t_n}{t_{elastic}}\sqrt{\frac{\text{meV}}{E_0}}\right)} - 0.015}. \quad (5.49)$$

¹⁶ Some of the given references give the phonon distribution on a frequency scale. The frequency range corresponding to the energy range from 20 to 30 meV can be calculated from eq. (4.5):

$$\omega = \frac{E}{\hbar} = \frac{20 \dots 30 \cdot 10^{-3} \text{ eV}}{6.5822 \cdot 10^{-16} \text{ eVs}} = 30 \dots 45 \cdot 10^{13} \frac{1}{\text{s}}, \quad f = \frac{\omega}{2\pi} = 4.8 \dots 7.3 \cdot 10^{13} \frac{1}{\text{s}}$$

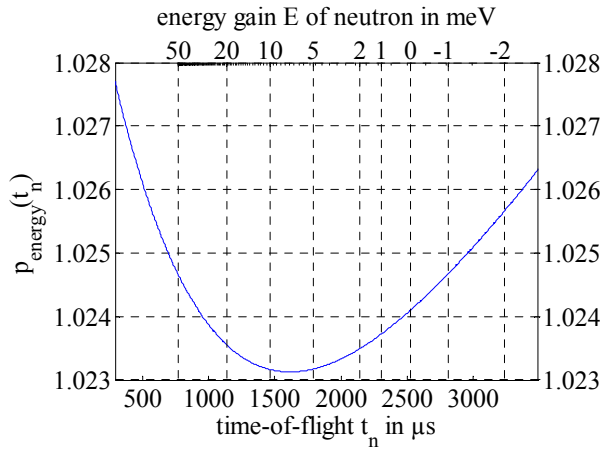


Figure 5-40: Empiric correction factor for the energy dependency of the detector systems shown as function of the measured time-of-flight of the neutrons.

Finally, the detector efficiency can be taken as a product of two terms, due to the separation with respect to detector variation and energy dependency, mentioned above. The first factor depends only on the detector number j and the second one only on the energy of the scattered neutrons. Furthermore, the factor given by the efficiency of the primary beam monitor at E_0 can be included as follows:

$$\frac{p_{\text{monitor}}(E_0) \cdot \Delta t_n \cdot (\Delta 2\theta(j) \Delta \varphi)}{p_{\text{eff}}(j, E_n(t_n))} = p_{\text{detector}}(2\theta) \cdot p_{\text{energy}}(E_n(t_n)). \quad (5.50)$$

This can be plugged into eq. (5.34) using eq. (5.44) leading to:

$$N \frac{\partial^2 \sigma(|\vec{q}|, E)}{\partial |\vec{q}| \partial E} \approx I_{\text{eff}}(2\theta(j), t_n) |J_{2\theta, t}|. \quad (5.51)$$

5.2.2.8 Wave Vector Transfer Calculation

The required transformation $T_{q,E} : (2\theta, t_n) \rightarrow (|\vec{q}|, E)$ consists of two components. In the treatment above the second component $(2\theta, t_n) \rightarrow (2\theta, E)$ is given in eq. (5.40). The first component of the overall transformation $(2\theta, t_n) \rightarrow (|\vec{q}|, E)$ can be obtained by calculating the modulus of the wave vector transfer \vec{q} in terms of scattering angle and time-of-flight. The wave vector transfer can be written as in eq. (4.3):

$$|\vec{q}| = \sqrt{|\vec{k}_i|^2 + |\vec{k}_n|^2 - 2|\vec{k}_i||\vec{k}_n|\cos(2\theta)}. \quad (5.52)$$

The magnitudes of the wave vectors of the neutrons from the incident beam $|\vec{k}_i|$ and that of the scattered neutron $|\vec{k}_n|$ in terms of the known quantities are:

$$|\vec{k}_i| = \frac{\sqrt{2m_n E_0}}{\hbar} = \frac{2\pi}{\lambda_0}, \quad (5.53)$$

$$|\vec{k}_n| = \frac{\sqrt{2m_n E_n}}{\hbar}. \quad (5.54)$$

The transformation can be obtained by combining eq. (5.52), (5.53) and (5.54):

$$\begin{aligned} |\vec{q}| &= \sqrt{\left(\frac{\sqrt{2m_n E_0}}{\hbar}\right)^2 + \left(\frac{\sqrt{2m_n E_n}}{\hbar}\right)^2 - 2\frac{\sqrt{2m_n E_0}}{\hbar}\frac{\sqrt{2m_n E_n}}{\hbar}\cos(2\theta)} \\ &= \frac{\sqrt{2m_n}}{\hbar}\sqrt{(E_0 + E_n) - 2\sqrt{E_0 E_n}\cos(2\theta)}. \end{aligned} \quad (5.55)$$

In combination with eq. (5.39), this leads to an intermediate transformation $(2\theta, E) \rightarrow (|\vec{q}|, E)$:

$$\begin{aligned} |\vec{q}| &= \frac{\sqrt{2m_n}}{\hbar}\sqrt{(E_0 + (E_0 + E)) - 2\sqrt{E_0(E_0 + E)}\cos(2\theta)} \\ &= \frac{\sqrt{2m_n E_0}}{\hbar}\sqrt{2 + \frac{E}{E_0} - 2\sqrt{1 + \frac{E}{E_0}}\cos(2\theta)}. \end{aligned} \quad (5.56)$$

This can be written even shorter using eq. (5.53) as in eq. (5.57):

$$|\vec{q}| = |\vec{k}_i|\sqrt{2 + \frac{E}{E_0} - 2\sqrt{1 + \frac{E}{E_0}}\cos(2\theta)}. \quad (5.57)$$

Eq. (5.56) can also be written with respect to the time-of-flight using eq. (5.40):

$$|\vec{q}| = \frac{\sqrt{2m_n E_0}}{\hbar}\sqrt{2 + \left(\frac{t_{elastic}}{t_n}\right)^2 - 1} - 2\sqrt{1 + \left(\frac{t_{elastic}}{t_n}\right)^2 - 1}\cos(2\theta). \quad (5.58)$$

This is finally the first component of the transformation $(2\theta, t_n) \rightarrow (|\vec{q}|, E)$ illustrated in Figure 5-41 and Figure 5-42:

$$|\vec{q}| = \frac{\sqrt{2m_n E_0}}{\hbar}\sqrt{1 + \left(\frac{t_{elastic}}{t_n}\right)^2 - 2\frac{t_{elastic}}{t_n}\cos(2\theta)}. \quad (5.59)$$

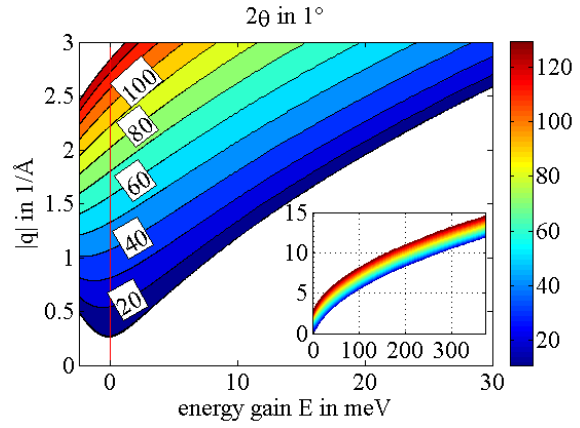
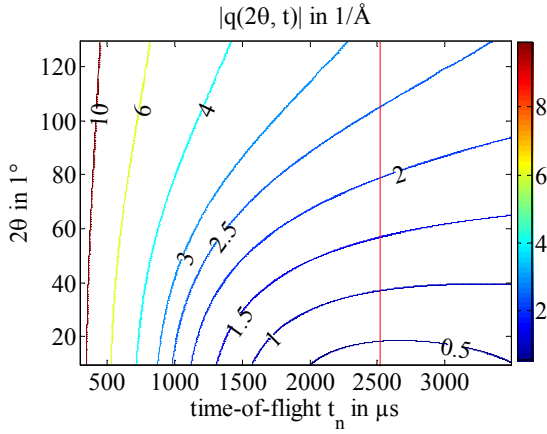


Figure 5-41: Dependency of the wave vector transfer on the scattering angle and the time-of-flight. Figure 5-42: Dependency of the scattering angle on the energy gain of the neutron and the wave vector transfer.

In Figure 5-41 and Figure 5-42 the elastic scattering events are shown with a red line. The displayed region is the full accessible 2θ - t_n -space from the time-of-flight instrument 'FOCUS' at 'SINQ' operating with incident neutrons of 4 Å wavelengths.

The intensity can be written with eq. (8.41) and (5.51) as follows, using the transformation given above and following appendix 8.3.2:

$$N \frac{\partial^2 \sigma}{\partial \Omega \partial E} (|\vec{q}|, E) \approx \left| \frac{-\sqrt{t_n^8 + t_n^6 t_{elastic}^2} - 2t_n^7 t_{elastic} \cos(2\theta)}{2t_{elastic}^3 \sin(2\theta)} \frac{1}{|\vec{k}_i| E_0} \right| I_{eff}(2\theta, t_n). \quad (5.60)$$

For the scattering angle 2θ in eq. (5.60) holds:

$$0 \leq 2\theta \leq 180^\circ \Rightarrow \sin(2\theta) \geq 0. \quad (5.61)$$

Consequently, the final form can be written as follows:

$$N \frac{\partial^2 \sigma}{\partial \Omega \partial E} (|\vec{q}|, E) \approx \frac{\sqrt{t_n^8 + t_n^6 t_{elastic}^2} - 2t_n^7 t_{elastic} \cos(2\theta)}{2t_{elastic}^3 \sin(2\theta) |\vec{k}_i| E_0} I_{eff}(2\theta, t_n). \quad (5.62)$$

The necessity¹⁷ of this transformation has already been stated by other authors, for example (Bée 1988)^{p. 70}, (Kölln 2000)^{eq. (3.1)}, (Dorner 2005)^{sec. 6}, (Tregenna-Piggott 2005)¹⁸, but apparently, there is no hint in the literature that the complete transformation has been used in

¹⁷ Most confusing in this context seems the article from Dorner, where the necessity is explained in detail in section 6 but in eq. (16b) of section 4 of the same article it is ignored.

¹⁸ This article focuses on the analysis of data obtained from indirect geometry time-of-flight instruments, basically reviewing the article from Dorner.

the data analysis process of inelastic neutron scattering experiments so far. Mostly, only the factor $\frac{\partial t_n}{\partial E}$ corresponding to eq. (5.42) seemed to be taken into account. A different Jacobian J_{Cowley} is given in (Cowley 2003)^{eq. (8)} for the case of direct geometry time-of-flight instruments, even though it has not been used there:

$$J_{Cowley} = 2 - \frac{|\vec{k}_i|}{|\vec{k}_n|} \cos(2\theta). \quad (5.63)$$

According to Cowley, this version can be traced back to J_{Waller} (Waller and Fröman 1952)^{eq. (3)}, written in terms of the group velocity $\vec{c}_{g,j} = \vec{\nabla}_{\vec{\chi}} \omega_{\vec{\chi}j}$ of the elastic wave corresponding to the fundamental frequencies $\omega_{\vec{\chi}j}$ of the assumed harmonic oscillators inside the sample excited by n for scattering into direction of the unit vector $\vec{e}_n := \frac{\vec{k}_n}{|\vec{k}_n|}$:

$$J_{Waller} = 1 + n \frac{|\vec{k}_i|}{|\vec{k}_n|} \vec{e}_n \cdot \frac{m_n}{\hbar |\vec{k}_i|} \vec{c}_{g,j} = 1 + n \frac{m_n}{\hbar |\vec{k}_n|} \vec{e}_n \cdot \vec{c}_{g,j}. \quad (5.64)$$

However, equations (5.63) and (5.64) are given in terms of the modulus of the wave vector \vec{k}_n of the scattered neutron. This wave vector is meant in the given references implicitly depending on the time-of-flight of the scattered neutron. Eq. (5.54) holds for this modulus and can be expressed in terms of time-of-flight using eq. (5.40) and (5.39), leading to:

$$J_{Cowley} = 2 - \frac{t_n}{t_{elastic}} \cos(2\theta) \quad (5.65)$$

and

$$J_{Waller} = 1 + \varepsilon \sqrt{\frac{m_n}{2E_0}} \frac{t_n}{t_{elastic}} \vec{e}_n \cdot \vec{c}_{g,j}. \quad (5.66)$$

Both versions differ slightly from eq. (8.41). The validity of eq. (5.66) and (5.65) has not been investigated, nor have they been used for the analysis of the experimental data. Apparently, the use of any of the proposed Jacobians is not common in the analysis of direct geometry time-of-flight experiments and still subject to discussions. Therefore, the influence of

the different steps of the necessary transformations on the computed results will be discussed in more detail in the following, for easy comparison with results reported elsewhere.

The influence of the Jacobian determinant in eq. (5.62) on the calculation is shown in Figure 5-43. The strong dependence on the scattering angle 2θ is clearly visible. Even if the Jacobian determinant is not taken into account during data analysis, the correction procedure based on the vanadium sample, as mentioned in chapter 0, still corrects for part of its influence, since the dependence of the measured signal along the elastic line is corrected with a scaling factor depending on detector angle, as shown in eq. (5.43). Consequently, in that case, only the dependency of $\frac{\partial 2\theta}{\partial |\vec{q}|}$ on the time-of-flight will be left uncompensated resulting in a wrong intensity distribution in the inelastic regions of the collected spectra.

If only a small energy region around the elastic line is used, for example to compute a diffraction diagram, as done for instance in normal diffraction experiments¹⁹, the resulting intensity distribution can be corrected for inelastic effects, as shown for example in (Bacon 1975)^{chap. 16.4} according to (Placzek 1952).

However, the full correction according to eq. (5.62) has been used in the analysis process carried out for the results presented in this study.

¹⁹ In this case in principle the instruments used do not deliver enough information about the energy of the scattered neutrons to calculate inelastic spectra. In fact the diffraction experiments perform integration along the energy axis in $(2\theta, E)$ -space.

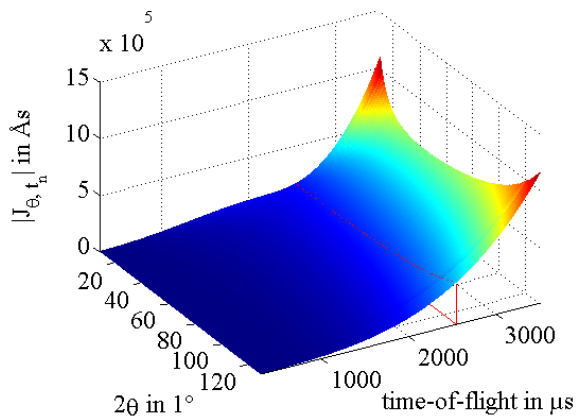


Figure 5-43: Transformation of the measured intensities from scattering angle and time-of-flight to wave vector transfer and energy gain of the neutron demands a scaling proportional to the Jacobian determinant of the inverse transformation shown here.

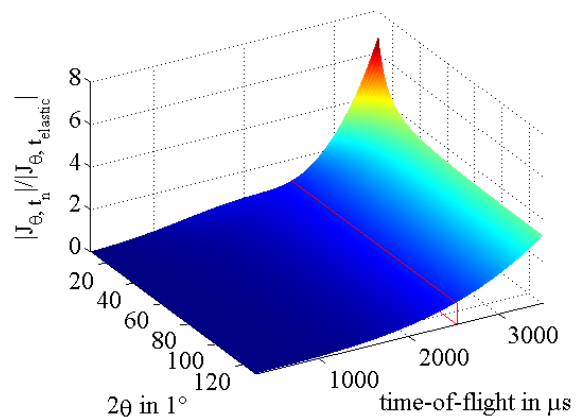


Figure 5-44: If only the calibration run with vanadium is taken into account during the transformation of the counter readings from scattering angle and time-of-flight to wave vector transfer and energy gain of the neutron the intensities are underestimated by the factor shown here.

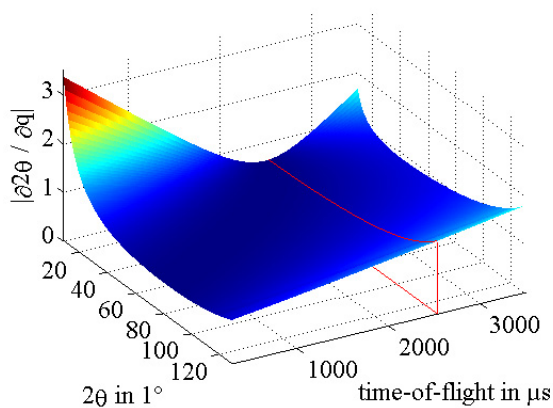


Figure 5-45: If only the transformation step from time-of-flight to energy gain of the neutron is scaled with the corresponding derivative and the transformation from scattering angle to wave vector transfer is not scaled with the appropriate derivative the results are underestimated by the factor shown here.

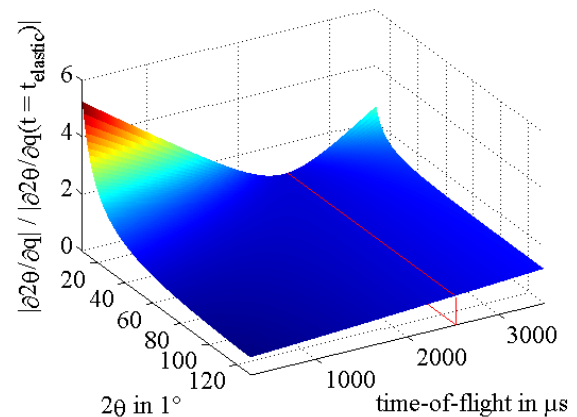


Figure 5-46: If the transformation from time-of-flight to energy gain and the calibration run with vanadium are performed correctly, but the transformation from scattering angle to wave vector transfer is not scaled by its derivative the results are underestimated by a factor shown here.

In Figure 5-43 to Figure 5-46 the elastic scattering events are shown with a red line. The calculation is performed on the maximum accessible space from the time-of-flight instrument 'FOCUS' at 'SINQ' considering operation with incident neutrons of 4 Å wavelength.

5.2.2.9 Error Estimation

The results of the experiments have been analysed with respect to their statistical uncertainties. The corresponding procedure of error estimation is shown in this section. The raw data obtained from the instrument are due to the counter readings linked to a statistical uncertainty estimated as follows assuming a *Poisson distribution*:

$$\Delta I_{raw}(2\theta, t_n) = \sqrt{I_{raw}(2\theta, t_n)} \quad (5.67)$$

and

$$\Delta I_{norm}(2\theta, t_n) = \frac{\Delta I_{raw}(2\theta, t_n)}{I_0} = \frac{\sqrt{I_{raw}(2\theta, t_n)}}{I_0}. \quad (5.68)$$

This uncertainty also influences the determination of the detector correction based on the vanadium sample according to eq. (5.45):

$$\Delta p_{detector}(2\theta) = \left| \frac{\partial p_{detector}}{\partial I_{raw, V}} \right| \cdot \Delta I_{raw, V} = \frac{I_{theory, V}}{(I_{V, diff})^2} \Delta I_{V, diff} = p_{detector}(2\theta) \cdot \frac{\Delta I_{V, diff}(2\theta)}{I_{V, diff}(2\theta)}. \quad (5.69)$$

To obtain the portion of the signal that is linked to the part of interest of the sample, some differences of two intensities $I_{norm,1}$ and $I_{norm,2}$ have to be computed, for example the subtraction of the empty chamber mentioned above. The uncertainties of these differences $I_{norm, difference}$ according to eq. (5.35) are given as follows:

$$\Delta I_{norm, difference} = \sqrt{(\Delta I_{norm,1})^2 + (\Delta I_{norm,2})^2}. \quad (5.70)$$

As a result, the overall error bars due to eq. (5.28) can be estimated with eq. (5.44) and (5.69).

$$\Delta I_{eff}(2\theta, t_n) = \sqrt{\left(\left| \frac{\partial I_{eff}}{\partial I_{norm}} \right| \Delta I_{norm} \right)^2 + \left(\left| \frac{\partial I_{eff}}{\partial p_{detector}} \right| \Delta p_{detector} \right)^2} \quad (5.71)$$

This can be written as:

$$\begin{aligned}
(\Delta I_{eff}(2\theta, t_n))^2 &= (p_{energy}(E_n(t_n)) p_{detector}(2\theta) \Delta I_{norm}(2\theta, t_n))^2 \\
&\quad + (p_{energy}(E_n(t_n)) I_{norm}(2\theta, t_n) \Delta p_{detector}(2\theta))^2 \\
&= (p_{energy} p_{detector} \Delta I_{norm})^2 + \left(p_{energy} I_{norm} p_{detector} \frac{\Delta I_{V,diff}}{I_{V,diff}} \right)^2 \\
&= (p_{energy} p_{detector})^2 \left((\Delta I_{norm})^2 + (I_{norm})^2 \frac{(\Delta I_{norm,V})^2 + (\Delta I_{norm,empty})^2}{(I_{norm,V} - I_{norm,empty})^2} \right).
\end{aligned} \tag{5.72}$$

This leads to the error bars for the double differential cross section in (\vec{q}, E) space according to eq. (5.28):

$$N\Delta \frac{\partial^2 \sigma}{\partial \Omega \partial E}(|\vec{q}|, E) = |J_{2\theta,t}| \Delta I_{eff}(2\theta, t_n) \tag{5.73}$$

$$\left(N\Delta \frac{\partial^2 \sigma}{\partial \Omega \partial E}(|\vec{q}|, E) \right)^2 = |J_{2\theta,t}|^2 (p_{energy} p_{detector})^2 \left((\Delta I_{norm})^2 + (I_{norm})^2 \frac{(\Delta I_{norm,V})^2 + (\Delta I_{norm,empty})^2}{(I_{norm,V} - I_{norm,empty})^2} \right). \tag{5.74}$$

Finally, the relative accuracy of the transformed signals can be written with eq. (5.73) and eq. (5.72) as follows:

$$\frac{\Delta \frac{\partial^2 \sigma}{\partial \Omega \partial E}(|\vec{q}|, E)}{\frac{\partial^2 \sigma}{\partial \Omega \partial E}(|\vec{q}|, E)} = \frac{|J_{2\theta,t}| \Delta I_{eff}(2\theta, t_n)}{|J_{2\theta,t}| I_{eff}(2\theta, t_n)} \tag{5.75}$$

and

$$\left(\frac{\Delta \frac{\partial^2 \sigma}{\partial \Omega \partial E}(|\vec{q}|, E)}{\frac{\partial^2 \sigma}{\partial \Omega \partial E}(|\vec{q}|, E)} \right)^2 = \left(\frac{\Delta I_{norm}(2\theta, t_n)}{I_{norm}(2\theta, t_n)} \right)^2 + \left(\frac{\Delta I_{V,diff}(2\theta)}{I_{V,diff}(2\theta)} \right)^2. \tag{5.76}$$

Clearly, the relative precision that is reached in the end will of course never exceed that of the calibration performed. The second term of eq. (5.76) represents this influence of the calibration. However, the relative error of the calibration run has to be calculated from the intensities found at the elastic line used for the calibration procedure. Hence, it is independent of the energy transfer observed in any actual inelastic experiment. In fact, for slow neutrons,

the intensity of the elastic line in general is several orders of magnitude higher than that of any inelastic effect. Therefore, only short calibration runs are necessary to gain sufficient overall accuracy.

Even after background subtraction, there is still some contamination of the data due to the Bragg reflections of the aluminium container used. This situation is illustrated in Figure 5-34. The huge intensity of the Bragg peak and its position are very sensitive to many parameters. Hence, the background subtraction is only partly successful in this region. To minimise errors of this kind, the detectors contaminated in this way have been left out during the further spectroscopic analysis. The same has been done for the ‘dead’ detector at a scattering angle of about 56° .

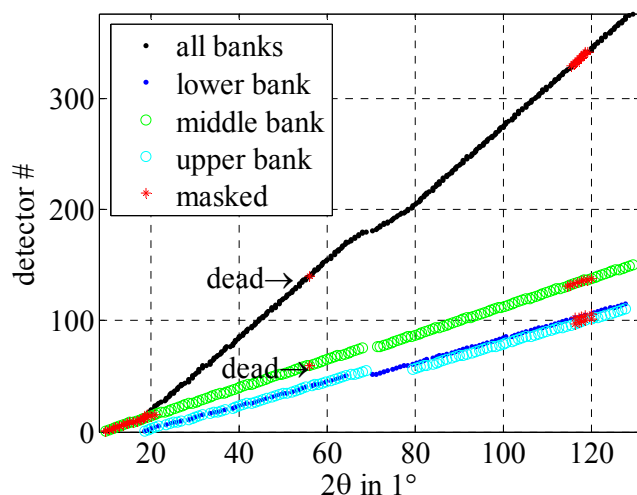


Figure 5-47: Detector mapping and masking of the three independent detector arrays used at ‘FOCUS’. The detectors left out are marked red. The detector at about 56° has been ‘dead’ and the region below 19° has been partially shadowed by the beam stop. The signals close to 120° have been contaminated due to the Bragg reflections from the aluminium container.

The signals collected from detectors below 19° have to be taken with caution. In this region the beam stop covers a fraction of the scattered neutrons. Hence, the signals are only originating from a part of the sample. This leads to a reduced intensity, as visible for example in Figure 5-33. The calibration with the vanadium standard compensates for this effect with respect to the value of the intensity. Nevertheless, different measurements are not comparable

in this domain if for example the flat sample is rotated in its plane, as illustrated in Figure 5-48. Such a rotation could put different parts of the sample into the ‘visible’ area of this low angle detectors. The experiments presented later are used to compare two sample orientations of exactly this type. So the detectors partially shadowed are also masked out and do not influence the accuracy of the spectroscopic analysis.

5.2.2.10 Integration and Presentation

In order to compare the results from inelastic neutron measurements with theoretical predictions or other experiments, it is helpful to present the data in a reduced form. This is typically done by integrating over one of the axes or by computing the Fourier transformation of the whole data set. The integration is approximated via a simple weighted sum. Due to the instrumental limits of the accessible regions in (\vec{q}, E) space, the integrals are presented after division by the corresponding interval lengths. Especially, the computation of the diffraction patterns is limited to the extension of the elastic line. The results of these integration are for example shown in Figure 5-39. In figures like that, the diffraction pattern is shown on the left side close to the axis of the wave vector transfer and computed as follows:

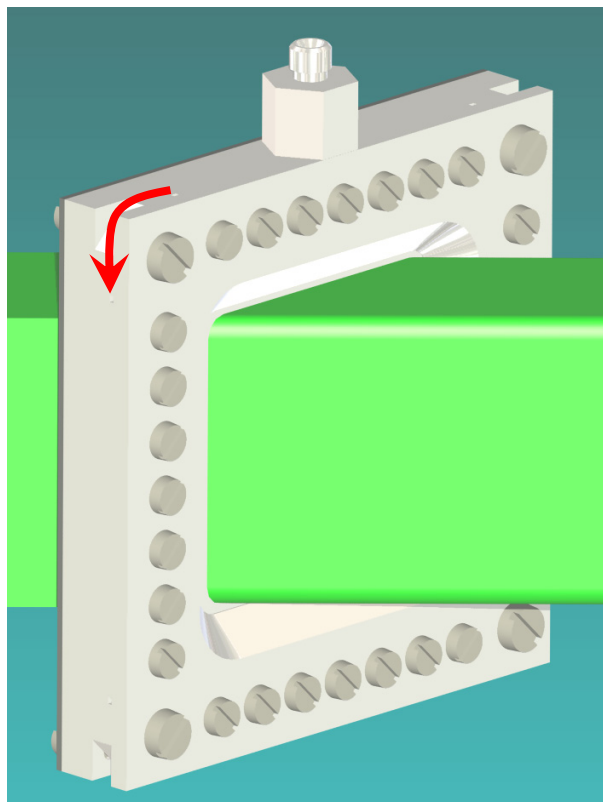
$$\frac{1}{\Delta E} \int_{-\frac{\Delta E}{2}}^{+\frac{\Delta E}{2}} N \frac{\partial^2 \sigma}{\partial \Omega \partial E}(|\vec{q}|, E) dE \approx \frac{1}{\sum \delta E_i} \sum_{|E_i| \leq \frac{\Delta E}{2}} N \frac{\partial^2 \sigma}{\partial \Omega \partial E}(|\vec{q}|, E_i) \cdot \delta E_i. \quad (5.77)$$

The reduced part of the data presenting the spectroscopic information is for instance shown on the bottom of Figure 5-39 and computed according to eq. (5.78):

$$\frac{1}{|\vec{q}_{\max}| - |\vec{q}_{\min}|} \int_{|\vec{q}_{\min}|}^{|\vec{q}_{\max}|} N \frac{\partial^2 \sigma}{\partial \Omega \partial E}(|\vec{q}|, E) d|\vec{q}| \approx \frac{1}{\sum \delta |\vec{q}|} \sum_{|\vec{q}_{\min}|}^{|\vec{q}_{\max}|} N \frac{\partial^2 \sigma}{\partial \Omega \partial E}(|\vec{q}|, E_i) \cdot \delta |\vec{q}|. \quad (5.78)$$

5.2.3 Neutron Spectroscopy of Anisotropic Dynamics

The texture of native cellulose may lead to anisotropic dynamic properties accessible with inelastic neutron scattering. To obtain results that reflect this orientation dependency with a time-of-flight instrument like 'FOCUS' it is necessary to rotate the sample. The results from measurements performed at different sample orientations have to be comparable. To ensure this, the orientation has to be determined accurately and the part of the sample illuminated by the neutron beam and 'seen' by the detectors has to be



identical. Both points have been fulfilled with a sample container especially designed for this purpose shown in Figure 5-48 and Figure 5-49.

In this construction, the orientation can be changed by a rotation by 90° of the sealed sample container in its frame without

Figure 5-48: Sample container for orientation dependent neutron scattering experiments designed for the instrument 'FOCUS'. The green beam illustrates the path of incident and transmitted neutrons travelling from left to right. The four bigger screws at the corners are released to allow the rotation of the container by any multiple of 90° , as indicated by the red arrow. The small screws are used to hold the container sealed. The thread and hexagon at the top allows an easy connection to the instrument's cryostat.

the need to open the container or to break its indium seal. At the source side of the frame, a cadmium aperture defines the shape of the primary beam to 30 mm horizontally and 42.4 mm vertically. The whole chamber holds an angle of 135° to the primary beam, minimising absorption and multiple scattering effects. The material of all components is aluminium except for the cadmium aperture and the indium seal, to reduce the background signal. The connection to the instrument's cryostat is established via a thread at the top of the frame. The sample measures 42.4 mm vertically and horizontally and has a thickness of 0.2 mm.

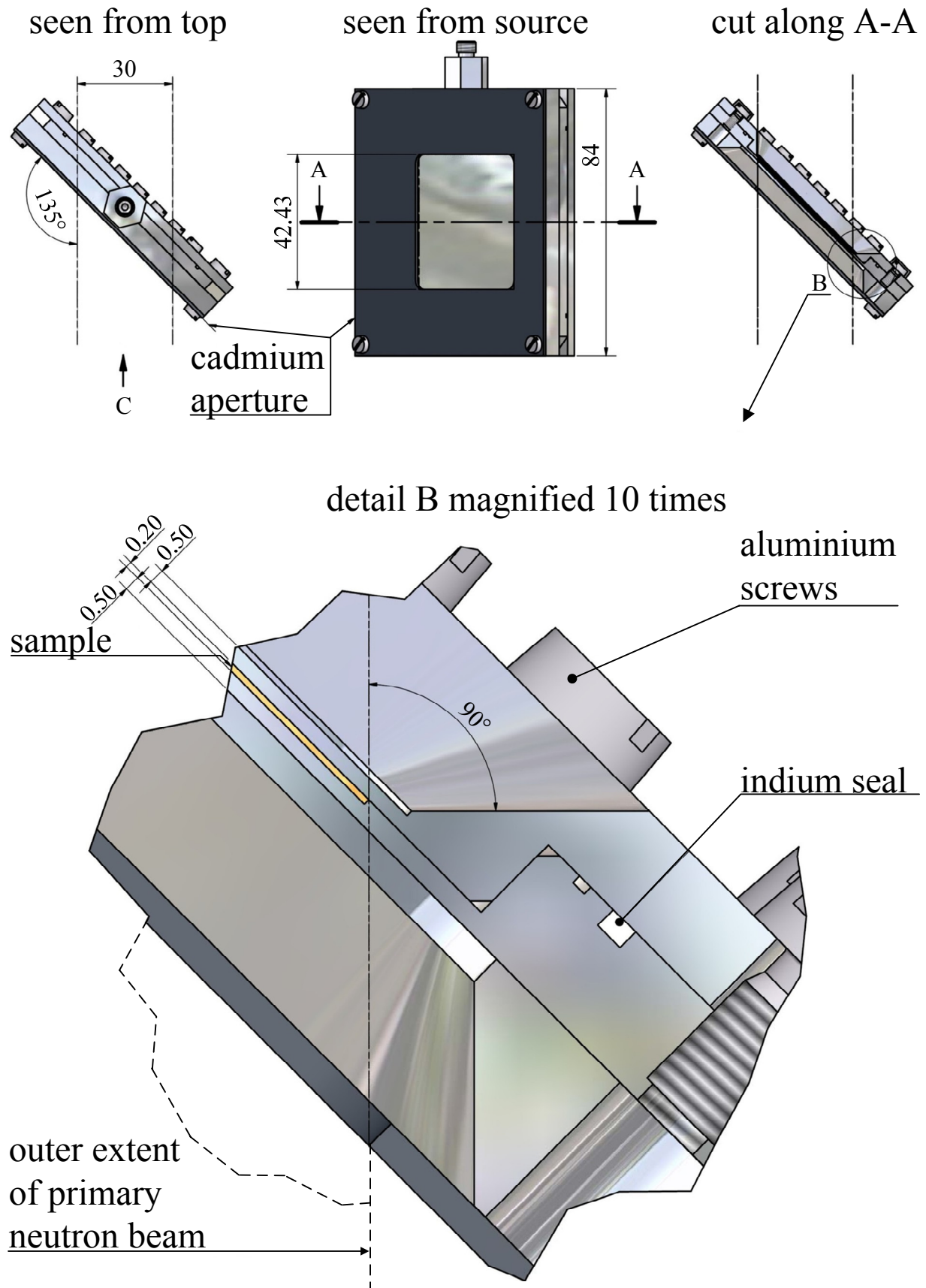


Figure 5-49: Aluminium sample container for neutron scattering experiments tuned for the instrument 'FOCUS'. The volume of the primary neutron beam is presented with the dashed lines. It enters the experiment along C. Dimensions are given in Millimetres.

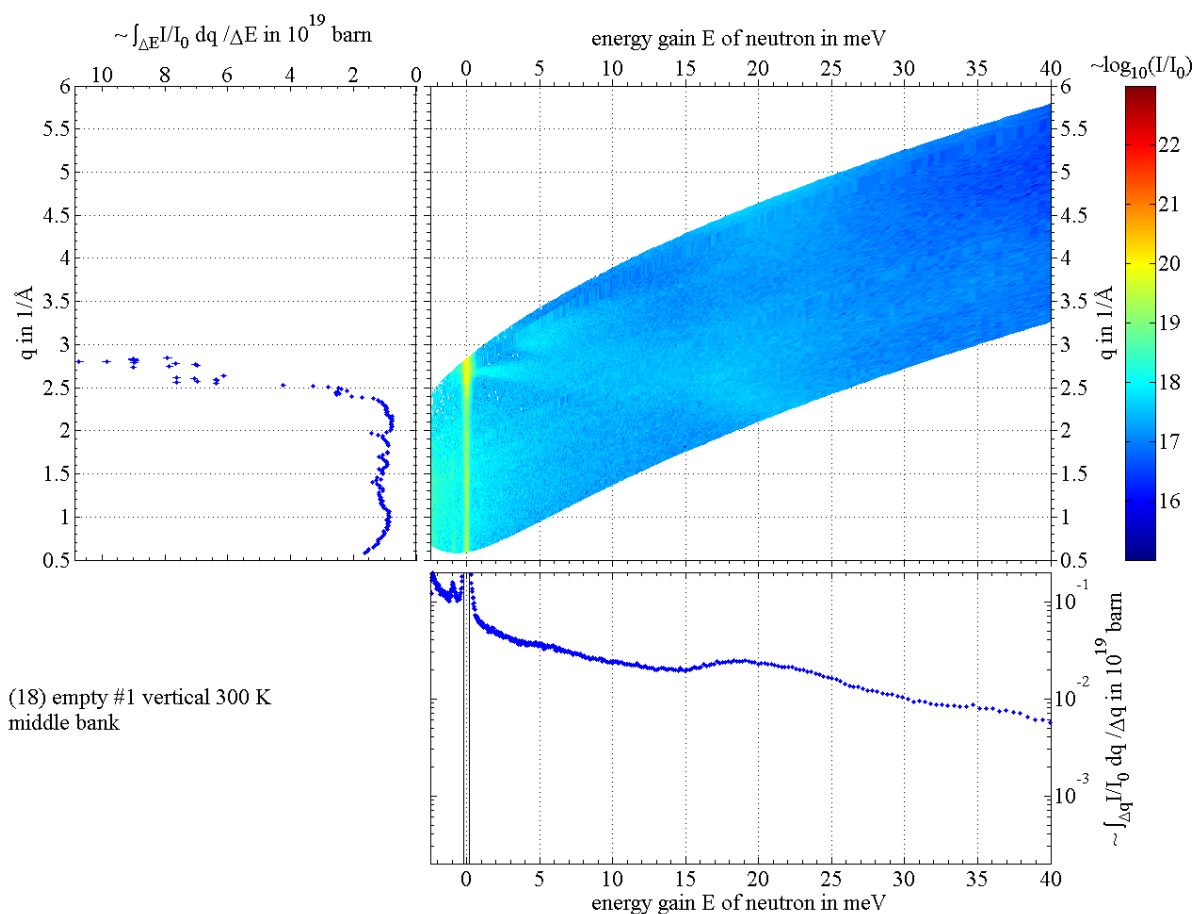


Figure 5-50: Background signal of the empty aluminium sample chamber in an inelastic neutron scattering experiment given for reference purposes. The intensity distribution is shown colour-coded on a logarithmic scale in the upper right graph versus energy gain of the neutron and wave vector transfer. In the upper left graph the same data are shown after integration on the black marked interval of ± 0.2 meV around the elastic line over the energy axis. The graph in the bottom shows the result after integration over all wave vector transfers.

The resulting background signal of the sample chamber in an inelastic neutron scattering experiment is shown in Figure 5-50 for reference purpose. Careful production of three sample chambers, identical with respect to their dimensions, leads to similar spectroscopic signal shown in Figure 5-51 for reference. Especially, the background signal of such a chamber is independent of its orientation in the instrument up to a very high degree, as shown in Figure 5-52 for two temperatures.

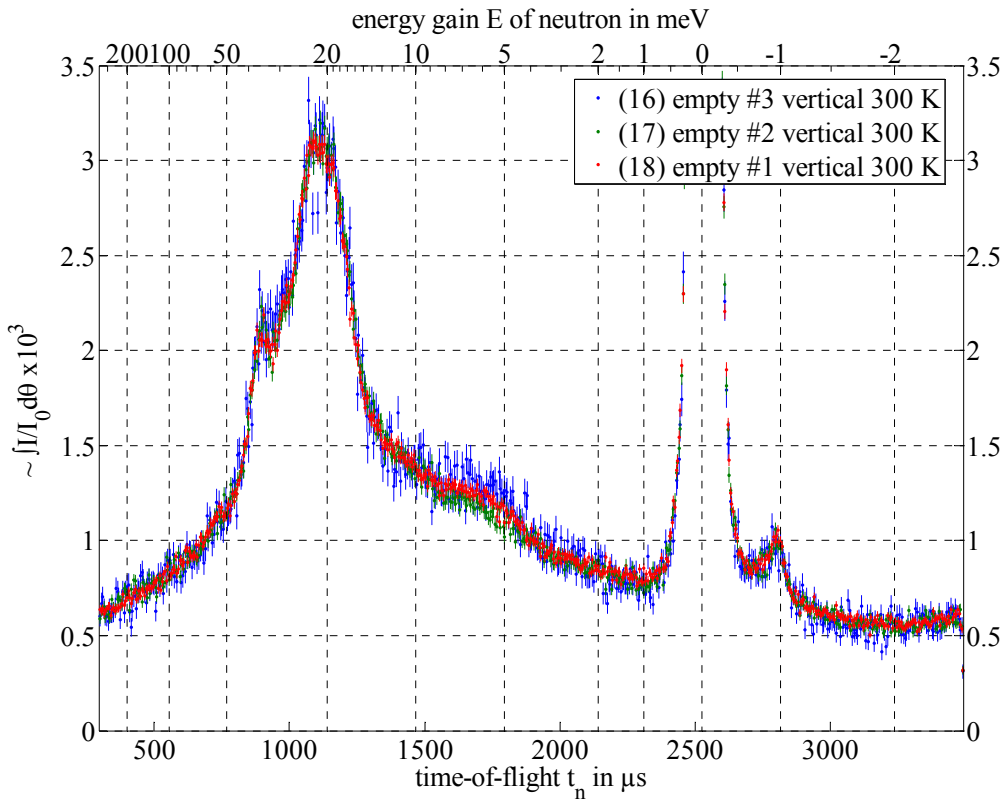


Figure 5-51: Inelastic neutron scattering signals from three different aluminium sample chambers, identical in construction, integrated over all scattering angles leading to similar background signals.

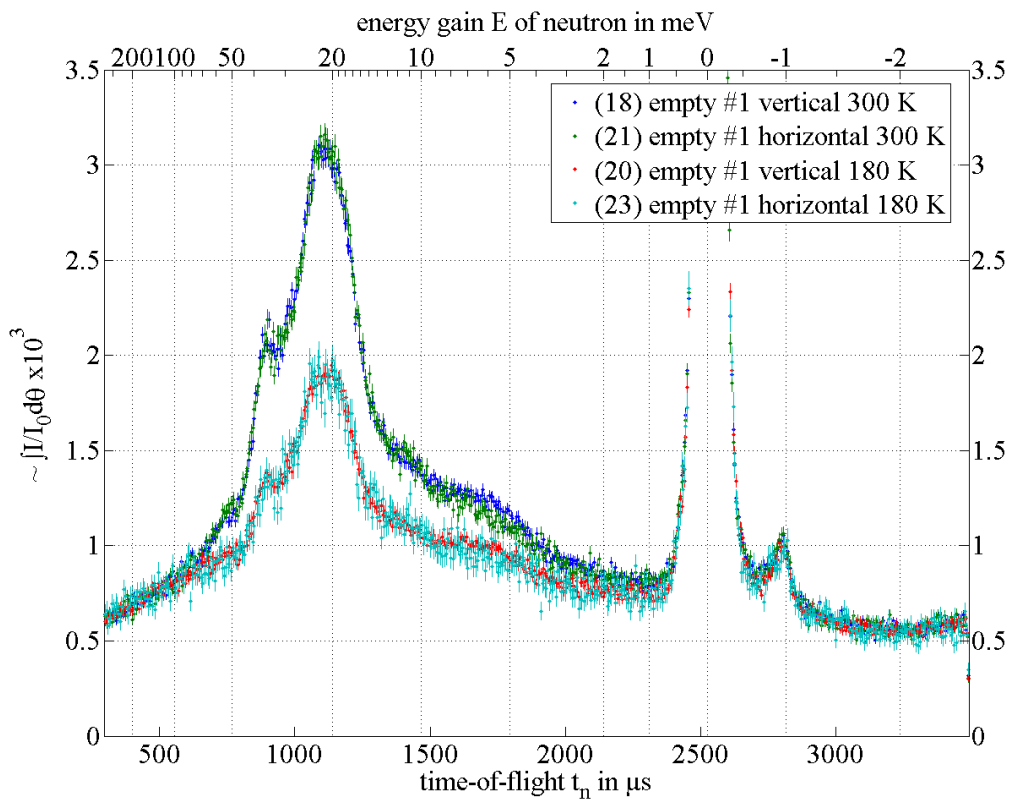


Figure 5-52: Inelastic neutron scattering signal of an aluminium sample chamber at different orientations and temperatures integrated over all scattering angles.

5.3 Water Content

Many properties of polymers change a lot when the water content is changed. In order to be able to investigate the influence of water on some of these properties the amount of water in the sample has to be controlled.

One way to measure the moisture content of a sample is the comparison of its weight before and after drying. The *rate of mass diffusion* \vec{m} occurring during drying is proportional by a factor D to the gradient of the *vapour pressure* p_{H_2O} as shown in (Bramhall 1995)^{eq. (8)}:

$$\vec{m} = D\vec{\nabla}p_{H_2O}. \quad (5.79)$$

The vapour pressure in eq. (5.79) depends exponentially on the temperature. The drying process can be accelerated dramatically in a vacuum oven. The end of the drying process is indicated, when the mass of the sample is no more decreasing. This way of measuring the moisture content is standardised in DIN 52183. It has been used for the flax sample investigated in the inelastic neutron scattering experiment presented in section 6.2.

To tune the water content in a sample to the desired value, a convenient opportunity is to control the humidity of the surrounding atmosphere. After some time, the moisture content inside the sample and the humidity outside of it are in equilibrium, leading to the so-called equilibrium moisture content. It depends on temperature and pressure and is well known for materials like wood. At 100 % relative humidity the maximum equilibrium moisture content is established in the sample. This is called the fibre saturation point for plant tissue.

If the amount of water in the sample should exceed that of the fibre saturation point, liquid water has to be offered. That means the sample has to be dipped into water. For any moisture content below the fibre saturation point, the necessary relative humidity surrounding the sample can be established via a surface of a saturated salt solution by controlling its temperature.

(This page is intentionally left blank.)

6 Results and Discussion

The influence of water on the mechanical properties of wood has been investigated by means of X-ray diffraction and inelastic neutron scattering experiments. In this way, it has been possible to monitor the structural and dynamical changes inside the composite material wood depending on its moisture content. The X-ray diffraction experiments have been performed at synchrotron radiation sources (HASYLAB, ESRF) and combined *in situ* with mechanical stretching tests. The results of these experiments on dry and wet pine earlywood are presented in the following section 6.1, concentrating on the properties of the crystallite microfibrils (lattice spacing, orientation). The inelastic neutron scattering experiments have been performed on a bundle of flax fibres at a spallation neutron source (SINQ). The sample has been investigated in wet and dry conditions. Taking difference spectra, one obtains spectroscopic data for the disordered regions of the cellulose that are accessible for water, as presented in section 6.2.

6.1 Synchrotron X-ray Experiments

The mechanical properties of wood are correlated with the orientation of the cellulose microfibrils inside the cell wall, as shown in section 3.1.1. Additionally, the macroscopic properties are strongly influenced by the water content of the material, as shown in section 3.2. An investigation of wood samples under tensile load with synchrotron X-ray radiation has been performed at different moisture contents to clarify the relation inside the cell wall between the water content and the cellulose with respect to the mechanics of the wood.

6.1.1 Experiments on Earlywood

The macroscopic behaviour of wood is the result of a composite of different types of wood as mentioned in chapter 3. Hence, the samples investigated have been chosen, to be small enough to consist of wood originating from only one growth period. All of the experiments presented in this subsection have been based on earlywood, taken from a tangential cut of a pine log.

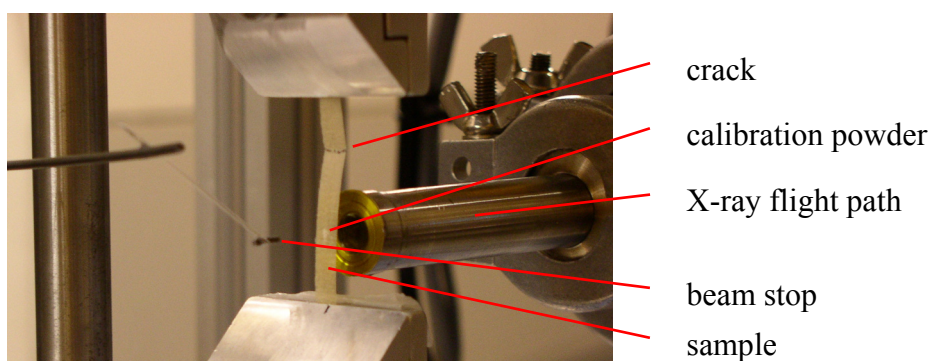


Figure 6-1: Wood sample investigated with X-ray diffraction using the big Kiel stretching device at HASYLAB beamline A2. The photo has been taken after fracture at the end of the experiment. The white powder permits online calibration of sample-to-detector distance. The X-ray flight path is kept in vacuum as close as possible to the sample. The small lead beam stop is glued to a glass capillary and positioned close behind the sample to minimize the background signal originating from air scattering.

The samples have been investigated with a stretching device at the HASYLAB synchrotron beamline A2, both described in section 5.1.3 and 5.1.1, respectively. The samples have been stretched with a constant strain rate of 2 μm per second, i.e. 0.005 %/s, until fracture. A picture of a typical sample after fracture at the end of an experimental run is shown in Figure 6-1. The white powder (Tripalmitin²⁰) on the surface of the sample has been applied before the experiment ensuring an ‘online’ calibration, as explained in more detail in section 5.1.6.3. The two-dimensional CCD-detector used to collect the X-ray diffraction patterns is specified in section 5.1.5. It has been synchronised with the stretching device and the fast

²⁰ 1,2,3-Propanetriol tris(hexadecanoate) or 1,2,3-propanetriyl ester, CAS-No. 555-44-2

shutter of the beamline to acquire images of 3 second accumulation time every 5 seconds. The raw data have been reduced following the procedure given in section 5.1.6. leading to diffraction patterns, as shown in Figure 6-2. The red circle in Figure 6-2 shows the powder ring used in the detector alignment calibration procedure. The regions-of-interest (ROIs) for the further analysis of the diffraction images are marked with red lines in Figure 6-3, where an example image is shown after transformation to polar coordinates. The exact limits are given in Table 6-2.

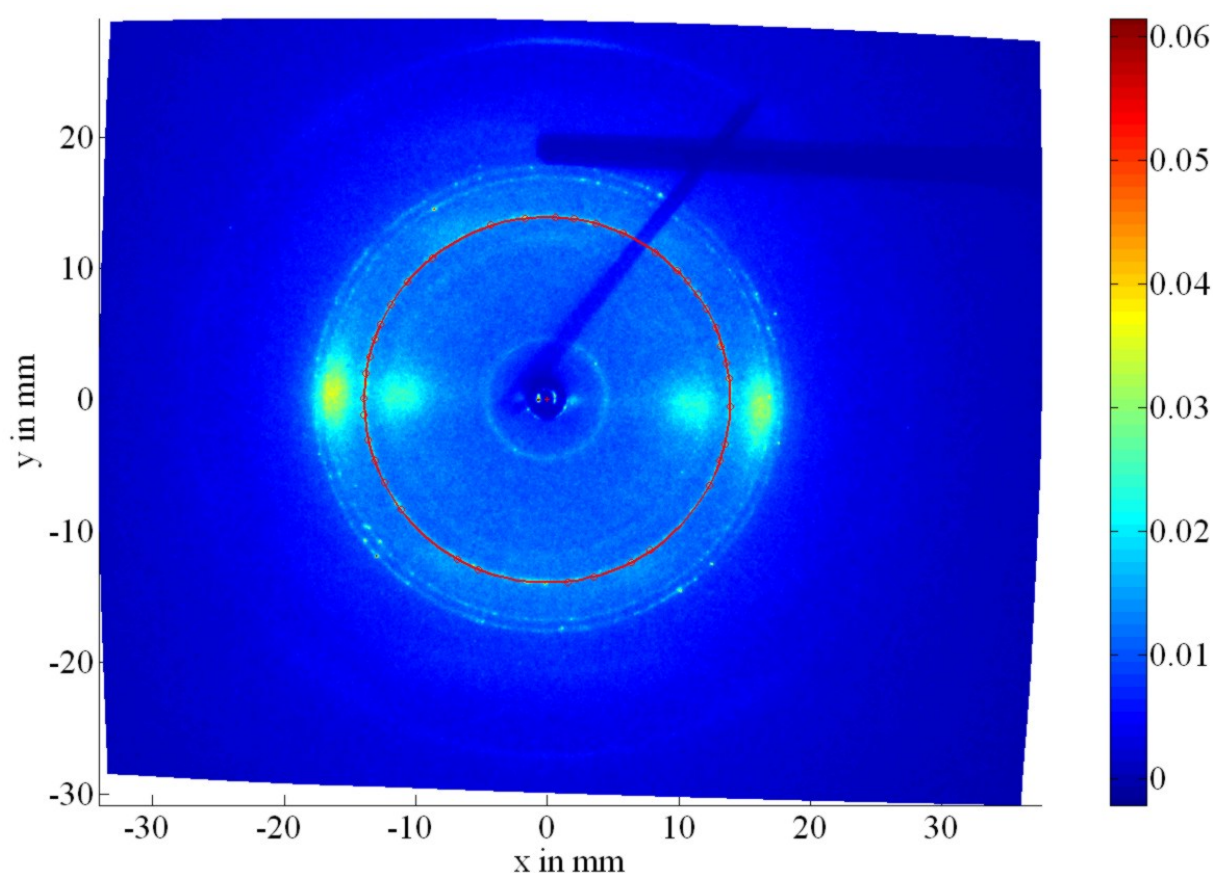


Figure 6-2: Diffraction pattern collected at A2 at HASYLAB with a piece of ‘dry’ pine early-wood and a calibration powder applied on its surface. The powder ring used for the calibration of the sample-to-detector distance and the detector alignment is shown with the big red circle. The small red circles show the supporting points used for the determination of the powder ring parameters. The centre of the primary beam is marked with a red cross. The shadowing due to the lead beam stop and its holder is visible in the centre and the upper right area. The intensity is shown colour-coded after summation of all 110 X-ray images each collected for 3 seconds during the combined diffraction and stretching experiment, leading to a total accumulation time of 330 seconds.

label	weight in mg	over all length in mm	cross section in mm ²	density in mg/mm ³	free length between clamps in mm	water content
'kiefer10'	18.2	55.5	5 × 0.2	0.328	40.07	dry
'kiefer11'	21.8	53.5	5 × 0.2	0.407	41.10	dry
'kiefer17'	11.9	52.5	5 × 0.2	0.227	40.00	wet
'kiefer18'	14.0	54.3	5 × 0.2	0.258	40.00	wet

Table 6-1: Parameters of the samples cut tangentially from pine earlywood and investigated at A2 at HASYLAB. The term 'dry' designates the moisture content established at indoor room conditions, about (10 ± 5) wt%, and the term wet designates a water content above the fibre saturation point.

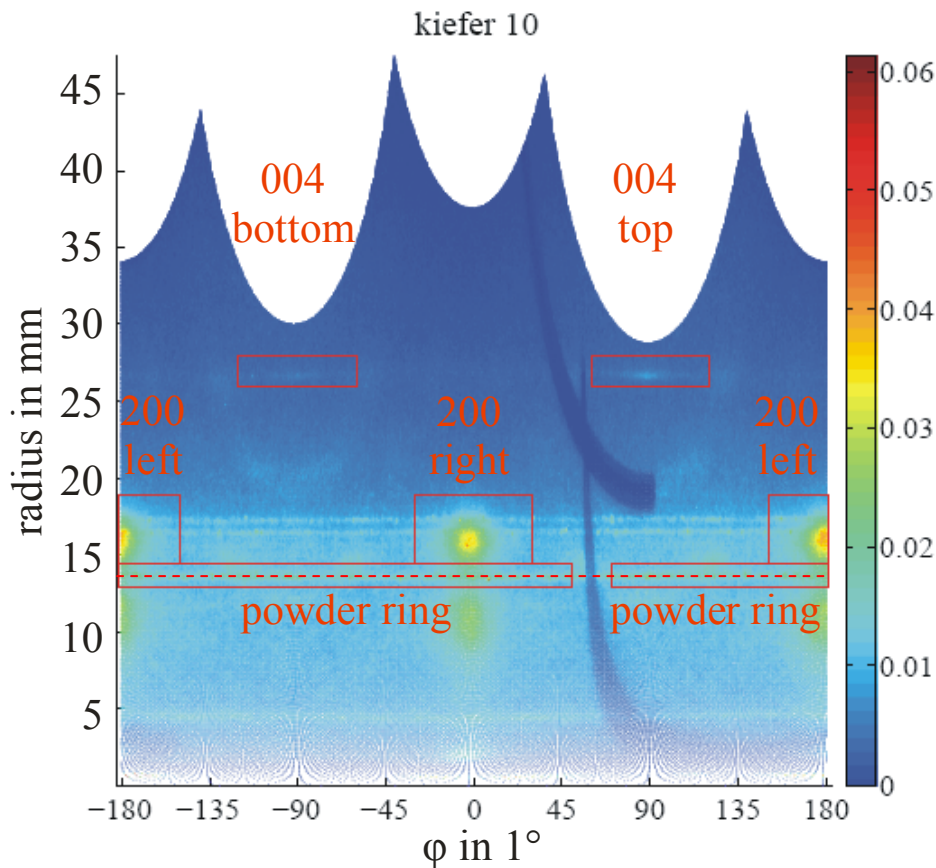


Figure 6-3: Diffraction pattern, as found in Figure 6-2 but only the first image from the series, collected at A2 at HASYLAB with a piece of dry pine earlywood and a calibration powder applied on its surface shown in polar coordinates. The powder ring used for the calibration of the sample-to-detector distance and the detector alignment is marked with the dashed red line. The intensity is shown colour-coded after 3 seconds accumulation time during the combined diffraction and stretching experiment. The red boxes give the regions-of-interest for the further peak analysis. The labels of the regions are given in red. The regions with identical labels ('200 left' and 'powder ring') have been combined in the analysis.

label	r_{min} in mm	r_{max} in mm	φ_{start}	φ_{end}
200 right	14.5	19.0	-30°	30°
200 left	14.5	19.0	-150°	150°
004 top	26.0	28.0	60°	120°
004 bottom	26.0	28.0	-60°	-120°
powder ring	13.0	14.5	70°	50°

Table 6-2: Parameters of the regions-of-interest (ROI) for the analysis of the diffraction patterns of the macroscopic samples of pine earlywood investigated at A2 at HASYLAB.

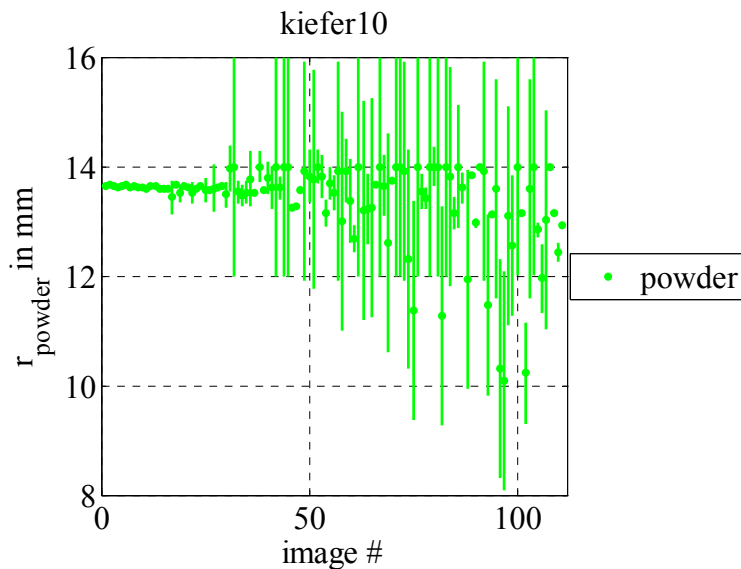


Figure 6-4: Results of the powder ring position versus number of the diffraction image, obtained from a Gaussian fit to the radial intensity distribution of the ROI 'powder ring'. The radial position turned out to be unreliable for images collected at higher strain, i.e. beyond image number 30. For details see text.

The ring-like pattern of the calibration powder can be used to calculate the detector distance in every single image separately, thus compensating any shifts of the sample along the primary beam direction during the stretching experiment. An example of this effect is illustrated in Figure 6-5, where the radial position of the powder ring is given versus time after starting the stretching experiment. From Figure 6-5 it is evident that the sample has been shifted from its starting position away from the detector into the direction of the X-ray source

(red dashed line). This ‘starting region’ corresponds to an only small increase in the force signal, as shown in Figure 6-5. Therefore, the scale of the strain axis is offset by the elongation that has been necessary to straighten the sample in this way, as given in Table 6-3. The force necessary to straighten the sample in this way leads to the non zero stress values given in all the stress-strain curves in the following. Unfortunately, the analysis of the powder ring position is strongly influenced by the underlying layer line, as visible in Figure 6-3. The radius obtained from the fit of the powder ring profile turned out to be unreliable, especially for images collected at higher strains, later in the experiment, as visible from Figure 6-4.

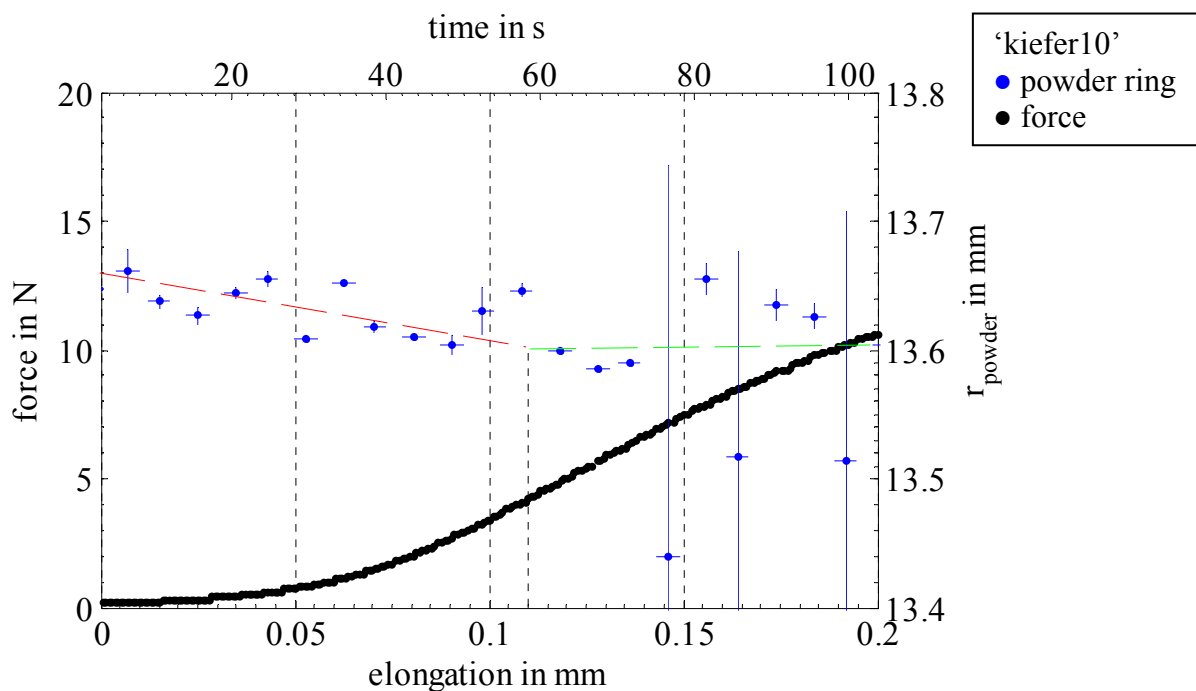


Figure 6-5: ‘Starting region’ of the stretching experiment performed on pine earlywood (‘kiefer10’) at A2 at HASYLAB with the big Kiel stretching device. The force is shown in black versus the elongation of the sample, taken from the upper clamp position of the stretching device. The radial position of the powder ring obtained from the diffraction pattern collected during the experiment is shown in blue. From the shape of the force-elongation curve and the tendencies of the radial position (red and green dashed lines) a shift of the sample away from the X-ray detector towards the X-ray source can be identified. For details see text.

Therefore, the results have been calculated for a sample-to-detector distance that has been assumed to be constant during the stretching experiment. The value chosen for this calculation has been taken from the more reliable fit results at the beginning of the stretching

experiments. Hence, the absolute values may be contaminated to some degree. Still, the effects and tendencies visible in the results calculated from the diffraction patterns in this way are unaffected.

In Table 6-1 the details of the investigated samples are given. The raw force values measured during the stretching experiments have been divided by the area and densities of the specimen given in Table 6-1 leading to the normalised stress $\sigma_{normalised}$, following eq. (3.1). In the same way, the elongations applied with the stretching machine have been divided by the length of the sample at its straight position, leading to the Cauchy strain ϵ . These values are used for the presentation of the results in the following, as done for example in Figure 6-9.

label	initial slope in Nm/t	final slope in Nm/t	elongation offset at strain 0% in mm	strain at rupture in %	water content
'kiefer10'	94.2	57.2	0.110	2.10	dry
'kiefer11'	102.9	79.7	0.066	2.23	dry
'kiefer17'	27.0	131.4	0.069	1.29	wet
'kiefer18'	27.2	93.3	0.100	1.28	wet

Table 6-3: Parameters obtained from the mechanical stretching experiments performed on pine earlywood pieces. Both, the initial slope of the normalised stress-strain curve and the slope close to rupture are given. The elongation values obtained from the stretching device have been shifted by the given offset values to set the values of zero strain.

The ROIs of the diffraction images mentioned above have been integrated along the radius and the azimuth, respectively. An example for such a ROI is given in Figure 6-6. Gaussian curves with linear background have been fitted to the integrated intensities of the ROIs to determine the position and to measure the width of the Bragg reflections. A selection of the results is shown in Figure 6-7 and Figure 6-8. The radial positions of the reflections have been used to calculate the corresponding lattice spacing that are given in the following for the 200

and 004 reflection of the cellulose crystals. Below the azimuthal width and position and the lattice spacing obtained this way are compared with the macroscopic stress-strain curves for the wet and dry samples, respectively.

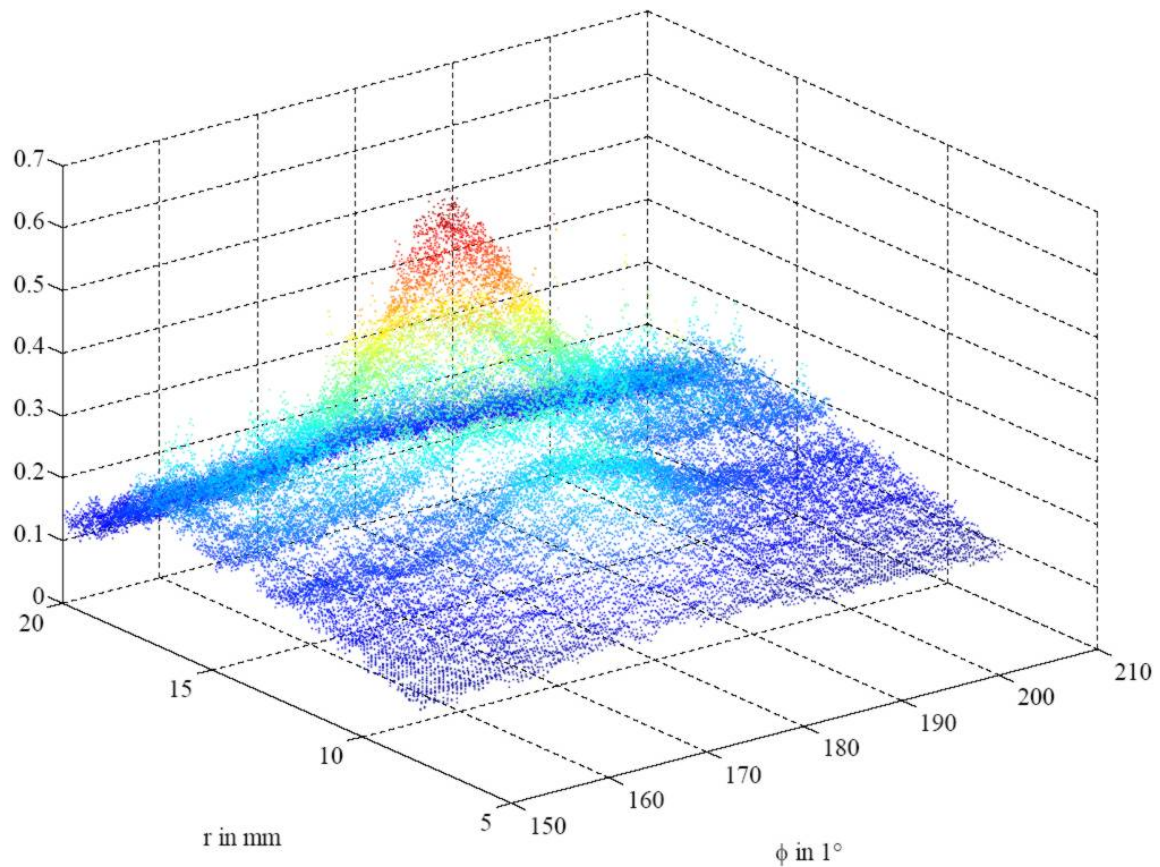


Figure 6-6: Region-of-interest (ROI) used for the analysis of the left 200 diffraction reflection collected in a combined stretching and X-ray diffraction experiment. The intensity found in the diffraction pattern is shown colour-coded versus radius and azimuthal position.

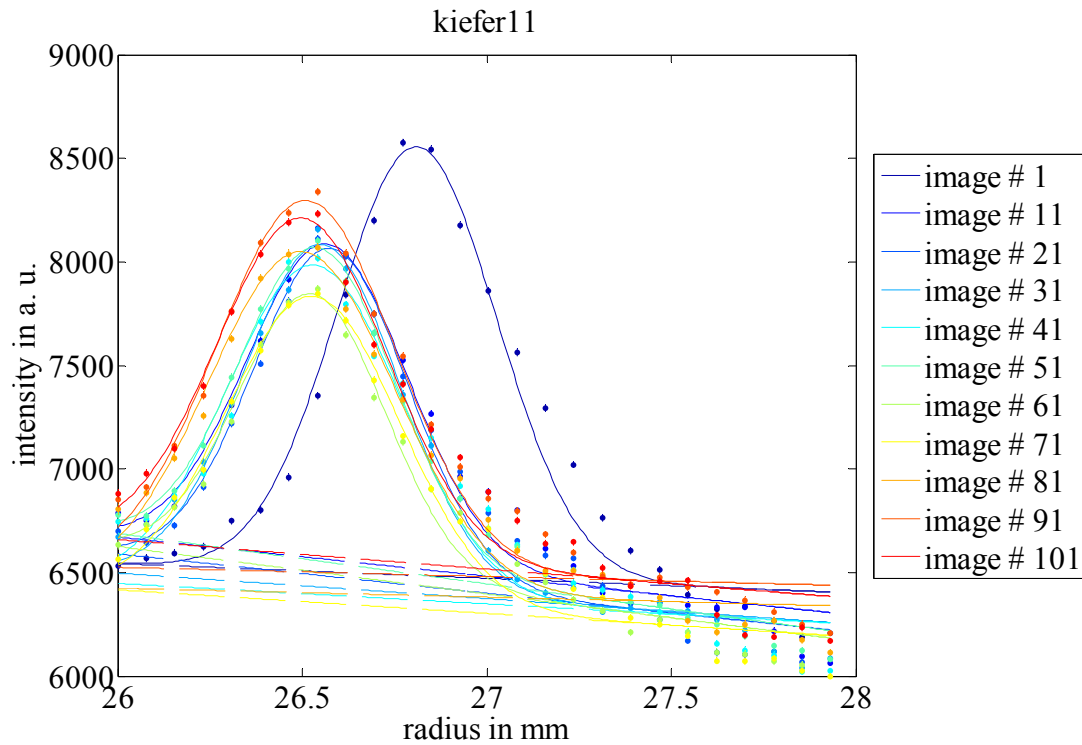


Figure 6-7: Results of the fits to the radial intensity distribution found in the ROI of the top 004 reflection of 'kiefer11'. The points of the radial intensity profile are given colour coded for every 10th diffraction pattern. The fits of a Gaussian distribution with linear background (dashed line) are shown as solid lines.

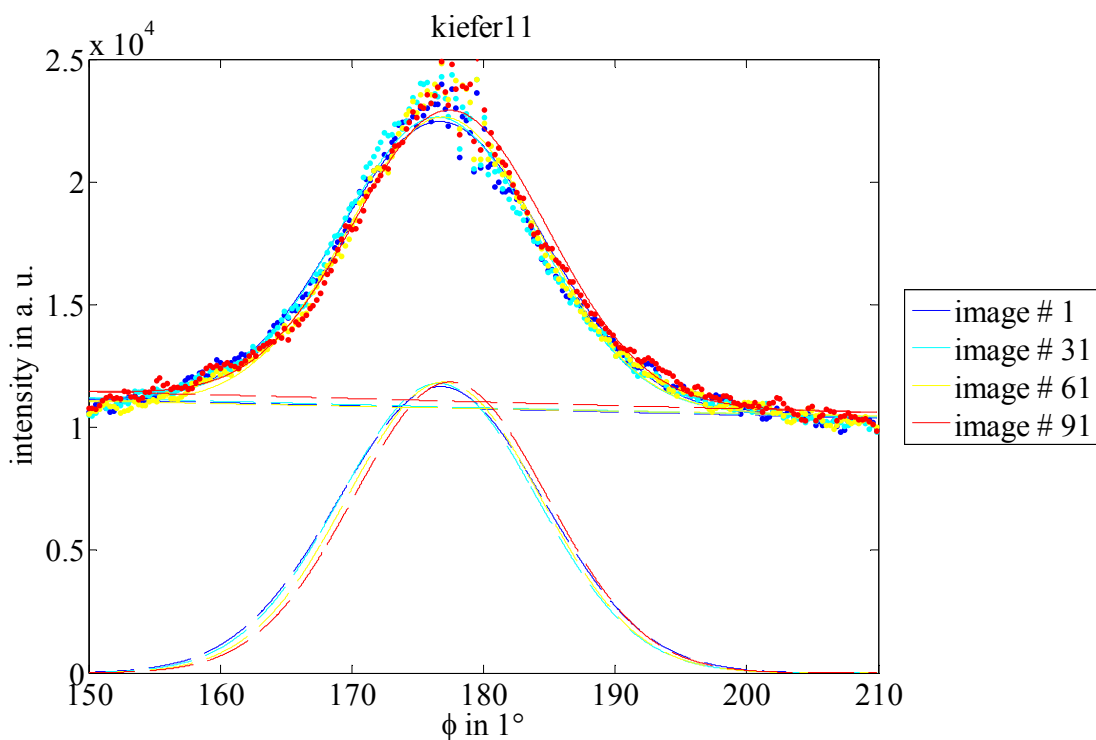


Figure 6-8: Results of the fits to the azimuthal intensity distribution found in the ROI of the left 200 reflection of 'kiefer11'. The points of the radial intensity profile are given colour coded for every 30th diffraction pattern. The fits of a Gaussian distribution (dashed line) with linear background (dashed line) are shown as solid lines.

6.1.1.1 Dry Pine Earlywood

The dry pieces cut tangentially from pine earlywood and tested under tensile tension show similar response in their stress-strain curves, as visible from the black curves given in Figure 6-9. Both samples have been stretched until fracture at about 2.1 to 2.2 % strain. The shape of the curves matches the shape discussed in section 3.1.2 and shown in Figure 3-9. Four different regions (A to D) can be distinguished²¹. The regions will be discussed in the following with respect to their corresponding strain limits²².

In the first region (A) the stress increases proportionally to the strain, as illustrated with the red straight line in Figure 6-9. In this region, the lattice spacing of the cellulose crystals along the *c*-axis of the unit cell obtained from the 004 diffraction reflection increases proportionally to the macroscopic strain, as visible in Figure 6-9 from the blue and green points for the top and bottom ROI, respectively. The region (A) ends at the proportional limit at about 0.2 % strain. The next region (B) shows a significantly smaller slope of the stress-strain curve up to about 1 % strain. In this region, the lattice spacing of the crystals increases further but with a smaller slope. The slope of the stress-strain curve increases again in the region (C) between 1 and 1.5 % strain. The lattice spacing of the crystals obtained from the two ROIs at top and bottom of the diffraction pattern differ. The spacing obtained from the top reflection increases with the same slope as in region (B), whereas the spacing obtained from the bottom one increases, if at all, at a smaller slope. The fourth region (D) of the stress-strain curve between 1.5 % strain and rupture shows clearly strain-hardening behaviour of the sample, resulting in a slope comparable to but smaller than the initial one of region (A). In the region (D) the 004 lattice spacing of the crystals does not increase any more, indicating a constant maximum strain of the crystals throughout this region.

²¹ The splitting into these four regions will be evident, in particular, with respect to the data obtained from the X-ray diffraction patterns that are shown in the following.

²² The strain limits of these regions given in the following discussion are no sharp boundaries. They may rather vary from sample to sample by about 0.1 percent points on the strain scale, as does the strain to rupture.

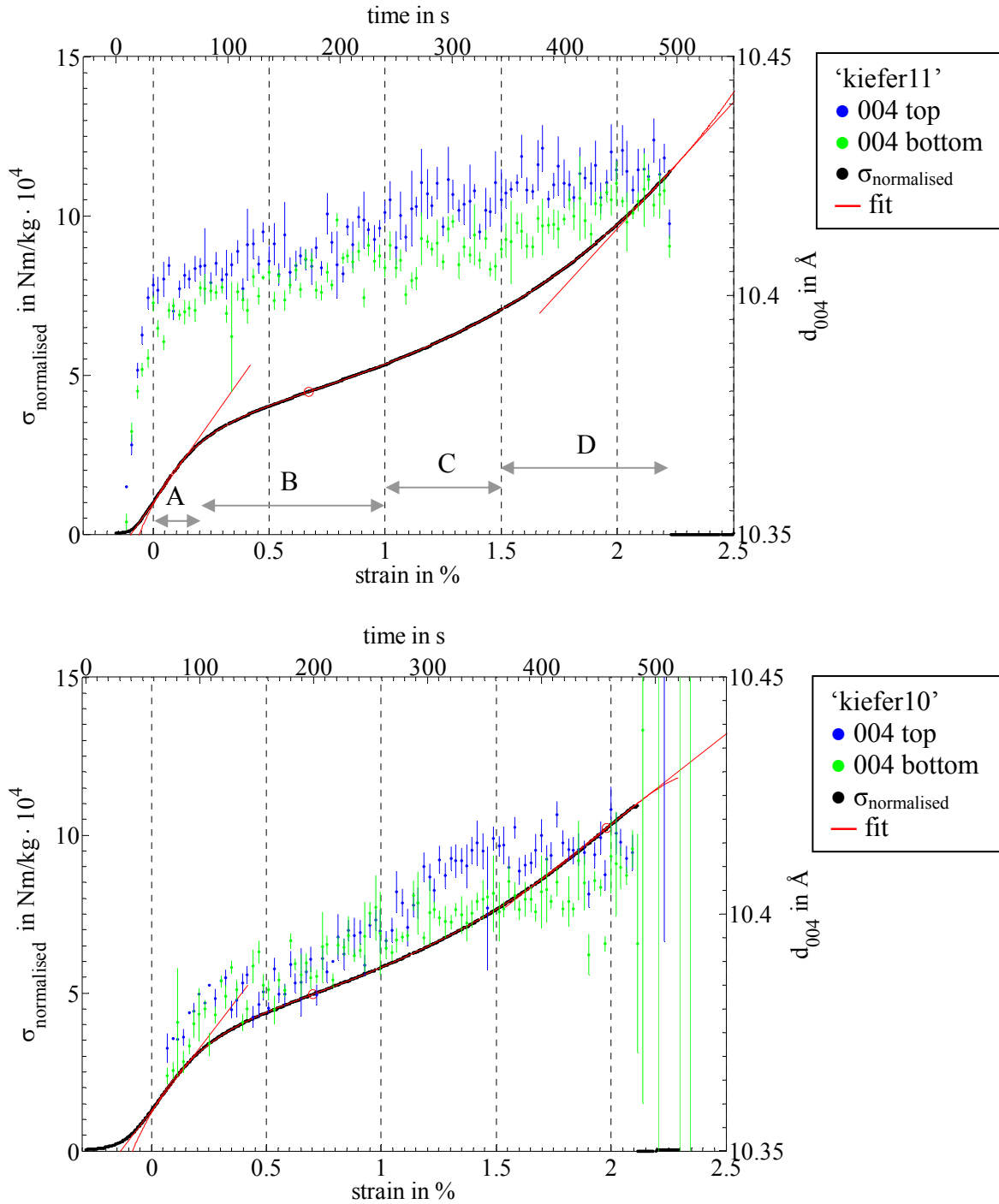


Figure 6-9: Normalized stress and lattice spacing obtained from the 004 diffraction reflection collected during a combined X-ray diffraction and tensile stretching experiment with a piece of dry pine earlywood ('kiefer11' top, 'kiefer10' bottom) at A2 at HASYLAB. The normalised stress σ is given in black. The lattice spacing obtained from the 004 reflection taken from the top (bottom) region in the diffraction patterns is shown in blue (green). The red straight lines show the slope at the beginning and at the end of the stretching curve. The small red circles mark the inflection points found with the polynomial fit shown as red line. No diffraction patterns have been collected during the first 70 seconds of the experiment on 'kiefer10' due to some technical complications. The values shown for the region after fracture at about 2.1 % strain are strongly influenced by shift and tilt of the broken sample and, therefore, not meaningful.

The lattice spacing of the cellulose crystals along the a -axis of the unit cell obtained from the two 200 diffraction reflections are shown in Figure 6-10. The lattice spacing along the a -axis follows the same tendency mentioned above for the spacing along the c -axis, indicating a slightly negative Poisson ratio for the direction perpendicular to the b - c -plane of the unit cell.

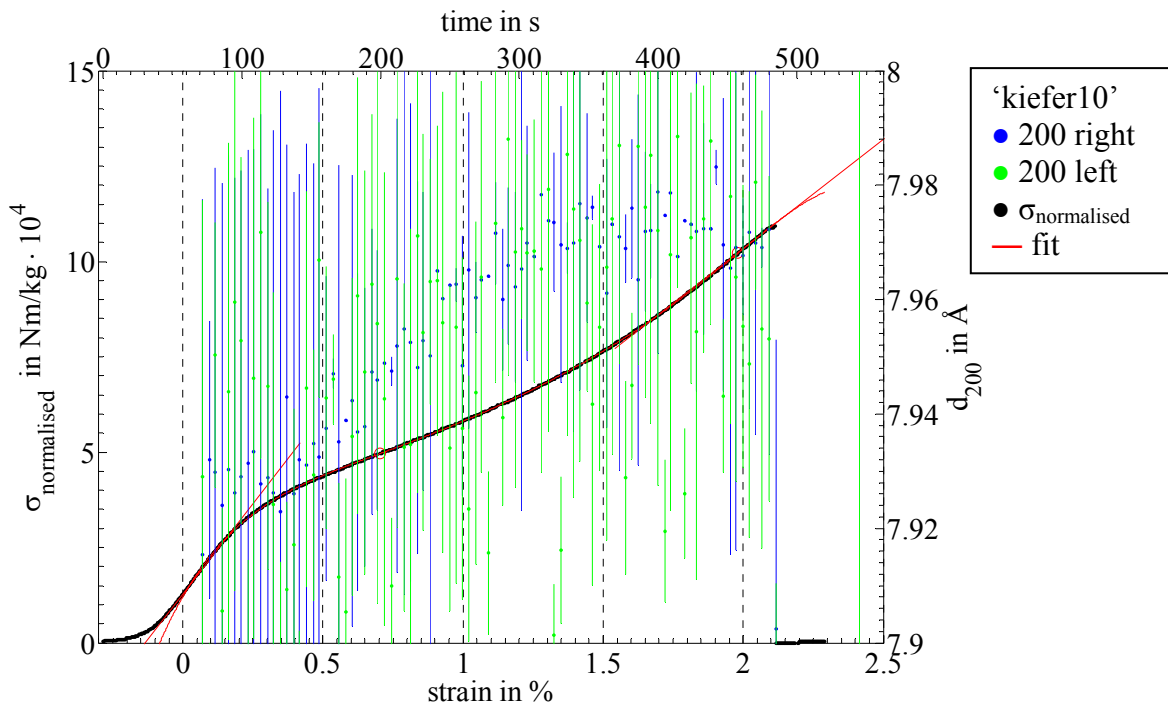


Figure 6-10: Normalized stress and lattice spacing obtained from the 200 diffraction reflection collected during a combined X-ray diffraction and tensile stretching experiment with a piece of dry pine earlywood ('kiefer10') at A2 at HASYLAB. For all other details see Figure 6-9.

The azimuthal position of the 200 diffraction reflection is shown in Figure 6-11. For both samples, the azimuthal positions obtained from the right and left ROI of the diffraction pattern change differently with strain. However, in the third region (C) of the stress-strain curve between 1 and 1.5 % strain the two ROIs show common behaviour for both samples. For the sample 'kiefer11', the azimuthal position obtained from the left ROI of the diffraction pattern increases with constant slope during the whole experiment, whereas the position obtained from the right ROI follows this tendency only up to 1.5 % strain. Beyond this strain

level, the right reflection turns back towards its starting position. The same ‘turn back’ behaviour of the azimuthal position can be found in the other dry sample ‘kiefer10’ but for both peaks of the diffraction pattern in common. An even more pronounced difference between the two samples can be seen in the regions (A) and (B) up to 1 % strain, where the two 200 reflections of ‘kiefer10’ turn towards a common value, reached at about 1 % strain.

The azimuthal position of the 004 diffraction reflection is given in Figure 6-12. The scatter of the data is higher than that of the position of the 200 reflection. This can be expected due to the geometry of the experiment, with the Bragg condition of the 004 reflection only being partially fulfilled. Nevertheless, for both samples the azimuthal position of the 004 reflection shows the same behaviour as the position of the 200 reflection, even though the tendencies of the 004 reflection are not as obvious as for the 200 reflection.

The azimuthal width of the 200 diffraction reflection measured with the full width at half maximum (FWHM) of the fitted Gaussian profile is given in Figure 6-13. The widths of the reflections obtained for the left and right ROI of the diffraction pattern show common behaviour within both individual stretching experiments. The width obtained for ‘kiefer11’ decreases up to 1 % strain and increases again slightly afterwards. The width obtained for ‘kiefer10’ decreases rapidly in the first region (A) of the stress-strain curve and increases afterwards up to about 1.5 % strain, and decreases again rapidly until fracture.

The rapid decrease of the azimuthal width of the 200 reflection found for ‘kiefer10’ coincides with the turning of the azimuthal position of the 200 and 004 reflection and the constant lattice spacing in a - and c -direction of the unit cell found for the same sample in the region between 1.5 % strain and fracture. The same effect is found in the data obtained from both 004 reflections of ‘kiefer11’ and for the azimuthal position of the right 200 reflection of that sample. The position of the left 200 reflection and the widths of both 200 reflections of ‘kiefer11’ do not show this behaviour. Nevertheless, the data from the diffraction patterns

show clear evidence for a different response of the cellulose crystals in the region (D) of the stress-strain curve, between 1.5 % and fracture, with respect to the preceding regions.

The changes in the azimuthal widths and positions of the diffraction peaks originate from changes in the orientation of the cellulose crystals. The common rotation of the reflections in the plane of the detector are due to tilts of the crystals in a plane parallel to the plane of the detector. The asymmetric tilts, seen for the 200 reflections, originate from tilts of the crystals in a plane perpendicular to the plane of the detector (Lichtenegger et al. 1997). The changes in the azimuthal width are linked to either a change of the mean MFA or to a smaller scatter of the helical angle of the crystals around the mean MFA. A decrease of the mean MFA would lead to a decrease of the azimuthal width of the 200 reflection, because the collected diffraction pattern is the summation of the patterns of all cell walls passed by the primary beam. For a small MFA, the 200 reflections from the walls at the front and back of the tracheids superimpose to one broad reflection as shown in Figure 6-2 combined with a centred peak due to the walls at either sides of cell.

A model-free measure for the orientation of the c -axis of the crystals along the axis of the tracheids is the Herman's orientation function $f_{\bar{a},x}$, as described in section 4.8. The orientation function is computed for the right (blue) and left (green) ROIs of the 200 reflection and shown in Figure 6-19. A value of one for the orientation function would indicate a perfect orientation of the crystals along the given axis. The changes in the orientation function, visible in Figure 6-19, mostly follow the tendencies found for the azimuthal width of the 200 reflection described above, reciprocally. However, there is an exception that is discussed in the following.

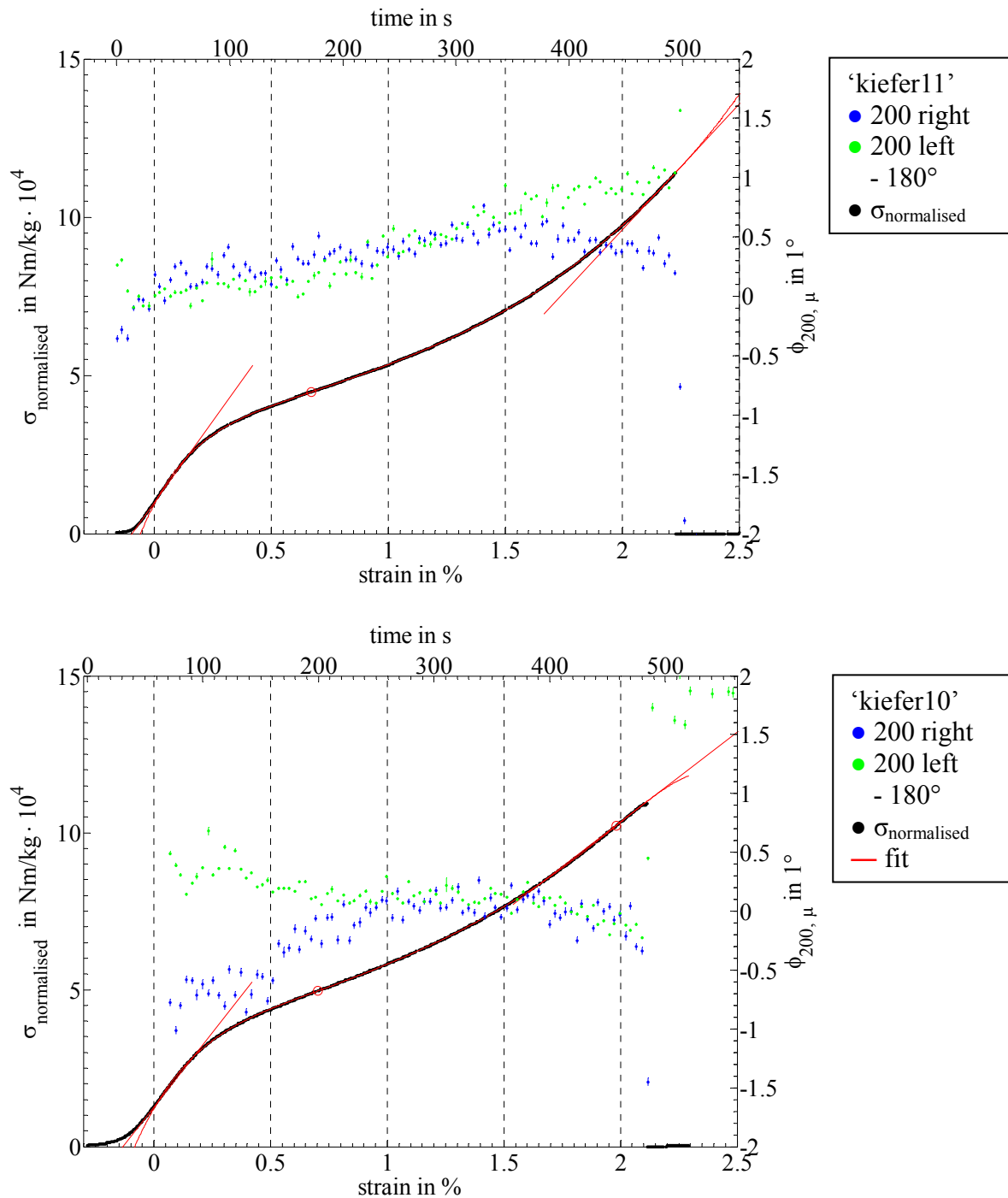


Figure 6-11: Normalized stress and azimuthal position of the 200 diffraction reflection collected during a combined X-ray diffraction and tensile stretching experiment with a piece of dry pine earlywood ('kiefer11' top, 'kiefer10' bottom) at A2 at HASYLAB. The normalized stress σ is given in black. The position of the 200 reflection taken from the right (left) region in the diffraction patterns is shown in blue (green). The red straight lines show the slope at the beginning and at the end of the stretching curve. The small red circles mark the inflection points found with the polynomial fit shown as red line. No diffraction patterns have been collected during the first 70 seconds of the experiment on 'kiefer10' due to some technical complications. The values obtained for the region after fracture at about 2.1 % strain are strongly influenced by shift and tilt of the broken sample, and, therefore, not meaningful.

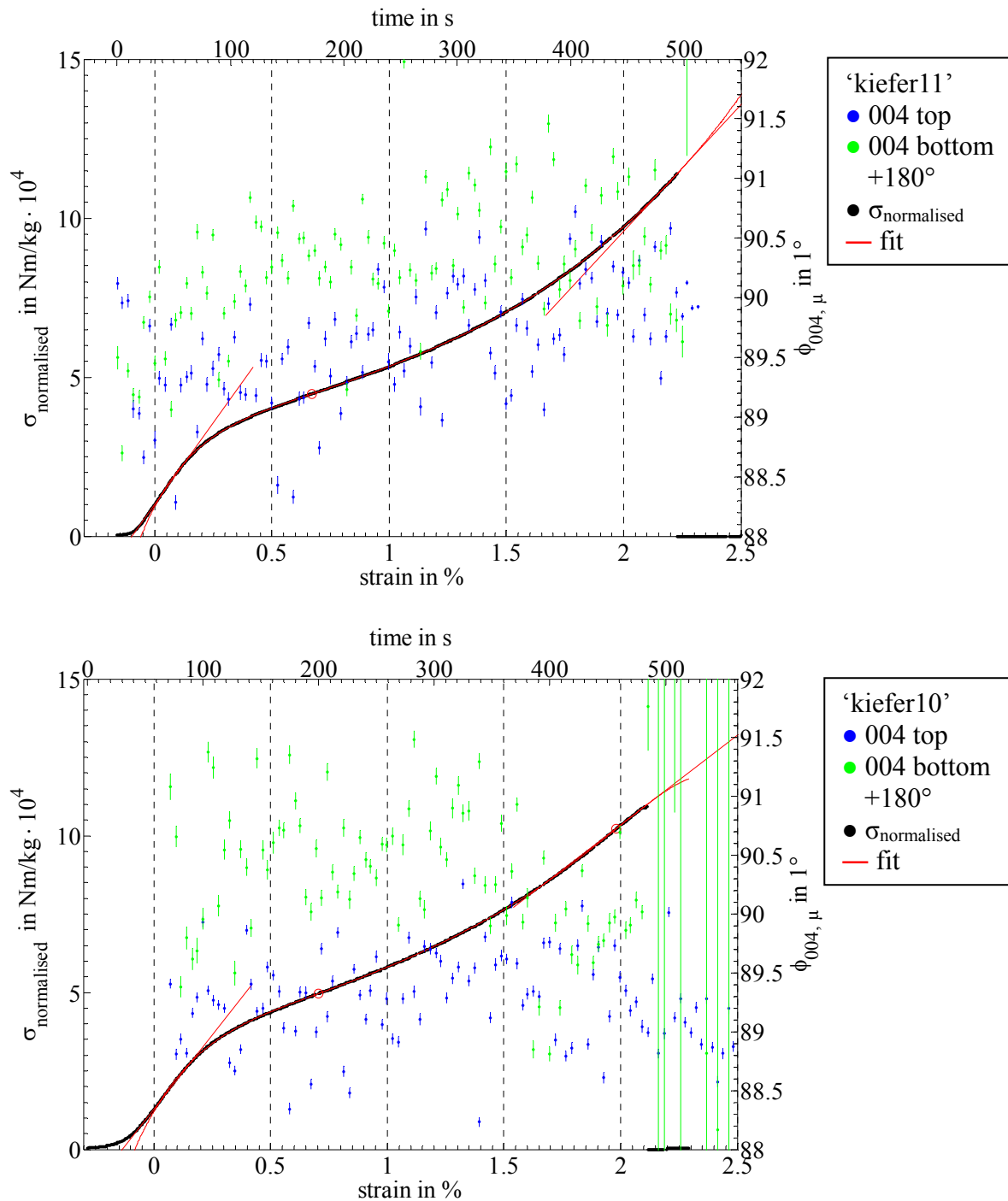


Figure 6-12: Normalized stress and azimuthal position of the 004 diffraction reflection collected during a combined X-ray diffraction and tensile stretching experiment with a piece of dry pine earlywood ('kiefer11' top, 'kiefer10' bottom) at A2 at HASYLAB. The normalized stress σ is given in black. The position of the 004 reflection taken from the top (bottom) region in the diffraction patterns is shown in blue (green). The red straight lines show the slope at the beginning and at the end of the stretching curve. The small red circles mark the inflection points found with the polynomial fit shown as red line. No diffraction patterns have been collected during the first 70 seconds of the experiment on 'kiefer10' due to some technical complications. The values obtained for the region after fracture at about 2.1 % strain are strongly influenced by shift and tilt of the broken sample, and, therefore, not meaningful.

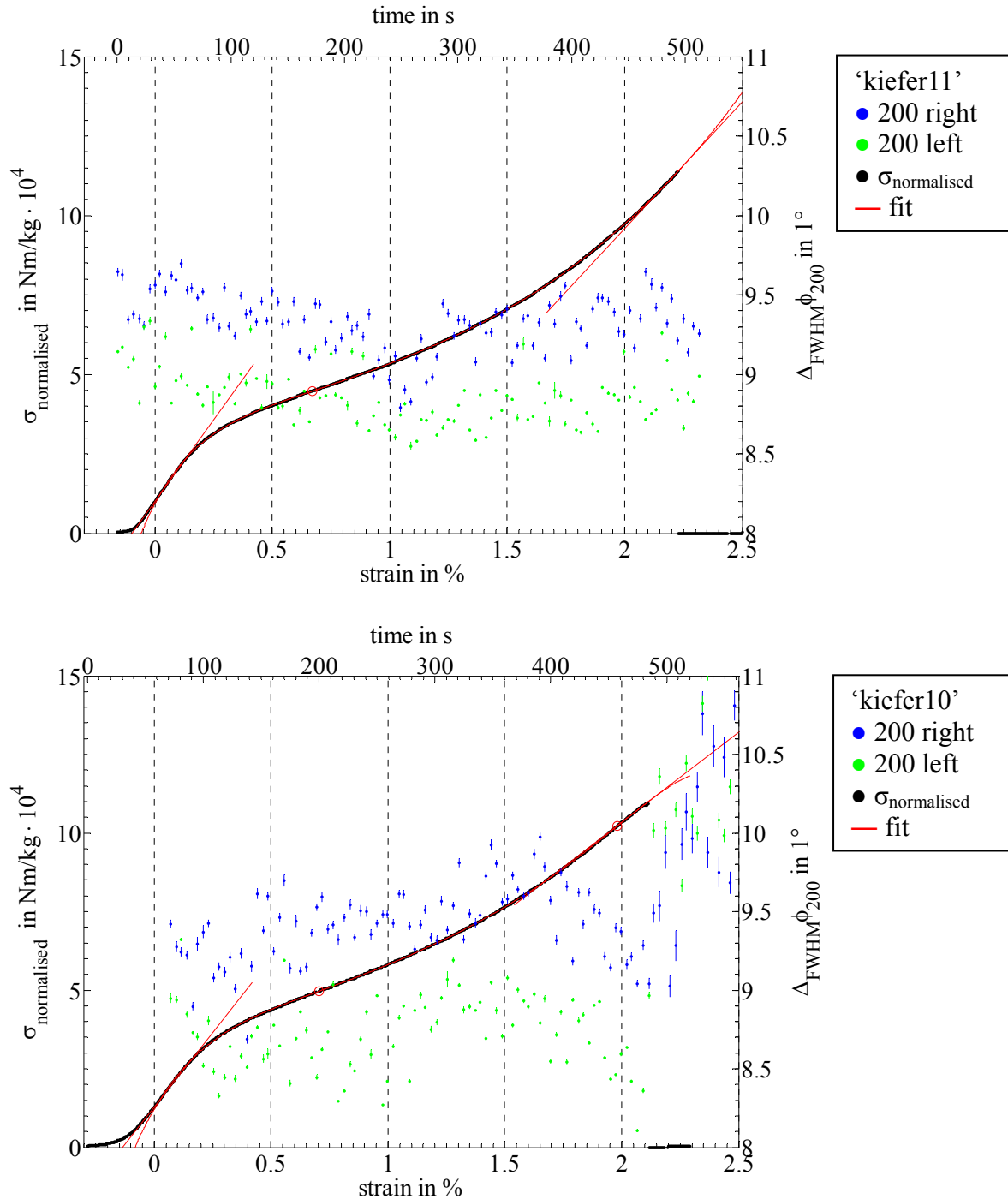


Figure 6-13: Normalized stress and full width at half maximum (FWHM) of the 200 diffraction reflection collected during a combined X-ray diffraction and tensile stretching experiment with a piece of dry pine earlywood ('kiefer11' top, 'kiefer10' bottom) at A2 at HASY-LAB. The normalized stress σ is given in black. The FWHM of the 200 reflection taken from the right (left) region in the diffraction patterns is shown in blue (green). The red straight lines show the slope at the beginning and at the end of the stretching curve. The small red circles mark the inflection points found with the polynomial fit shown as red line. No diffraction patterns have been collected during the first 70 seconds of the experiment on 'kiefer10' due to some technical complications. The values obtained for the region after fracture at about 2.1 % strain are strongly influenced by shift and tilt of the broken sample, and, therefore, not meaningful.

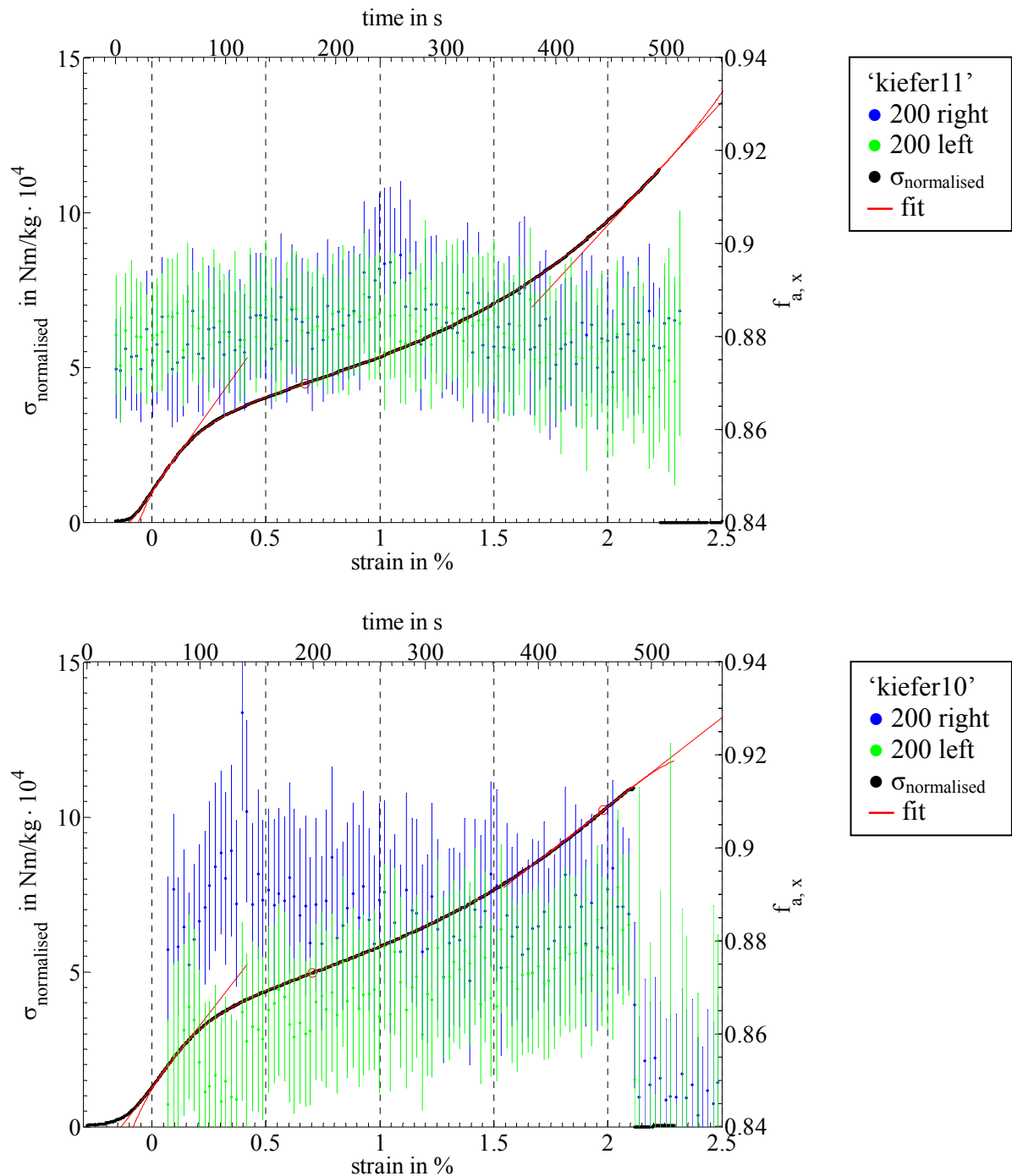


Figure 6-14: Normalized stress and Hermann's orientation function $f_{\bar{a},x}$ of the 200 diffraction reflection collected during a combined X-ray diffraction and tensile stretching experiment with a piece of dry pine earlywood ('kiefer11' top, 'kiefer10' bottom) at A2 at HASY-LAB. The normalized stress σ is given in black. The orientation function of the 200 reflection calculated for the right (left) region in the diffraction patterns is shown in blue (green). The red straight lines show the slope at the beginning and at the end of the stretching curve. The small red circles mark the inflection points found with the polynomial fit shown as red line. No diffraction patterns have been collected during the first 70 seconds of the experiment on 'kiefer10' due to some technical complications. The values obtained for the region after fracture at about 2.1 % strain are strongly influenced by shift and tilt of the broken sample, and, therefore, not meaningful.

The exception is a pronounced feature for ‘kiefer10’. The orientation function obtained from the left ROI between 0.2 and 0.4 % strain decreases, whereas $f_{\bar{a},x}$ from the right ROI increases. The azimuthal width obtained from the same ROIs show common changes, and the azimuthal positions turns into different directions, but for a longer strain region. Hence, the pronounced feature of $f_{\bar{a},x}$ indicates rapid changes in the crystal orientation that are different for the two sides of the diffraction pattern and not due to changes in the mean MFA. The constant increase of $f_{\bar{a},x}$ from the left ROI in contrast to the constant $f_{\bar{a},x}$ from the right ROI between 0.4 and 1 % strain indicates a ‘lining up’ behaviour of the crystals that first have been showing decreasing orientation between 0.2 and 0.4 % strain.

Additionally, the behaviour of $f_{\bar{a},x}$ compared to the tendencies of the azimuthal width of the 200 reflections found for ‘kiefer11’ shows a pronounced feature at about 1.05 % strain. The increase of the orientation obtained from the right 200 reflection is more pronounced than the corresponding decrease in azimuthal width of the same reflection. A comparable peak-like character can be found for ‘kiefer10’ at about 0.4 % strain for the same reflection. Both features indicate a tendency of the crystals to ‘relax orientation’ after sudden increase. Due to the limited beam size (250 $\mu\text{m} \times 250 \mu\text{m}$) the effects monitored this way can be expected to be localised and scattered across the sample.

The results from the two dry pine earlywood samples ‘kiefer10’ and ‘kiefer11’ can be summarised as follows:

- The stress-strain curve of dry pine earlywood shows strain-hardening.
- The tangential Young’s modulus at rupture resemble the initial one.
- There are four regions between 0 % strain and rupture, divided at the strain limits 0.2, 1.0 and 1.5 % strain that show qualitatively different behaviour of the cellulose crystals.
- The crystals react to the load with elongation along their c -axis.
- The crystal ‘line-up’ until highest possible orientation level is reached.
- The crystals ‘relax orientation’ locally after sudden increase.

The shape of the stress-strain curve and the points given above are consistent with the model explained in section 3.1.2. Especially, experimental evidence is found for the tilts of the crystals assumed in that model. In addition to the model one more region on the stress-strain curve has been identified, leading to a split of the second region of the model into regions (B) and (C). The region (B) is dominated by tilting effects of the mean MFA due to higher orientation of all crystals, and region (C) is dominated by decreasing orientation of the crystals, probably due to increasing scattered local damages in the material.

6.1.1.2 Wet Wood

The wet pieces cut tangentially from pine earlywood and tested under tensile tension show similar response in their stress-strain curves, as visible from the black curves given in Figure 6-16. Both samples have been stretched until fracture at about 1.3 % strain. The shape of the curves matches the shape of the dry samples presented above, but the initial slope is smaller and the stress is much lower at the proportional limit of only 0.1 % strain. Also, the strain at rupture is much smaller. These differences between dry and wet wood are well known and already illustrated in Figure 3-13.

The behaviour of the cellulose crystals has been monitored by means of X-ray diffraction in the same way, as for the dry samples described above. An averaged diffraction pattern obtained after summation of all diffraction patterns during one stretching experiment is given in Figure 6-15. The powder rings are evident and have been used to calibrate the sample-to-detector distance, as explained above. Especially, the small-angle scattering signal and the broad diffuse halo originating from the water content of the sample are visible (Jakob et al. 1996; Müller et al. 1998). These features can be found in all the diffraction images of the wet samples, indicating the successful humidification of the samples.

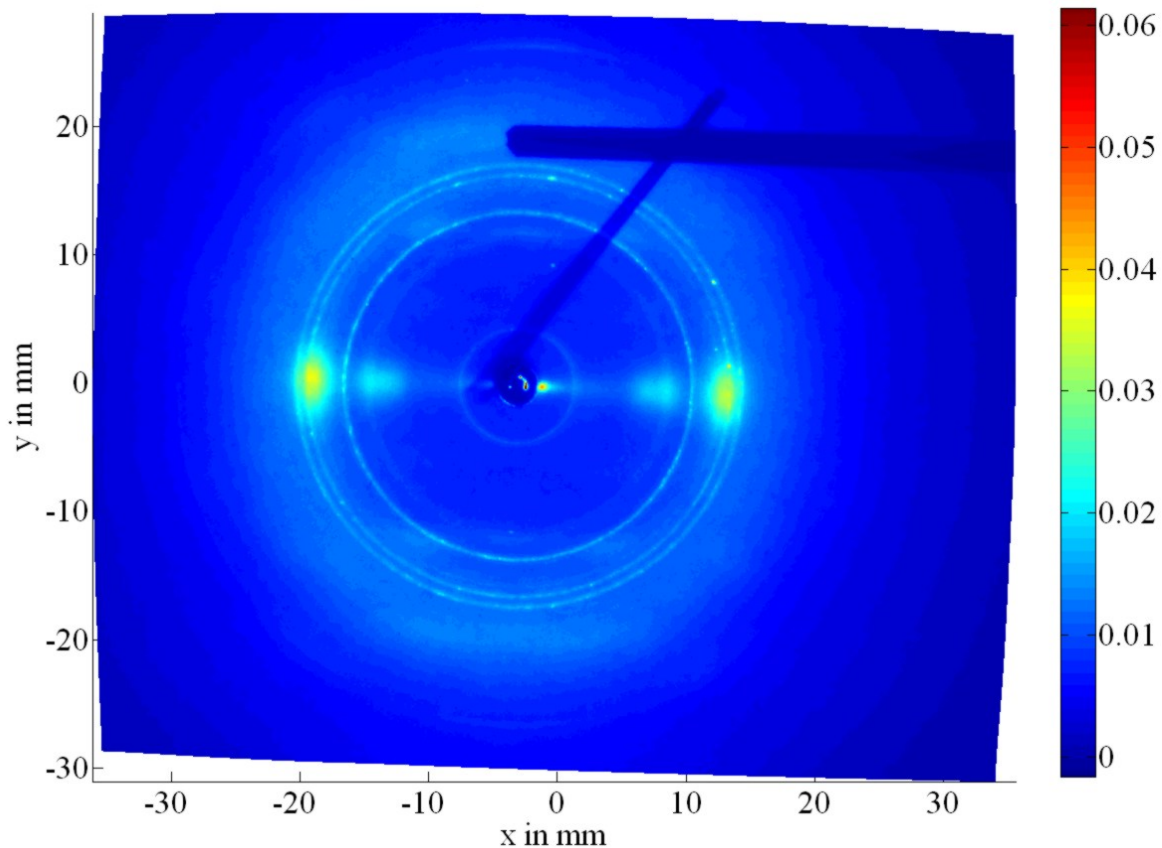


Figure 6-15: Diffraction pattern collected at A2 at HASYLAB with a piece of wet pine early-wood. The shadowing due to the lead beam stop and its holder is visible in the centre and the upper right area. The intensity is shown colour-coded after summation of all 77 X-ray images each collected for 3 seconds during the combined diffraction and stretching experiment, leading to a total accumulation time of 231 seconds.

The lattice spacing obtained from the top and bottom ROIs of the 004 diffraction reflection show common behaviour for both samples, as shown in Figure 6-16. There is no significant influence of the stretching on the lattice spacing along the c -axis up to 0.1 % strain. Contrarily, the spacing increases with strain beyond that strain limit of 0.1 % until rupture. This indicates a negligible load transfer from the matrix material to the crystals in the first region (A) of the stress-strain curve, and remarkable straining of the crystals afterwards. The slope of the elongation of the crystals increases beyond 0.6 % strain for ‘kiefer18’ and 1 % for ‘kiefer17’. This level indicates an onset of increased crystal response to the load. The same onset points can be identified for the tilt of the azimuthal position of the 200 reflection shown in Figure 6-17. The strain values found for these onset points differ for the two experiments, however, they both lie in the strain-hardening region (D) of the stress-strain curve. The strain

values for these points may vary due to the local probing of properties originating from the small beam size ($250 \mu\text{m} \times 250 \mu\text{m}$).

The azimuthal widths of the 200 diffraction reflections are shown in Figure 6-18. They show common tendencies for both ROIs and both samples. In the region (A) up to 0.1 % strain the width decreases in all ROIs. The widths obtained from the right (blue) ROIs stay constant between the following strain region from 0.1 to 0.5 % strain, whereas the widths obtained from the left (green) ROIs further decrease. However, at 0.5 % strain the widths obtained from all ROIs change slope, mostly increasing, and hold that slope until rupture over the full strain-hardening region (D). The first decrease of the widths may originate from a decrease in MFA or a decrease of orientation scatter of the crystals, as discussed for the dry samples. The later increase in region (D) is probably due to an increase of orientation scatter.

The increase in orientation scatter of the crystals in region (D) is evident from the values of the orientation function $f_{\bar{a},x}$ shown in Figure 6-19. The orientation function changes slope and starts to decrease at about 0.5 % strain, even though the scatter and uncertainties of the values obtained from the wet samples are bigger than that from the dry samples shown in Figure 6-14. This tendency may be a hint on increasing damages in the material, allowing isolated areas of the sample to relax. Additionally, $f_{\bar{a},x}$ found for ‘kief17’ increases clearly in the region (A) up to 0.1 % strain, similarly to the findings for the dry sample ‘kief10’.

In summary, the wet samples ‘kief17’ and ‘kief18’ show the following behaviour:

- The stress-strain curves have similar general shape as those of the dry samples.
- The tangential Young’s modulus at rupture of the wet samples resemble the initial one of the dry samples.
- The initial Young’s modulus and proportional strain limits are smaller than those of the dry samples.
- The stress-strain curve can be divided in at least three regions at limits of 0.1 and 0.5 % strain.
- The crystals react to the load with elongation along their c -axis.
- The crystal ‘line-up’ until highest possible orientation level is reached.
- The crystal ‘relax orientation’ after a certain strain limit (greater than 0.5 %) is reached.

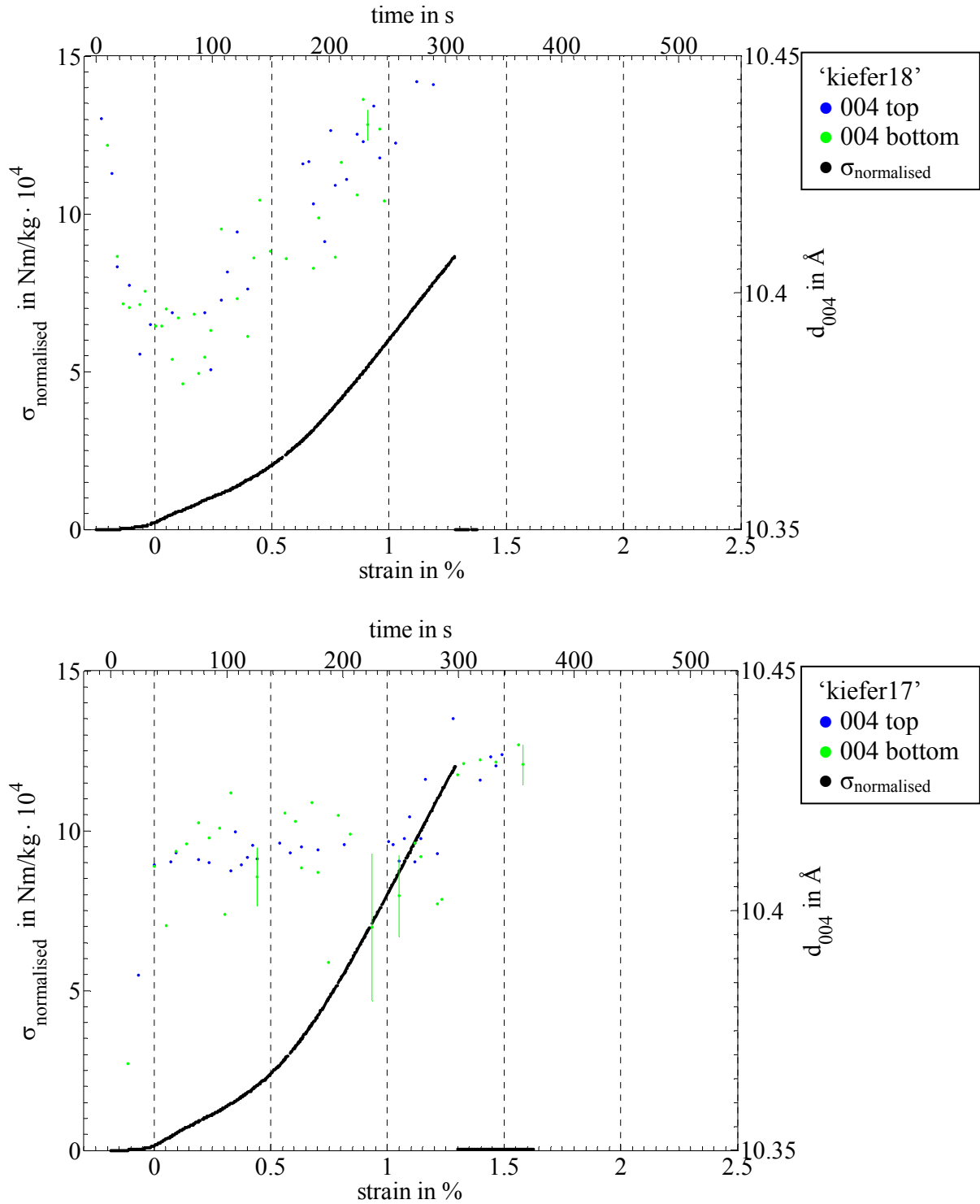


Figure 6-16: Normalized stress and lattice spacing obtained from the 004 reflection collected during a combined X-ray diffraction and tensile stretching experiment with a piece of wet pine earlywood ('kiefer18' top, 'kiefer17' bottom) at A2 at HASYLAB. The normalized stress σ is given in black. The lattice spacing obtained from the 004 reflection taken from the top (bottom) region in the diffraction patterns is shown in blue (green).

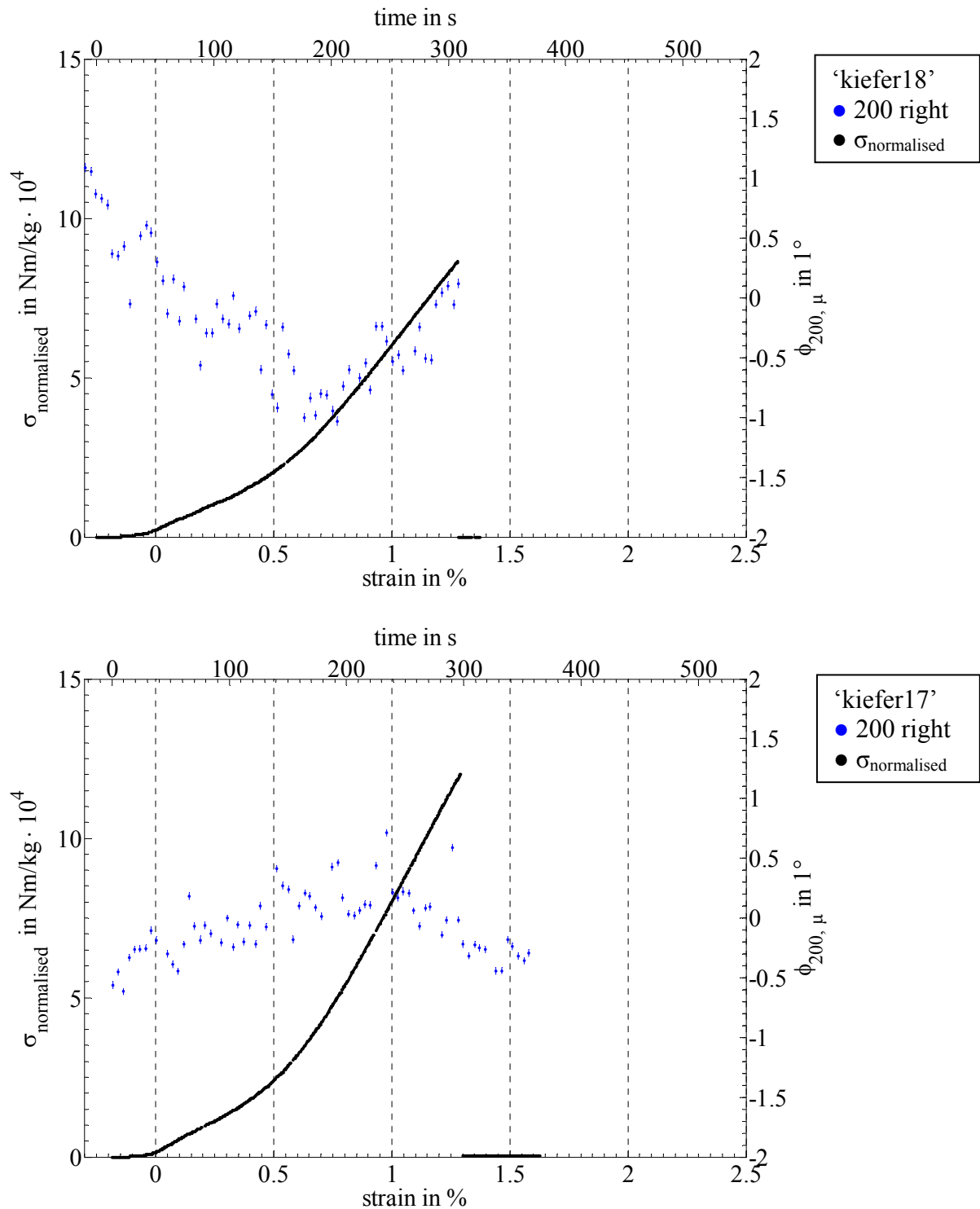


Figure 6-17: Normalized stress and azimuthal position of the 200 diffraction reflection collected during a combined X-ray diffraction and tensile stretching experiment with a piece of wet pine earlywood ('kiefer18' top, 'kiefer17' bottom) at A2 at HASYLAB. The normalized stress σ is given in black. The position of the 200 reflection taken from the right region in the diffraction patterns is shown in blue.

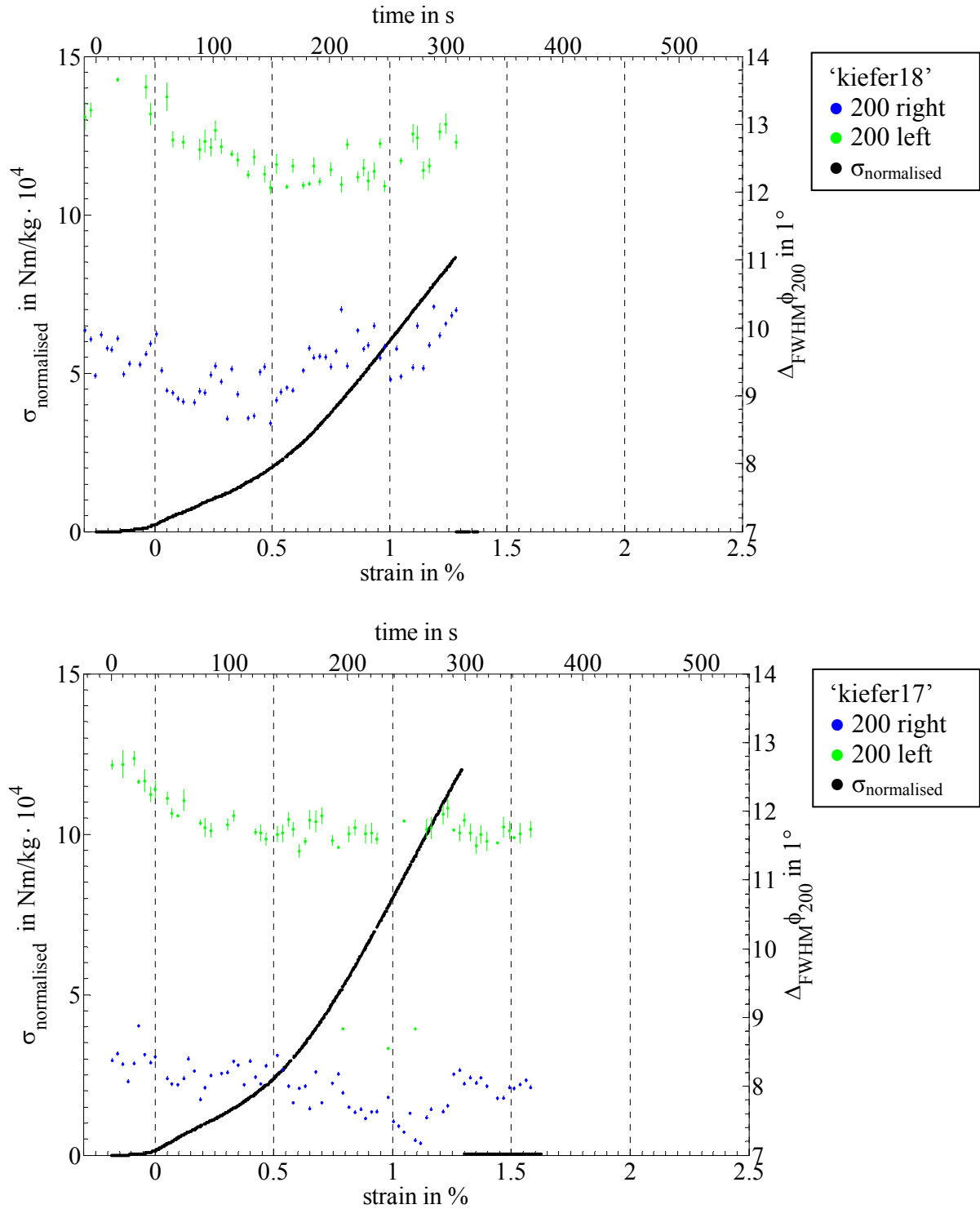


Figure 6-18: Normalized stress and full width at half maximum (FWHM) of the 200 diffraction reflection collected during a combined X-ray diffraction and tensile stretching experiment with a piece of wet pine earlywood ('kiefer18' top, 'kiefer17' bottom) at A2 at HASY-LAB. The normalized stress σ is given in black. The FWHM of the 200 reflection taken from the right (left) region in the diffraction patterns is shown in blue (green).

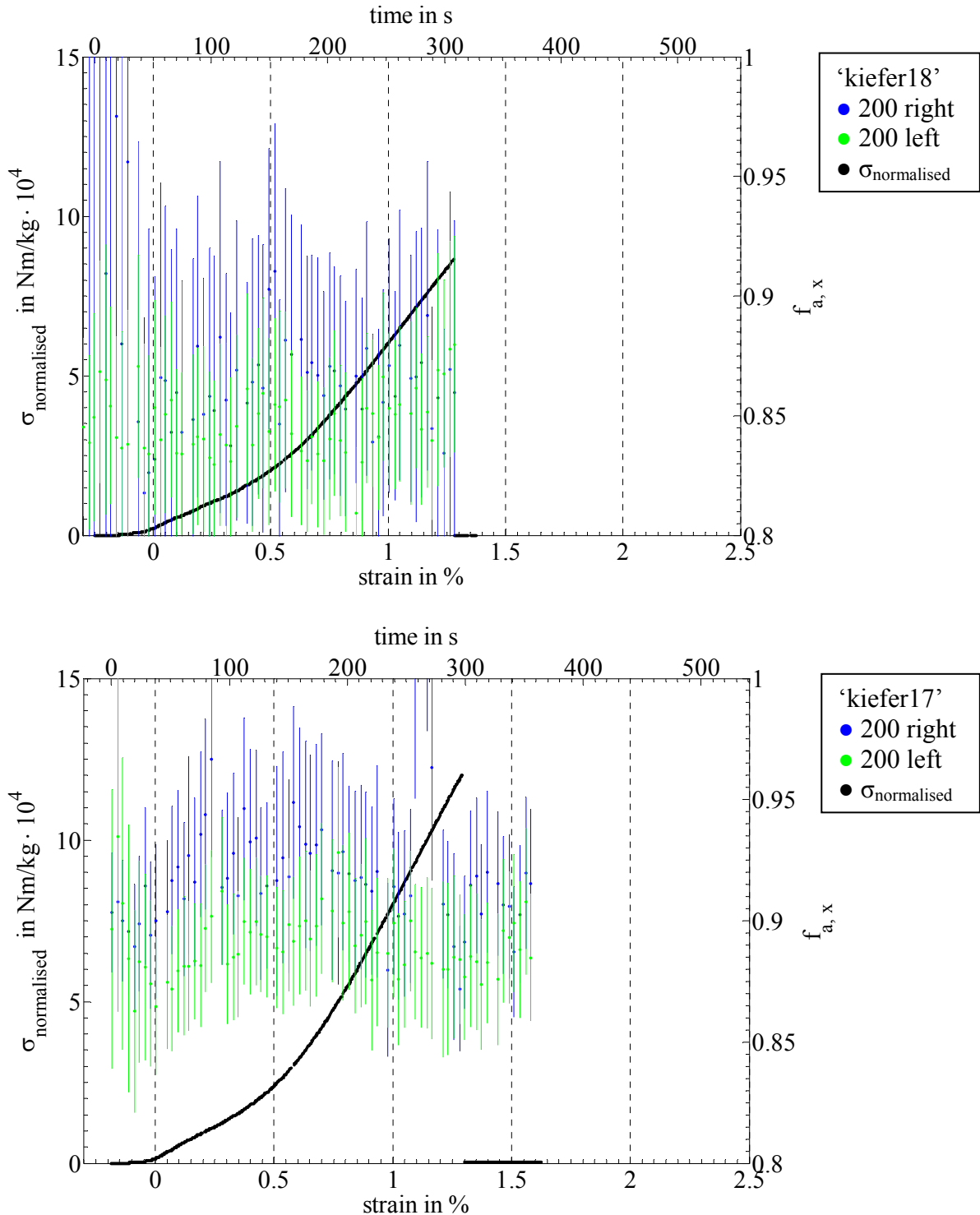


Figure 6-19: Normalized stress and Hermann's orientation function of the 200 diffraction reflection collected during a combined X-ray diffraction and tensile stretching experiment with a piece of wet pine earlywood ('kiefer18' top, 'kiefer17' bottom) at A2 at HASYLAB. The normalized stress σ is given in black. The orientation function of the 200 reflection calculated for the right (left) region in the diffraction patterns is shown in blue (green).

6.1.1.3 Comparison of dry and wet samples

The points above and the points found for the dry samples (section 6.1.1.1) allow to conclude on a general mechanism acting in pine earlywood under tensile load. The similar behaviour in the strain-hardening region found for wet and dry material, especially, the similar tangential Young's modulus of the stress-strain curve and decreasing orientation function probably originate from the same mechanism, which is described in the context of the model proposed in (Navi 1997) and explained in section 3.1.2. The assumed local damages scattered across the material and the domination of the Young's modulus by the weakest part of the composite are consistent with the findings presented above. The ongoing damage of the material under increasing strain lines up all the microfibrils, as far as possible, leading to an increase in the Young's modulus (strain-hardening). The behaviour in the **strain-hardening** region is **not** influenced by the water content of the sample.

Furthermore, the tendencies found at the beginning of the stress-strain curve in region (A) indicate a softening of the matrix, surrounding the cellulose crystals, due to the adsorbed water. Obviously less stress is necessary to 'line-up' the crystals in the presence of water. Nevertheless, the finally reached tangential Young's modulus shows no significant softening. Hence, the regions of the cellulose chains that connect sequencing crystals are very likely not accessible for water, or at least are not softened by its presence. Otherwise, the tangential Young's modulus close to rupture should show a similar softening as the initial modulus.

6.1.2 Single Fibre Experiments

The results of the experiments on macroscopic samples of pine earlywood concerning the stress-strain curve and the X-ray diffraction patterns show the effects present in a composite material consisting of several single tracheids ‘glued’ together via the lignin rich middle lamella. In order to distinguish between the contribution from the single tracheids and their interaction similar experiments on single tracheids from pine earlywood have been performed. To enable such experiments several technical challenges have been overcome and a special humidity controlled stretching device (HUSTEN) has been designed and built, as described in section 5.1.4. It has been operated at ID13 at the ESRF and some first results²³ are presented in the following.

The investigated samples of up to 4 mm length and about 50 μm diameter have been extracted with tweezers from a humidified piece of pine earlywood under a stereo light microscope. The samples have been glued onto a supporting frame, as shown in Figure 6-20. The supporting frame has been used as a carrier to mount the sample in the sample holder of HUSTEN. Then the supporting frame has been cut with a soldering gun and the sample holder has been transferred into HUSTEN. The free length of the sample prepared in this way has been 600 μm , as visible in Figure 6-20.

The samples have been stretched (along the y -axis) with a constant elongation rate and X-ray diffraction patterns have been collected during the stretching process. The position of HUSTEN and, hence, the position of the sample with respect to the primary X-ray beam has been changed with a translation stage during the experiment. This movement has been oriented perpendicularly (along the x -axis) to the direction of the elongation of the sample. The

²³ Due to the limited time at synchrotron radiation sources, the experiments on single fibres have had to be concentrated on this feasibility study. However, a detailed investigation will be performed soon.

rows of diffraction patterns illustrated in Figure 6-21 have been collected in this way. The movement has been performed in steps of $10\ \mu\text{m}$ between the collection of the diffraction patterns, leading to 21 images per scan. Each diffraction pattern has been accumulated with the detector described in section 5.1.5 for one second every two seconds. After each perpendicular scan the sample has been moved back to the starting position and another perpendicular scan has been started. During all the time the sample has been continuously elongated inside HUSTEN. In this way a map of diffraction patterns has been collected for each sample, as given in Figure 6-21, where each row has been taken roughly at the same height on the sample, but at different times. This enables the tracing of one particular position on the sample with a time resolution of about 42 seconds even if the sample might have been shifted laterally.

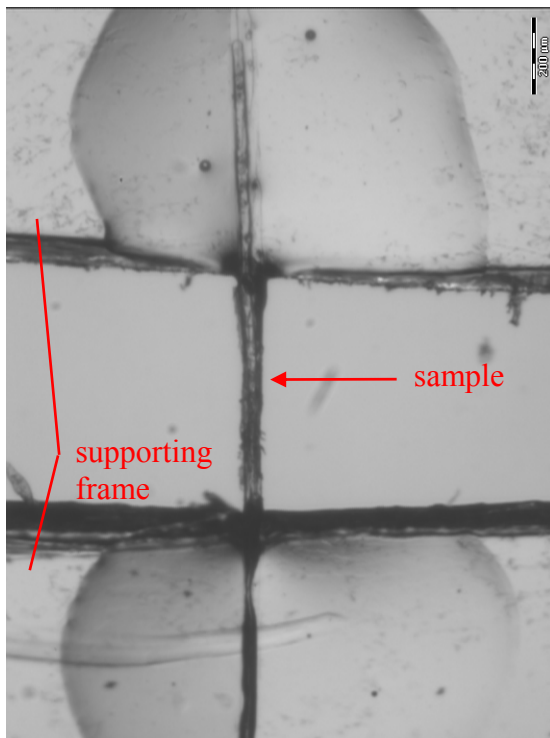


Figure 6-20: Single fibre of pine earlywood glued on a supporting frame used for a combined X-ray diffraction and stretching experiment in HUSTEN at ID13 at the ESRF. The bar on the top right side measures $200\ \mu\text{m}$. The free length of the sample is about $600\ \mu\text{m}$ and its width measures about $50\ \mu\text{m}$. The photograph has been taken with an optical microscope before the stretching experiment.

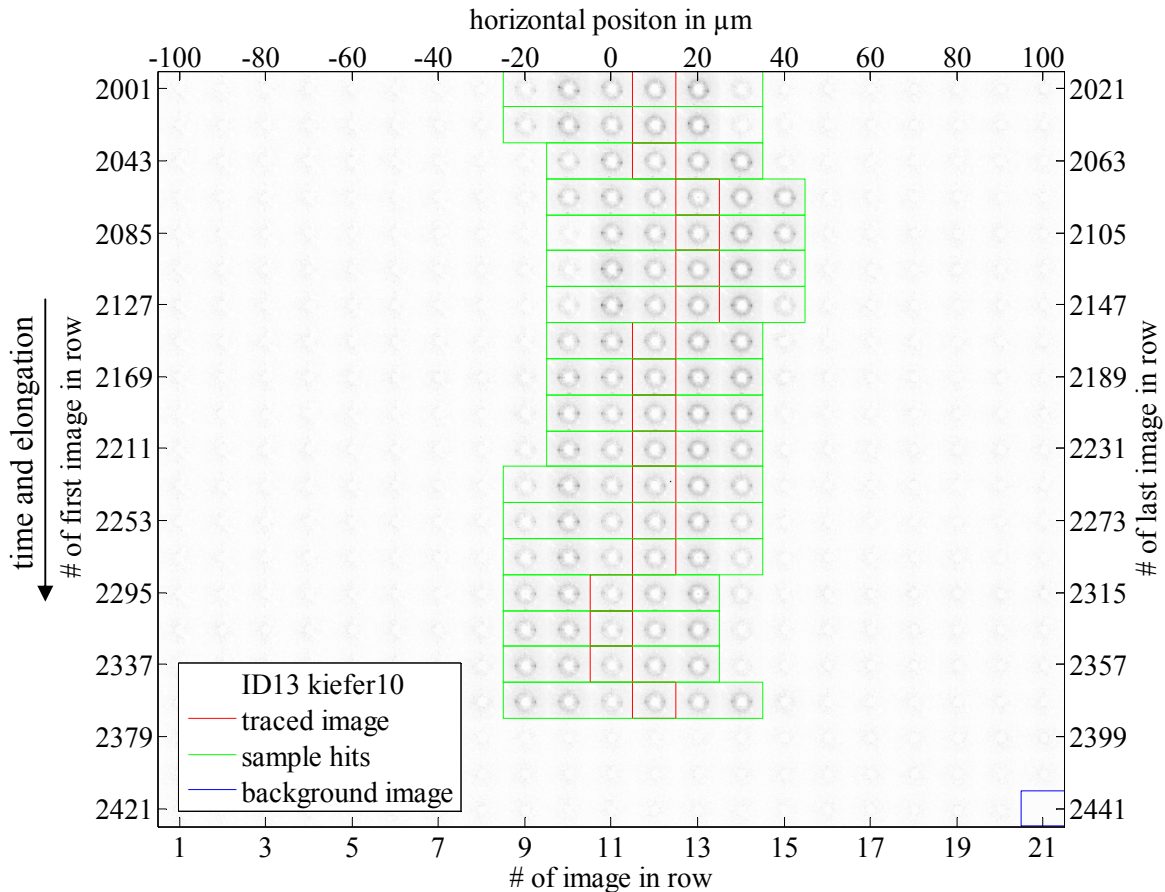


Figure 6-21: Overview on all X-ray images collected during a combined diffraction and stretching experiment with a single fibre of pine earlywood in HUSTEN at ID13 at the ESRF. The sample has been moved horizontally by $10\ \mu\text{m}$ with respect to the X-ray beam of $5\ \mu\text{m} \times 5\ \mu\text{m}$ size between each two images of any shown row. The images have been taken every two seconds for one second. The sample has been stretched continuously mechanically with HUSTEN. The images containing diffraction patterns from the sample are encased in green, corresponding to the sample width of about $50\ \mu\text{m}$ (compare Figure 6-20). The middle images, bordered with red lines, have been used for the further analysis. The raw images are given in this overview, only corrected for background, taken from the last image, marked blue. The last three rows do not contain any sample information due to fracture of the fibre. The experiment has been started with image number 2001 for technical reasons only.

The procedure described above has been chosen, because former investigations on single fibres, for example in the context of (Kölln 2004), have revealed considerable lateral movements of the sample during the tensile tests. However, the stretching device HUSTEN has hold the sample in its initial position during the full experiment until rupture with an accuracy of at least $\pm 10\ \mu\text{m}$, as visible from Figure 6-21.

Unfortunately, the force-elongation curves collected during the combined experiments had been containing some artefacts, as described in section 5.1.4. Nevertheless, general tendencies can still be identified.

The map of diffraction patterns given in Figure 6-21 has been produced after subtraction of the last image taken (blue) in order to estimate the background. The images that contain diffraction patterns from wood are marked with green boxes in Figure 6-21. The central image, marked with a red box, has been taken for the further analysis of the diffraction patterns. The averaged diffraction pattern accumulated over all the traced centre images is given in Figure 6-22. For further data reduction the procedure explained in section 5.1.6 has been used. The analysis has been concentrated on the regions-of-interest (ROI) shown in Figure 6-23. The exact values for the limits of the ROIs are given in Table 6-4.

The results obtained from the diffraction patterns are shown in combination with the force-elongation curve (black) in Figure 6-24 and Figure 6-25. In Figure 6-24 the azimuthal position of the 200 diffraction reflection is shown, as obtained from the right (blue) and left (green) ROIs. The ‘starting region’ of the sample with huge changes in the azimuthal position is visible up to an elongation about 30 μm . These changes correspond to the small lateral movements of the sample evident from Figure 6-21. Up to 30 μm elongation the rotation of the 200 reflections are not accompanied by changes in the lattice spacing obtained from the 004 diffraction reflection, as shown in Figure 6-25. The azimuthal position of the 200 reflection turns slightly back between 30 μm and 38 μm elongation (Figure 6-24). The change in slope of the force-elongation curve at about 38 μm is followed by a rapid change in the azimuthal position of the 200 reflection in the strain-hardening region until rupture at about 49 μm elongation.

The lattice spacing of the cellulose crystals along their *c*-axis obtained from the 004 diffraction reflections increases continuously in the region from 30 μm elongation until rupture at about 48 μm . The slope of this increase in lattice spacing changes slightly at about 38 μm to higher values.

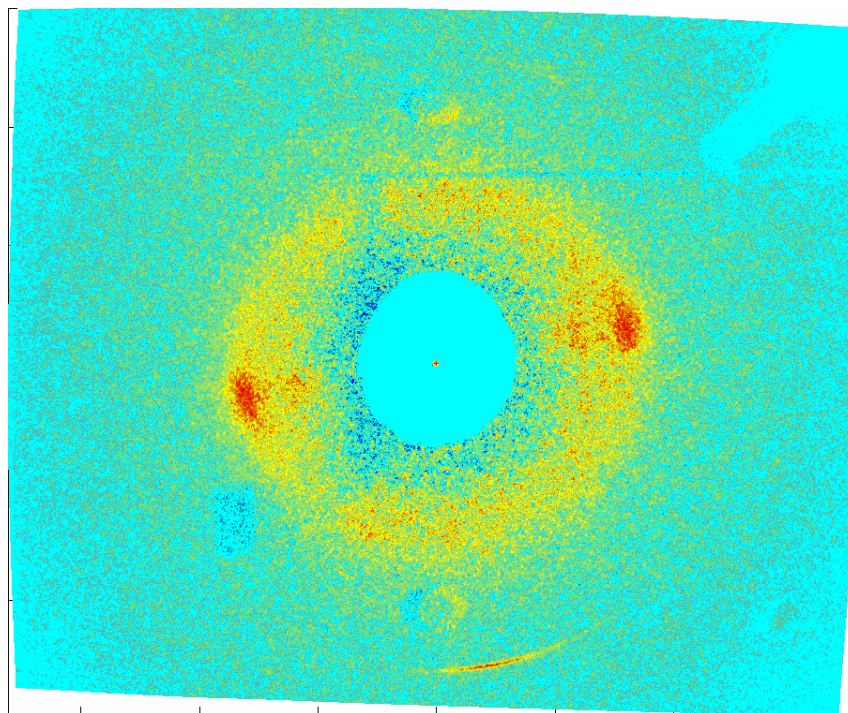


Figure 6-22: Diffraction pattern of a single fibre of pine earlywood collected at ID13 at the ESRF. The image shown here is the summation of all 18 traced images marked with a red box in Figure 6-21, each collected for one second leading to a total accumulation time of 18 seconds.

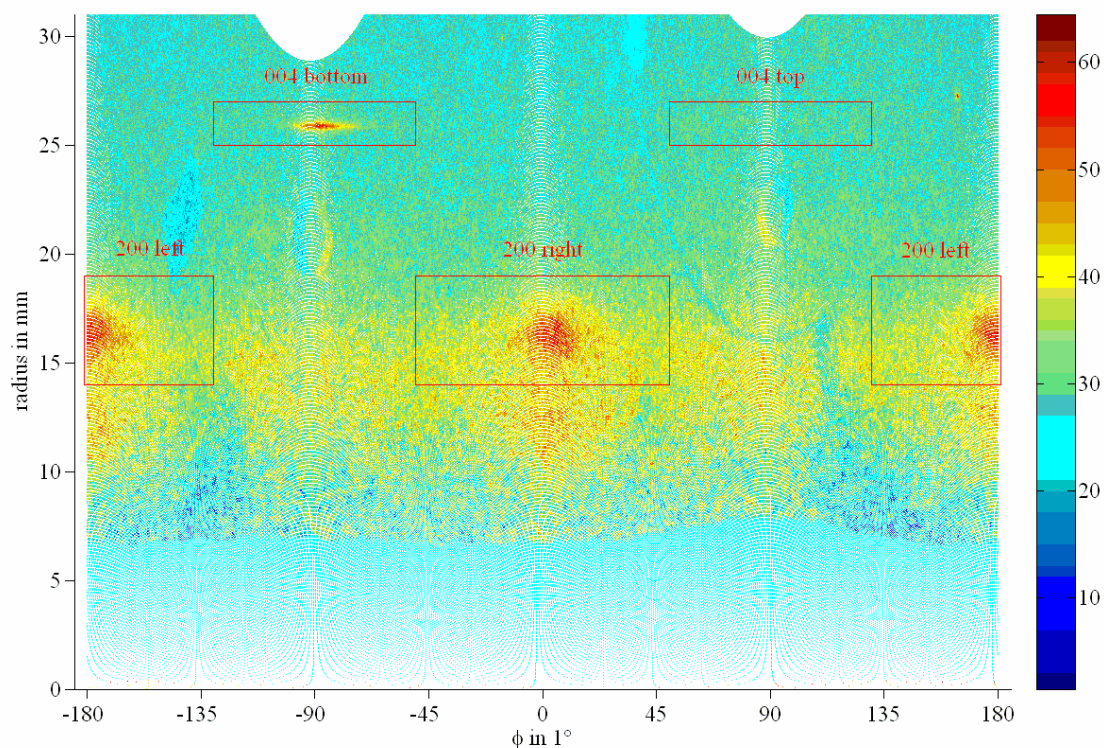


Figure 6-23: Diffraction pattern of a single fibre of pine earlywood shown in polar coordinates collected at ID13 at the ESRF. The red boxes give the regions-of-interest for the further peak analysis. The labels of the regions are given in red. The intensity is shown colour-coded and taken from Figure 6-22. The two regions '200 left' have been combined in the analysis.

label	r_{min} in mm	r_{max} in mm	φ_{start}	φ_{end}
200 right	14.0	19.0	-50°	50°
200 left	14.0	19.0	-50°	50°
004 top	25.0	27.0	50°	130°
004 bottom	25.0	27.0	-50°	-130°

Table 6-4: Parameters of the regions-of-interest for the analysis of the diffraction patterns of the single fibres of pine earlywood investigated at ID13 at the ESRF.

In summary the results presented for the measurements on a single tracheid of pine earlywood are as follows:

- The stretching device HUSTEN allows for combined stretching and X-ray diffraction experiments on single fibres without limiting damage of the sample during the preparation of the experiment and with precise alignment of the sample during the tensile test (better than $\pm 10 \mu\text{m}$).
- The force-elongation curve of the single fibre of pine wood shows strain-hardening behaviour.
- The cellulose crystals react to the external load with elongation along their c -axis, with greater elongation in the strain-hardening region.
- The cellulose crystals react to the external load with different tilt behaviour before and after the onset of strain-hardening.

Clearly, the time resolution reached in this experiment can be further improved, due to the demonstrated precision of the mechanical parts of HUSTEN, allowing for a sharper identification of the different regions found. However, the findings presented above allow for some speculations about the composite nature of the material, as given in the conclusion, and are consistent with the model proposed in (Navi 1997) and explained in section 3.1.2.

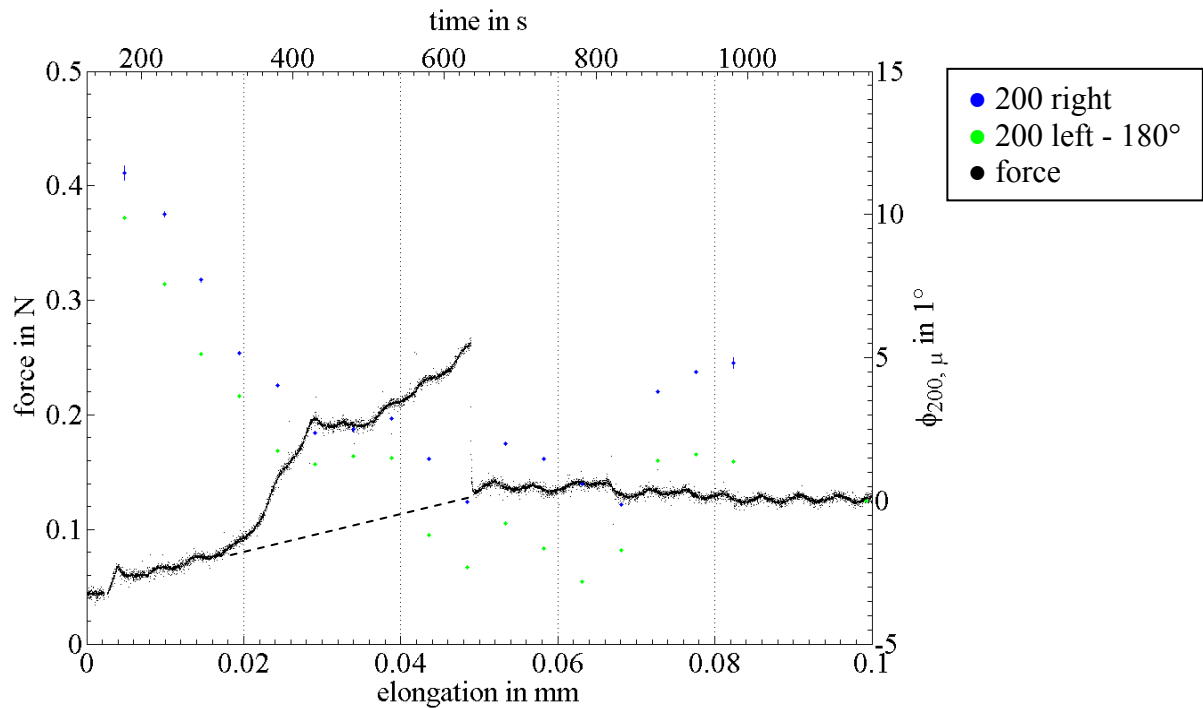


Figure 6-24: Force and azimuthal position of the 200 diffraction reflection collected during a combined X-ray diffraction and tensile stretching experiment with a **single fibre** of pine earlywood in HUSTEN at ID13 at the ESRF. The force is given in black. The small oscillations and the small peak at the beginning are due to a mechanical artefact of the stretching device as explained in section 5.1.4. The position of the 200 reflection taken from the right (left) region in the diffraction patterns is shown in blue (green).

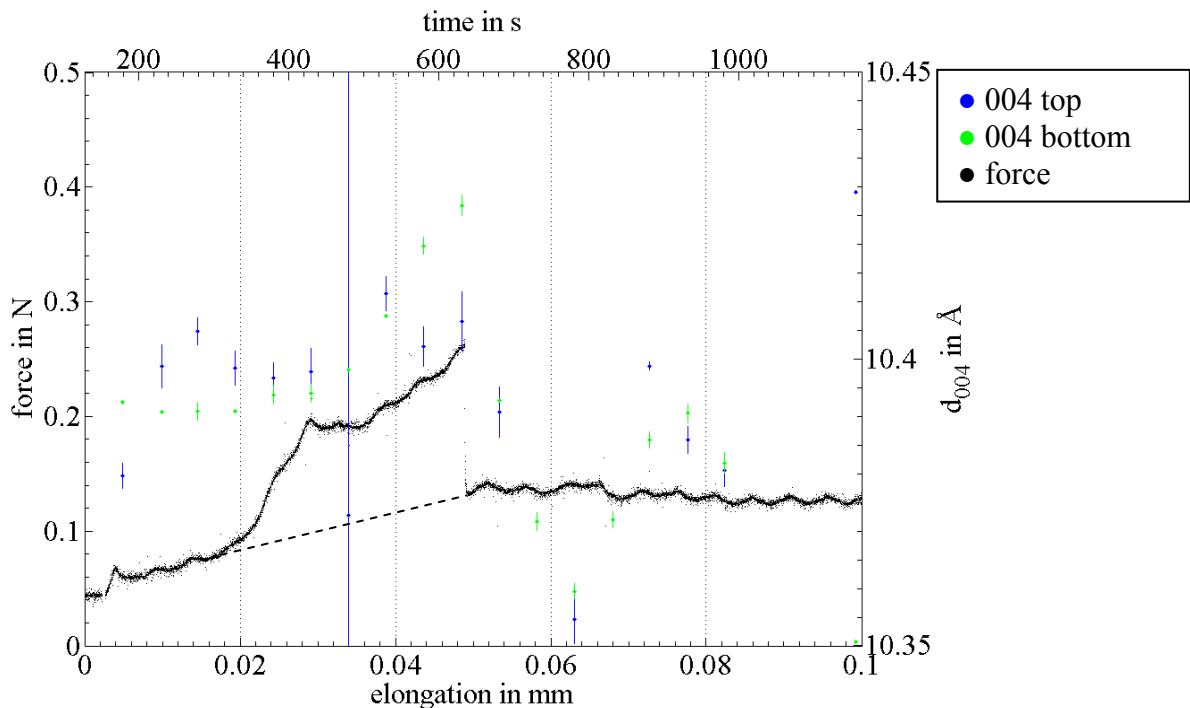


Figure 6-25: Force and lattice spacing obtained from the 004 diffraction reflection collected during a combined X-ray diffraction and tensile stretching experiment with a **single fibre** of pine earlywood in HUSTEN at ID13 at the ESRF. The force is given in black. The small oscillations and the small peak at the beginning are due to a mechanical artefact of the stretching device as explained in section 5.1.4. The lattice spacing obtained from the 004 reflection taken from the top (bottom) region in the diffraction patterns is shown in blue (green).

6.2 Inelastic Neutron Scattering Experiments

In models for water adsorption to cellulose, the water molecules are thought to be inserted between individual hydrogen bonded cellulose chains. Due to the anisotropic structure of the cellulose crystals the dynamics of such inserted water molecules may show a similar anisotropy. An investigation of oriented cellulose fibres with inelastic neutron scattering has been performed to clarify this point.

6.2.1 Measurement Schedule

The model system used has been a bundle of flax fibres, as shown in Figure 6-26. Its moisture content has been controlled, as explained in section 5.3. The inelastic neutron scattering experiment has been carried out with the setup described in section 5.2, also the data reduction process is explained in full detail in that section.

The orientation and moisture content of the sample have been set during the experiment following the schedule given in Table 6-5. The sample has been used in two

different orientations. In one case it has been mounted in a way that the fibres have been aligned horizontally, i.e. the fibres have been lying in the scattering plane defined by the middle detector bank of the instrument. In the other case the fibres have been aligned vertically, i.e. with the fibre axis perpendicular to the scattering plane.

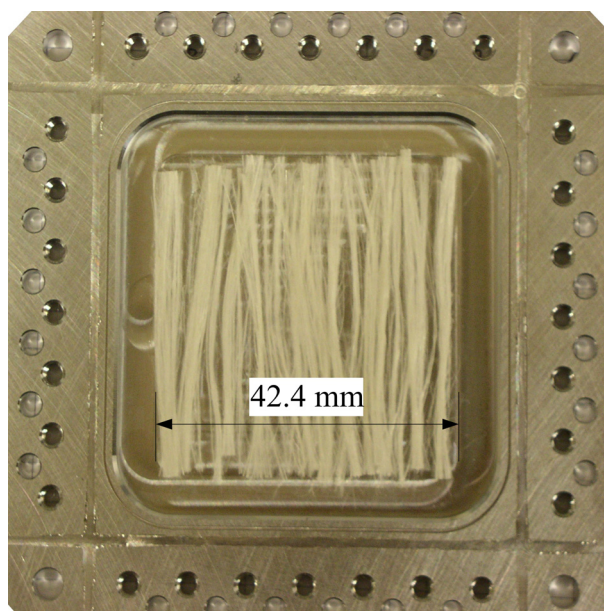


Figure 6-26: Bundle of flax fibres in the open sample container used in an inelastic neutron scattering experiment performed at 'FOCUS'. Photo has been taken after the measurements.

The weight of the sealed sample container has been checked with a balance before and after every step of the measurement schedule showing no differences in weight, indicating a proper sealing of the container. The temperature of the sample has been controlled with a closed loop controller with an accuracy of ± 4 K heating the sample chamber against a closed cycle helium cryostat.

Weight ± 0.5 mg	Removable water content	Orientation	Temperature ± 4 K	Label
79.5 mg	10.3 mg ± 1 mg 14.9 % ± 1 %	vertical	300 K	wet vertical 300 K
			180 K	wet vertical 180 K
		horizontal	300 K	wet horizontal 300 K
			180 K	wet horizontal 300 K
69.2 mg	0.0 mg ± 1 mg 0.0 % ± 1 %	vertical	300 K	dry vertical 300 K
			180 K	dry vertical 180 K
		horizontal	300 K	dry horizontal 300 K
			180 K	dry horizontal 180 K
78.9 mg	9.7 mg ± 1 mg 14.0 % ± 1 %	vertical	300 K	room vertical 300 K
			255 K	room vertical 255 K
			180 K	room vertical 180 K
69.2 mg	0.0 mg ± 1 mg 0.0 % ± 1 %	vertical	300 K	redry vertical 300 K
			255 K	redry vertical 255 K

Table 6-5: Schedule of the inelastic neutron measurements performed in the given order with a bundle of flax fibres.

6.2.2 Neutron Diffraction Patterns

The diffraction patterns collected during the experiments reveal a good alignment of the fibre bundle and the cellulose crystals therein. The widths of the Bragg reflections are comparable to those found with X-ray diffraction at the same sample afterwards. The diffraction pattern of the dry flax bundle at 180 K is shown in Figure 6-27 and in Figure 6-28 for 300 K. The corresponding patterns of the wet sample are given in Figure 6-29 and Figure 6-30, respectively. The shapes of the 200 and 004 reflections are clearly visible in all cases. No significant change in the width of the orientation distribution is visible throughout the four figures. A fit of a Gaussian profile (red curve) to the azimuthal distribution of the 200 reflection shows in all cases a full width at half maximum (FWHM) of about 22° and the orientation misalignment between wet and dry sample has been no more than 2° as visible from the centre position of the Gaussian profile at ϕ_μ .

Fits of a Gaussian distribution with linear background to the 200 and 004 reflection peaks in the diffraction patterns lead to the values given in Table 6-6. An example of these fits is given in Figure 6-31. There is no significant change in the width or the intensity of the peaks visible, indicating that in all cases the amount of illuminated cellulose crystals has been the same and that the size of the crystals did not vary significantly with temperature or humidity.

There is no significant shift visible for the position of the 004 reflection, even though the Bragg condition for this reflection has been fulfilled nearly due to the tilt of the fibre axis with respect to the incident neutron beam of about 45° compared to the exact Bragg angle²⁴ of about 50° (compare section 5.2.3 and Figure 5-49). Hence, any major changes in the corresponding lattice constant due to thermal expansion should have been visible with this setup. Nevertheless, this finding is consistent with the behaviour of cellulose crystals in wood reported in (Hori and Wada 2005) and (Müller et al. 2006).

²⁴ The Bragg angle of the 004 reflection for incident neutrons of wave lengths λ_0 is given by $4\lambda_0 = 2|\vec{c}|\sin\theta$. With the relevant values for this experiment this leads to an angle $\theta = \arcsin(4 \cdot 4\text{\AA}/2 \cdot 10.4\text{\AA}) = 50.3^\circ$.

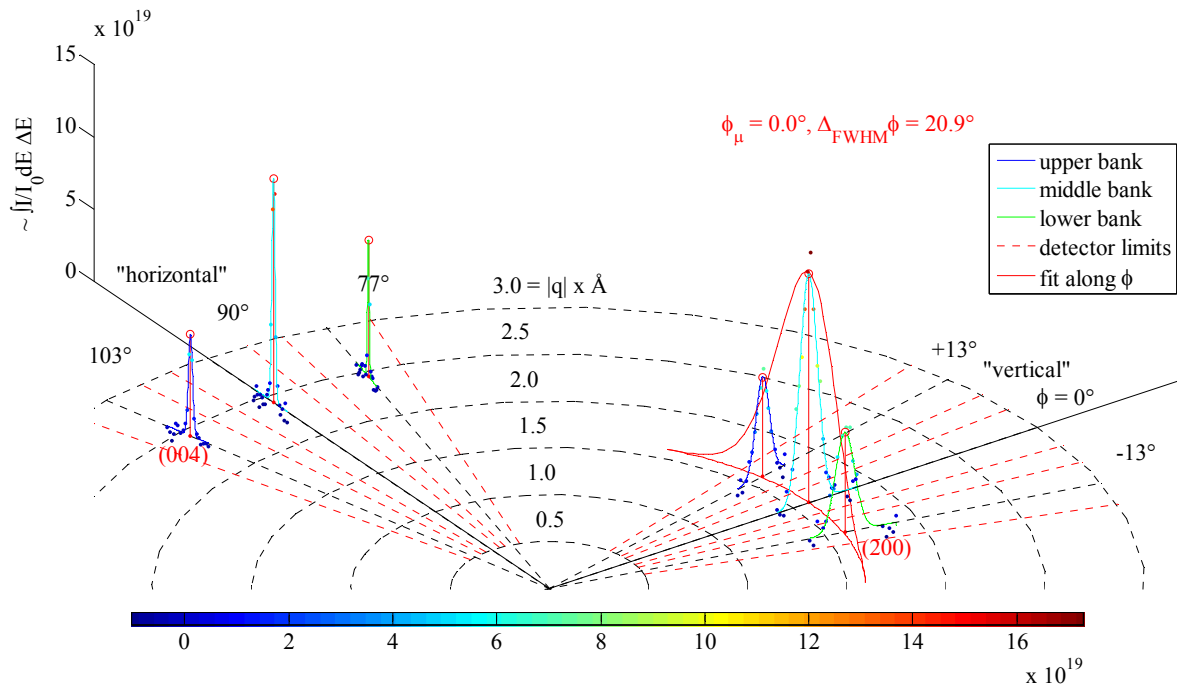


Figure 6-27: Diffraction pattern of the dry flax bundle at 180 K composed from the neutron scattering measurements of the horizontally and vertically aligned sample.

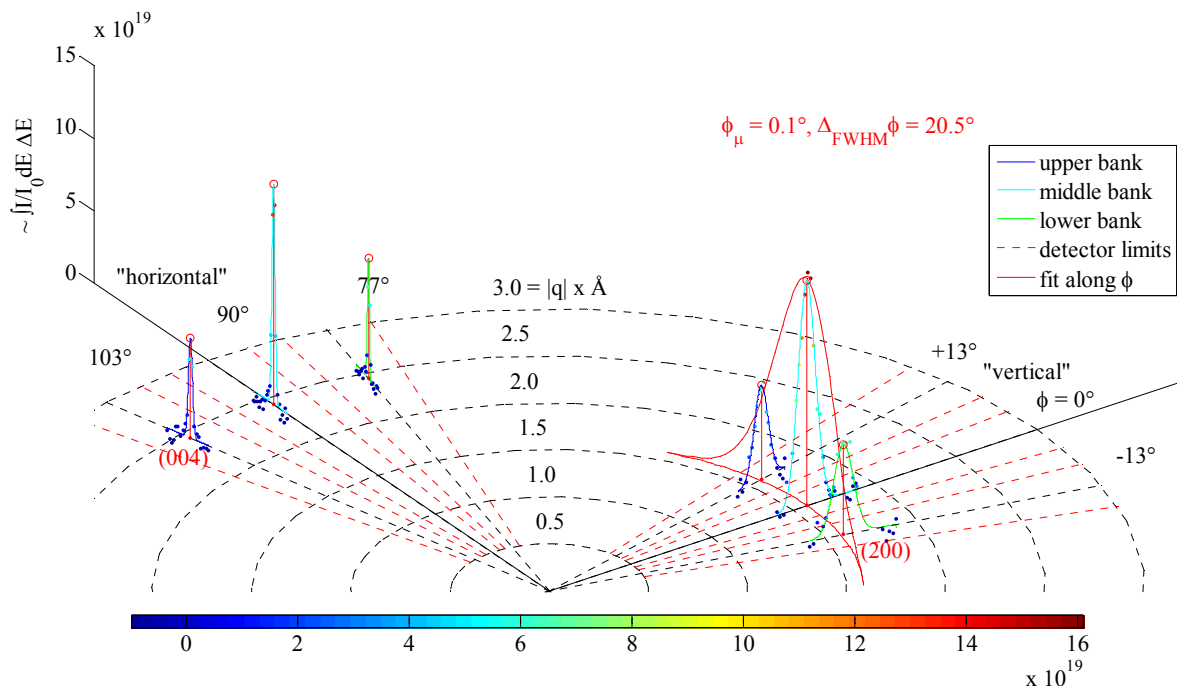


Figure 6-28: Diffraction pattern of the dry flax bundle at 300 K composed from the neutron scattering measurements of the horizontally and vertically aligned sample.

In Figure 6-27 and Figure 6-28 the scattered points show the measured intensities colour-coded. The full lines represent the results of the fits to those points. The dashed red lines highlight the angular limits of the detectors used. The results of a Gaussian fit along the azimuth are shown in red. Details are given in the text.

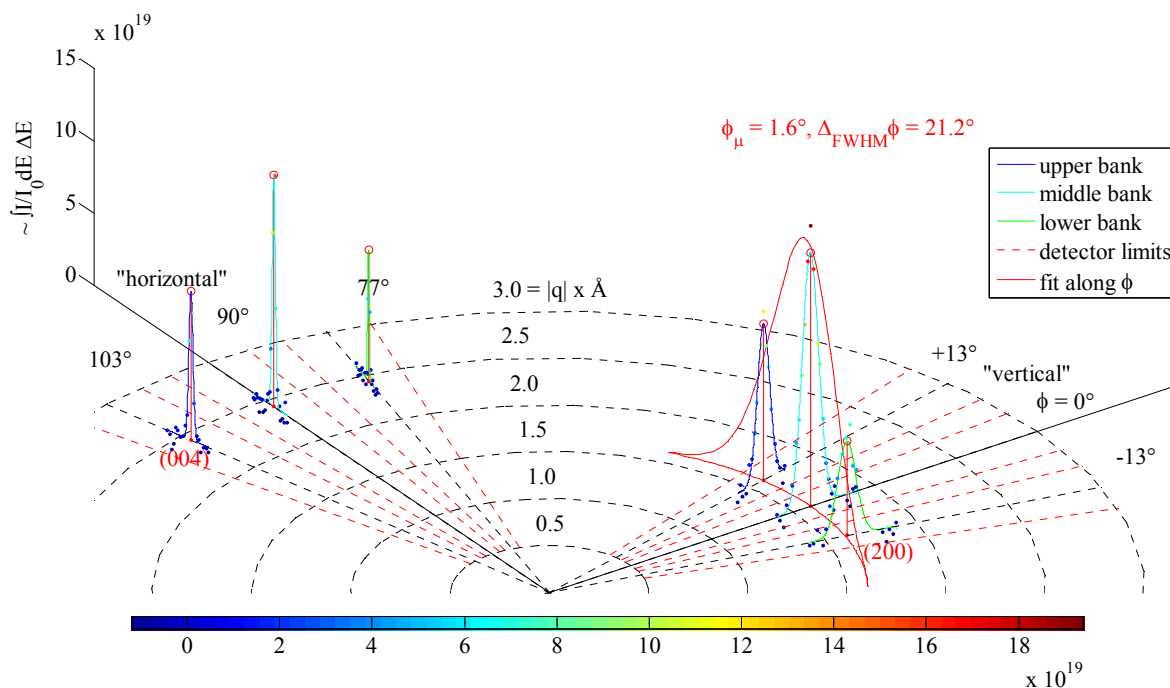


Figure 6-29: Diffraction pattern of the wet flax bundle at 180 K composed from the neutron scattering measurements of the horizontally and vertically aligned sample.

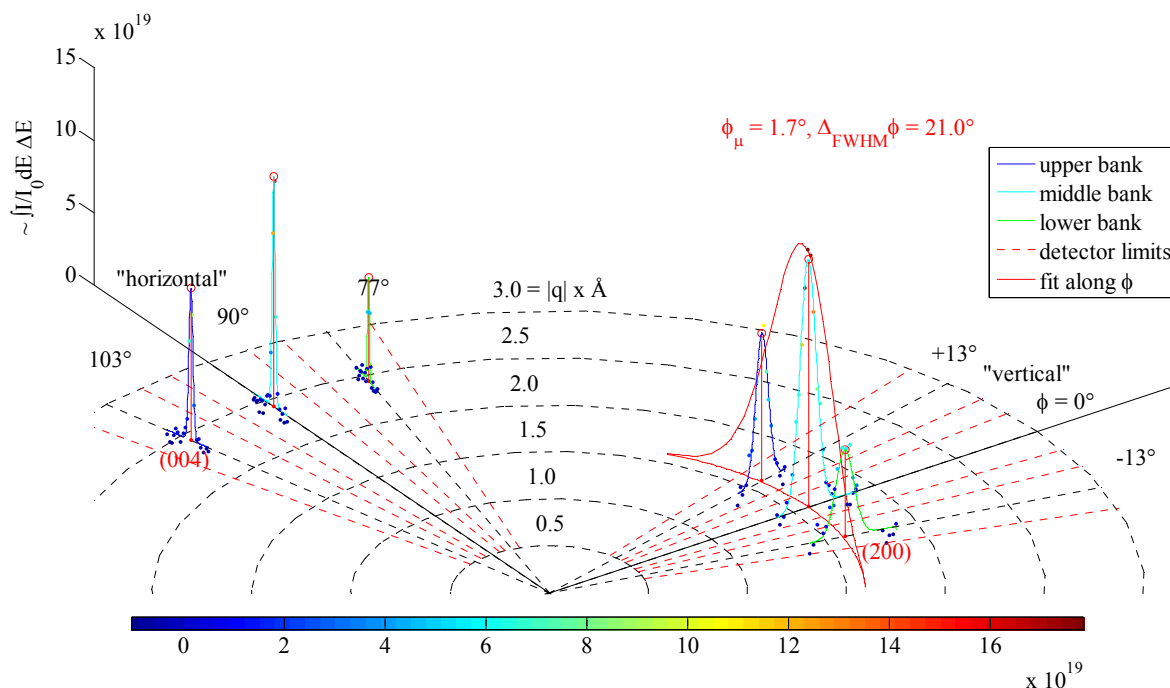


Figure 6-30: Diffraction pattern of the wet flax bundle at 300 K composed from the neutron scattering measurements of the horizontally and vertically aligned sample.

In Figure 6-29 and Figure 6-30 the data points show the measured intensities colour-coded. The full lines represent the results of the fits to those points. The dashed red lines highlight the angular limits of the detectors used. The results of a Gaussian fit along the azimuth are shown in red. Details are given in the text.

Orientation	Reflection	Water content in % ± 1 %	Temperature in K ± 4 K	Peak Intensity in arbitrary units	Peak Position $ q $ in $1/\text{\AA}$	Unit cell lattice spacing ²⁵ in \AA	Peak full width at half maximum (FWHM) in $1/\text{\AA}$
vertical	200	14.9	300	21.1 \pm 0.8	1.592 \pm 0.001	7.893 \pm 0.005	0.058 \pm 0.002
			180	21.9 \pm 0.9	1.605 \pm 0.001	7.830 \pm 0.005	0.058 \pm 0.002
	0.0	300	20.6 \pm 0.8	1.583 \pm 0.001	7.938 \pm 0.005	0.062 \pm 0.002	
		180	21.3 \pm 0.9	1.594 \pm 0.001	7.884 \pm 0.005	0.063 \pm 0.002	
horizontal	004	14.9	300	5.5 \pm 0.2	2.4181 \pm 0.0005	10.394 \pm 0.002	0.016 \pm 0.001
			180	5.7 \pm 0.3	2.4178 \pm 0.0005	10.395 \pm 0.002	0.017 \pm 0.001
	0.0	300	5.4 \pm 0.2	2.4207 \pm 0.0005	10.382 \pm 0.002	0.017 \pm 0.001	
		180	5.6 \pm 0.2	2.4209 \pm 0.0005	10.382 \pm 0.002	0.017 \pm 0.001	

Table 6-6: Results of a Gaussian fit to the neutron diffraction patterns of a flax bundle measured with the middle detector bank of the time-of-flight instrument 'FOCUS'.

The position of the 200 reflection shifts with increasing temperature to smaller values indicating a thermal elongation of the cellulose crystals in the dry and wet sample. This is illustrated in Figure 6-32 and Figure 6-33. The achieved precision of the lattice spacing a at the temperatures $T_1 = 180$ K and $T_2 = 300$ K in this experiment permits the calculation of the linear thermal expansion coefficient $\alpha_{thermal}$ as follows (Hori and Wada 2005)^{eq. (1)}:

$$\alpha_{thermal} = \frac{1}{a(T_1)} \frac{a(T_2) - a(T_1)}{T_2 - T_1}. \quad (6.1)$$

The corresponding uncertainty $\Delta\alpha_{thermal}$ of the thermal expansion factor can be estimated as follows:

$$\Delta\alpha_{thermal} = \alpha_{thermal} \left(\frac{\Delta T_1}{T_1} + \frac{\Delta T_2}{T_2} \right) + \frac{\Delta a(T_2) + \frac{a(T_2)}{a(T_1)} \Delta a(T_1)}{(T_2 - T_1) a(T_1)}. \quad (6.2)$$

²⁵ This spacing has been calculated from the given peak positions for the 200 reflection with $|\vec{a}| = 2 \cdot 2\pi/|\vec{q}|$ and for the 004 reflection with $|\vec{c}| = 4 \cdot 2\pi/|\vec{q}|$. The uncertainty has been estimated via $\Delta|\vec{a}| = |\vec{a}| \cdot \Delta|\vec{q}|/|\vec{q}|$.

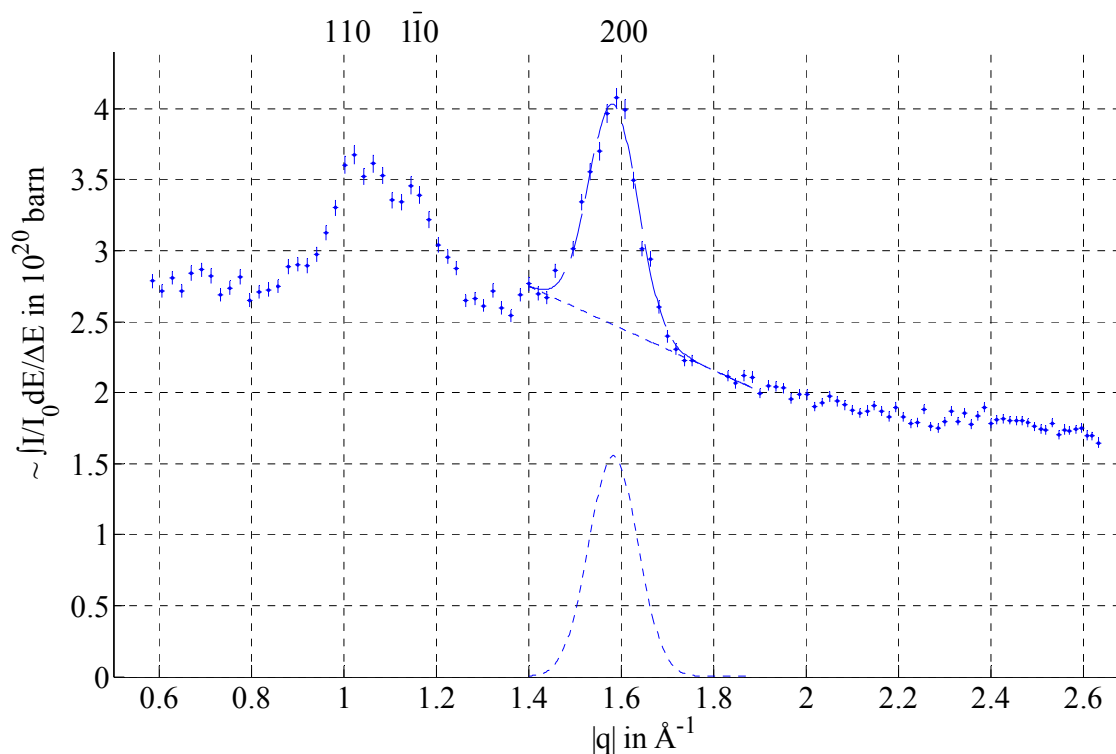


Figure 6-31: Energy integrated intensity versus wave vector transfer from a diffraction pattern of the 200 cellulose reflection collected during an inelastic neutron scattering experiment with a bundle of wet flax fibres. The dashed lines show the result of a Gaussian fit with linear background. The dashed curve at the bottom represents the Gaussian part of the fitted curve.

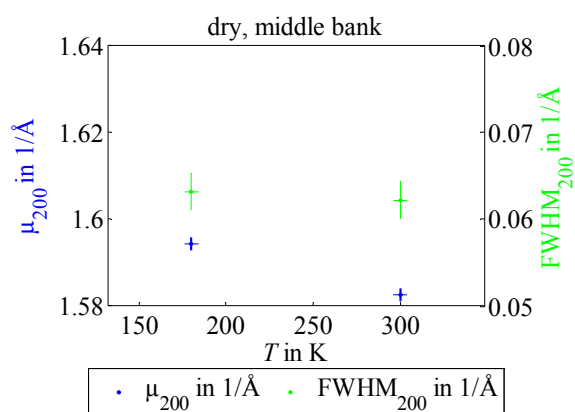


Figure 6-32: Temperature dependence of the position μ (left axis, blue) and width FWHM (right axis, green) of the 200 diffraction reflection of a dry flax bundle

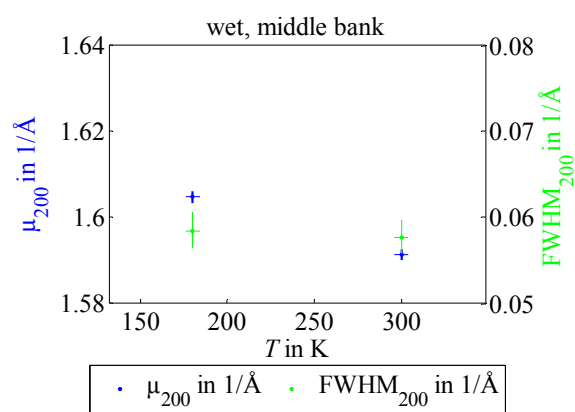


Figure 6-33: Temperature dependence of the position μ (left axis, blue) and width FWHM (right axis, green) of the 200 diffraction reflection of a wet flax bundle

The numbers given in Table 6-6 in combination with eq. (6.1) and (6.2) lead to a value of $\alpha_{thermal, dry} = (5.8 \pm 1.3) \cdot 10^{-5} \text{ K}^{-1}$ for the dry sample and of $\alpha_{thermal, wet} = (6.8 \pm 1.3) \cdot 10^{-5} \text{ K}^{-1}$ for the wet sample. These results are smaller but of the same order of magnitude as the value of $13.6 \cdot 10^{-5} \text{ K}^{-1}$ reported in (Hori and Wada 2005) for the thermal expansion coefficients of cellulose crystals in wood, where the value has been determined for the temperature range between about 290 K and 450 K. A smaller value of $9.9 \cdot 10^{-5} \text{ K}^{-1}$ for the temperature range between 200 K and 295 K for cellulose crystals in wood can be found in (Müller et al. 2006). Interestingly, a value of $(7 \dots 8) \cdot 10^{-5} \text{ K}^{-1}$ is reported in (Seitsonen and Mikkonen 1973) for cellulose crystals in cotton for the range from 122 K to 273 K, which agrees with the measurements presented here for the crystals in flax with a water content of about 15 wt% between 180 K and 300 K. The value for the dry sample given above is close to that of $4.6 \cdot 10^{-5} \text{ K}^{-1}$ reported in (Langan et al. 2005) for the range between 100 K and 273 K for crystals in tunicate cellulose.

Recapitulatory, the thermal expansion of the cellulose crystals in flax fibres is highly anisotropic. This corresponds to the anisotropic molecular bonding in the crystals. An extensive discussion of this topic can be found in (Müller et al. 2006).

The influence of the water content on the positions of the reflections at constant temperature is shown in Figure 6-34 and Figure 6-36 for the 004 reflection and in Figure 6-35 and Figure 6-37 for the 200. There is a significant decrease visible of the position of the 004 reflection and a clear increase of the position of the 200 reflection with increasing moisture content. This shows changes in the corresponding lattice constants. Specifically, an increase of the lattice spacing in the direction of the chains of the cellulose molecules of about 1.2 % independent of temperature is found if the moisture content is increased by about 15 % of the dry sample weight. Additionally, there is a decrease in the direction perpendicular to the chains of about 5.7 % at 300 K and 6.9 % at 180 K. From these findings it is clear that the influence of the water content on the lattice spacing perpendicular to the molecular chains in the cellulose crystals is lower at higher temperatures, where the lattice spacing is enlarged due

to thermal expansion. Additionally, the changes in the lattice spacing give a hint on the pressure applied to the crystals perpendicularly to the chains, due to the swelling of the matrix caused by the water. Therefore, such a swelling pressure is also present in the matrix, and hence, sensed by the water molecules.

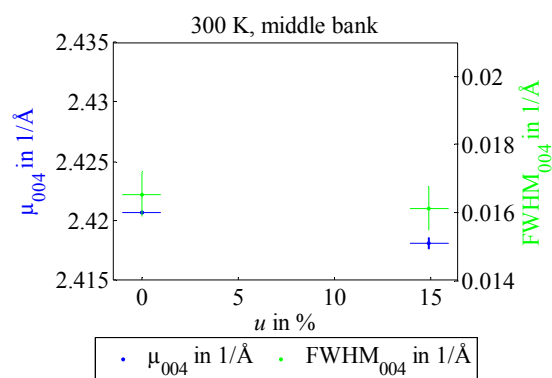


Figure 6-34: Position μ (left axis, blue) and width FWHM (right axis, green) of the 004 diffraction reflection of a flax bundle at 300 K with different moisture contents u .

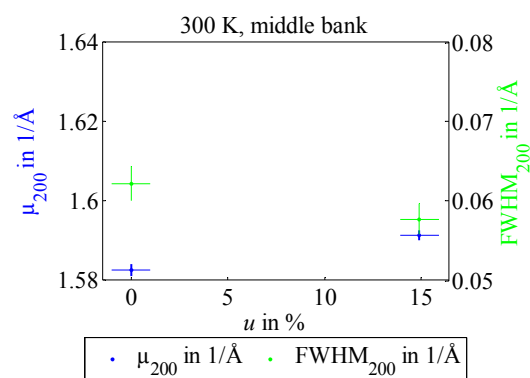


Figure 6-35: Position μ (left axis, blue) and width FWHM (right axis, green) of the 200 diffraction reflection of a flax bundle at 300 K with different moisture contents u .

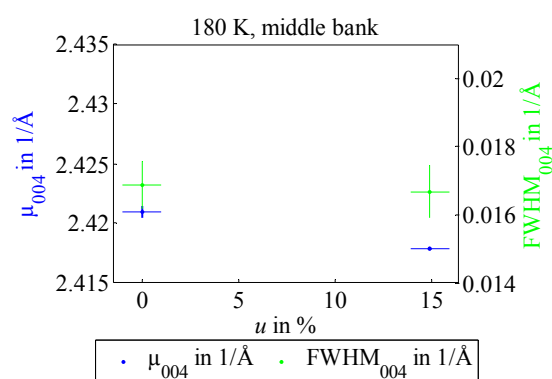


Figure 6-36: Position μ (left axis, blue) and width FWHM (right axis, green) of the 004 diffraction reflection of a flax bundle at 180 K with different moisture contents u .

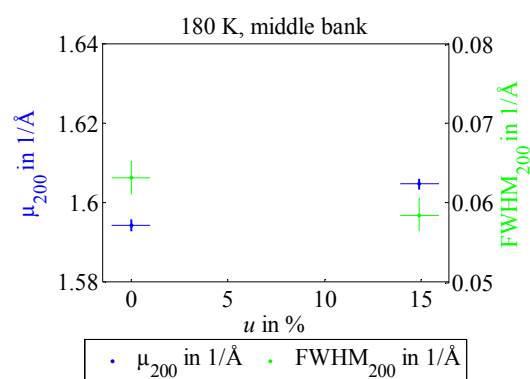


Figure 6-37: Position μ (left axis, blue) and width FWHM (right axis, green) of the 200 diffraction reflection of a flax bundle at 180 K with different moisture contents u .

No formation of ice is visible in any of the diffraction diagrams collected, even at 180 K for the wet sample. This is clear evidence that no free water has been in the sample, i.e. any water present in the container has been adsorbed and remained adsorbed during the experiment. Furthermore, in none of the diffraction diagrams a contribution is visible that corre-

sponds to the structure factor found for non-crystalline heavy water in amorphous cellulose, as reported in (Czihak et al. 2000a)^{fig. 1.}, (Czihak 2000)^{Figure 4.7} or (Czihak et al. 2000b)^{Figure 1.}, where a broad bump in the structure factor at $|\vec{q}| = 2 \text{ \AA}^{-1}$ is visible.

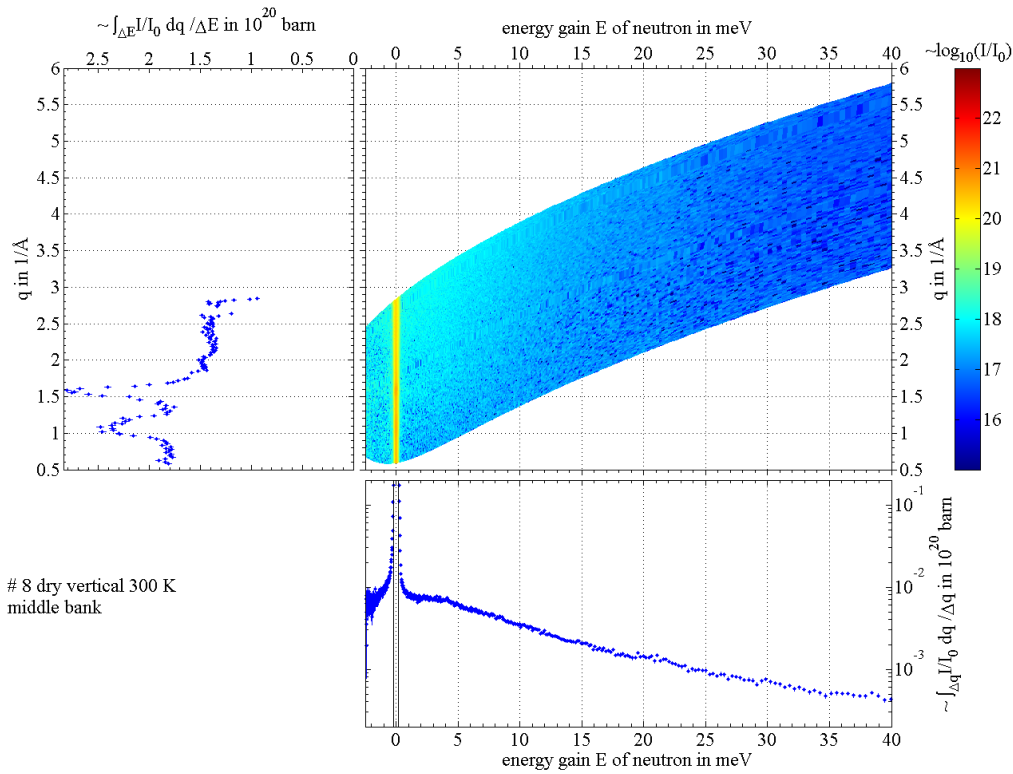


Figure 6-38: Intensity distribution measured with inelastic neutron scattering on a dry flax bundle oriented vertically to the scattering plane. The upper right graph shows on a logarithmic scale the normalised intensities depending on energy transfer and wave vector transfer. The left graph gives the intensity versus wave vector transfer. The blue points show the intensities integrated over the region marked with the black lines in the bottom graph. The bottom graph displays the intensities integrated over the full accessible range of wave vector transfers. All integrated values are scaled with the corresponding integration intervals.

6.2.3 Neutron Spectroscopy on Wet and Dry Flax

The results of the inelastic neutron scattering experiment performed with a bundle of dry flax fibres at 300 K are shown in Figure 6-38 as an example. In that figure, the intensity of the scattered neutrons is plotted versus energy gain of the neutrons and wave vector transfer on a logarithmic scale with a colour code in the upper right graph. The intensity integrated over the elastic line is shown in blue on the left side of Figure 6-38 versus wave vector transfer, i.e. for scattering events with no more than ± 0.2 meV energy transfer to or from the neutron. This integration range is marked with a black box in the two graphs on the right side of the figure. In the lower right graph of Figure 6-38 the intensity is shown after integration over all measured wave vector transfers. Both integrated intensities are displayed after scaling to the width of the corresponding integration intervals taking the varying regions into account that are accessible with the instrument used. The blue intensity distribution shown on the left side of Figure 6-38 has been used as intensity along the $\phi = 0^\circ$ line in the diffraction pattern shown in Figure 6-28.

The spectroscopic data are shown in Figure 6-39 for different orientations and two temperatures of the wet sample. The same is done in Figure 6-40 for the dry sample. The integrated intensity is shown in these figures versus the time-of-flight to make the comparison with earlier measurements easier, for example (Müller et al. 2000b)^{Figure 2}. The transformation between the time-of-flight and the energy scale is described in more detail in section 5.2.2.6.

There is a high anisotropy clearly visible in the signal from the dry and the wet sample in the range between 1 and 12 meV, as it can be expected for the anisotropic crystals of cellulose. This effect is known for the disordered regions of dry flax, as reported in (Müller et al. 2000b)^{Figure 4}, where an anisotropy can be seen between about 3 and 30 meV. The signal increases with water content as visible from Figure 6-41, shown for the vertical orientation. Interestingly, this increase with moisture in the spectra in the direction perpendicular to the cellulose crystals is not directly proportional to the water content as can be seen in Figure 6-41.

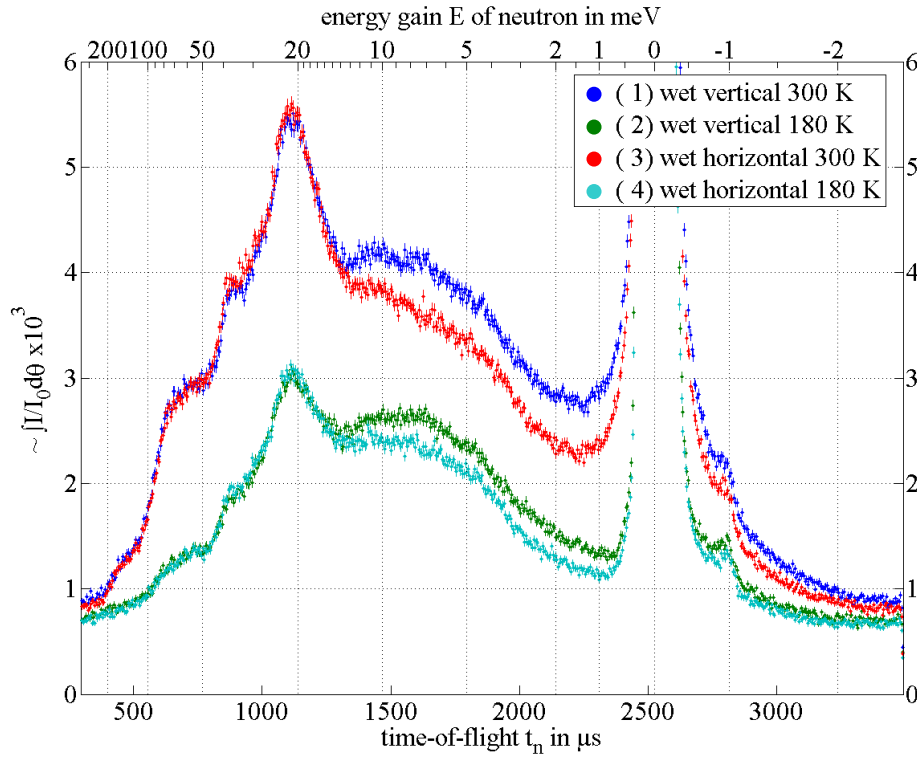


Figure 6-39: Intensity distribution collected in an inelastic neutron scattering experiment with a wet bundle of flax fibres integrated over all scattering angles shown against the time-of-flight of the scattered neutrons.

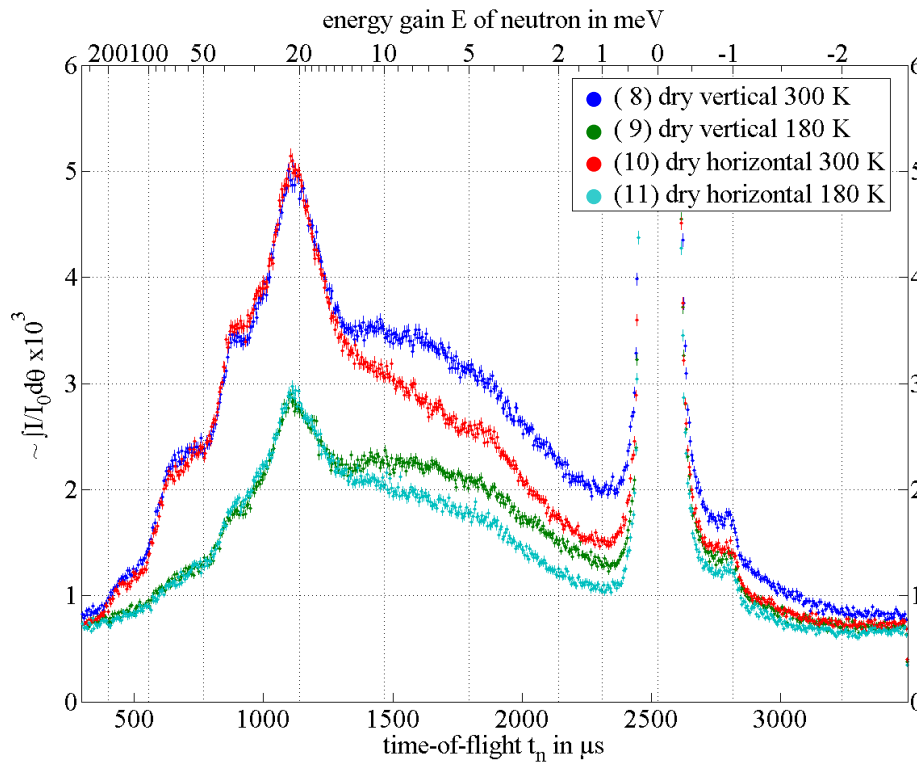


Figure 6-40: Intensity distribution collected in an inelastic neutron scattering experiment with a dry bundle of flax fibres integrated over all scattering angles shown against the time-of-flight of the scattered neutrons.

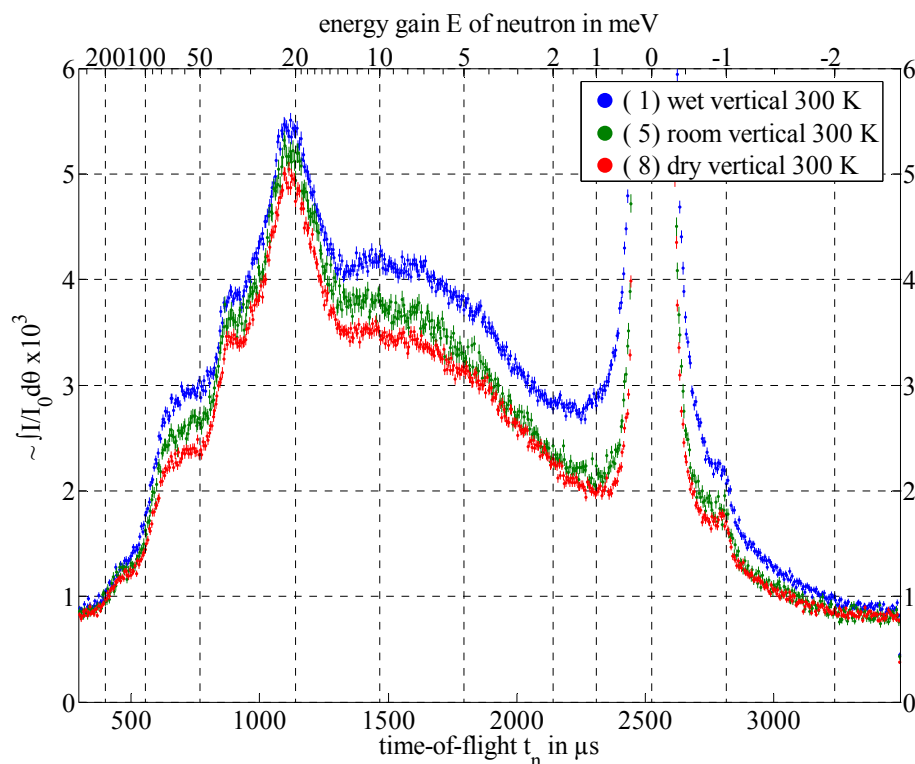


Figure 6-41: Inelastic intensity distribution integrated over all scattering angles collected in an inelastic neutron scattering experiment with a bundle of flax fibres at different moisture contents labelled 'dry', 'room' and 'wet'. Details are given in the text.

The part of the spectroscopic information that has been measured from the dry and wet samples can be easily compared when the corresponding signals are subtracted. This has been performed for both orientations and two temperatures, as shown in Figure 6-42. The signal shown there is that of all three detector banks of the instrument in contrast to all previously shown figures where only the middle bank has been used. (Details to this technical topic are explained in section 5.2.1.) The difference spectra obtained in this way are labelled 'water', even though this signal might not only be due to the dynamics of the adsorbed water but to a combination of the signal produced by the adsorbed water molecules and the changes in the cellulose, as will be discussed in section 6.2.4.

It is evident from Figure 6-42 that the adsorbed water causes a significant anisotropy in the region between 2 and 7 meV, even at 180 K, leading to a higher intensity for the horizontal orientation of the fibres.

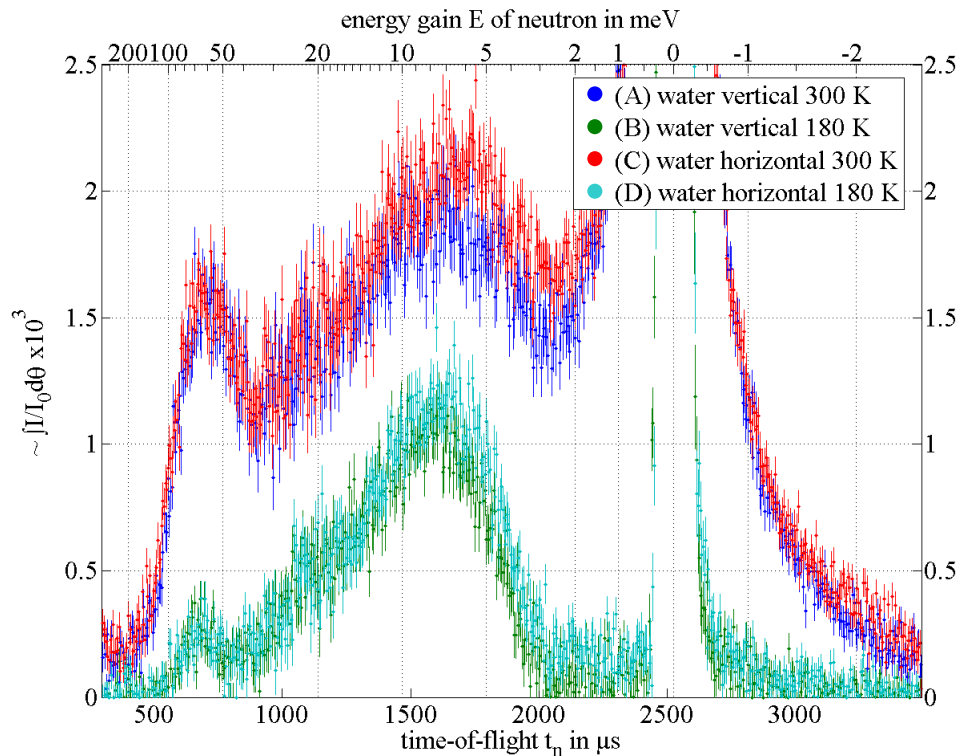


Figure 6-42: Differences of the intensity distributions collected in an inelastic neutron scattering experiment with a dry and a wet bundle of flax fibres integrated over all scattering angles shown against the time-of-flight of the scattered neutrons estimating the influence of the adsorbed water on the dynamics.

No significant change has been observed for both orientations in the quasielastic region ± 1 meV around the elastic line, as visible in Figure 6-42. This energy range is linked to rotational and translational diffusion of water. These motions are ‘equally populated’ in both sample orientations showing isotropic behaviour and indicating the frozen state at 180 K through their absence. A study on this signal for water in amorphous cellulose is given in (Czihak et al. 1999).

The signal from the sample dried again after one full cycle of measurements is compared to that obtained after the first drying in Figure 6-43. It is evident from this measurement that no change in the signal occurs due to the thermal treatment and the wetting process.

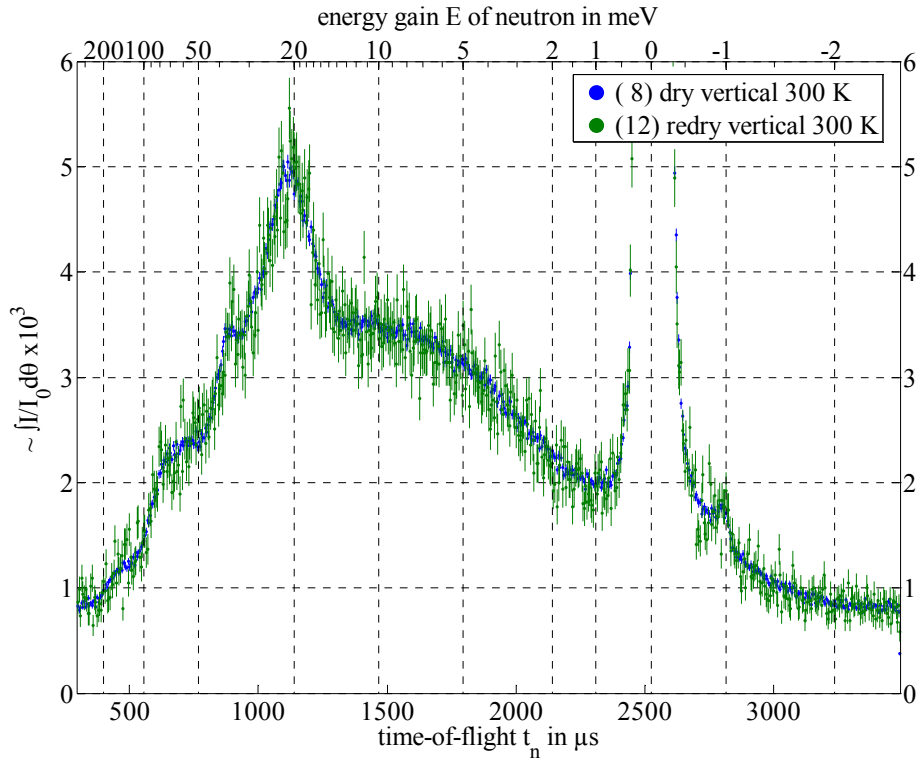


Figure 6-43: Inelastic intensity distribution integrated over all scattering angles collected in an inelastic neutron scattering experiment with a bundle of dry flax fibres shown before and after a wetting and drying cycle.

The complete dispersion graphs of the difference spectra ‘water’ at 180 K are shown in Figure 6-44 and Figure 6-45 for the two investigated orientations. The same is done for the measurements at 300 K in Figure 6-46 and Figure 6-47. The higher intensity seen in Figure 6-42 of the horizontal orientation in the region between 2 and 7 meV can be found in the dispersion graphs. This inelastic effect increases with increasing wave vector transfer as it can be expected from theory (see chapter 4).

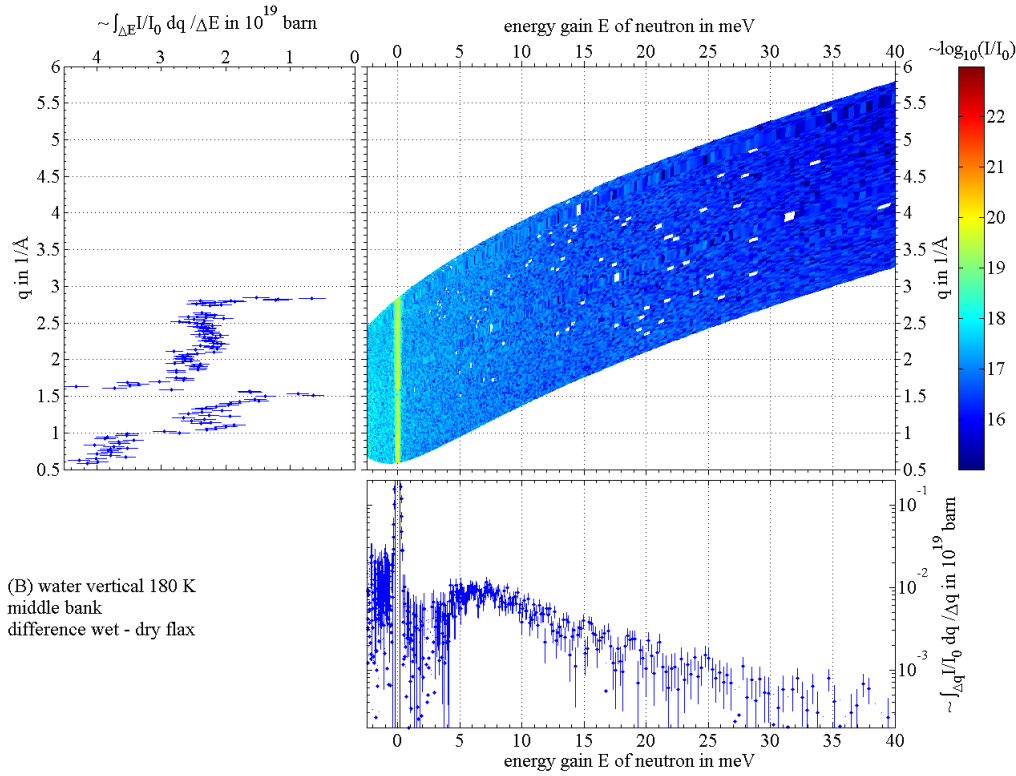


Figure 6-44: Difference spectra collected in an inelastic neutron scattering experiment with a dry and a wet bundle of flax fibres estimating the influence of the adsorbed water on the dynamics.

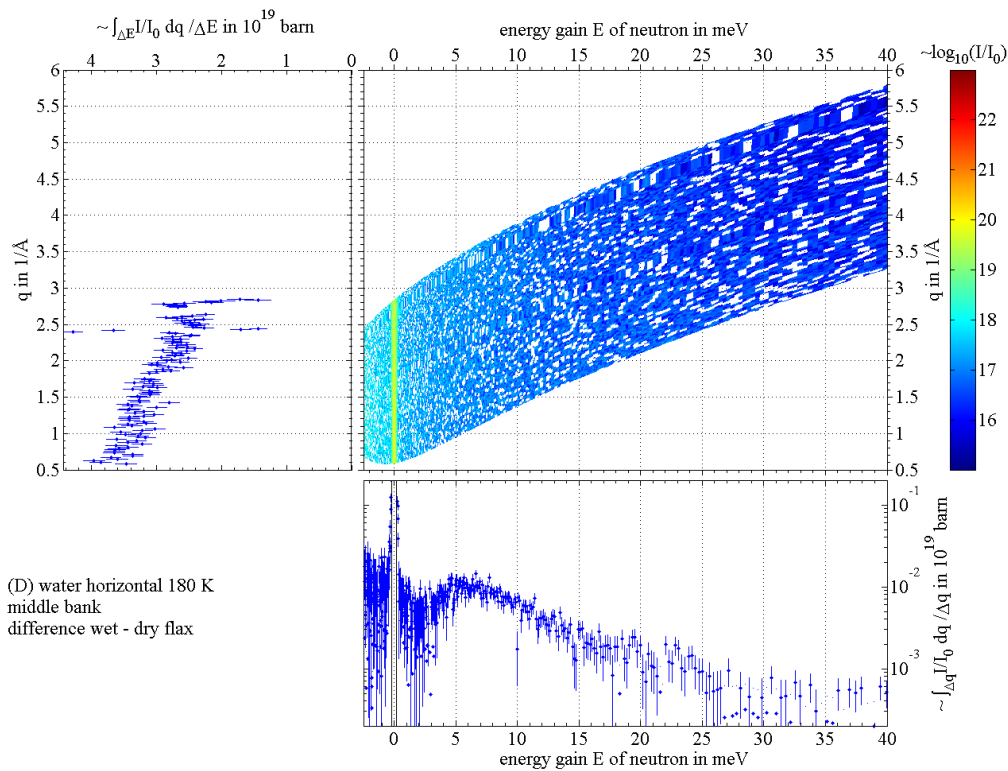


Figure 6-45: Difference spectra collected in an inelastic neutron scattering experiment with a dry and a wet bundle of flax fibres estimating the influence of the adsorbed water on the dynamics.

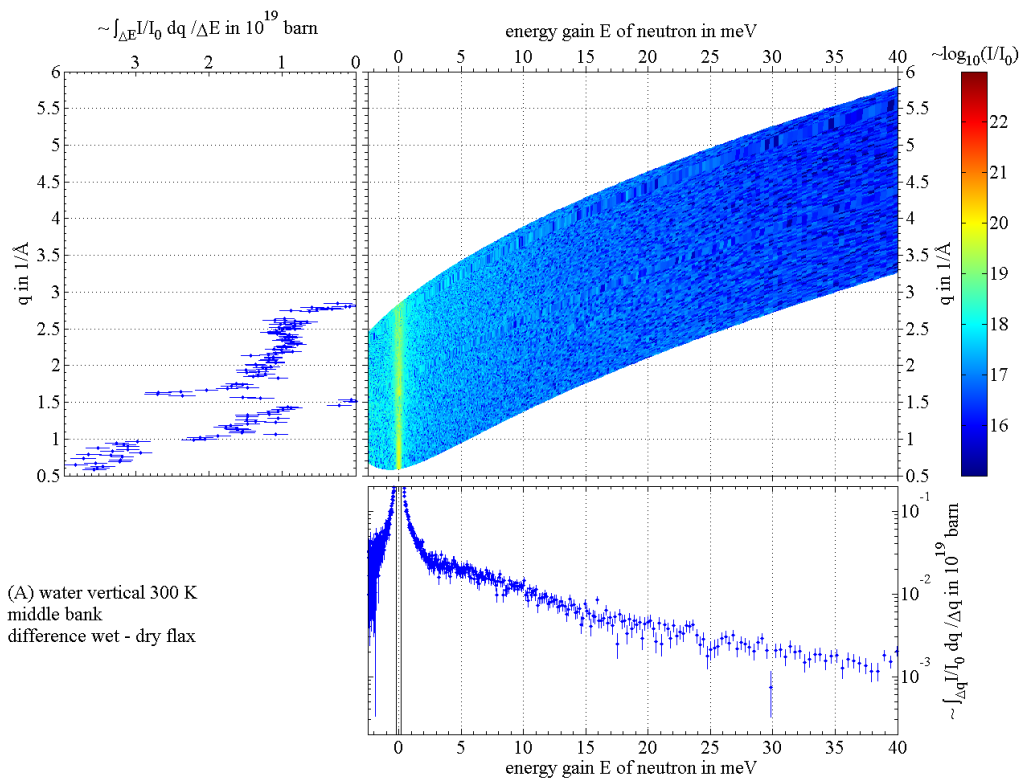


Figure 6-46: Difference spectra collected in an inelastic neutron scattering experiment with a dry and a wet bundle of flax fibres estimating the influence of the adsorbed water on the dynamics.

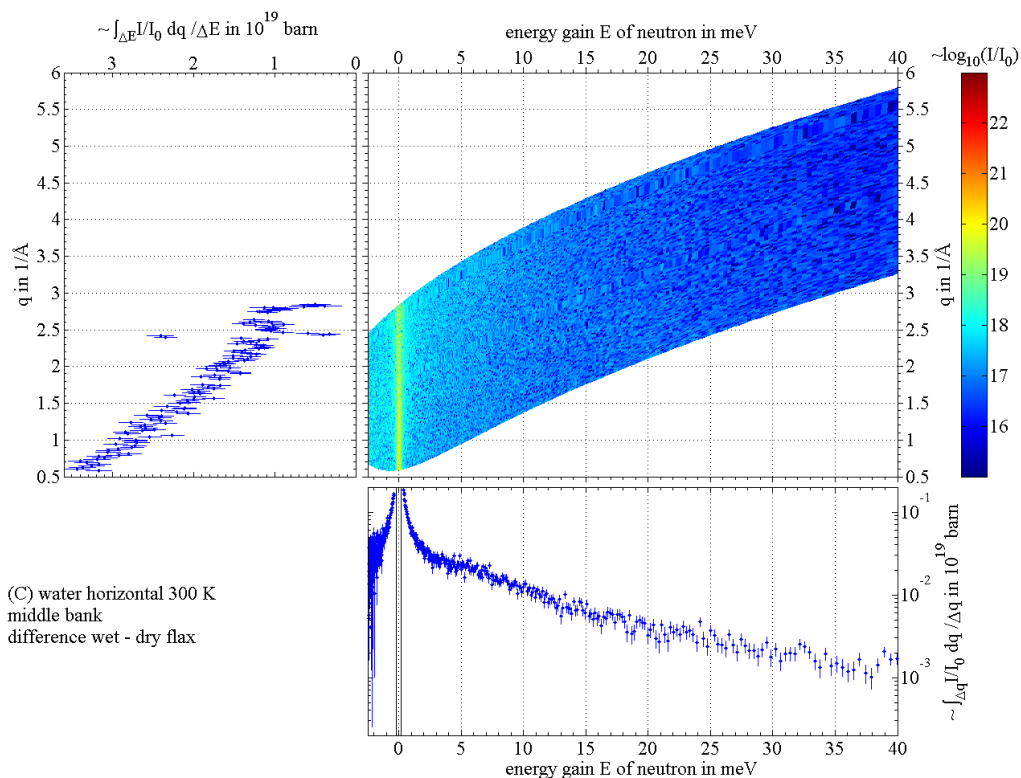


Figure 6-47: Difference spectra collected in an inelastic neutron scattering experiment with a dry and a wet bundle of flax fibres estimating the influence of the adsorbed water on the dynamics.

6.2.4 Discussion

There are at least two ways to explain the anisotropy in the dynamics observed in this study. First, the anisotropy can be linked to an anisotropy in the dynamics of the adsorbed water molecules only. Second, the dynamic response of the cellulose itself might have changed due to the presence of the adsorbed water molecules. It is known that the water molecules cannot penetrate into the cellulose crystals (Ioelovitch and Gordeev 1994). Therefore, a change in the dynamics originated directly to the motions of the water molecules must be located in the amorphous regions of the cellulose. This would imply an anisotropic environment of the water molecules, as is imaginable especially in the region close to the crystal surfaces. Particularly, the higher intensity for the motions observed at about 5 meV along the fibre direction give rise to a close relationship to low density amorphous ice.

Additionally, a change in the dynamics of the cellulose due to the water molecules can be a combination of two effects. It is conceivable that the hydroxyl groups at the surfaces of the crystals show a different response if water molecules are located in the vicinity of or even inserted into some of the hydrogen bonds between the crystals and the surrounding amorphous region, indicating a surface effect. Also it could be that the change in the dynamics is linked to a volume effect inside the crystals. This could be originating from compressed lattice spacing, caused by the swelling of the amorphous regions at higher moisture content. Eventually, this effect could be limited to a few top most layers beyond the surface.

Finally, the experimental findings might be a combination of all effects mentioned above. Nevertheless, the results show clear evidence for an anisotropy in the dynamics that is correlated with the adsorbed water. This suggests the direct influence of the water molecules on a molecular level.

7 Conclusions and Outlook

The mechanical properties of pine earlywood have been studied in combined X-ray diffraction and stretching experiments at different water content. Additionally, the spectroscopic information, as obtained from inelastic neutron scattering experiments of wet and dry cellulose fibres, have been compared. The results of these investigations are summarised in the following.

The reaction of wood under mechanical tension has been measured in a stretching experiment combined *in situ* with the collection of X-ray diffraction patterns, monitoring the cellulose crystal lattice spacing and microfibril orientation inside the composite material. The stress-strain curve can be divided into four regions, three of which are already visible in the macroscopic curve. The first region (A) is characterised by proportionally increasing stress and strain. The next region (B,C) shows a smaller slope of the stress-strain curve and the transition to the final strain-hardening region (D) is smooth. These regions are accompanied by corresponding changes in the orientation and elongation of the cellulose crystals. The split of the second region into (B) and (C) is visible from the orientation behaviour of the crystals only. The corresponding mechanisms become clear from the comparison of dry and wet samples. The material softening is localised in the beginning of the stress-strain curve (A-C), additionally, the strain-hardening (D) found in all samples is independent of moisture content. The experiments are consistent with the macroscopic model proposed in (Navi 1997), but an additional splitting into region (B) and (C) has been identified on a molecular level. The ‘lining up’ behaviour of the cellulose crystals (Figure 7-1) assumed in the model has been proven experimentally. The macroscopic softening of the material originates from the matrix surrounding the crystals.

Inelastic neutron scattering experiments have been performed on flax fibres with highly oriented microfibrils leading to different spectroscopic data for the directions along and perpendicular to the cellulose crystals. The water molecules adsorbed in the matrix are very likely incorporated in the weak hydrogen bonds at the surface of the cellulose crystals, influencing the dynamics probed with the inelastic neutron scattering experiments and, elsewhere, with FT-IR spectroscopy (Hofstetter et al. 2006). Possibly, the water molecules are situated in an anisotropic network, consisting of a few water molecules between the hydroxyl groups of the polymer chains, as illustrated in Figure 7-2. Both methods show results that lead to the conclusion that water does not affect the strong bonds along the cellulose chains. This finding can explain the independence of the strain-hardening behaviour that has been found in the mechanical stretching experiments on the water content: The final stiffness is only defined by the Young's modulus of the cellulose chains after lining up into the direction of the external force.

The technical improvements presented in this thesis have been critical for the wet-dry-comparison central to this work. The distortion compensation procedure has enabled the use of an X-ray detector with short readout time, resulting in a high time resolution during the diffraction experiments. The newly developed humid stretching environment HUSTEN has been used in combined stretching and X-ray diffraction experiments on pine earlywood, in particular on single tracheids and, additionally, on silk as shown elsewhere. Furthermore, the low-background design of a new sample chamber has made the inelastic neutron scattering experiments possible despite the smallness of the anisotropy of the spectra. Additionally, refinements of the calculus necessary in the data reduction process of direct geometry time-of-flight experiments has ensured a correct representation of the small effects observed.

The investigations concerning the mechanical properties have been limited to certain constant strain rates. The mechanics of a viscoelastic material are expected to be time-

dependent, hence, further investigations with different strain rates should be carried out. Additionally, studies on different types of wood, e.g. latewood or hardwood, are necessary in order to clarify the generality of the found mechanisms. Finally, the higher time efficiency possible at synchrotron radiation sources, due to the interchangeable sample holder and accuracy of the device HUSTEN, should be exploited in future to investigate the spread of the characteristic values of a biomaterial like wood, e.g. its Young's modulus.

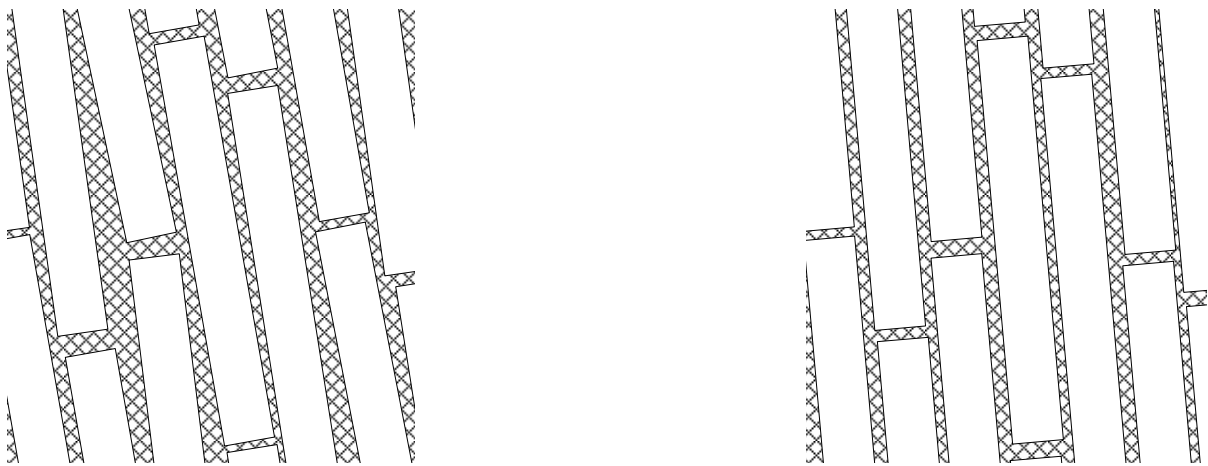


Figure 7-1: Schematic drawing of the 'lining-up' of the cellulose crystallites (white boxes) hindered by the surrounding matrix (crosshatch) and the hydrogen bonds therein. The initial scatter of the crystallite orientation (left) changes into a higher degree of orientation (right) during macroscopic elongation (vertical).

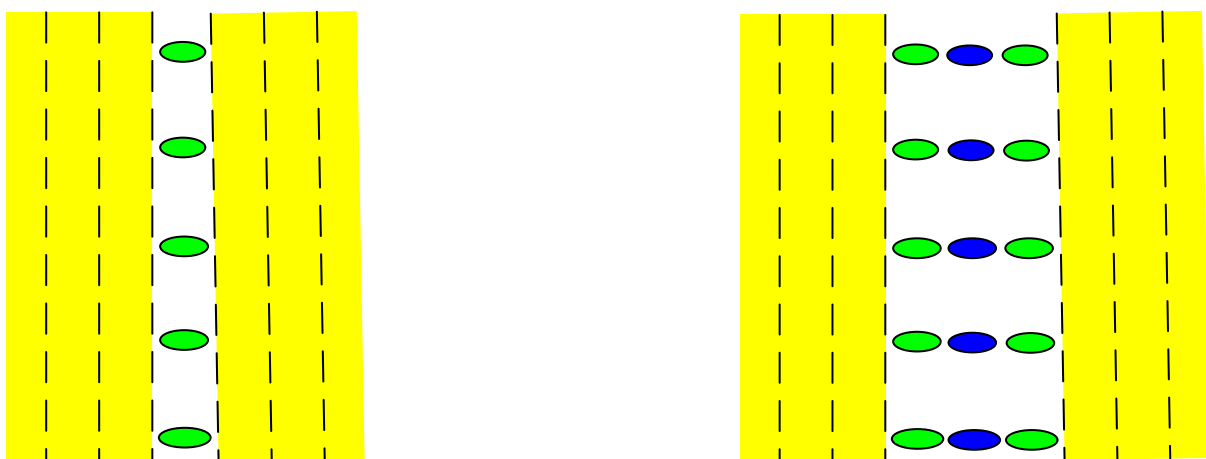


Figure 7-2: Simplified model for the softening of the hydrogen bonding (green) between adjacent crystallites (yellow) due to water (blue) uptake. The cellulose chains are marked with black dashed lines. The water molecules are incorporated into the hydrogen bonds in this model leading to a swelling of the material and an anisotropic dynamic.

(This page is intentionally left blank.)

8 Appendix

8.1 Broadening of Time-of-Flight Spectra due to Slab-Angle

Slab-like samples are often used in time-of-flight experiments. The resulting geometry found for a slab sample of width w_s situated in the instrument holding an angle γ_s between sample surface and primary beam direction is illustrated in Figure 8-1. The influence of such a geometry on the time-of-flight spectra obtained under different scattering angles 2θ will be discussed in the following. The neutrons transmitted or scattered in forward direction are shown in green. Such neutrons would reach an hypothetical detector placed in forward direction, i.e. at the location where normally a beam stop is placed, after travelling the same distance, regardless of the point where they have been hitting the sample. Contrarily, neutrons that are scattered at opposite sides of the sample into the same scattering angle $2\theta \neq 0^\circ$ have to travel different distances until they reach the same detector. The difference in path length to travel is given by δ_i for the distance the incoming neutron on one side of the primary beam of width w_i has to travel further then on the other side of the sample in order to reach the sample. The same neutron has to travel an additional distance δ_n after leaving the sample in order to reach the detector. Finally, the following equations hold for this situation, as is evident from Figure 8-1.

$$\delta_i = -w_i \tan \gamma_s \quad (8.1)$$

$$\delta_n = w_s \cos(\gamma_s - 2\theta) \quad (8.2)$$

$$\frac{w_i}{w_s} = \sin \gamma_s \quad (8.3)$$

Hence, the resulting difference in travel distance accumulates to δ_r as follows:

$$\begin{aligned}
 \delta_r &= \delta_n + \delta_i \\
 &= \frac{w_i}{\sin \gamma_s} \cos(\gamma_s - 2\theta) - w_i \tan \gamma_s \\
 &= w_i \left(\frac{\cos(\gamma_s - 2\theta)}{\sin \gamma_s} - \tan \gamma_s \right).
 \end{aligned} \tag{8.4}$$

It takes the neutrons of energy E_0 and mass m_n the time t_δ to fly the distance δ_r if they are scattered elastically:

$$t_\delta = \frac{\delta_r}{v_0} = \frac{\delta_r}{\sqrt{\frac{2E_0}{m_n}}} = \delta_r \sqrt{\frac{m_n}{2E_0}}. \tag{8.5}$$

The difference in time-of-flight results in a broadening δE of the energy spectra obtained in a time-of-flight experiment. It can be calculated from eq. (5.39) and (8.5):

$$\begin{aligned}
 \delta E &= \left| E \left(t_n = t_0 + \frac{t_\delta}{2} \right) \right| \\
 &= \left| \frac{m_n}{2} \left(\frac{s_d}{t_0 + \frac{t_\delta}{2}} \right)^2 - E_0 \right| \\
 &= \left| \frac{m_n}{2} \left(\frac{s_d}{\frac{s_d}{v_0} + \frac{\delta_r}{2v_0}} \right)^2 - E_0 \right| \\
 &= \left| \left(\left(\frac{s_d}{s_d + \frac{1}{2}\delta_r} \right)^2 - 1 \right) E_0 \right| \\
 &= \left| \frac{s_d^2 - \left(s_d + \frac{1}{2}\delta_r \right)^2}{\left(s_d + \frac{1}{2}\delta_r \right)^2} E_0 \right| \\
 &= \left| \frac{\frac{1}{2}\delta_r - 2s_d}{\left(s_d + \frac{1}{2}\delta_r \right)^2} \frac{1}{2}\delta_r E_0 \right|.
 \end{aligned} \tag{8.6}$$

The maximum broadening due to sample geometry will be found at $2\theta = \gamma_s$, as is obvious from Figure 8-1 and eq. (8.4). The actual parameters of the inelastic neutron scattering experiments presented in this study $w_i = 30$ mm, $\gamma_s = 135^\circ$, $E_0 = 5.11$ meV, $s_d = 2.5$ m lead to:

$$\begin{aligned}\delta_r &= 30 \text{ mm} \left(\frac{\cos(135^\circ - 2\theta)}{\sin 135^\circ} - \tan 135^\circ \right) \\ &= 30 \text{ mm} \left(\frac{\cos(135^\circ - 2\theta)}{\frac{1}{\sqrt{2}}} - (-1) \right) \\ &= 30 \text{ mm} (\sqrt{2} \cos(135^\circ - 2\theta) + 1).\end{aligned}\quad (8.7)$$

The corresponding time computes to:

$$\begin{aligned}t_s &= 30 \text{ mm} (\sqrt{2} \cos(135^\circ - 2\theta) + 1) \sqrt{\frac{1.6749 \cdot 10^{-27} \text{ kg}}{2 \cdot 5.11 \text{ meV}} \frac{\text{e}}{1.6022 \cdot 10^{-19} \text{ As}} \frac{\text{mVA}}{10^{-3} \text{ W}} \frac{\text{Ws}}{\text{Nm}} \frac{\text{N}}{\text{kgm}} \frac{\text{s}^2}{\text{m}^2}} \\ &= 30 \text{ mm} (\sqrt{2} \cos(135^\circ - 2\theta) + 1) \sqrt{\frac{1.6749}{2 \cdot 5.11 \cdot 1.6022} 10^{-27+19+3} \frac{\text{s}^2}{\text{m}^2}} \\ &= 30 \text{ mm} (\sqrt{2} \cos(135^\circ - 2\theta) + 1) \sqrt{0.102 \cdot 10^{-5} \frac{\text{s}}{\text{m}} \frac{\text{m}}{10^3 \text{ mm}}} \\ &= 30 \cdot (\sqrt{2} \cos(135^\circ - 2\theta) + 1) \cdot 1.01 \cdot 10^{-6} \text{ s} \\ &= 30.3 \mu\text{s} \cdot (\sqrt{2} \cos(135^\circ - 2\theta) + 1).\end{aligned}\quad (8.8)$$

Finally, the broadening on the energy scale is found to:

$$\delta E = \frac{2 \cdot 2.5 \text{ m} - 30 \text{ mm} \frac{1}{2} (\sqrt{2} \cos(135^\circ - 2\theta) + 1)}{\left(2.5 \text{ m} + 30 \text{ mm} \frac{1}{2} (\sqrt{2} \cos(135^\circ - 2\theta) + 1) \right)^2} \frac{1}{2} E_0 \cdot 30 \text{ mm} (\sqrt{2} \cos(135^\circ - 2\theta) + 1). \quad (8.9)$$

The maximum is found at $2\theta = \gamma_s$ to $\delta_r = 42.4$ mm, $t_s = 42.9$ μs and

$$\begin{aligned}\delta E &= \left| \frac{\frac{1}{2} \cdot 42.4 \text{ mm} - 2 \cdot 5,000 \text{ mm}}{\left(5,000 \text{ mm} + \frac{1}{2} \cdot 42.4 \text{ mm} \right)^2} 42.4 \text{ mm} \cdot 5.11 \text{ meV} \right| \\ &= \frac{9,978.8 \text{ mm}}{(5,021.2 \text{ mm})^2} 21.2 \text{ mm} \cdot 5.11 \text{ meV} \\ &= 42.9 \mu\text{eV}.\end{aligned}\quad (8.10)$$

This effect is visible for example in Figure 5-39.

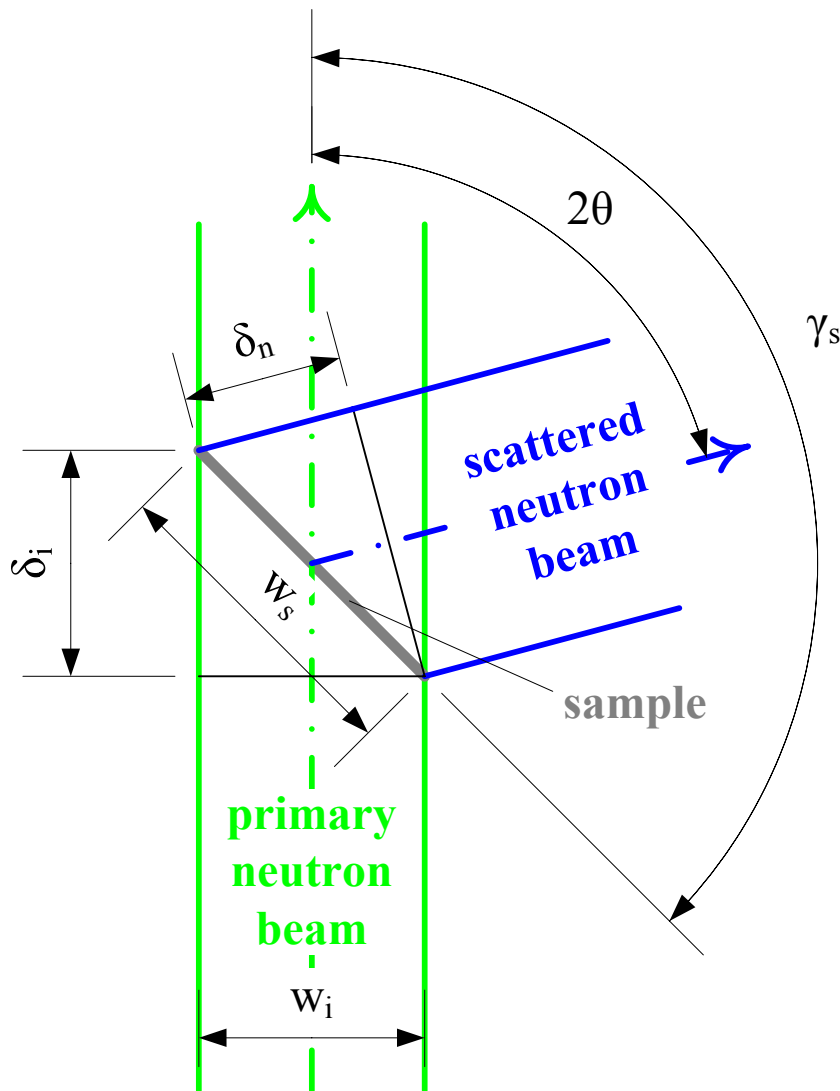


Figure 8-1: Sketch of the geometry found for a slab sample (grey) tilted in the scattering plane with respect to the primary beam (green) by a slab-angle γ_s . The geometry is given for neutrons scattered (blue) at an angle 2θ and a width of the primary beam w_i that fully illuminates the sample of width w_s . The path of the neutrons scattered at opposite sides of the sample differ by the distances δ_i and δ_n leading to a small difference in time-of-flight even in the case of elastic scattering.

8.2 Technical Details

The equipment used in the experiments presented in chapter 6 has been build partly by the university of Kiel, but some apparatuses have been delivered by external suppliers. These components are listed in Table 8-1.

supplier	component	description
National Instruments	PCI-GPIB IEE 488.2	GPIB-interface card for PCs
	PCI 6035E	data acquisition card for PCs, 16-bit resolution, differential mode ADC, 10 V range (± 7.56 mV), 0.5 V range (± 0.399 mV)
	BNC-2090	BNC adapter box
	SH68-68-EP	shielded cable, 2 m
Kern & Sohn GmbH	ABS 80-4	electronic balance, resolution 0.1 mg
Mastech	HY1502D	DC power supply
TTi	QL355TP	DC power supply, used at $10\text{ V} \pm 8\text{ mV}$
Dr. Johannes Heidenhein GmbH	MT2581	linear gauge, $\pm 0.2\text{ }\mu\text{m}$ nominal, checked to $\pm 0.09\text{ }\mu\text{m}$.
	IK220	counter card for PCs
HIOKI E. E. Co.	HIOKI 3532-50	LCR-meter
Entran SA	ELPM-T3M-2.5KN-/L3M	2,500 N force sensor
	ELPM-T2M-125N-/L3M	125 N force sensor
	ELPM-T1M-25N-/L3M	25 N force sensor
	ELG-H-5N-/Z2L2M	5 N force sensor
	ELGH-H-0,5N-/Z2/L2M	0.5 N force sensor
Micos	71609511	SMC pollux I 2SM-controller box
	71609522	SMC pollux power supply 60 W
	71609520	SMC pollux RS232-cabel, 3 m
	K3310155	Motor 4H4018L0201-A
	72009021	Motor cable MK-052-SM VGA
Lumenera Co.	Lu205c	$\frac{1}{2}$ " format CCD, 1600×1200 pixel of $4.2\text{ }\mu\text{m}^2$, 8-bit resolution.
THK Co Ltd.	KR2001A+100LP 0-0000	compact high precision ball screw guide actuator unit, positioning accuracy reproducibility $\pm 3\text{ }\mu\text{m}$, running parallelism $10\text{ }\mu\text{m}$
Photonic Science	GemStar-2 HS	image intensified X-ray camera, 1200×1003 pixel of $67\text{ }\mu\text{m}^2$, 12-bit resolution
Sensor-Tec	SMTHS10	Smartec humidity sensor, temperature dependency - 0.15 \%RH/K , linearity $\pm 2\text{ \%RH}$
Labfacility	Pt100 B/3	platinum temperature sensor. accuracy 1/3 of DIN EN 60751 class B
LakeShor Cryo- tronics, Inc.	Model 340	temperature controller

Table 8-1: List of the components that have been delivered by the mentioned suppliers. The descriptions given here are based on the product information offered by the suppliers.

8.3 Jacobian Determinants of the Transformations

8.3.1 The Time-of-Flight to Energy Gain Transformation

As shown in chapter 5.2.2.4 the energy gain of an inelastic scattered neutron can be calculated from its time-of-flight measured in an inelastic neutron scattering experiment using eq. (5.40):

$$E = E_0 \left(\left(\frac{t_{elastic}}{t_n} \right)^2 - 1 \right). \quad (8.11)$$

This equation can be written as follows:

$$t_n = \sqrt{\frac{E_0}{E_0 + E}} t_{elastic}. \quad (8.12)$$

Within the context of transformation, the Jacobian determinant has to be calculated.

This is done in this one dimensional case directly with the first derivative of eq. (8.12):

$$\frac{\partial t_n}{\partial E} = \frac{\partial}{\partial E} \left(\sqrt{\frac{E_0}{E_0 + E}} t_{elastic} \right). \quad (8.13)$$

$$\begin{aligned} \frac{\partial t_n}{\partial E} &= \frac{1}{2\sqrt{\frac{E_0}{E_0 + E}}} t_{elastic} \frac{\partial}{\partial E} \left(\frac{E_0}{E_0 + E} \right) \\ &= -\frac{1}{2\sqrt{\frac{E_0}{E_0 + E}}} t_{elastic} E_0 \frac{\partial}{\partial E} \left(\frac{1}{E_0 + E} \right) \end{aligned} \quad (8.14)$$

$$= -\frac{1}{2\sqrt{\frac{E_0}{E_0 + E}}} t_{elastic} E_0 \frac{-1}{(E_0 + E)^2} \frac{\partial}{\partial E} (E_0 + E)$$

$$= -\frac{1}{2\sqrt{\frac{E_0}{E_0 + E}}} t_{elastic} E_0 \frac{-1}{(E_0 + E)^2} 1$$

$$\frac{\partial t_n}{\partial E} = \frac{-t_{elastic}}{2E_0} \left(1 + \frac{E}{E_0} \right)^{-\frac{3}{2}} \quad (8.15)$$

This leads to the Jacobian determinant as written in eq. (8.16):

$$|J_{t_n}| = \left| \frac{-t_{elastic}}{2E_0} \left(1 + \frac{E}{E_0} \right)^{-\frac{3}{2}} \right| = \frac{t_{elastic}}{2E_0} \left(1 + \frac{E}{E_0} \right)^{-\frac{3}{2}}. \quad (8.16)$$

For a convenient use of this result, for example in a computer program, the energy gain will be calculated according to eq. (8.11). Combined with the Jacobian determinant from eq. (8.16), this leads to eq. (8.17):

$$|J_{t_n}| = \frac{t_{elastic}}{2E_0} \left(1 + \frac{E_0 \left(\left(\frac{t_{elastic}}{t_n} \right)^2 - 1 \right)}{E_0} \right)^{-\frac{3}{2}}. \quad (8.17)$$

$$|J_{t_n}| = \frac{t_n^3}{2E_0 t_{elastic}^2} \quad (8.18)$$

8.3.2 Wave Vector Transfer Calculation

As shown in chapter 0, the wave vector transfer that occurs in an inelastic neutron scattering experiment can be calculated using eq. (5.59):

$$|\vec{q}| = |\vec{k}_i| \sqrt{1 + \left(\frac{t_{elastic}}{t_n} \right)^2 - 2 \frac{t_{elastic}}{t_n} \cos(2\theta)}. \quad (8.19)$$

Inversion of this equation leads to the following expression:

$$2\theta = \arccos \left(\frac{-t_n}{2t_{elastic}} \left(\left(\frac{|\vec{q}|}{|\vec{k}_i|} \right)^2 - 1 - \left(\frac{t_{elastic}}{t_n} \right)^2 \right) \right). \quad (8.20)$$

The time-of-flight in this expression can be substituted according to eq. (8.12) to achieve the first component of the transformation $(|\vec{q}|, E) \rightarrow (2\theta, t_n)$:

$$2\theta = \arccos \left(\frac{-\sqrt{\frac{E_0}{E_0 + E}} t_{elastic}}{2t_{elastic}} \left(\left(\frac{|\vec{q}|}{|\vec{k}_i|} \right)^2 - 1 - \left(\frac{t_{elastic}}{\sqrt{\frac{E_0}{E_0 + E}} t_{elastic}} \right)^2 \right) \right). \quad (8.21)$$

$$2\theta = \arccos\left(\frac{1}{2}\sqrt{\frac{E_0}{E_0+E}}|\vec{k}_i|^{-2}\left(|\vec{k}_i|^2-|\vec{q}|^2\right)+\frac{1}{2}\sqrt{\frac{E_0+E}{E_0}}\right) \quad (8.22)$$

This can also be written in terms of wave vectors instead of the energies as follows:

$$2\theta = \arccos\left(\frac{1}{2}\sqrt{\frac{|\vec{k}_i|^2}{|\vec{k}_n|^2}}|\vec{k}_i|^{-2}\left(|\vec{k}_i|^2-|\vec{q}|^2\right)+\frac{1}{2}\sqrt{\frac{|\vec{k}_n|^2}{|\vec{k}_i|^2}}\right). \quad (8.23)$$

$$2\theta = \arccos\left(\frac{1}{2}\frac{|\vec{k}_i|^2-|\vec{q}|^2+|\vec{k}_n|^2}{|\vec{k}_n||\vec{k}_i|}\right) \quad (8.24)$$

From this term or from eq. (8.22), the last missing elements of the Jacobian in eq. (5.25) can be determined as shown in the following.

$$\frac{\partial 2\theta}{\partial |\vec{q}|} = \frac{\partial}{\partial |\vec{q}|} \arccos\left(\frac{1}{2}\frac{|\vec{k}_i|^2-|\vec{q}|^2+|\vec{k}_n|^2}{|\vec{k}_n||\vec{k}_i|}\right) \quad (8.25)$$

$$\begin{aligned} \frac{\partial 2\theta}{\partial |\vec{q}|} &= \frac{-1}{\sqrt{1-\left(\frac{1}{2}\frac{|\vec{k}_i|^2-|\vec{q}|^2+|\vec{k}_n|^2}{|\vec{k}_n||\vec{k}_i|}\right)^2}} \frac{\partial}{\partial |\vec{q}|} \left(\frac{1}{2}\frac{|\vec{k}_i|^2-|\vec{q}|^2+|\vec{k}_n|^2}{|\vec{k}_n||\vec{k}_i|}\right) \\ &= \frac{-1}{\sqrt{1-\left(\frac{1}{2}\frac{|\vec{k}_i|^2-|\vec{q}|^2+|\vec{k}_n|^2}{|\vec{k}_n||\vec{k}_i|}\right)^2}} \left(-\frac{1}{2}\frac{2|\vec{q}|}{|\vec{k}_n||\vec{k}_i|}\right) \\ &= \frac{|\vec{q}|}{|\vec{k}_n||\vec{k}_i| \sqrt{1-\frac{|\vec{q}|^4-2|\vec{q}|^2\left(|\vec{k}_n|^2+|\vec{k}_i|^2\right)+|\vec{k}_i|^4+2|\vec{k}_i|^2|\vec{k}_n|^2+|\vec{k}_n|^4}{4|\vec{k}_n|^2|\vec{k}_i|^2}}} \end{aligned} \quad (8.26)$$

In combination with the quadratic version of eq. (5.52), this leads to:

$$\frac{\partial 2\theta}{\partial |\vec{q}|} = \frac{|\vec{q}|}{|\vec{k}_n||\vec{k}_i| \sqrt{1-\frac{|\vec{q}|^4-2\left(|\vec{k}_i|^2+|\vec{k}_n|^2-2|\vec{k}_i||\vec{k}_n|\cos(2\theta)\right)\left(|\vec{k}_n|^2+|\vec{k}_i|^2\right)+|\vec{k}_i|^4+2|\vec{k}_i|^2|\vec{k}_n|^2+|\vec{k}_n|^4}{4|\vec{k}_n|^2|\vec{k}_i|^2}}}}. \quad (8.27)$$

$\underbrace{\hspace{15em}}_{=:\frac{N}{Z}}$

With the abbreviation defined above, this can be expanded step by step as follows:

$$\begin{aligned}
N &= |\vec{q}|^4 - 2\left(|\vec{k}_i|^2 + |\vec{k}_n|^2 - 2|\vec{k}_i||\vec{k}_n|\cos(2\theta)\right)\left(|\vec{k}_n|^2 + |\vec{k}_i|^2\right) + |\vec{k}_i|^4 + 2|\vec{k}_i|^2|\vec{k}_n|^2 + |\vec{k}_n|^4 \\
&= |\vec{q}|^4 - 2\left(|\vec{k}_n|^2 + |\vec{k}_i|^2\right)^2 + 4\left(|\vec{k}_n|^2 + |\vec{k}_i|^2\right)|\vec{k}_i||\vec{k}_n|\cos(2\theta) + \underbrace{|\vec{k}_i|^4 + 2|\vec{k}_i|^2|\vec{k}_n|^2 + |\vec{k}_n|^4}_{\left(|\vec{k}_n|^2 + |\vec{k}_i|^2\right)^2} \quad (8.28) \\
&= |\vec{q}|^4 + 4\left(|\vec{k}_n|^2 + |\vec{k}_i|^2\right)|\vec{k}_i||\vec{k}_n|\cos(2\theta) - |\vec{k}_i|^4 - 2|\vec{k}_i|^2|\vec{k}_n|^2 - |\vec{k}_n|^4.
\end{aligned}$$

The first term can be expanded with eq. (5.52) as follows:

$$\begin{aligned}
|\vec{q}|^4 &= \left|\sqrt{|\vec{k}_i|^2 + |\vec{k}_n|^2 - 2|\vec{k}_i||\vec{k}_n|\cos(2\theta)}\right|^4 \\
&= \left(|\vec{k}_i|^2 + |\vec{k}_n|^2 - 2|\vec{k}_i||\vec{k}_n|\cos(2\theta)\right)^2 \quad (8.29) \\
&= |\vec{k}_i|^4 + 2|\vec{k}_i|^2|\vec{k}_n|^2 + |\vec{k}_n|^4 - 4\left(|\vec{k}_i|^2 + |\vec{k}_n|^2\right)|\vec{k}_i||\vec{k}_n|\cos(2\theta) + 4|\vec{k}_i|^2|\vec{k}_n|^2\cos^2(2\theta).
\end{aligned}$$

This leads to another version of eq. (8.28):

$$\begin{aligned}
N &= \left(|\vec{k}_i|^4 + 2|\vec{k}_i|^2|\vec{k}_n|^2 + |\vec{k}_n|^4 + 4\left(|\vec{k}_i|^2 + |\vec{k}_n|^2\right)|\vec{k}_i||\vec{k}_n|\cos(2\theta) + 4|\vec{k}_i|^2|\vec{k}_n|^2\cos^2(2\theta)\right) \\
&\quad - 4\left(|\vec{k}_n|^2 + |\vec{k}_i|^2\right)|\vec{k}_i||\vec{k}_n|\cos(2\theta) - |\vec{k}_i|^4 - 2|\vec{k}_i|^2|\vec{k}_n|^2 - |\vec{k}_n|^4 \quad (8.30) \\
&= 4|\vec{k}_i|^2|\vec{k}_n|^2\cos^2(2\theta).
\end{aligned}$$

This equation combined with eq. (8.27) leads to the following:

$$\frac{\partial 2\theta}{\partial |\vec{q}|} = \frac{|\vec{q}|}{|\vec{k}_n||\vec{k}_i|\sqrt{1 - \frac{4|\vec{k}_i|^2|\vec{k}_n|^2\cos^2(2\theta)}{4|\vec{k}_n|^2|\vec{k}_i|^2}}}. \quad (8.31)$$

$\underbrace{\hspace{10em}}_{= \frac{N}{Z}}$

Finally, this can be simplified to the short version of the derivative that will be used later in the Jacobian:

$$\frac{\partial 2\theta}{\partial |\vec{q}|} = \frac{|\vec{q}|}{|\vec{k}_n||\vec{k}_i|\sin(2\theta)}. \quad (8.32)$$

In order to cross-check this result, the transformation from eq. (5.52) can be used in combination with the rule about the derivative of an inverse function as done in (Howie 2001)^{theo. 4.15.}:

$$\frac{\partial 2\theta}{\partial |\vec{q}|} = \frac{1}{\frac{\partial |\vec{q}|}{\partial 2\theta}} = \frac{1}{\frac{\partial}{\partial 2\theta} \left(\sqrt{|\vec{k}_i|^2 + |\vec{k}_n|^2 - 2|\vec{k}_i||\vec{k}_n|\cos(2\theta)} \right)}. \quad (8.33)$$

$$\begin{aligned} \frac{\partial 2\theta}{\partial |\vec{q}|} &= \frac{1}{\frac{1}{2\sqrt{|\vec{k}_i|^2 + |\vec{k}_n|^2 - 2|\vec{k}_i||\vec{k}_n|\cos(2\theta)}} \frac{\partial}{\partial 2\theta} \left(|\vec{k}_i|^2 + |\vec{k}_n|^2 - 2|\vec{k}_i||\vec{k}_n|\cos(2\theta) \right)} \\ &= \frac{1}{\frac{1}{2\sqrt{|\vec{k}_i|^2 + |\vec{k}_n|^2 - 2|\vec{k}_i||\vec{k}_n|\cos(2\theta)} - 2|\vec{k}_i||\vec{k}_n| \frac{\partial}{\partial 2\theta} (\cos(2\theta))}} \\ &= \frac{1}{\frac{1}{2\sqrt{|\vec{k}_i|^2 + |\vec{k}_n|^2 - 2|\vec{k}_i||\vec{k}_n|\cos(2\theta)} (-2)|\vec{k}_i||\vec{k}_n| (-\sin(2\theta))}} \end{aligned} \quad (8.34)$$

$$\frac{\partial 2\theta}{\partial |\vec{q}|} = \frac{\sqrt{|\vec{k}_i|^2 + |\vec{k}_n|^2 - 2|\vec{k}_i||\vec{k}_n|\cos(2\theta)}}{|\vec{k}_i||\vec{k}_n|\sin(2\theta)} = \frac{|\vec{q}|}{|\vec{k}_i||\vec{k}_n|\sin(2\theta)} \quad (8.35)$$

This is exactly the same as shown in eq. (8.32). The other missing derivatives of the transformation are $\frac{\partial 2\theta}{\partial E}$ and $\frac{\partial t_n}{\partial |\vec{q}|}$. The latter is zero, as can be seen from eq. (8.12). The Jacobian determinant can be expanded, as shown in eq. (8.36). From this, it is discernible that only the first two derivatives have to be computed as done in eq. (8.15) and (8.32).

$$J_{\theta,t} = \begin{vmatrix} \frac{\partial 2\theta}{\partial |\vec{q}|} & \frac{\partial 2\theta}{\partial E} \\ \frac{\partial t_n}{\partial |\vec{q}|} & \frac{\partial t_n}{\partial E} \end{vmatrix} = \frac{\partial 2\theta}{\partial |\vec{q}|} \frac{\partial t_n}{\partial E} - \frac{\partial 2\theta}{\partial E} \frac{\partial t_n}{\partial |\vec{q}|} \quad (8.36)$$

Insertion of eq. (8.32) and (8.15) leads to:

$$J_{\theta,t} = \frac{|\vec{q}|}{|\vec{k}_n||\vec{k}_i|\sin(2\theta)} \frac{-t_{elastic}}{2E_0} \left(1 + \frac{E}{E_0} \right)^{-\frac{3}{2}}. \quad (8.37)$$

With eq. (5.39), (5.59), (5.53) and (5.54), the variables in (8.37) can be substituted to show the dependence on the measured time-of-flight.

$$J_{\theta,t} = \frac{\frac{\sqrt{2m_n E_0}}{\hbar} \sqrt{1 + \left(\frac{t_{elastic}}{t_n}\right)^2 - 2\frac{t_{elastic}}{t_n} \cos(2\theta)}}{\frac{\sqrt{2m_n (E_0 + E)}}{\hbar} \frac{\sqrt{2m_n E_0}}{\hbar} \sin(2\theta)} \frac{-t_{elastic}}{2E_0} \left(1 + \frac{E}{E_0}\right)^{-\frac{3}{2}} \quad (8.38)$$

$$J_{\theta,t} = \frac{\sqrt{1 + \left(\frac{t_{elastic}}{t_n}\right)^2 - 2\frac{t_{elastic}}{t_n} \cos(2\theta)}}{\frac{\sqrt{2m_n}}{\hbar} \sqrt{\frac{(E_0 + E)^4}{E_0^3}} \sin(2\theta)} \frac{-t_{elastic}}{2E_0} \quad (8.39)$$

$$= \frac{\sqrt{1 + \left(\frac{t_{elastic}}{t_n}\right)^2 - 2\frac{t_{elastic}}{t_n} \cos(2\theta)}}{(E_0 + E)^2 \sin(2\theta)} \frac{-t_{elastic}}{2} \frac{\hbar \sqrt{E_0}}{\sqrt{2m_n}}$$

Finally, this can be written with respect to eq. (5.40) or (8.11) as follows:

$$\begin{aligned} J_{\theta,t} &= \frac{\sqrt{1 + \left(\frac{t_{elastic}}{t_n}\right)^2 - 2\frac{t_{elastic}}{t_n} \cos(2\theta)}}{\left(E_0 + E_0 \left(\left(\frac{t_{elastic}}{t_n}\right)^2 - 1\right)\right)^2 \sin(2\theta)} \frac{-t_{elastic}}{2} \frac{\hbar \sqrt{E_0}}{\sqrt{2m_n}} \\ &= \frac{-\sqrt{1 + \left(\frac{t_{elastic}}{t_n}\right)^2 - 2\frac{t_{elastic}}{t_n} \cos(2\theta)}}{2t_{elastic}^3 \sin(2\theta)} \frac{\hbar}{\sqrt{2m_n E_0^3}} t_n^4 \\ &= \frac{-\sqrt{t_n^8 \left(1 + \left(\frac{t_{elastic}}{t_n}\right)^2 - 2\frac{t_{elastic}}{t_n} \cos(2\theta)\right)}}{2t_{elastic}^3 \sin(2\theta)} \frac{\hbar}{\sqrt{2m_n E_0^3}} \\ &= \frac{-\sqrt{t_n^8 + t_n^6 t_{elastic}^2 - 2t_n^7 t_{elastic} \cos(2\theta)}}{2t_{elastic}^3 \sin(2\theta)} \frac{\hbar}{\sqrt{2m_n E_0^3}}. \end{aligned} \quad (8.40)$$

This can be written also as:

$$J_{\theta,t} = \frac{-\sqrt{t_n^8 + t_n^6 t_{elastic}^2 - 2t_n^7 t_{elastic} \cos(2\theta)}}{2t_{elastic}^3 \sin(2\theta)} \frac{1}{|\bar{k}_i| E_0}. \quad (8.41)$$

(This page is intentionally left blank.)

9 References and Notes

ALEXANDER1979

Alexander, Leroy E.:
"X-Ray Diffraction Methods in Polymer Science"; reprint ed. ed.,
Krieger, Huntington, New York, (1979)
ISBN: 0-88275-801-2

ARNOLD1999A

Arnold, D. H. and Mauseth, J. D.:
"Effects of environmental factors on development of wood";
American Journal of Botany; Vol. **86** (3), pages 367-371 (1999)

ASHCROFT1976

Ashcroft, Neil W. and Mermin, N. David:
"Solid State Physics";
Saunders College, Philadelphia, (1976)
ISBN: 0-03-083993-9

AUTHIER1998

Authier, A. and Malgrange, C.:
"Diffraction physics";
Acta Crystallographica Section A; Vol. **54** (6 #1), pages 806-819 (1998)
DOI: 10.1107/S0108767398011271

BACON1975

Bacon, G. E.:
"Neutron Diffraction"; 3rd ed.,
Oxford University Press, Oxford, (1975)
ISBN: 19-851353-4

BEALS1977

Beals, H. O. and Davis, T. C.:
"Figure in Wood - An Illustrated Review"
<http://www.ag.auburn.edu/aaes/communications/bulletins/figureinwood/figure2.html>. (1977)
Reference Type: Electronic Citation

BÉE1988

Bée, Marc:
"Quasielastic Neutron Scattering";
Adam Hilger by Institute of Physics Publishing, Bristol, (1988)
ISBN: 0-85274-371-8

BERTAGNOLLI1976

Bertagnolli, H., Chieux, P., and Zeidler, M. D.:
"A neutron-diffraction study of liquid acetonitrile - I. CD₃C¹⁴N";
Molecular Physics; Vol. **32** (3), pages 759-773 (1976)

BRAMHALL1995

Bramhall, G.:
"Diffusion and the Drying of Wood";
Wood Science and Technology; Vol. **29** (3), pages 209-215 (1995)
DOI: 10.1007/BF00204588

BROCKHOUSE1955

Brockhouse, B. N.:
"Neutron Scattering and the Frequency Distribution of the Normal Modes of Vanadium Metal";
Canadian Journal of Physics; Vol. **33** (12), pages 889-891 (1955)

BROWN1992

Brown, Lisa Gottesfeld:
"A survey of image registration techniques";
ACM Computing Surveys; Vol. **24** (4), pages 325-376 (1992)
DOI: 10.1145/146370.146374

BRÜCKEL2002

Brückel, Th.:
"Scattering"
Forschungszentrum Jülich GmbH, Jülich, (2002)

BYRNE1994

Byrne, J.:
"Neutrons, Nuclei and Matter - An Exploration of the Physics of Slow Neutrons";
Institute of Physics Publishing Ltd., Brighton, (1994)
ISBN: 0-7503-0264-X

CALIEBE1997

Caliebe, Wolfgang A.:
"Inelastic X-Ray Scattering with High Energy Resolution"
Mathematisch-Naturwissenschaftliche Fakultät, Christian-Albrechts-Universität (1997) Kiel
Dissertation

CEULEMANS2002

Ceulemans, R., Jach, M. E., Van de Velde, R., Lin, J. X., and Stevens, M.:
"Elevated atmospheric CO₂ alters wood production, wood quality and wood strength of Scots pine (*Pinus sylvestris* L) after three years of enrichment";
Global Change Biology; Vol. **8** (2), pages 153-162 (2002)
DOI: 10.1046/j.1354-1013.2001.00461.x

COWLEY1995

Cowley, John Maxwell:
"Diffraction Physics"; 3rd ed.,
Elsevier Science B. V., Amsterdam, (1995)
ISBN: 0-444-82218-6

COWLEY2003

Cowley, R. A.:
"Quantum entanglement and neutron scattering experiments";
Journal of Physics-Condensed Matter; Vol. **15** (24), pages 4143-4152 (2003)
DOI: 10.1088/0953-8984/15/24/308

CZIHAK1999

Czihak, Christoph, Müller, Martin, Schober, Helmut, Heux, L., and Vogl, Gero:
"Dynamics of water adsorbed to cellulose";
Physica B; Vol. **266**, pages 87-91 (1999)

CZIHAK2000A

Czihak, Christoph, Müller, Martin, Schober, Helmut, and Vogl, Gero:
"Relaxational motion and ice formation of water adsorbed to cellulose";
Journal de Physique IV - Proceedings; Vol. **10** (Pr7), pages 199-202 (**2000b**)

CZIHAK2000

Czihak, Christoph, Müller, Martin, Schober, Helmut, and Vogl, Gero:
"Ice formation in amorphous cellulose";
Physica B; Vol. **276-278**, pages 286-287 (**2000a**)
DOI: 10.1016/S0921-4526(99)01468-4

CZIHAK2000B

Czihak, Christoph Andreas:
"Cellulose: Structure and dynamics of a naturally occurring composite material as investigated by inelastic neutron scattering" (**2000**) Wien
Dissertation

DAY1969

Day, D. H., Johnson, D. A. G., and Sinclair, R. N.:
"The use of vanadium scattering to intercalibrate an array of thermal neutron detectors";
Nuclear Instruments & Methods; Vol. **70** (2), pages 164-168 (**1969**)
DOI: 10.1016/0029-554X(69)90375-9

DIETENBERGER1999

Dietenberger, Mark A., Green, David W., Kretschmann, David E., Hernandez, Roland, Highley, Terry L., Ibach, Rebecca E., Liu, Jen Y., McDonald, Kent A., Miller, Regis B., Moody, Russel C., Rowell, Roger M., Simpson, William T., Soltis, Lawrence A., TenWolde, Anton, Wolfe, Ronald W., Vick, Charles B., White, Robert H., Williams, R. Sam, Winandy, Jerrold E., and Youngquist, John A.:
"Wood Handbook - Wood as an Engineering Material"
U.S. Department of Agriculture, Forest Service, Forest Products Laboratory Report No. FPL-GTR-113, (**1999**)

DILG1974

Dilg, W.:
"Redetermination of the slow neutron scattering cross section for vanadium";
Nuclear Instruments & Methods; Vol. **122**, pages 343-346 (**1974**)
DOI: 10.1016/0029-554X(74)90497-2

DORNER2005B

Dorner, Bruno:
"Normalisation of the resolution function in TOF technique";
Journal of Neutron Research; Vol. **13** (4), pages 267-274 (**2005**)
DOI: 10.1080/10238160512331330189

EIKENBERRY1991

Eikenberry, E. F., Tate, M. W., Belmonte, A. L., Lowrance, J. L., Bilderback, D., and Gruner, S. M.:
"A Direct-Coupled Detector for Synchrotron X-Radiation Using A Large Format Ccd";
Ieee Transactions on Nuclear Science; Vol. **38** (2), pages 110-118 (**1991**)
DOI: 10.1109/23.289282

EISENHAUER1958

Eisenhauer, C. M., Pelah, I., Hughes, D. J., and Palevsky, H.:
"Measurement of Lattice Vibrations in Vanadium by Neutron Scattering";
Physical Review; Vol. **109** (4), pages 1046-1051 (**1958**)
DOI: 10.1103/PhysRev.109.1046

ENGELNMÜLLGES2005

Engeln-Müllges, Gisela, Niederdrenk, Klaus, and Wodicka, Reinhard:
"Numerik-Algorithmen"; 9 ed., (2005)
ISBN: 3-540-62669

ENQUIST1999

Enquist, B. J., West, G. B., Charnov, E. L., and Brown, J. H.:
"Allometric scaling of production and life-history variation in vascular plants";
Nature; Vol. **401** (6756), pages 907-911 (1999)
DOI: 10.1038/44819

FAVIER1995A

Favier, V., Chanzy, H., and Cavaille, J. Y.:
"Polymer Nanocomposites Reinforced by Cellulose Whiskers";
Macromolecules; Vol. **28** (18), pages 6365-6367 (1995)

FENGEL1971

Fengel, D.:
"Ideas on the ultrastructural organization of the cell wall components";
Journal of Polymer Science Part C; Vol. **36**, pages 383-392 (1971)

FENGEL1984

Fengel, Dietrich and Wegener, Gerd:
"Wood: Chemistry, Ultrastructure, Reactions";
Walter de Gruyter, Berlin, New York, (1984)
ISBN: 3-11-008481-3

FREYWYSSELING1954

Frey-Wysseling, A.:
"The fine structure of cellulose microfibrills";
Science; Vol. **119**, pages 80-82 (1954)

FREYWYSSELING1937

Frey-Wysseling, A.:
"Röntgenometrische Vermessung der submikroskopischen Räume in Gerüstsubstanzen";
Protoplasma; Vol. **27** (1), pages 372-411 (1937)
DOI: 10.1007/BF01599405

GAO1993

Gao, T., Li, Y. J., Rousseau, J., Linliu, K., and Chu, B.:
"An Economical X-Ray Area Detector Based on An Intensified Ccd Unit";
Review of Scientific Instruments; Vol. **64** (2), pages 390-396 (1993)
DOI: 10.1063/1.1144262

HAAS1963

Haas, R., Kley, W., Krebs, K. H., and Rubin, R.:
"Phonon Frequency Distribution of Vanadium"
International Atomic Energy Agency, Vienna, (1963)

HAMMERSLEY1996

Hammersley, A. P., Svensson, S. O., Hanfland, M., Fitch, A. N., and Hausermann, D.:
"Two-dimensional detector software: From real detector to idealised image or two-theta scan";
High Pressure Research; Vol. **14** (4-6), pages 235-248 (1996)

HAMMERSLEY1994

Hammersley, A. P., Svensson, S. O., and Thompson, A.:
"Calibration and Correction of Spatial Distortions in 2D Detector Systems";
Nuclear Instruments & Methods in Physics Research Section A-Accelerators Spectrometers Detectors
and Associated Equipment; Vol. **346** (1-2), pages 312-321 (**1994**)

HELBERT1998

Helbert, William, Nishiyama, Yoshiharu, Okano, Takeshi, and Sugiyama, Junji:
"Molecular imaging of *Halocynthia papillosa* cellulose";
Journal of Structural Biology; Vol. **124**, pages 42-50 (**1998**)

HERMANS1946

Hermans, P. H.:
"Contribution to the physics of cellulose fibres - A study in sorption, density, refractive power and orientation";
Elsevier Publishing Company Inc., Amsterdam, Brussels, London, New York, (**1946**), Vol. 3

HOADLEY2000

Hoadley, R. Bruce:
"Understanding wood: A craftsman's guide to wood technology";
Taunton Press, Newtown, CT, (**2000**)
ISBN: 1-56158-358-8

HOFSTETTER2006

Hofstetter, K., Hinterstoisser, B., and Salmen, L.:
"Moisture uptake in native cellulose - the roles of different hydrogen bonds: a dynamic FT-IR study using Deuterium exchange";
Cellulose; Vol. **13** (2), pages 131-145 (**2006**)
DOI: 10.1007/s10570-006-9055-2

HORI2005

Hori, R. and Wada, M.:
"The thermal expansion of wood cellulose crystals";
Cellulose; Vol. **12** (5), pages 479-484 (**2005**)
DOI: 10.1007/s10570-005-5967-5

HOWIE2001

Howie, John Mackintosh:
"Real Analysis";
Springer-Verlag, London, (**2001**)
ISBN: 1-85233-314-6

IMAI1998A

Imai, Tomoya and Sugiyama, Junji:
"Nanodomains of I_α and I_β cellulose in algal microfibrils";
Macromolecules; Vol. **31** (18), pages 6275-6279 (**1998**)
DOI: 10.1021/ma980664h

IOELOVITCH1994

Ioelovitch, M. and Gordeev, M.:
"Crystallinity of cellulose and its accessibility during deuteration";
Acta Polymerica; Vol. **45** (2), pages 121-123 (**1994**)
DOI: 10.1002/actp.1994.010450211

IVANOV2000

Ivanov, A. S. and Rumiantsev, A. Y.:
"Phonon dispersion in vanadium metal";
Physica B; Vol. **276**, pages 197-199 (**2000**)
DOI: 10.1016/S0921-4526(99)01247-8

JAKOB1994

Jakob, H. F., Fratzl, P., and Tschegg, S. E.:
"Size and arrangement of elementary cellulose fibrils in wood cells: a small-angle X-ray scattering study of *Picea abies*";
Journal of Structural Biology; Vol. **113**, pages 13-22 (**1994**)

JAKOB1996

Jakob, H. F., Tschegg, S. E., and Fratzl, P.:
"Hydration dependence of the wood-cell wall structure in *Picea abies*. A small-angle X-ray scattering study";
Macromolecules; Vol. **29** (26), pages 8435-8440 (**1996**)
DOI: 10.1021/ma9605661

JAMES1982

James, R. W.:
"The optical principles of the diffraction of x-rays";
Ox Bow Press, Woodbridge, (**1982**)
ISBN: 0-918024-23-4

JANSSEN2000

Janssen, S., Altorfer, F., Holitzner, L., and Hempelmann, R.:
"Time-of-flight spectrometer FOCUS at SINQ: first results";
Physica B; Vol. **276**, pages 89-90 (**2000**)
DOI: 10.1016/S0921-4526(99)01253-3

JANSSEN1997

Janssen, S., Mesot, J., Holitzner, L., Furrer, A., and Hempelmann, R.:
"FOCUS: A hybrid TOF-spectrometer at SINQ";
Physica B; Vol. **234-236**, pages 1174-1176 (**1997**)
DOI: 10.1016/S0921-4526(97)00209-3

JURANYI2003

Juranyi, F., Janssen, S., Mesot, J., Holitzner, L., Kagi, C., Tuth, R., Burge, R., Christensen, M., Wilmer, D., and Hempelmann, R.:
"The new mica monochromator for the time-of-flight spectrometer FOCUS at SINQ";
Chemical Physics; Vol. **292** (2-3), pages 495-499 (**2003**)
DOI: 10.1016/S0301-0104(03)00175-7

JURANYI2006

Juranyi, F.:
"Detector Efficiency Compensation"
Grotkopp, Ingo. (**2006**)
Reference Type: Internet Communication

JURANYI2004

Juranyi, F.:
"Focus Description"
http://sinq.web.psi.ch/sinq/instr/focus/focus_description.html. (**2004**)
-Paul Scherrer Institut.
Reference Type: Electronic Citation

KAMAL1978

Kamal, M., Malik, S. S., and Rorer, D.:

"Neutron incoherent elastic scattering study of the temperature dependence of the Debye-Waller exponent in vanadium";

Physical Review B; Vol. **18**, pages 1609-1617 (**1978**)

DOI: 10.1103/PhysRevB.18.1609

KECKES2003

Keckes, Jozef, Burgert, Ingo, Fruhmann, Klaus, Müller, Martin, Kölln, Klaas, Hamilton, Myles, Burghammer, Manfred, Roth, Stephan V., Stanzl-Tschegg, Stefanie, and Fratzl, Peter:

"Cell-wall recovery after irreversible deformation of wood";

Nature Materials; Vol. **2** (12), pages 810-814 (**2003**)

DOI: 10.1038/nmat1019

KOCH1994

Koch, A.:

"Lens Coupled Scintillating Screen Ccd X-Ray Area Detector with A High Detective Quantum Efficiency";

Nuclear Instruments & Methods in Physics Research Section A-Accelerators Spectrometers Detectors and Associated Equipment; Vol. **348** (2-3), pages 654-658 (**1994**)

KÖLLN2000

Kölln, Klaas:

"Untersuchung der Rotations- und Translationsdynamik von Propan in der SiO₂-Modifikation MCM-41 mit Neutronenstreuung"

Institut für Experimentelle und Angewandte Physik der Christian-Albrechts-Universität (**2000**) Kiel
Diploma Thesis

KÖLLN2004

Kölln, Klaas:

"Morphologie und mechanische Eigenschaften von Zellulosefasern; Untersuchungen mit Röntgen- und Neutronenstreuung"

Mathematisch-Naturwissenschaftliche Fakultät der Christian-Albrechts-Universität zu Kiel (**2004**)
Dissertation

KÖLLN2005

Kölln, Klaas, Grotkopp, Ingo, Burghammer, Manfred, Roth, S. V., Funari, Sergio S., Dommach, Martin, and Müller, Martin:

"Mechanical properties of cellulose fibres and wood. Orientational aspects in situ investigated with synchrotron radiation";

Journal of Synchrotron Radiation; Vol. **12** (6), pages 739-744 (**2005**)

DOI: 10.1107/S0909049505011714

KRANTZ2004

Krantz, Steven George:

"Real Analysis and Foundations"; 2nd ed.,

CRC Press, (**2004**), Vol. 44

ISBN: 1-58488-483-5

KRÄSSIG1993

Krässig, Hans A.:

"Cellulose: Structure, Accessibility and Reactivity";

Gordon and Breach Science Publishers, Yverdon, (**1993**), Vol. 11

ISBN: 2-88124-798-9

KROONBATENBURG1996

Kroon-Batenburg, L. M. J., Bouma, B., and Kroon, J.:
"Stability of cellulose structures studied by MD simulations. Could mercerized cellulose II be parallel?";
Macromolecules; Vol. **29** (17), pages 5695-5699 (1996)
DOI: 10.1021/ma9518058

LANGAN2005

Langan, P., Sukumar, N., Nishiyama, Y., and Chanzy, H.:
"Synchrotron X-ray structures of cellulose I β and regenerated cellulose II at ambient temperature and 100K";
Cellulose; Vol. **in press**(2005)

LICHTENEGGER1999A

Lichtenegger, H., Müller, M., Paris, O., Riekkel, C., and Fratzl, P.:
"Imaging of the helical arrangement of cellulose fibrils in wood by synchrotron X-ray microdiffraction";
Journal of Applied Crystallography; Vol. **32**, pages 1127-1133 (1999)

LICHTENEGGER1997

Lichtenegger, H., Reiterer, A., Tschegg, S., and Fratzl, P.:
"Determination of Spiral Angles of Elementary Fibrils in the Wood Cell Wall: Comparison of Small-Angle X-Ray Scattering and Wide-Angle X-Ray Diffraction"
University of Canterbury, (1997)

LOVESEY1984

Lovesey, Stephen W.:
"Theory of Neutron Scattering from Condensed Matter; Vol. I: Nuclear Scattering";
Clarendon Press, Oxford, (1984), Vol. 1
ISBN: 0-19-852015-8

LOVESEY1977

Lovesey, Stephen W. and Springer, Tasso
Lovesey, Stephen W., Springer, Tasso, Comès, R., Dorner, B., Loveluck, J. M., Mountain, R. D., and White, J. W.:
"Dynamics of Solids and Liquids by Neutron Scattering";
Springer-Verlag, Berlin, (1977), Vol. 3
ISBN: 3-540-08156-9

MAINTZ1998

Maintz, J. B. and Viergever, M. A.:
"A survey of medical image registration";
Medical Image Analysis; Vol. **2** (1), pages 1-36 (1998)
DOI: 10.1016/S1361-8415(01)80026-8

MATTHECK1991

Mattheck, C.:
"Trees - The Mechanical Design";
Springer-Verlag, Berlin, (1991)
ISBN: 3-540-54276-0

MATTHECK1995

Mattheck, Claus and Kubler, Hans:
"Wood - The Internal Optimization of Trees";
Springer-Verlag, Berlin, Heidelberg, New York, (1995)

MAYERS1984

Mayers, J.:
"The use of vanadium as a scattering standard for pulsed source neutron spectrometers";
Nuclear Instruments & Methods in Physics Research; Vol. **221** (3), pages 609-618 (**1984**)
DOI: 10.1016/0167-5087(84)90073-5

MEINGUET1979

Meinguet, Jean:
"Multivariate interpolation at arbitrary points made simple";
Zeitschrift für Angewandte Mathematik und Physik; Vol. **30** (2), pages 292-304 (**1979**)
DOI: 10.1007/BF01601941

MESOT1996

Mesot, J., Janssen, S., Holitzner, L., and Hempelmann, R.:
"Focus: Project of a Space and Time Focussing Time-of-Flight Spectrometer for Cold Neutrons at the
Spallation Source SINQ of the Paul Scherrer Institute";
Journal of Neutron Research; Vol. **3**, pages 293-310 (**1996**)

MODERSITZKI2004

Modersitzki, Jan:
"Numerical Methods for Image Registration";
Oxford University Press, Oxford, New York, (**2004**)
ISBN: 0-19-852841-8

MÜLLER1996

Müller, Martin:
"Anordnung und Dynamik der NH₂-Ionen in Kalium- und Strontiumamid: Untersuchungen mit Neu-
tronenstreuung"
Mathematisch-Naturwissenschaftliche Fakultät, Christian-Albrechts-Universität (**1996**) Kiel
Dissertation

MÜLLER2006

Müller, M., Burghammer, M., and Sugiyama, J.:
"Direct investigation of the structural properties of tension wood cellulose microfibrils using mi-
crobeam X-ray fibre diffraction". (**2006**)
Reference Type: Unpublished Work

MÜLLER2000B

Müller, Martin, Czihak, Christoph, Burghammer, Manfred, and Riekkel, Christian:
"Combined X-ray microbeam small-angle scattering and fibre diffraction experiments on single native
cellulose fibres";
J.Appl.\ Cryst.; Vol. **33**, pages 817-819 (**2000a**)

MÜLLER2000A

Müller, Martin, Czihak, Christoph, Schober, Helmut, Nishiyama, Yoshiharu, and Vogl, Gero:
"All disordered regions of native cellulose show common low-frequency dynamics";
Macromolecules; Vol. **33** (5), pages 1834-1840 (**2000b**)
DOI: 10.1021/ma9912271

MÜLLER1998

Müller, Martin, Czihak, Christoph, Vogl, Gero, Fratzl, Peter, Schober, Helmut, and Riekkel, Christian:
"Direct observation of microfibril arrangement in a single native cellulose fiber by microbeam small-
angle X-ray scattering";
Macromolecules; Vol. **31** (12), pages 3953-3957 (**1998**)
DOI: 10.1021/ma980004c

MYERS1997

Myers, H. P.:
"Introductory Solid State Physics"; 2nd ed.,
Taylor & Francis Ltd., London, (1997)
ISBN: 0-7484-0659-X

NAVI1997

Navi, Parviz:
"The influence of microfibril angle on wood cell and wood mechanical properties, experimental and numerical study"
University of Canterbury, (1997)

NAVI1995

Navi, Parviz, Rastogi, K., Gress, V., and Tolou, A.:
"Micromechanics of wood subjected to axial tension";
Wood Science and Technology; Vol. 29, pages 411-429 (1995)

NEWTON2002

Newton, Roger G.:
"Scattering theory of waves and particles"; 2nd, Dover ed.,
Dover Publications Inc., Mineola, New York, (2002)
ISBN: 0-486-42535-5

NIKLAS1992

Niklas, Karl J.:
"Plant Biomechanics: An Engineering Approach to Plant Form and Function";
The University of Chicago Press, Chicago, London, (1992)
ISBN: 0-226-58631-6

NISHIYAMA2003A

Nishiyama, Y., Kim, U. J., Kim, D. Y., Katsumata, K. S., May, R. P., and Langan, P.:
"Periodic disorder along ramie cellulose microfibrils";
Biomacromolecules; Vol. 4 (4), pages 1013-1017 (2003a)
DOI: 10.1021/bm025772x

NISHIYAMA2003

Nishiyama, Y., Sugiyama, J., Chanzy, H., and Langan, P.:
"Crystal structure and hydrogen bonding system in cellulose I α , from synchrotron X-ray and neutron fiber diffraction";
Journal of the American Chemical Society; Vol. 125 (47), pages 14300-14306 (2003b)
DOI: 10.1021/ja037055w

NISHIYAMA2002A

Nishiyama, Yoshiharu, Langan, Paul, and Chanzy, Henri:
"Crystal structure and hydrogen-bonding system in cellulose I β from synchrotron X-ray and neutron fiber diffraction";
Journal of the American Chemical Society; Vol. 124 (31), pages 9074-9082 (2002)
DOI: 10.1021/ja0257319

OSULLIVAN1997

O'Sullivan, Antoinette C.:
"Cellulose: the structure slowly unravels";
Cellulose; Vol. 4 (3), pages 173-207 (1997)
DOI: 10.1023/A:1018431705579

OTTONELLO1994

Ottonello, P., Rottigni, G. A., Zanella, G., and Zannoni, R.:
"Hard X-Ray-Imaging with High Detection Efficiency and High-Spatial-Resolution";
Nuclear Instruments & Methods in Physics Research Section A-Accelerators Spectrometers Detectors
and Associated Equipment; Vol. **346** (1-2), pages 379-384 (1994)

PAGE1983

Page, D. H. and El-Hosseiny, F.:
"The mechanical properties of single wood pulp fibres. Part IV, Fibril angle and the shape of the stress-strain curve.";
Journal of Pulp and Paper Science; Vol. **9** (4), pages 1-2 (1983)

PAGE1967

Page, D. I.:
"The phonon frequency distribution of vanadium";
Proceedings of the Physical Society; Vol. **91**, pages 76-85 (1967)

PEURA2006

Peura, M., Grotkopp, I., Lemke, H., Vikkula, A., Laine, J., Muller, M., and Serimaa, R.:
"Negative Poisson ratio of crystalline cellulose in Kraft cooked Norway spruce";
Biomacromolecules; Vol. **7** (5), pages 1521-1528 (2006a)
DOI: 10.1021/bm050722o

PEURA2006A

Peura, M., Grotkopp, I., Lemke, H., Vikkula, A., Laine, J., Muller, M., and Serimaa, R.:
"Negative Poisson ratio of crystalline cellulose in Kraft cooked Norway spruce";
Biomacromolecules; Vol. **7** (5), pages 1521-1528 (2006b)

PLACZEK1952

Placzek, G.:
"The Scattering of Neutrons by Systems of Heavy Nuclei";
Physical Review; Vol. **86** (3), pages 377-388 (1952)
DOI: 10.1103/PhysRev.86.377

PRESTON1974

Preston, R. D.:
"The Physical Biology of Plant Cell Walls";
Chapman and Hall, London, (1974)
ISBN: 0-412-11600-6

PRICE1986

Sköld, Kurt and Price, David L.
Price, David L., Sköld, Kurt, Carpenter, John M., Yelon, William B., Windsor, Colin G., Werner, Samuel A., Klein, Anthony G., Schultz, Arthur J., Stassis, C., Pawley, G. Stuart, and Sears, Varley F.:
"Neutron Scattering Part A";
Academic Press, Inc., Orlando, (1986), Vol. 23
ISBN: 0-12-475965-3

ROTH2005

Roth, S. V.:
"Small Angle X-Ray Scattering @ Hasylab - Overview"
http://www-hasylab.desy.de/science/groups/saxs_group/pic/optics.gif. (2005)
Reference Type: Electronic Citation

SAXENA2005

Saxena, I. M. and Brown, R. M.:
"Cellulose biosynthesis: Current views and evolving concepts";
Annals of Botany; Vol. **96** (1), pages 9-21 (**2005**)
DOI: 10.1093/aob/mci15

SCHWEINGRUBER1993

Schweingruber, F. H.:
"Trees and Wood in Dendrochronology";
Springer-Verlag, Berlin, (**1993**)
ISBN: 3-540-54915-3

SEITSONEN1973

Seitsonen, S. and Mikkonen, I.:
"X-ray study on the thermal expansion of cotton cellulose";
Polymer Journal; Vol. **5**, pages 263-267 (**1973**)

SIMMONS2003

Simmons, Ralph O.:
"Scattering Studies of Condensed Helium Isotopes"
"Lecture Notes in Physics"
Springer-Verlag, Berlin, Heidelberg, New York, (**2003**)

SKAAR1988

Skaar, Christen:
"Wood-Water Relations";
Springer-Verlag GmbH, Berlin, Heidelberg, New York, (**1988**)
ISBN: 3-540-19258-1

SPRINGER1972

Höhler, G.
Springer, Tasso:
"Quasielastic Neutron Scattering for the Investigation of Diffusive Motions in Solids and Liquids";
Springer-Verlag, Berlin, (**1972**), Vol. 64
ISBN: 3-540-05808-7

SQUIRES1978

Squires, G. L.:
"Introduction to the theory of thermal neutron scattering";
Cambridge University Press, Cambridge, (**1978**)
ISBN: 0-521-21884-5

STEWART1958

Stewart, A. T. and Brockhouse, B. N.:
"Vibration Spectra of Vanadium and a Mn-Co Alloy by Neutron Spectrometry";
Review of Modern Physics; Vol. **30** (1), pages 250-255 (**1958**)
DOI: 10.1103/RevModPhys.30.250

SUGIYAMA1985

Sugiyama, Junji, Harada, Hiroshi, Fujiyoshi, Yoshinori, and Uyeda, Natsu:
"Lattice images from ultrathin sections of cellulose microfibrils in the cell wall of *Valonia macrophysa* Kütz";
Planta; Vol. **166**, pages 161-168 (**1985**)

TREGENNAPIGGOTT2005

Tregenna-Piggott, P. L. W.:
"Data Reduction on Time-of-Flight Instruments";
Swiss Neutron News; Vol. **28**, pages 4-12 (**2005**)

TURCHIN1965

Turchin, V. F.:
"Slow Neutrons";
Israel Program for Scientific Translation Ltd., (1965)

TYREE2002

Tyree, Melvin T. and Zimmermann, Martin H.:
"Xylem Structure and the Ascent of Sap"; 2nd ed.,
Springer-Verlag GmbH, Berlin, Heidelberg, New York, (2002)
ISBN: 3-540-43354-6

VINCENT1990

Vincent, Julian F. V.:
"Structural Biomaterials"; revised ed. ed.,
Princeton University Press, Princeton, New Jersey, (1990)
ISBN: 0-691-02513-4

VOLINO1978

Volino, F.:
"Spectroscopic Methods for the Study of Local Dynamics in Polyatomic Fluids"
"NATO advanced study institute series: Series B, Physics"
Plenum Publishing Corporation, New York, London, (1978)

WALLER1952

Waller, I. and Fröman, P. O.:
"On neutron diffraction phenomena according to the kinematical theory. I";
Arkiv för Fysik; Vol. 4 (5), pages 183-189 (1952)

WARDROP1953

Wardrop, A. B.:
"The fine structure of the conifer tracheid";
Holzforschung; Vol. 8 (1), pages 12-29 (1953)

WARREN1990

Warren, B. E.:
"X-Ray Diffraction";
Dover Publications Inc., New York, (1990)
ISBN: 0-486-66317-5

WILLIS1975

Willis, B. T. M. and Pryor, A. W.:
"Thermal Vibrations in Crystallography";
Cambridge University Press, (1975)
ISBN: 0-521-20447-X

WILSON1992

Wilson, A. J. C.
Wilson, A. J. C.:
"International Tables for Crystallography - Mathematical, physical and chemical tables";
KLUWER ACADEMIC PUBLISHERS, Dordrecht, Boston, London, (1992), Vol. C
ISBN: 0-792-3-16-38-X

WOODCOCK1980

Woodcock, Carrie and Sarko, Anatole:
"Packing analysis of carbohydrates and polysaccharides. 11. Molecular and crystal structure of native ramie cellulose";
Macromolecules; Vol. 13 (5), pages 1183-1187 (1980)

YARNELL1973

Yarnell, J. L., Katz, M. J., Wenzel, R. G., and Koenig, S. H.:
"Structure Factor and Radial Distribution Function for Liquid Argon at 85 °K";
Physical Review A; Vol. 7 (6), pages 2130-2144 (1973)
DOI: 10.1103/PhysRevA.7.2130

ZANEVSKY1995A

Zanevsky, Y. V., Chernenko, S. P., Cheremukhina, G. A., Fateev, O. V., Kheiker, D. M., Andrianova, M. E., and Sulianov, S. N.:
"Test results of the parallax-free X-ray area detector SD-1000 in the diffractometer CARD-7";
Nuclear Instruments & Methods in Physics Research Section A-Accelerators Spectrometers Detectors and Associated Equipment; Vol. 367 (1-3), pages 76-78 (1995)
DOI: 10.1016/0168-9002(95)00650-8

ZIMMERMANN1971

Zimmermann, Martin H., Brown, Claud L., and Tyree, Melvin T.:
"Trees - Structure and Function";
Springer-Verlag, Berlin, (1971)
ISBN: 3-540-05367-0

ZWEIFEL1999

Zweifel, Roman:
"The rhythm of trees - Water storage dynamics in subalpine Norway spruce."
Swiss Federal Institute of Technology (1999) Zürich
Dissertation

Teile dieser Arbeit wurden bereits veröffentlicht:

PEURA2006

Peura, M., Grotkopp, I., Lemke, H., Vikkula, A., Laine, J., Muller, M., and Serimaa, R.:
"Negative Poisson ratio of crystalline cellulose in Kraft cooked Norway spruce";
Biomacromolecules; Vol. 7 (5), pages 1521-1528 (**2006a**)
DOI: 10.1021/bm050722o

KÖLLN2005

Kölln, Klaas, Grotkopp, Ingo, Burghammer, Manfred, Roth, S. V., Funari, Sergio S., Dommach, Martin, and Müller, Martin:
"Mechanical properties of cellulose fibres and wood. Orientational aspects in situ investigated with synchrotron radiation";
Journal of Synchrotron Radiation; Vol. 12 (6), pages 739-744 (**2005**)
DOI: 10.1107/S0909049505011714

Lebenslauf

Name: Ingo Grotkopp
geboren: am 12.01.1971 in Hamburg
Staatsangehörigkeit: deutsch
Familienstand: verheiratet (ab 23.06.06)
Anschrift: Nettelbeckstraße 10, 24105 Kiel

Ausbildungsgang

1977 - 1981 Grundschule in Leezen
1981 - 1987 Realschule am Seminarweg in Bad Segeberg
05.06.1987 Realschulabschluss
1987 - 1990 Berufsausbildung zum Industriemechaniker Fachrichtung Geräte- und Feinwerktechnik bei der Olympus Winter & Ibe GmbH und an der G16 in Hamburg
20.06.1990 „Gesellenbrief“ zum Industriemechaniker
1990 - 1991 Fachoberschule Technik der Beruflichen Schulen des Kreises Segeberg
22.06.1991 Fachhochschulreife
1991 - 1992 Grundwehrdienst
1992 - 1995 Studium der Feinwerktechnik Studienschwerpunkt Konstruktion und Produktion an der Fachhochschule Kiel
31.01.1994 Vordiplom
26.09.1994 - berufspraktisches Studiensemester in den Unternehmensbereichen der Olympus Winter & Ibe GmbH in Hamburg
24.02.1995
12.05.1995 - Diplomarbeit bei der Groni-Metall GmbH in Groß Niendorf zum Thema „Aufbau einer Anlage zur Laserbeschriftung zylindrischer Werkstücke“
11.08.1995
28.09.1995 Diplom-Ingenieur (Fachhochschule)
1995 - 2002 Physikstudium an der Christian-Albrechts-Universität zu Kiel
27.10.1997 Diplom-Vorprüfung mit Nebenfach Chemie
23.09.2002 Diplom-Physiker mit Nebenfach Mathematik
2002 - 2006 Promotion an der Christian-Albrechts-Universität zu Kiel

Berufstätigkeit

1994 - 1995 Geschäftsführer der Groni-Metall GmbH in Groß Niendorf
1996 - 1999 Gesellschafter-Geschäftsführer der Groni-Metall GmbH in Groß Niendorf und Itzstedt
2002 - 2006 Wissenschaftlicher Mitarbeiter der Christian-Albrechts-Universität zu Kiel

Erklärung

Hiermit erkläre ich, dass die Abhandlung – abgesehen von der Beratung durch meinen Betreuer und den angegebenen Quellen – nach Inhalt und Form meine eigene Arbeit ist. Diese Arbeit wurde weder ganz noch in Teilen an anderer Stelle im Rahmen eines Prüfungsverfahrens vorgelegt. Diese Arbeit ist unter Einhaltung der Regeln guter wissenschaftlicher Praxis entstanden. Frühere Promotionsversuche wurden von mir nicht vorgenommen.

Kiel, den 31.05.2006

(Ingo Grotkopp)

Acknowledgements

First of all I would like to thank Prof. Dr. Martin Müller for the opportunity to work on this fascinating subject and for all his support during the last years. It has been a great pleasure for me to become a part of his team and to do so many wonderful experiments with him.

Most of the experiments that I presented in this thesis have been performed at large scale research facilities. Hence, I would like to thank the nearly infinite number of people that had been involved there. Without any order I would namely thank therefore Sergio Funari and Martin Dommach from the HASYLAB, Christian Riekkel, Manfred Burghammer and Richard Davies from the ESRF, Fanni Juranyi, Thierry Strässle, Andrew Padlesnyak, Lothar Holitzner and Stefan Janssen from the PSI. Also I give many thanks to my co-workers at this beam times, for example Marko Peura, Claas Behrend, Klaas Kölln and very ambitious Henrik Lemke.

It goes without saying, that a lot of financial support has been necessary to enable research, as presented in this study. Therefore, I express great thanks for foundation to the DFG (Mu 1673/3-1), the BMBF via the Saarland University, the HASYLAB (II-01-054, II-04-051) and the University of Kiel.

Nevertheless, to enable us to do any of these measurements there have been a lot of helping hands in advance, as there is Ms. Monika Seeger, our world class Secretary, her husband Arnd, our high speed technician and, very important, our system administrator. To complete this list I like to thank Joost Jacobs, our vacuum expert, especially for his natural talent to organise things like cars within our university even if there are actually non present. And for his permanent ground readiness with respect to any question and his support, not only limited to radiation protection, I have to thank Jochim Stettner.

Beside this, there has been a lot of mechanical equipment built especially designed for our needs, that has been conjured from a team of wizards in our mechanical workshop. Therefore, great thanks to Mr. Brix and his people, e.g. Mario Kreft. Again, I have to thank Klaas Kölln in this context for not offering too much resistance against my guidance during the development of the first big stretching device, that he also used in his work.

The actual status of this thesis is directly related to the efforts all the readers had spent during proofreading of the manuscript to find typos and to Figure out all the other obscurities, that have been invisible for me. Therefore, my thanks for their patience to them, namely Jörn Kanzow, Bridget Murphy, the Sowada family and my wife.

Additional thanks are directed to our group of coffee drinkers, e.g. Daniel Esch and Prof. Dr. Helbig, who helped me hundreds times in everlasting discussions about light and everything else.

In the same way, I want to thank my mother for here constant backing and her partner Heinz for his spiritual guidance.

Very special thanks go to Prof. Dr. Ulrich Sowada and his wife Gabriele. They started to become a very important part of my life since my days at the University for Applied Science and have ever since provided me with endless support and best advice even in hardest times.

Finally, I express my most important thanks from the bottom of my heart to my sunlight, my wife Janina, for the good fortune that she brings into my life every day again.